Feedback-Mediated Dynamics in the Kidney:

Mathematical Modeling and Stochastic Analysis

by

Hwayeon Ryu

Department of Mathematics
Duke University

Date: _____

Approved:

_____
Anita T. Layton, Co-Supervisor

_____
James Nolen, Co-Supervisor

_____
Michael C. Reed

_____
Thomas P. Witelski

Dissertation submitted in partial fulfillment of the requirements for the degree of
Doctor of Philosophy in the Department of Mathematics
in the Graduate School of Duke University
2014

Abstract

Feedback-Mediated Dynamics in the Kidney: Mathematical Modeling and Stochastic Analysis

by

Hwayeon Ryu

Department of Mathematics
Duke University

Date: _____

Approved:

_____
Anita T. Layton, Co-Supervisor

_____
James Nolen, Co-Supervisor

_____
Michael C. Reed

_____
Thomas P. Witelski

An abstract of a dissertation submitted in partial fulfillment of the requirements for the degree of Doctor of Philosophy in the Department of Mathematics in the Graduate School of Duke University
2014

Abstract

One of the key mechanisms that mediate renal autoregulation is the tubuloglomerular feedback (TGF) system, which is a negative feedback loop in the kidney that balances glomerular filtration with tubular reabsorptive capacity. In this dissertation, we develop several mathematical models of the TGF system to study TGF-mediated model dynamics.

First, we develop a mathematical model of compliant thick ascending limb (TAL) of a short loop of Henle in the rat kidney, called TAL model, to investigate the effects of spatial inhomogeneous properties in TAL on TGF-mediated dynamics. We derive a characteristic equation that corresponds to a linearized TAL model, and conduct a bifurcation analysis by finding roots of that equation. Results of the bifurcation analysis are also validated via numerical simulations of the full model equations.

We then extend the TAL model to explicitly represent an entire short-looped nephron including the descending segments and having compliant tubular walls, developing a short-looped nephron model. A bifurcation analysis for the TGF loop-model equations is similarly performed by computing parameter boundaries, as functions of TGF gain and delay, that separate differing model behaviors. We also use the loop model to better understand the effects of transient as well as sustained flow perturbations on the TGF system and on distal NaCl delivery.

To understand the impacts of internephron coupling on TGF dynamics, we further develop a mathematical model of a coupled-TGF system that includes any finite

number of nephrons coupled through their TGF systems, coupled-nephron model. Each model nephron represents a short loop of Henle having compliant tubular walls, based on the short-looped nephron model, and is assumed to interact with nearby nephrons through electrotonic signaling along the pre-glomerular vasculature. The characteristic equation is obtained via linearization of the loop-model equations as in TAL model. To better understand the impacts of parameter variability on TGF-mediated dynamics, we consider special cases where the relation between TGF delays and gains among two coupled nephrons is specifically chosen. By solving the characteristic equation, we determine parameter regions that correspond to qualitatively differing model behaviors.

TGF delays play an essential role in determining qualitatively and quantitatively different TGF-mediated dynamic behaviors. In particular, when noise arising from external sources of system is introduced, the dynamics may become significantly rich and complex, revealing a variety of model behaviors owing to the interaction with delays. In our next study, we consider the effect of the interactions between time delays and noise, by developing a stochastic model. We begin with a simple time-delayed transport equation to represent the dynamics of chloride concentration in the rigid-TAL fluid. Guided by a proof for the existence and uniqueness of the steady-state solution to the deterministic Dirichlet problem, obtained via bifurcation analysis and the contraction mapping theorem, an analogous proof for stochastic system with random boundary conditions is presented. Finally we conduct multiscale analysis to study the effect of the noise, specifically when the system is in subcritical region, but close enough to the critical delay. To analyze the solution behaviors in long time scales, reduced equations for the amplitude of solutions are derived using multiscale method.

To my family

Contents

List of Tables

List of Figures

List of Abbreviations and Symbols

Symbols

$\mathbb{R}$	The set of real numbers
$\mathbb{C}$	The set of complex numbers
$\mathbb{N}$	The set of natural numbers
$\mathcal{C}$	The set of continuous functions
$\mathcal{X}$	The set of functions in $\mathcal{C}([0,1]) \times \mathcal{C}([0,\tau])$
$\mathcal{B}$	The Banach space $\mathcal{C}([0,1])$
$\mathcal{H}$	The Banach space $\mathcal{C}([0,1] \times [0,T])$
Ω	The sample space
$\mathcal{F}$	σ-algebra associated with Ω
$\mathbb{P}$	Probability measure function
$\mathbb{E}$	Expected value

Abbreviations

TGF	Tubuloglomerular Feedback
AA	Afferent Arterial
EA	Efferent Arterial
PCT	Proximal Convoluted Tubule
PST	Proximal Straight Tubule
DL	Descending Limb

TAL	Thick Ascending Limb
DCT	Distal Convoluted Tubule
MD	Macula Densa
GFR	Glomerular Filtration Rate
SNGFR	Single Nephron Glomerular Filtration Rate
ATP	Adenosine Tri-Phosphate
JGA	Juxtaglomerular Apparatus
LCO	Limit-Cycle Oscillation
CRA	Cortial Radial Artery
SHR	Spontaneously Hypertensive Rats
ODE	Ordinary Differential Equation
PDE	Partial Differential Equation
SDE	Stochastic Differential Equation
SDDE	Stochastic Delay Differential Equation
SPDE	Stochastic Partial Differential Equation

Acknowledgements

I would like to thank numerous people who have supported me during my five years of graduate study at Duke University. First and foremost, I would like to thank two of my advisors, Anita T. Layton and James Nolen. Dr. Layton has been a wonderful mentor and has helped me to explore many interesting problems in mathematical physiology. I am grateful for her patience, enthusiasm, and tremendous help. Dr. Nolen has been a great teacher for me to learn various subjects and has helped me to go through a wide range of problems. I would like to express sincere thank to him for his valuable discussion.

Many thanks also go to the other members of my dissertation committee, Michael C. Reed and Thomas P. Witelski. Dr. Reed has been a great mentor from the very beginning of graduate program, so I would like to sincerely thank him for his willingness to listen to my concern and to guide me in the right direction. Also, I would like to thank Dr. Witelski for his invaluable suggestion and help.

In addition to my research experience, I have enjoyed my many teaching opportunities at Duke University and I am thankful for the teaching mentorship of Professors Lewis Blake, Jack Bookman, and Sarah Schott. I am also deeply grateful to my fellow graduate students in the Mathematics Department at Duke University for their collaboration and encouragement. I have been privileged to be supported by several fellowships during my graduate study and I would like to thank the National Science Foundation for support through a Mathematical Biology Research Training

Grant DMS-0943760 to the Department of Mathematics at Duke university as well as support through grant DMS-1007572 to Dr. James Nolen, National Institutes of Health for support through grant DK089066 to Dr. Anita T. Layton.

Finally, I would like to thank my family for their unconditional love and support. My wonderful husband, Timothy Changwon Lee, has been a constant source of encouragement and support for me to go through all the challenges of completing this thesis. I am, in particular, grateful for his spiritual support through his continuous prayer. I am also deeply grateful for my parents, sisters, and brother in South Korea, and all of family-in-law here in Raleigh, NC. Without their faithful prayers, this dissertation would have not been possible. Lastly, I would like to thank God for his endless blessings and amazing love. All of the gifts and abilities he has provided have enabled me to complete this dissertation.

1

Biological Background

In this chapter, we provide the biological background necessary to develop and understand our mathematical models of the tubuloglomerular feedback (TGF) in the kidney. We start by describing basic anatomy of the fundamental unit of the kidney, the nephron, and its functional properties. Then we explain renal autoregulation and its associated mechanisms at the level of the nephron. Finally we provide an overview of previous mathematical modeling studies in TGF.

1.1 The Nephron

The kidney plays a vital role in removing metabolic waste from the body while maintaining whole-organism chemical and physical stability. In particular, the kidney maintains a balance of volume, osmolarity, mineral composition, and acidity of blood plasma within the narrow limits that are compatible with effective cellular function; and the kidney participates in blood pressure regulation and in the maintenance of steady whole-organism water volume (Eaton and Pooler (2004)).

Most of the basic renal regulatory functions are achieved by multiple mechanisms that are associated with the individual functional unit of the kidney, called the

nephron. Each rat kidney is composed of about 38,000 nephrons (Han et al. (1992)); each human kidney contains up to a million nephrons (Nyengaard and Bendtsen (1992)). Each nephron consists of an initial filtering component called the renal corpuscle and a renal tubule containing a U-shaped loop of Henle, which is specialized for reabsorption and secretion.

Nephrons are classified depending on the location of their renal corpuscles and the length of their associated loop of Henle. The renal corpuscles of all nephrons are located in the cortex, which is the outer portion of the kidney. Short-looped, or cortical, nephrons have their loop of Henle in the cortex and the outer medulla. Specifically, depending on the relative location of their corpuscle within the cortex, cortical nephrons are divided into two different nephrons: superficial cortical nephrons with their renal corpuscle near the surface of the kidney and midcortical nephrons with their corpuscle deep down the cortex relative to the superficial nephrons. Long-looped, or juxtamedullary, nephrons have their loop that extends further into the inner medulla. Since many of transport properties of long-looped nephrons in the inner medulla have not been well characterized, we will consider the superficial, short-looped nephron based on its relatively well-discovered anatomic, biochemical, and functional characteristics. A schematic diagram of a short-looped nephron is shown in Fig. 1.1.

The renal corpuscle is the site of formation of the glomerular filtrate, and is composed of a glomerulus and Bowman's capsule. A glomerulus, labeled 'G' in Fig. 1.1, is a ball-shaped structure composed of capillary blood vessels that is surrounded by Bowman's capsule. Blood enters and leaves Bowman's capsule through an afferent arterial (AA) and an efferent arteriole, respectively. Through glomerular capillaries, approximately 20% of water and solutes in the blood are driven by pressure gradient into the space formed by Bowman's capsule. This filtrate then enters the first portion of the nephron tubule. The remainder of the blood leaves each glomerulus through

the efferent arteriole.

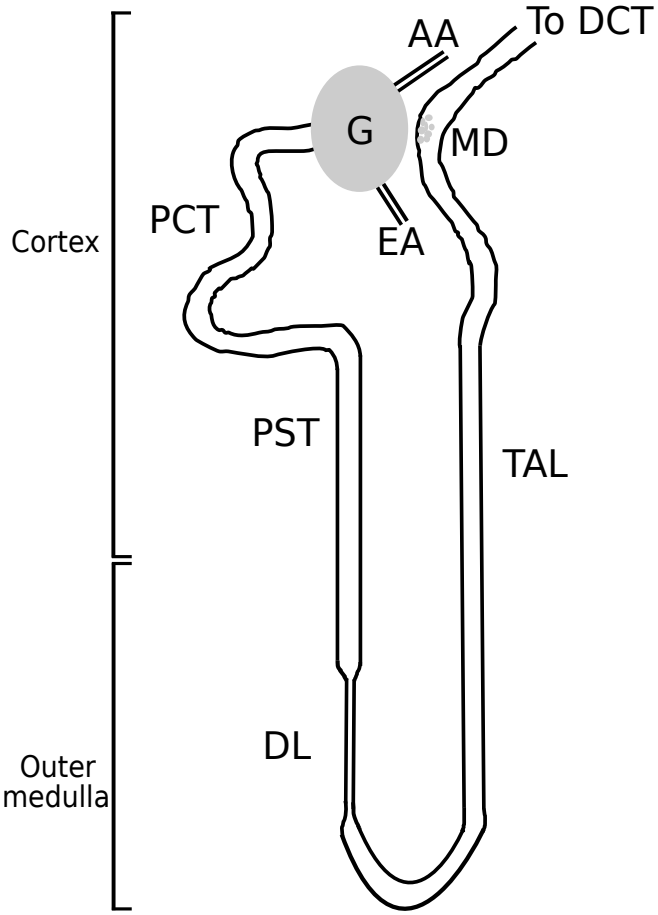

FIGURE 1.1: A schematic diagram of a short-looped nephron and its renal corpuscle, afferent arteriole (AA), and efferent arteriole (EA). Initially, blood enters via AA into a spherical filtering component, the glomerulus (G), through which the filtrate is generated and flows into the tubule. The first portion of the tubule, the proximal convoluted tubule (PCT), extends from the renal corpuscle and is followed by proximal straight tubule (PST) and descending limb (DL). At the boundary between outer and inner medullas, the terminal part of DL turns into the loop bend where the thick ascending limb (TAL) begins to rise back into the cortex. The macula densa (MD) cells located at the end of the TAL walls are adjacent to the AA and sense the chloride concentration in the downstream fluid. Once it passes through the MD, the fluid streams through the distal convoluted tubule (DCT) and flows into the collecting duct system (not shown), where the formation of urine occurs. Reprinted from Ryu and Layton (2013c).

One functional advantage of containing interconnected, narrow glomerular capillaries in the glomerulus is its ability to filter large amount of blood relative to

their mass while separating the filtrate from relatively large size of particles such as large plasma proteins, making the glomerular filtrate nearly protein-free. Despite the presence of smaller proteins such as many of the peptide hormones in the filtrate, the total mass of them is negligibly small compared to that of large plasma proteins within the blood (Eaton and Pooler (2004)).

A nephron tubule has walls made up of a single layer of epithelial cells and extends from the renal corpuscle into the proximal convoluted tubule, proximal straight tubule, and descending limb. Following the loop bend, the thick ascending limb (TAL) extends through the connecting tubule into the distal convoluted tubule that is followed by the collecting duct system. See Fig. 1.1. The structural and functional properties of those epithelial cells vary along the different segments of the tubule, allowing each segment to participate in its primary transport processes.

The proximal tubule consists of a coiled segment, the proximal convoluted tubule that is located in the cortex, and an outer medullary segment, the proximal straight tubule, which terminates at the boundary between the outer and inner stripe within outer medulla (approximately 0.6 mm from the cortico-medullary boundary). Along the proximal tubule, about two thirds of the filtered water and NaCl are reabsorbed to surrounding interstitial area (Young and Marsh (1981)), which eventually flows into the general circulation. The next segment, the descending limb, has an initial water-permeable segment, which spans the first $\sim$60% of the inner strip, and a terminal water-impermeable segment (Wade et al. (2000)), which spans the remainder of the inner strip. Beyond the terminal part of the descending limb, the TAL, which is water impermeable, rises back into the cortex, returns into Bowman's capsule, and passes by the afferent and efferent arterioles. Segments containing both the descending limb and TAL are called the loop of Henle. The macula dense (MD) cells, located at the end of the TAL walls and adjacent to the AA, are specialized in sensing the chloride concentration in the downstream fluid.

1.2 Autoregulation

The water volume and blood pressure regulation in the kidney begins with the formation of the glomerular filtrate. The volume of filtrate formed per unit time is called the glomerular filtration rate (GFR) and, in particular, GFR in single nephron is known as the single nephron GFR or SNGFR which is of ∼30 nl/min in a short-looped nephron of normal rats. The level of GFR is dependent on capillary hydrostatic pressure that is significantly influenced by arterial blood pressure. A higher GFR increases the tubular fluid flow rate, resulting in a rise in the distal fluid and sodium delivery. To keep the GFR at an appropriate level and regulate the water-volume of the body, the kidney operates several mechanisms to achieve renal autoregulation.

One such regulatory mechanism is the myogenic response, which is characterized by a constriction (or dilation) of the AA vessels in response to an increase (or decrease) of transmural arterial pressure (Loutzenhiser et al. (2002)). The myogenic response, an intrinsic property of smooth muscle along the pre-glomerular vasculature, acts as a fast mediator. For example, once an increase in arterial blood pressure is sensed, this mechanism shortly induces a vasoconstriction of the AA vessel, via a depolarization of AA smooth muscle cells, to increase vascular resistance, thereby reducing intravascular pressure downstream.

The second mechanism is a negative feedback system, called the tubuloglomerular feedback (TGF), by which the nephron controls the incoming blood flow from the AA, and thus GFR to stabilize the fluid and solute delivery into the distal nephron. TGF operates as a slow mediator of GFR relative to myogenic response and modifies the muscle tension in the AA, according to the level of chloride concentration in the fluid leaving the loop of Henle. Several other mechanisms (Just (2007); Ren et al. (2007); Siu et al. (2009)), which are not well characterized, exist, but they are generally known to make a minor contribution to autoregulation.

The two major autoregulatory mechanisms, the myogenic response and TGF, operate together to substantially attenuate the fluctuations present in the blood flow by changing the muscle tone of the AA. Specifically, both of these responses affect the intravascular fluid pressure along pre-glomerular vasculature, regulating the amount of the blood flowing into the filtering component. By these means, the kidney protects the glomerular capillaries from excessive variations in arterial blood pressure, thus maintaining GFR within a range that is compatible with the glomerular filtering capacity.

1.3 Tubuloglomerular Feedback

1.3.1 Dynamic properties of tubuloglomerular feedback

The TGF system is a unique renal regulatory mechanism for GFR in a nephron (or SNGFR), in which information of the tubular fluid flow rate can be transferred to the glomerulus to stabilize variations in tubular flow. This process is known to be involved with a primary signal and its signaling agent. A specialized cluster of cells, MD, which are located in the tubular walls near the end of TAL, acts as the signaling agent to detect changes in the chloride concentration near the MD and to report this information to the glomerulus to consequently adjust SNGFR.

The TGF response is initiated by the deviation in the MD chloride concentration, which directly depends on TAL fluid flow rate. Because the water-impermeable TAL actively transports NaCl out of the luminal fluid by transepithelial transport processes, low flow rate along the TAL allows more reabsorption of chloride ions (Cl^-) into the surrounding interstitium. This results in the decreased chloride concentration at the MD. Once MD chloride concentration is below a target value, MD cells detect the deviation and produce signals that affect the smooth muscle cells of the adjacent AA to induce vasodilation, resulting in an increase in the diameter of AA vessel. This then reduces the intravascular resistance downstream, causing

an increase of blood flow into the glomerulus and consequently of higher SNGFR. More fluid flowing into the tubular system increases TAL flow rate and yields a rise in MD chloride concentration due to less chloride reabsorption along the TAL. In the case where the MD chloride concentration exceeds the target value because of high TAL flow, the effect of MD response is opposite. Once the AA constricts, the pre-glomerular vascular resistance rises, thereby reducing intravascular downstream flow rate. This results in a reduction in SNGFR, leading to the decreased TAL flow rate, by which the MD chloride concentration decreases to the target value again. By this negative feedback mechanism, the TGF system attenuates variations in the tubular system and, thus, effectively regulates SNGFR.

1.3.2 Feedback delay

The TGF response for SNGFR to the changes in MD chloride concentration is not instantaneous, but rather delayed relative to the time when an initial perturbation in MD chloride concentration occurs. This TGF delay is caused by signal propagation via a series of different biological events. Its primary source is the time needed for the AA to constrict or dilate in response to the signal, produced by a release of adenosine triphosphate (ATP), from the MD.

One major difficulty in experimentally assessing the delay measurement or the dynamics of the MD response in 1980s and early 1990s was the inaccessibility of the juxtaglomerular apparatus (JGA) (Holstein-Rathlou and Marsh (1994b)). The JGA is a highly complex structure consisting of three cell types: juxtaglomerular, extraglomerular mesangial, and MD cells. Several layers of extraglomerular mesangial cells separate the AA from the MD cells. Despite the difficulty of studying the detailed cellular interactions within the JGA, a number of *in vivo* and *in vitro* micropuncture studies (e.g. Young and Marsh (1981); Persson et al. (1991); Bell et al. (1991)) have been alternatively conducted to identify the basic characteristics of the

TGF mechanism. Moreover, many of modern imaging techniques, such as two- or multi-photon fluorescence microscopy (e.g. Dunn et al. (2002); Peti-Peterdi et al. (2002); Yu et al. (2005); Kang et al. (2006)), have since been developed to provide more accurate pictures of the underlying mechanism for the TGF regulation. With an aid of those imaging work, *in vivo* dynamic processes and multiple regulatory functions in the kidney can be visualized with high optical resolution.

An experimental development to measure the AA response by Casellas and Navar (1984) and a subsequent study by Casellas and Moore (1990) have shown that the average time for the full activation of the TGF response, i.e., a rapid decrease (or increase) in the diameter of the AA caused by increased (or decreased) MD chloride concentration, is ∼4–5 s. Specifically, results of Casellas and Moore (1990) have indicated that the intravascular diameter begins to change after a discrete (or pure) delay time, followed by subsequent effect that requires additional time delay, called distributed (or filtered) delay. A previous modeling study by Pitman et al. (1993) has shown that the bifurcation loci separating different dynamic behaviors of the TGF system with the combined effect of pure and distributed delays remain nearly same as those of the system with the pure delay only. Based on these experimental and modeling observation, the feedback delay in our study will be represented by the pure delay.

In addition to the TGF time delay, a full response of MD chloride concentration to TGF-mediated SNGFR through the tubular system, called the transit time, is typically measured to be 8–10.5 s in experiments (Holstein-Rathlou and Marsh (1989)). Although most of important qualitative features of the AA response to MD chloride concentration within TGF activation have been well discovered, each individual step involved in the signal transmission pathway from the MD to the AA and its corresponding detailed dynamics have not been fully elucidated in experimental studies.

1.3.3 Experimental and modeling evidence of tubuloglomerular feedback

Early experiments in normotensive rats (Leyssac and Baumbach (1983); Leyssac and Holstein-Rathlou (1986)) have demonstrated that the feedback regulation can become unstable and generate self-sustained oscillations in proximal tubular pressure and related variables in the nephron with a typical period of 30–40 s (Holstein-Rathlou and Marsh (1990)). Later experimental studies have also indicated that the emergence of regular oscillations in nephron flow is a consequence of TGF activation (Holstein-Rathlou and Marsh (1989, 1994b)).

To better understand the phenomena that have been reported in the above experimental studies, a series of mathematical models for the TGF system in a single nephron of the kidney have been developed (Jensen et al. (1986); Holstein-Rathlou and Leyssac (1987); Holstein-Rathlou and Marsh (1990); Layton et al. (1991, 1995); Budu-Grajdeanu et al. (2007); Layton (2010)). These model results have shown that TGF-mediated oscillations arise from a Hopf bifurcation; if the feedback-loop gain or feedback delay becomes sufficiently large, the dynamic state of nephron changes, i.e., from one type of stable solution (e.g., a time-independent steady state) to another type of stable solution (e.g., limit-cycle oscillation (LCO)). For example, if the feedback delay exceeds its critical threshold, a feedback loop may lose its stability so that the stable behavior of the TGF system becomes a sustained oscillation.

1.3.4 Interaction between neighboring nephrons

Most of early experiments developed to investigate the role of TGF control in the renal regulatory function generally assumed that the TGF response in each nephron is independent of that in other nephrons, excluding the possibility that interaction among nephrons can occur and affect the overall response of the kidney. However, many experimental studies for tubular pressure oscillations in neighboring nephrons (Holstein-Rathlou (1987); Källskog and Marsh (1990); Holstein-Rathlou et al. (2001))

have indicated that the interaction between nephrons arising from the common cortical radial artery (CRA) may exist, considerably affecting qualitative features of TGF-mediated dynamics in nephrons such as the emergence of synchronization. Moreover, in a comparison study between normotensive and spontaneously hypertensive rats (SHR), Yip et al. (1992) showed clear evidence that suggests nephrons originating from the same artery interact with each other.

In addition to the presence of interactions among neighboring nephrons, tubular pressure oscillations in SHR appear as highly irregular fluctuations that exhibit a high degree of spectral complexity with multiple strong peaks in the range of ∼10–50 mHz, exhibiting characteristics similar to deterministic chaos (Holstein-Rathlou and Leyssac (1986, 1987); Yip et al. (1991)). That irregularity of oscillations in SHR is a notably different feature compared to oscillations in normal rats, in that the latter exhibit regular with one sharp peak in the power spectrum. Also, coupling effect among nephrons in SHR is known to be stronger than in normotensive rats (Chen et al. (1995); Wagner et al. (1997)). For the study of the emergence of irregular oscillation observed in SHR, it has been suggested that those irregular oscillations arise, in part, from the interactions between nearby nephrons through their TGF systems, i.e., internephron coupling (Layton et al. (2006, 2009)). Specifically, the coupling effect is mediated by propagation of TGF-induced electrotonic signals along the pre-glomerular vasculature, as observed in experiments (Holstein-Rathlou (1987); Källskog and Marsh (1990); Yip et al. (1992)). For instance, if two AAs associated with two nephrons share a common CRA, then the contraction of one nephron's AA likely causes the other AA to contract. A schematic representation of two coupled nephrons is illustrated in Fig. 1.2.

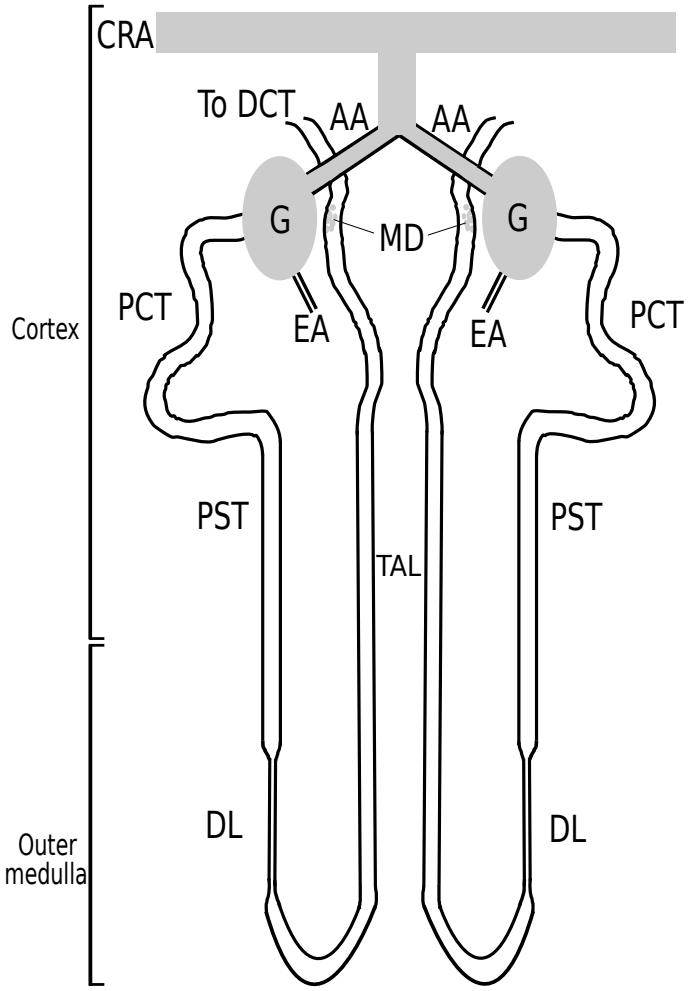

FIGURE 1.2: A schematic diagram of two short-looped nephrons and their renal corpuscles, afferent arterioles (AA), and efferent arterioles (EA). The nephrons receive blood through their AAs that are connected with a small connecting artery (unlabeled), arising from a common cortical radial artery (CRA). Through a filtering component, the glomerulus (G), the filtrate from blood plasma is formed and flows into a tubule consisting of the proximal convoluted tubule (PCT), proximal straight tubule (PST), descending limb (DL), and the thick ascending limb (TAL). Once the fluid reaches the terminal part of the TAL, to which the AA is adjacent, the macula densa (MD) cells at the tubular walls sense the chloride concentration and produce a signal that modifies the smooth muscle tension of AA. This signal electrotonically propagates to the smooth muscle cells of the neighboring AA, affecting fluid dynamics along that tubule. The fluid continues to flow into the distal convoluted tubule (DCT) and enters the collecting duct system (not shown), where the formation of urine occurs. Reprinted from Ryu and Layton (2013b).

1.4 Previous Mathematical Models

1.4.1 Tubuloglomerular feedback operation

The emergence of oscillations in the tubular fluid pressure and flow rate of the rat kidney's nephron was first demonstrated by Leyssac and Baumbach (1983). Based on this observation, a number of modeling studies (Jensen et al. (1986); Holstein-Rathlou and Leyssac (1987); Pitman and Layton (1989); Holstein-Rathlou and Marsh (1990); Layton et al. (1991); Holstein-Rathlou and Marsh (1994a); Barfred et al. (1996); Pitman et al. (2002); Ditlevsen et al. (2005, 2007); Layton (2010)) have since been conducted to show that those oscillations arise from the TGF operation. Although each model's emphasis differs from each other, one common goal of those studies was to identify the important parameters that determine the qualitatively different behaviors, i.e., the generation of sustained oscillations, and to show the systematic dependence of the stability for the TGF system on the parameter values within the physiologic range.

Holstein-Rathlou and collaborators first developed a relatively simple model of the TGF system (Jensen et al. (1986); Holstein-Rathlou and Leyssac (1987)), which includes a quasi-steady-state description of the GFR based on the previous models by Deen et al. (1972); Jensen et al. (1981). The delay, which was assumed to arise from both the signal transmission from MD to AA and the signal propagation through the tubular system (Marsh (1982)), was modeled by a third-order delay (lag) function, a linear system of three coupled-differential equations. The AA response to the MD signal and the TGF activation were described by a second-order ODE and an empirical relation for the steady-state feedback response (Briggs and Schnermann (1987, 1990)), respectively (Holstein-Rathlou and Marsh (1994b)). The model revealed a variety of qualitatively different TGF-mediated dynamic behaviors that are consistent with experimental observation. Specifically, model results indicated

that the strength of the feedback gain and the length of the feedback delay can be important bifurcation parameters in determining the stability of the feedback loop (Holstein-Rathlou and Leyssac (1987)).

A subsequent mathematical model (Holstein-Rathlou and Marsh (1990)) extended the above-mentioned model to explicitly represent the detailed dynamics of the fluid and solute transport processes along the tubular system. Based on a reduced version of Navier-Stokes equation to describe the tubular fluid pressure and flow rate previously introduced by Young and Marsh (1981), and a mass conservation equation to describe the motion of the chloride ions in the fluid, the model consistently predicted the phase relations between the tubular fluid pressure, flow rate, and the MD chloride concentration (Holstein-Rathlou and Marsh (1990)) as well illustrated in their experimental data (Holstein-Rathlou and Marsh (1989)). Using this model formulation, they then thoroughly examined the role of the TGF system in the context of autoregulation of renal blood in comparison to the experimental results (Holstein-Rathlou and Marsh (1994a)). Bifurcation analysis of nephron pressure and flow regulation was also conducted to investigate how the dynamic behaviors of the detailed TGF model systematically depend on important bifurcation parameters such as the feedback gain and delay (Barfred et al. (1996)).

In a more recent study using the model (Holstein-Rathlou and Marsh (1990)), a different approach to assess the role of TGF mediation in regular and irregular oscillations was obtained by Ditlevsen et al. (2005, 2007). A key parameter, TGF gain value, in determining the stability of the feedback system was assumed to undergo abrupt changes over time due to various external perturbations such as heart beat, blood pressure, and hormone levels; thus, to be modeled by a random (stochastic) process (Ditlevsen et al. (2005)). The previous deterministic TGF models in a single nephron (Holstein-Rathlou and Marsh (1990, 1994a)) assumed the constant or discrete TGF gain value and predicted only regular tubular pressure oscillations with

constant period and amplitude, given the parameters within the physiologic range. In contrast, this stochastic model reproduced irregular behaviors in model solutions as demonstrated in the experimental data of SHR. The model results, thus, suggested that the irregular characteristics observed in nephron's flow of SHR may be explained by the intrinsic noise present in the TGF bifurcation parameters (Ditlevsen et al. (2005)).

Another TGF model for a short-looped of Henle having rigid walls was developed by Pitman and collaborators (Pitman and Layton (1989)). The model, which represented the interactions of the descending limb, TAL, and collecting duct system, was formulated based on a single-solute dynamic model for a short-looped nephron in the renal medulla (or called a central core), originally introduced by Stephenson (1972). This model was similar to the model by Holstein-Rathlou and Marsh (1990) in that the detailed dynamics along the short-looped of Henle were explicitly represented to study the TGF operation in response to perturbations in MD chloride concentration. However, unlike the model by Holstein-Rathlou and Marsh (1990), the proximal tubule was not explicitly incorporated and the dynamics of the AA and glomerulus were described using a relatively simple resistance network in the model by Pitman and Layton (1989). Regardless of these differences, model results exhibited sustained oscillations in the tubular system as a result of sufficiently long feedback delay, as similarly discovered in the results by (Holstein-Rathlou and Marsh (1990)) and experiments.

The TGF model by Pitman and Layton (1989) included the detailed TGF-mediated dynamics but their model results fully relied on numerical simulations owing to the complication of the model formulation. To alleviate this complication, they instead introduced a minimal or rigid-TAL model of the TGF system (Layton et al. (1991)), in which the dynamic behaviors of the chloride concentration in the rigid-TAL were modeled, as a key component, to study the TGF-mediated tubular

oscillations. The model formulation was based on the observation that TGF response is initiated by perturbations present in the tubular fluid chloride concentration at the MD (Schnermann and Briggs (2008)). By means of linear stability and bifurcation analyses, they showed that the model exhibits qualitatively important features of the TGF system, specifically sustained tubular flow oscillations for sufficiently long delay, which are in good agreement with experimental evidence and model results by Holstein-Rathlou and Marsh (1990). Because of its simplicity which makes a more comprehensive analysis possible, the minimal model has been widely used in their following studies. For example, the role of feedback loop gain and delay in determining the stability of the TGF system (Pitman et al. (1993); Layton et al. (1995)), the nonlinear filter properties of the TGF loop (Layton et al. (1997a,b)), and the effect of TGF-mediated LCO in the distal fluid and NaCl delivery (Layton et al. (2000)) were subsequently investigated.

To further facilitate computational simplicity, a reduced integral model (Pitman et al. (2002)), a simplification of the minimal PDE model (Layton et al. (1991)), was also derived. Given the assumption of no NaCl backleak along the TAL, they obtained a functional ODE arising from the linearization of the original PDE. Both models yielded the identical characteristic equation, indicating that the reduced integral model has qualitatively similar behaviors to the minimal model if bifurcation parameters are near their respective critical values. These results combined with significantly reduced computational cost suggested that the reduced integral model can be alternatively used for the study of large systems of the coupled-nephrons (Pitman et al. (2002)). However, because of the assumption on zero diffusion permeability, which was critical for its derivation, the integral model cannot be used to study the case of nonzero NaCl backleak along the TAL unlike the minimal model.

The minimal model (Layton et al. (1991)) consists of only simple components, the detailed transport processes along the TAL only, to study the TGF-mediated

dynamics. Specifically, the TAL walls were assumed to be rigid and only the chloride ion was explicitly represented to describe a single solute in the TAL fluid with constant volumetric flow rate, which was prescribed by a fixed fraction of SNFGR. *In vivo*, however, the TAL is likely subject to transmural fluid pressure, for which it may expand or contract to consequently affect TAL fluid pressure, flow rate, and the overall TAL dynamics.

To resolve the rigid-tube assumption and assess the impact of the compliant wall movement on the TGF-mediated dynamics, Layton (2010) recently developed an extended TGF model, in which the TAL fluid pressure and flow rate are directly computed to determine the chloride concentration along the compliant TAL. Results of bifurcation analysis demonstrated that, given a set of the parameter values within the physiologically relevant range, a variety of different dynamic behaviors become attainable, as similarly shown in Layton et al. (1991) and in previous experiments. Specifically, a comparison of bifurcation diagrams that illustrate qualitatively different model behaviors between the rigid- and compliant-TAL models, suggested that the compliance of the TAL walls reduces the stability of the model TGF system (Layton (2010)), as can be shown by the decreased parameter region supporting the steady-state solution.

More recently, Layton et al. (2012a) thoroughly investigated nonlinear properties of the TGF loop using the compliant-TAL model (Layton (2010)). Model results were consistent with those of similar TGF models, which explicitly included the compliant tubular walls in the model formulation (Young and Marsh (1981); Sakai et al. (1986); Holstein-Rathlou and Marsh (1990)), that high-frequency pressure perturbations present in SNGFR are damped at the MD more than low-frequency perturbations, indicating that a compliant TAL operates as a low-pass filter for pressure oscillations (Layton et al. (2012a)). However, due to the differences in TAL fractional chloride reabsorption and TAL flow rate, the nonlinearity in TGF trans-

duction, i.e., the degree of waveform distortions in MD chloride concentration, was more marked in model results by (Layton et al. (2012a)) than (Holstein-Rathlou and Marsh (1990)).

1.4.2 Tubuloglomerular feedback in coupled-nephron system

Interactions between nephron pairs in coupled-nephron system have been investigated in a series of modeling studies by Holstein-Ratholu and coworkers (Holstein-Rathlou et al. (2001); Andersen et al. (2002); Sosnovtseva et al. (2003); Marsh et al. (2005a,b, 2007, 2013)). These studies include a vascular coupling on TGF-mediated dynamics to explain the mechanisms responsible for behaviors observed in experimental data from normal rats and SHR.

Early modeling studies (Holstein-Rathlou et al. (2001); Andersen et al. (2002); Sosnovtseva et al. (2003)) have developed a model of two coupled nephrons, based on the single-nephron model of Barfred et al. (1996) that provides a detailed representation of the nonlinear phenomena arising from the response of AA to the TGF mechanism. Although their coupled-nephron model includes an explicit representation of hemodynamic and vascular coupling along the renal microvasculature, it represents the dynamics of the individual nephron with relatively simple formulation of three first-order ODEs. Despite its simplicity, the model demonstrated that internpehron coupling can introduce the complexity in TGF-mediated model behaviors, e.g., irregular oscillations, in nephron tubular pressure similar to those found in SHR.

In recent studies, Holstein-Ratholu and coworkers extended the above-mentioned early model to include a detailed representation of interactions between TGF and the myogenic mechanism (Marsh et al. (2005a,b, 2013)) and to represent a system of many nephrons, a multinephron network, each of which is supplied with blood from a common CRA (Marsh et al. (2007, 2013)). Although there are substantial differences

in the scope of each modeling study, all of those studies consistently predicted in-phase, anti-phase (out-of-phase), and even chaotic phase synchronization as well as irregular oscillations in coupled-nephron behaviors within physiologically realistic parameter regimes, as can be similarly observed in nephron's behaviors of SHR.

Pitman and coworkers developed the coupled-nephron model for two nephrons (Pitman et al. (2004)), each of which includes relatively simple but key components for the TGF system, based on their previous rigid-TAL model (Layton et al. (1991)). As in the single-nephron model, the systematic dependence of the stability for the coupled-TGF system on the important bifurcation parameters was analogously identified by means of bifurcation analysis. Model results indicated that the region supporting oscillatory solutions increases with internephron coupling (Pitman et al. (2004)). Although their model included a detailed representation of tubular transport processes in each nephron, the structural components of AA, glomerulus, and EA were not explicitly included unlike models by Holstein-Ratholu and coworkers. Specifically, as a result of the lack of hemodynamic coupling effect in model formulation, the model by Pitman et al. (2004) predicted only in-phase regular oscillations.

Another assumption made in the model by Pitman et al. (2004) was zero NaCl backleak along the TAL, simplifying the derivation of characteristic equation for two-coupled nephrons. However, experimental evidence obtained by Mason et al. (1979); Wittner et al. (1988) indicated that the TAL is NaCl permeable with a low but nonzero diffusion permeability. To assess more realistic effects of chloride diffusion on coupled-TGF system, Hattaway (2004) developed a TGF model of two coupled nephrons with nonzero NaCl diffusion parameter unlike (Layton et al. (1991); Pitman et al. (2004)) but with appropriate external chloride concentration adapted from (Kevrekidis and Whitaker (2003)) so that the steady-state chloride concentration profile is consistent with experimental data. Hattaway's model predicted that nonzero (or increased) diffusion permeability results in the enlarged parameter re-

gion that corresponds to the stable steady-state solution, which is consistent with numerical results previously shown in (Layton et al. (1991)).

The coupled-nephron model was further extended to a system of coupled-nephrons (Bayram (2006); Bayram et al. (2009)). Based on the reduced integral equation (Pitman et al. (2002)) with zero diffusion permeability, model results consistently supported the previous finding that internephron coupling tends to increase the likelihood of LCO in the coupled-TGF system. However, due to the lack of the detailed representation of the dynamics along the microvasculature, only regular oscillations were predicted in the model simulations similar to the results by Pitman et al. (2004).

Layton and coworkers (Layton et al. (2006, 2009)) developed another model of many coupled-nephrons, based on the rigid-TAL model (Layton et al. (1991)) but with nonzero NaCl diffusion permeability, to examine the role of internephron coupling in the emergence of complex dynamic behaviors that have been reported in experimental studies of SHR. They derived the characteristic equation for two coupled-nephrons with different combinations of parameter values such as TGF gain, delay, TAL transit time, and NaCl diffusion parameter (Layton et al. (2009)), and found corresponding roots of that equation as in a single-nephron model (Layton et al. (1991)). Model results demonstrated that the coupled-TGF system exhibits substantially increased multistability in its solution behaviors compared to the uncoupled TGF system (Layton et al. (2006, 2009)). In addition, their model suggested that nonzero NaCl permeability increases the parameter region where the steady-state behavior is supported (Layton et al. (1991, 2006, 2009)), which is consistent with the previous finding by Hattaway (2004).

As noted above, most of previous coupled-nephron models by Pitman's and Layton's groups were developed based on the single-nephron rigid-TAL model (Layton et al. (1991)); the impact of compliant TAL walls on the coupled-TGF system was not explicitly incorporated in those models. To describe physiologically more real-

istic coupled-TGF system with tubular compliance, Layton and coworkers (Layton et al. (2011)) further developed a model of two coupled nephrons, each of which is modeled based on their previous compliant-TGF model in a single (or uncoupled) nephron (Layton (2010)). Results of bifurcation analysis of the corresponding characteristic equation for two-coupled TALs with supplemental numerical simulations demonstrated that both compliance of TAL walls (Layton (2010)) and internephron coupling (Pitman et al. (2004); Layton et al. (2006, 2009)) significantly reduces the stability of coupled-TGF system. Moreover, their model reproduced irregular tubular flow oscillations with a high degree of spectral complexity in the physiologic parameter range, supporting the previous finding by Layton et al. (2006, 2009) that internephron coupling contributes to the complex model behaviors exhibited in nephron's flow of SHR.

1.5 Stochastic Model

Feedback delays play a fundamental role in determining qualitatively and quantitatively different TGF-mediated dynamic behaviors as demonstrated in previous TGF modeling studies. Specifically, the length of feedback delays can be an important bifurcation parameter to affect the stability of the TGF system; for a fixed feedback gain value within the physiologic range, the feedback loop may lose the stability to exhibit stable sustained oscillations as the delay exceeds its critical threshold.

Most of previous TGF models have been formulated in the deterministic setting, excluding the possibility of the presence of external random effects. *In vivo*, however, the TGF system is likely subject to a variety of continuous external perturbations, for example, arising from the breathing activity and heart movement. Those (unknown) effects, generally called noise, may interact with the deterministic TGF dynamics to generate significantly rich and complex behaviors that would have not been appeared in the deterministic system. Specifically, even though the parameter values of the

deterministic TGF system lie in the steady-state regime, the introduction of noise may induce sustained oscillations in model solutions, so-called stochastic resonance, as a result of the interaction with delay. To assess how the stability of TGF system is affected by unknown external sources, it is, thus, essential to thoroughly examine the role of noise interacting with the delay in the TGF-mediated dynamics.

The role of time delay which is one of the key parameters in determining dynamic behaviors has been investigated in a number of different biological and engineering problems, such as neuronal networks (Beuter et al. (1993); Crook et al. (1997); Ermentrout and Ko (2009); Gils et al. (2013)), cellular replication (Mackey and Rudnick (1994)), machine tool vibrations (Buckwar et al. (2006)), and coupled oscillators (Kim et al. (1997); Choi et al. (2000); Earl and Strogatz (2003)). Specifically, the interaction of delays with noise that represents external fluctuations, in the context of stochastic resonance, has been an important subject for understanding delayed feedback mechanisms.

To study the influence of noise in stochastic delayed dynamical systems, a variety of numerical studies have been developed; however, only a few analytical approaches have been attempted to describe the dynamics due to the difficulty of rigorous analysis. One of widely used analytic tools to study the solution behaviors is multiscale analysis, in which slow-scale variable that is independent of fast-scale variable is introduced and a leading order approximation to the solutions is subsequently derived. This method has been also used in many deterministic models with delays (Giacomelli and Politi (1998); Pieroux et al. (2000); Das and Chatterjee (2002)) and stochastic models without delays (Yu et al. (2006); Kuske et al. (2007)).

Kuske (2003) first developed the multiscale approach for stochastic differential equation (SDE), specifically, stochastic Duffing-van der Pol equation. Kuske showed that multiscale method provides an efficient way to analyze the dynamics where the amplitude of oscillations corresponding to the deterministic system near Hopf

bifurcation slowly varies due to the influence of noise (Kuske (2003)). By deriving the slowly varying amplitude equation according to a stochastic process, a leading order approximation of the solution was obtained. This approach enables one to better understand the systematic dependence of the stability of the system, i.e., the generation of sustained oscillations, on important parameters.

Based on this observation, Kuske and collaborators (Kuske (2005); Klosek and Kuske (2005)) considered both linear (with additive as well as multiplicative noise) and logistic (with additive noise) stochastic delay differential equation (SDDE). For example, the linear SDDE with additive noise studied in (Klosek and Kuske (2005)) is given by

$$dx = [-\alpha x(t) + \beta x(t-\tau)]dt + \delta dW(t),$$
$$\tau = \tau_0 + \epsilon^2 \tau_1,$$

where $\alpha > 0$ and $\beta < 0$ are constants, $W(t)$ is an one-dimensional Brownian motion, τ_0 is the critical value of the delay in the deterministic system, and $\epsilon \ll 1$ is used to measure the proximity of the delay to its critical value with an $O(1)$ constant, $\tau_1 = -1$. They looked for the leading order approximation of the solution with the form

$$x \sim \hat{x} = A(T)\cos\omega t + B(T)\sin\omega t, \quad T = \epsilon^2 t,$$

where $A(T)$ and $B(T)$ are functions of a slow time T, which is treated as independent of a fast-time variable t, and ω represents the natural frequency of the oscillation associated with the bifurcation of the deterministic system. Moreover, the equations for A and B were assumed to have the following SDEs:

$$dA = \psi_A dT + \sigma_A \xi_1(T),$$
$$dB = \psi_B dT + \sigma_B \xi_2(T),$$

where ψ_i and σ_i for $i = A, B$ are unknown constants to be determined, and $\xi_i(T)$ for $i = 1, 2$ are independent Brownian motions with respect to a slow time variable

T. Using asymptotic expansions and multiscale techniques, the above stochastic envelops or amplitudes of deterministic oscillations, i.e., $A(T)$ and $B(T)$, which approximate the solution behaviors over long time scales, were rigorously derived. Although their analytical results describe the detailed stochastic dynamical behaviors near bifurcations of the system, their model equation as a simple first-order differential equation was not specifically related to a biological system with delays, but rather intended to consider a general case of the delayed feedback system.

Another multiscale-analysis study was conducted by Blömker et al. (2007), in which SPDE without the delay arising from modeling surface phenomena was considered. They rigorously obtained the amplitude equation of the solution, which stochastically varies on a slow time variable, under the assumption that the noise acts only on the stable modes and the proximity of the delay to its critical value is sufficiently small relative to the strength of the noise (Blömker et al. (2007)). Applying the multiscale techniques, they showed that noise that only acts on the fast-scale dynamics also affects the slow-scale dynamics, resulting in a diffusion effect on the amplitude equation.

1.6 Introduction to Subsequent Chapters

In this section, we provide the motivation of the development of three TGF models in relation to previous experimental and modeling studies, and describe each model's emphasis and main goal.

We first consider the *TAL model* which explicitly represents the detailed TAL dynamics with spatially inhomogeneous TAL's luminal radius and maximum NaCl transport rate to study the impact of those inhomogeneity on the stability of the TGF system. By means of bifurcation analysis for a characteristic equation that corresponds to a linearized model and with numerical simulations using the full TGF model equations, we thoroughly examine how the stability of the TGF dynamics

is affected by TAL physical and transport inhomogeneous properties. The *TAL-model* formulation is based on experimental evidence, indicating that TAL radius and maximum transport rate vary along the TAL, i.e., spatially inhomogeneous (Knepper et al. (1977); Garg et al. (1982)). Because of this spatial dependence, *TAL model* extends the previous TAL-only models (Layton et al. (1991); Layton (2010)), in which the TAL's luminal radius and maximum NaCl transport rate were assumed to be spatially homogeneous.

Despite an inclusion of the spatial inhomogeneous TAL properties, the above-mentioned *TAL model* explicitly represents the TAL only; the dynamic behaviors along the proximal tubule and the descending limb are represented by means of simple, phenomenological relations. In our next modeling study, we extend our *TAL model* to include an explicit representation of the entire short loop of Henle and we use the resulting model, which we call *short-looped nephron model*, to better understand factors that impact the stability of the TGF system. Specifically, using this whole-nephron representation, we study how tubular fluid and chloride delivery are affected or mediated by the TGF system. The effects of sustained flow perturbation on the TGF autoregulatory mechanism are also investigated.

The previous study of coupled nephrons (Layton et al. (2011)) represents two nephrons, each of which explicitly includes the compliant TAL only based on the (uncoupled) TAL model (Layton (2010)). To better understand the impact of transport processes along the proximal tubule and descending limb as well as of internephron coupling on overall coupled-TGF system, we extend the (uncoupled) *short-looped nephron model*, to include two nephrons coupled through their TGF systems. With this *coupled-nephron model*, we aim to investigate (1) how coupling may impact the TGF-mediated dynamics of the single-nephron model, and (2) to what extent coupling contributes to the complexities in TGF-mediated model behaviors, as have been observed in SHR (Layton et al. (2006, 2009, 2011)).

To answer above questions, we analyze the model by means of linearization and numerical simulations, as in our *TAL model*. Finding roots of corresponding characteristic equation for the coupled-TGF model equations, we systematically identify how qualitatively different model behaviors are determined dependent on physiological model parameters. Also, we show how complex model behaviors, i.e., irregular TGF-mediated oscillations, emerge and how the region supporting multistable LCO is affected in the presence of internephron coupling.

Based on model results from the above-mentioned three TGF modeling studies, we then develop the stochastic model to study the effect of noise on the stability of TGF system. We are specifically interested in how the feedback delay interacts to the external noise to determine the stability of TGF-mediated dynamics. We begin with a time-delayed transport equation to represent the dynamics of chloride concentration in the rigid-TAL fluid. We first show the existence and uniqueness of the steady-state solution for the deterministic Dirichlet boundary problem. Using bifurcation analysis in which the critical delay can be explicitly found, we determine the stability of the steady-state solution dependent on the feedback delay. An alternative way to show the systematic dependence of the stability on delays will be also considered via the contraction mapping theorem. Applying similar analytic techniques that are used for the deterministic system, we then extend our analysis to the stochastic system with random boundary conditions; we provide an analogous proof for the existence and uniqueness of the statistically stationary solution for sufficiently small feedback delay.

Finally we conduct multiscale analysis for a linear time-delayed transport equation. We are particularly interested in the case when the system is in the subcritical region but close enough to the critical delay to investigate how the noise can interact with the delay of system, affecting overall behaviors of solutions, e.g,. the generation of oscillatory solutions that would not appear in the deterministic system. Using mul-

tiscale analysis as well as asymptotic expansions, we derive approximate stochastic (reduced) equations for the amplitudes of solutions near the critical delay.

In sum, Chapter 2 provides respective description of the above-mentioned three different TGF models, *TAL, short-looped nephron*, and *coupled-nephron*. The respective model results and analysis are summarized in Chapter 3, which are adapted from the published results in Ryu and Layton (2013a) (TAL model), Ryu and Layton (2013c) (short-looped nephron model), and Ryu and Layton (2013b) (coupled-nephron model) after minor changes with permission of reprints. Chapter 4 describes analytical and numerical results for stochastic model. Discussion of model results and future research work is given in Chapter 5.

2

Mathematical Model

In this chapter, we describe model formulation, model parameters, and numerical method for the *TAL model*, *short-looped nephron model*, and *coupled-nephron* model. Each nephron considered in all three models is specified to be a superficial nephron.

2.1 Thick Ascending Limb Model

2.1.1 Model formulation

The TAL model is a mathematical model of a TGF system that explicitly represents a TAL with compliant tubular walls. The model consists of four differential equations, which predict tubular fluid pressure, volumetric flow rate, tubular radius, and fluid chloride concentration within the TAL as functions of time and space. We model pressure-driven flow within a compliant tubule which expands and contracts based on transmural fluid pressure gradient, based on the previous compliant-TGF model by Layton (2010). The model represents tubular chloride concentration because the chloride concentration at the MD is believed to be the primary signal that initiates the TGF response (Schnermann and Briggs (2008)). Note that the sodium-potassium pumps (Na-K-ATPase) in the epithelium transport sodium across the tubular wall

with chloride transported passively and secondary to sodium.

Boundary conditions for fluid pressure are needed at the two ends of the TAL. At the entrance of the TAL, the inflow pressure is determined by the TGF response. At the end of the TAL, tubular fluid pressure is assumed to be known *a priori*. However, because tubular pressure at the MD is not well-characterized in experimental data, we instead introduce a downstream resistance tube and impose the outflow pressure value at the end of the (longer) model tubule. Thus, the model tubule extends in space from $x = 0$ at the entrance of loop bend to $x = L_0$ at the end of collecting duct, where fluid pressure in rats has shown to be $\sim$1–3 mmHg, based on measurements in the interstitium, vessels, and the pelvic space (Angell et al. (1998); Gottschalk (1952); Gottschalk and Mylle (1957)). Cl^- concentration is represented only along the TAL, from $x = 0$ at loop bend to $x = L$ at the MD ($L \leqslant L_0 = 4L$). A schematic diagram for the TAL-model TGF system is given in Fig. 2.1.

The model equations are

$$\frac{\partial}{\partial x}P(x,t) = -\frac{8\mu}{\pi R(x,t)^4}Q(x,t), \tag{2.1}$$

$$\frac{\partial}{\partial x}Q(x,t) = -\left(2\pi R(P(x,t))\frac{dR}{dP}\right)\frac{\partial}{\partial t}P(x,t), \tag{2.2}$$

$$\begin{aligned}\frac{\partial}{\partial t}(\pi R^2(P(x,t))C(x,t)) = &-\frac{\partial}{\partial x}(Q(x,t)C(x,t)) - 2\pi R_{\rm ss}(x) \\ &\times\left(\frac{V_{\max}(x)C(x,t)}{K_M + C(x,t)} + \kappa(x)(C(x,t) - C_e(x))\right),\end{aligned} \tag{2.3}$$

$$R(P(x,t)) = \alpha(P(x,t) - P_e) + \beta(x), \tag{2.4}$$

$$P_o(t) = \bar{P}_o + K_1\tanh(K_2(C_{\rm op} - C(L,t-\tau))). \tag{2.5}$$

Equations 2.1 and 2.2 describe intratubular fluid pressure and fluid flow rate, where x is axial position along the extended tubule ($0 \leqslant x \leqslant L_0$), t is time, $P(x,t)$ is the tubular fluid pressure, $Q(x,t)$ is the tubular flow rate, and $R(P(x,t))$ is the

tubular radius, which is a function of the fluid pressure (see below). The inflow pressure $P_o(t) = P(0,t)$ is assumed to be given by the TGF response, and the outflow pressure $P_1 = P(L_0,t)$ is considered fixed.

Equation 2.3 represents solute concentration in the TAL's tubular fluid by conservation law, where $0 \leqslant x \leqslant L$, $C(x,t)$ is TAL tubular fluid chloride concentration, $C_e(x)$ is the time-independent extratubular (interstitial) chloride concentration which is assumed to be fixed. The first component on the right-hand side represents axial advective chloride transport at the intratubular volumetric flow rate $Q(x,t)$. The two terms inside the large pair of parentheses corresponds to outward-directed active solute transport characterized by Michaelis-Menten-like kinetics (with maximum Cl^- transport rate $V_{\max}$ and Michaelis constant K_M) and transepithelial Cl^- diffusion (with backleak permeability κ). We assume that chloride channels are insensitive to the stretch of the tubular walls, and that such stretch does not render accessible parts of the membrane that might be previously folded. Thus, solute transport is not affected by changes in tubular radius, which implies that the solute flux term in Eq. (2.3) is proportional to $R_{\text{ss}}(x)$ instead of $R(x,t)$ (Layton (2002)). The boundary condition $C(0,t) = C_o$ is considered to be fixed so that fluid entering the TAL has a constant chloride concentration.

Equation 2.4 represents a compliant tube, such that its tubular luminal radius varies as a function of transmural pressure difference. P_e denotes the extratubular (interstitial) pressure, α specifies the degree of tubular compliance, and $\beta(x)$ is the unpressurized TAL radius (see below).

Equation 2.5 defines the feedback-mediated loop-bend pressure. K_1 denotes half of the range of pressure variation around its reference value $\bar{P}_o$; K_2 quantifies TGF sensitivity; the target concentration C_{op} is the time-independent steady-state TAL tubular fluid chloride concentration alongside the MD when $P(0,t) = \bar{P}_o$ (i.e., when $C_{\text{op}} = C(L, t-\tau)$); and $C(L,t-\tau)$ is the chloride concentration alongside the MD

at the time $t-\tau$, where τ represents the TGF delay. The TGF response in Eq. (2.5) is based on experimental data by Briggs (1982); Schnermann and Briggs (2008), which suggests a sigmoidal relationship between inflow pressure and time-delayed MD chloride concentration.

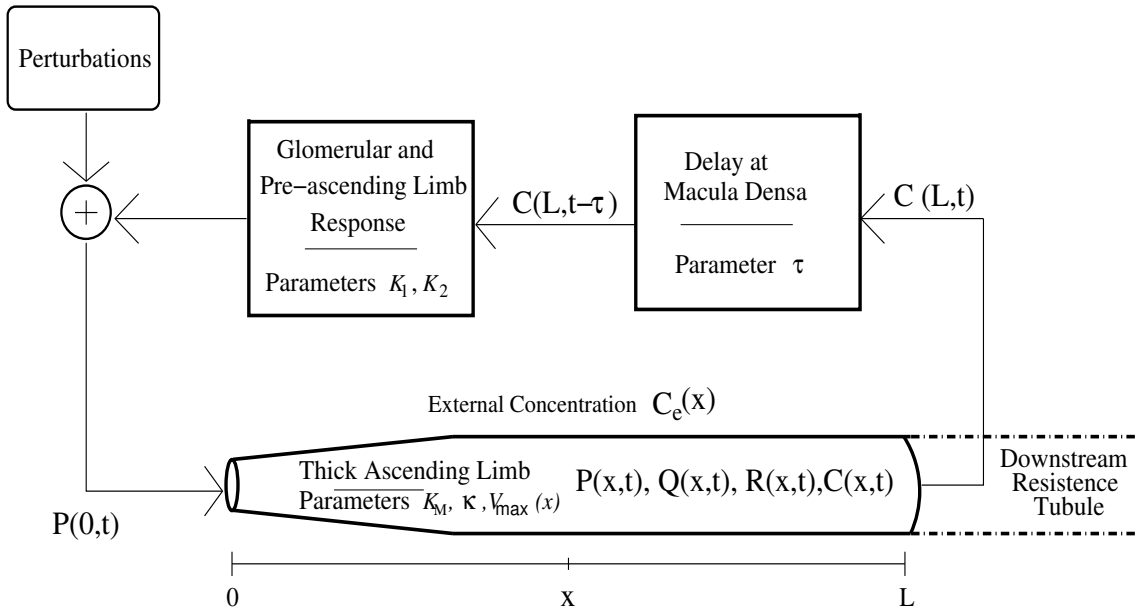

FIGURE 2.1: A schematic representation of the TAL-model TGF system. Model represents three essential elements of the TGF pathway: (i) compliant thick ascending limb (TAL), which is modeled by Eqs. (2.1)–(2.4) with spatially inhomogeneous R_{ss} and $V_{\max}$, (ii) delay at the MD (right square), and (iii) TGF response function (left square). Symbols are identified in Table 2.1. Perturbations enter as adjustments to hydrodynamics pressure $P(0,t)$ that drives flow into TAL entrance ($x=0$) at time t. Oscillations in pressure result in oscillations in TAL flow $Q(x,t)$, radius $R(x,t)$, and tubular fluid chloride concentration $C(x,t)$. Reprinted from Ryu and Layton (2013a).

2.1.2 Model cases

To better understand the individual and combined effects of TAL NaCl active transport rate, tubular radius, and tubular compliance on the TGF dynamics, we considered five cases: one spatially homogeneous model (H) and four spatially inhomogeneous models (IR, IT, IRT, CIRT):

H: spatially homogeneous TAL radius and maximum active chloride transport rate (i.e., constant R_{ss} and $V_{\max}$); rigid TAL ($\alpha = 0$).

IR: spatially homogeneous maximum active chloride transport rate; spatially inhomogeneous TAL luminal radius (i.e., piecewise-function R_{ss}); rigid TAL ($\alpha = 0$).

IT: spatially homogeneous TAL radius; spatially inhomogeneous maximum active chloride transport rate (i.e., piecewise-function $V_{\max}$); rigid TAL ($\alpha = 0$).

IRT: spatially inhomogeneous TAL radius; spatially inhomogeneous maximum active chloride transport rate; rigid TAL ($\alpha = 0$).

CIRT: spatially inhomogeneous TAL luminal radius; spatially inhomogeneous maximum active chloride transport rate; compliant TAL.

Profiles for TAL radii and maximum chloride transport rates for different model cases are given in Fig. 2.2. Defining parameters for each case are given in Table 2.2. Arrows indicate that a quantity varies as a function of increasing x; see Fig. 2.2.

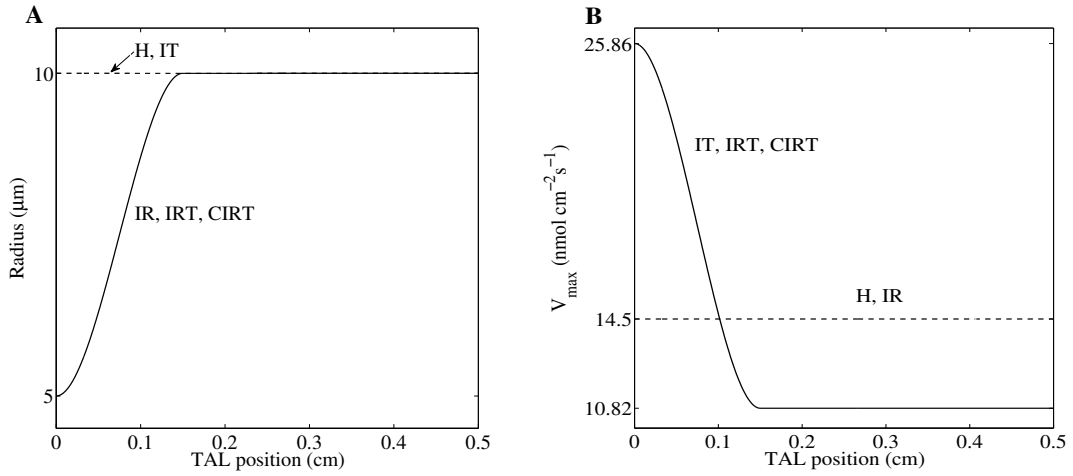

FIGURE 2.2: TAL radius (A) and maximum active NaCl transport rate (B) for five considered cases: H, homogeneous; IR, inhomogeneous radius; IT, inhomogeneous transport; IRT, inhomogeneous radius and transport; CIRT, inhomogeneous radius and transport with the compliant walls. Defining parameters for each case are given in Table 2.2. Reprinted from Ryu and Layton (2013a).

Table 2.1: Glossary for TAL model

Independent Parameters	
α	TAL compliance (cm mmHg^{-1})
C_o	[Cl$^-$] at TAL entrance (mM)
$C_{e,1}$	interstitial [Cl$^-$] at the loop bend (mM)
$\bar{P}_o$	base-case fluid pressure at the loop bend (mmHg)
β_0	initial boundary value for $\beta_{0,1}(x)$ (μm)
β_1	end boundary value for $\beta_{0,1}(x)$ (μm)
β_2	end boundary value for $\beta_{1,2}(x)$ (μm)
κ	TAL chloride permeability (cm s^{-1})
K_1, K_2	parameters for TGF response
K_M	Michaelis constant (mM)
L_0	length of model nephron (cm)
L	length of TAL (cm)
μ	fluid viscosity (g cm^{-1}s^{-1})
P_1	pressure at end of nephron (mmHg)
Specified Functions	
$\beta(x)$	unpressurized TAL radius (μm)
$R_{ss}(x)$	steady-state TAL radius (μm)
$V_{\max}(x)$	maximum active Cl$^-$ transport rate (nmole cm^{-2}s^{-1})
$C_e(x)$	extratubular [Cl$^-$] (mM)
$P_o(t)$	pressure at loop bend (mmHg)
$P_e(x)$	extratubular pressure (mmHg)
Dependent Parameters and Variables	
t_o	base-case steady-state TAL transit time (s)
T_o	steady-state TAL transit time (s)
C_{op}	steady-state chloride concentration alongside MD (mM)
$C(x,t)$	TAL [Cl$^-$] (mM)
$P(x,t)$	Tubular fluid pressure (mmHg)
$Q(x,t)$	Tubular fluid flow (nl min^{-1})
$R(x,t)$	luminal radius (μm)

Table 2.2: Individual parameter values for five model cases

Parameter (units)	H	IR	IT	IRT	CIRT
α (cm mmHg^{-1})	0	0	0	0	0.266×10^{-5}
R_{ss} (μm)	10	$5 \to 10$	10	$5 \to 10$	$5 \to 10$
β_0 (μm)	10	5	10	5	4.867
β_1 (μm)	10	10	10	10	9.92
β_2 (μm)	5.57	5.89	5.57	5.89	5.92
$V_{\max,1}$ (nmol cm^{-2}s^{-1})	14.50	14.50	25.86	25.86	25.86
$V_{\max,2}$ (nmol cm^{-2}s^{-1})	14.50	14.50	10.82	10.82	10.82
K_M (mM)	70	60.4	48.3	34.0	34.1
C_{op} (mM)	31.98	31.97	32.04	32.02	32.01
T_o (s)	15.70	13.79	15.70	13.79	13.79

2.1.3 Model parameters

Model parameters that are common to all five cases are given in Table 2.3. Parameters that differ among the cases are displayed in Table 2.2.

For case IT, IRT, and CIRT, the TAL maximum active transport rate $V_{\max}(x)$ is assumed to decrease linearly over the first 30% of the TAL, and then remains constant afterwards; i.e.,

$$V_{\max}(x) = \begin{cases} V_{\max,1} - (V_{\max,1} - V_{\max,2})\frac{x}{0.3L}, & 0 \leqslant x \leqslant 0.3L, \\ V_{\max,2}, & 0.3L \leqslant x \leqslant L, \end{cases} \tag{2.6}$$

where $V_{\max,1}$ and $V_{\max,2}$ are parameters given in Table 2.2.

The unpressurized tubular radius parameter $\beta(x)$ is given (in μm) by the piecewise function:

$$\beta(x) = \begin{cases} \beta_{0,1}(x), & 0 \leqslant x \leqslant 0.3L, \\ \beta_1, & 0.3L \leqslant x \leqslant 1.5L, \\ \beta_{1,2}(x), & 1.5L \leqslant x \leqslant L_0, \end{cases} \tag{2.7}$$

where $\beta_{i,j}(x)$ denotes a cubic polynomial defined in $x_0 \leqslant x \leqslant x_1$ such that $\beta_{i,j}(x_0) = \beta_i$ and $\beta_{i,j}(x_1) = \beta_j$, and $\beta'(x_0) = \beta'(x_1) = 0$. The parameters β_i and β_j are chosen such that in the time-independent steady state (when Q is a constant in time and space), the model yields a target TAL radius and a target outflow pressure $P(L_0)$.

Table 2.3: Model parameter values common to all five cases

Parameter	Dimensional Value
Independent Parameters	
$C_o,\ C_{e,1}$	275 mM
Q_o	6 nl min^{-1}
R_o	10 μm
κ	1.5×10^{-5} cm s^{-1}
L_0	2 cm
L	0.5 cm
μ	7.2×10^{-3} g cm^{-1}s^{-1}
P_e	5 mmHg
$\bar{P}_o$	10 mmHg
P_1	2 mmHg
t_o	15.708 s

Extratubular concentration is specified by

$$C_e(x) = C_{e,1}(A_1 \exp(-A_3(x/L)) + A_2), \tag{2.8}$$

where $A_1 = (1 - C_e(L)/C_{e,1})/(1 - \exp(-A_3))$, $A_2 = 1 - A_1$, and $A_3 = 2$, and where $C_e(L)$ corresponds to a cortical interstitial concentration of 150 mM.

2.1.4 Numerical method

To simulate the tubular fluid motions, we take the spatial derivative of Eq. (2.1) and use the resulting equation to eliminate the fluid flow gradient term $\partial Q/\partial x$ from Eq. (2.2). This yields an advection-diffusion equation for the pressure P

$$\frac{\partial}{\partial t}P(x,t) - \frac{R^2(x,t)}{4\mu\frac{\partial R}{\partial P}}\frac{\partial}{\partial x}R(x,t)\frac{\partial}{\partial x}P(x,t) = \frac{R^3(x,t)}{16\mu\frac{\partial R}{\partial P}}\frac{\partial^2}{\partial x^2}P(x,t), \tag{2.9}$$

subject to the boundary conditions $P(0,t) = P_o(t)$ and $P(L_0,t) = P_1$.

Eq. (2.9) was advanced in time using numerical method that is second order in space and time, based on the numerical scheme described in Ref. Layton et al. (2012a). Let Δx and Δt be the spatial and time step, respectively. Then, we write

$P_j^n = P(j\Delta x, n\Delta t)$ and use the analogous notation for R. P_j^n is advanced to P_j^{n+1} in each time step by using the discretized version of Eq. (2.9),

$$\left(\frac{P_j^{n+1} - P_j^{n-1}}{2\Delta t}\right) - \left(\frac{(R_j^n)^2}{4\mu\alpha}\right)\left(\frac{R_{j+1}^n - R_{j-1}^n}{2\Delta x}\right)\left(\frac{P_{j+1}^n - P_{j-1}^n}{2\Delta x}\right)$$

$$= \frac{(R_j^n)^3}{2 \cdot 16\alpha}\left(\frac{P_{j+1}^{n+1} - 2P_j^{n+1} + P_{j-1}^{n+1}}{(\Delta x)^2} + \frac{P_{j+1}^{n-1} - 2P_j^{n-1} + P_{j-1}^{n-1}}{(\Delta x)^2}\right), \tag{2.10}$$

where $\frac{\partial R}{\partial P}$ was substituted by α from Eq. (2.4). Once P_j^{n+1} was obtained, the radius R_{n+1}^j using (2.4) and the flow rate Q_j^{n+1} using (2.2) were updated. The discretized verison of Eq. (2.2) is given by

$$Q_j^{n+1} = -\frac{\pi(R_j^{n+1})^4}{8\mu}\left(\frac{P_{j+1}^{n+1} - P_{j-1}^{n+1}}{2\Delta x}\right). \tag{2.11}$$

The chloride concentration $C_j^n = C(j\Delta x, n\Delta t)$ was advanced by one time step using

$$\pi C_j^n\left(\frac{(R_j^{n+1})^2 - (P_j^n)^2}{\Delta t}\right) + \pi(R_j^n)^2\left(\frac{C_j^{n+1} - C_j^n}{\Delta t}\right) = -C_j^n\left(\frac{Q_j^{n+1} - Q_j^n}{\Delta x}\right) \tag{2.12}$$

$$- Q_j^n\left(\frac{C_j^n - C_{j-1}^n}{\Delta x}\right) - 2\pi R_{\mathrm{ss},j}\left(\frac{(V_{\max})_j C_j^n}{(K_M)_j + C_j^n} + \kappa_j(C_j^n - C_{e,j})\right).$$

A time step of $\Delta t = 1/320$ s was applied on a spatial grid of 1280 subintervals, which yield a space step of $\Delta x = L_0/1280 = 2/1280$ cm.

2.2 Short-Looped Nephron Model

2.2.1 Model formulation

A short-looped nephron model of a TGF system explicitly represents the proximal tubule, the descending limb, and the TAL of a short loop of Henle. As in the TAL model, the loop model is analogously formulated as a boundary value problem and

predicts tubular fluid rate, fluid pressure, and tubular radius as functions of time and space. Also, we similarly use an extended model tubule to represent a short loop of Henle, which extends in space from $x = 0$ at the entrance to the proximal tubule, through $x = L$ at the loop bend and $x = 2L$ at the MD, to $x = L_0(= 5L)$ at the end of collecting duct. Boundary condition for inflow fluid pressure is now prescribed at the entrance of the proximal tubule at $x = 0$, which is determined by the TGF response. By assuming the tubular walls to be compliant and representing the chloride ion (Cl^-) as the principal signaling agent for TGF activation, the mathematical equations for loop model are same as those for TAL model, given in Eqs. (2.1)–(2.5), with Eq. (2.2) and (2.5) replaced by the following equations, respectively,

$$\frac{\partial}{\partial x}Q(x,t) = -\left(2\pi R(P(x,t))\frac{dR}{dP}\right)\frac{\partial}{\partial t}P(x,t) - \Phi(x,t), \tag{2.13}$$

$$P_o(t) = \bar{P}_o + K_1 \tanh(K_2(C_{\rm op} - C(2L, t-\tau))), \tag{2.14}$$

where $\Phi(x,t)$ is the transmural water flux per unit length, taken to be positive out of the tubule (see below). Note that because the model includes the descending portions of the loop, the boundary condition $C(0,t) = C_o$, which is considered to be fixed, is prescribed at the entrance of the proximal tubule. A schematic diagram for the short-looped TGF system is given in Fig. 2.3.

2.2.2 Model parameters

New parameter values for short-looped model, which were not appeared in Table 2.1 or differ from TAL model, are given in Table 2.4. The model tubule is divided into three functionally distinct segments: the proximal tubule (the proximal convoluted and straight tubules), the descending limb, and the TAL. As previously noted, anatomical findings have indicated the proximal straight tubule terminates at the boundary between the outer and inner stripe within outer medulla (approximately 0.6 mm from the cortico-medullary boundary). An initial water-permeable descend-

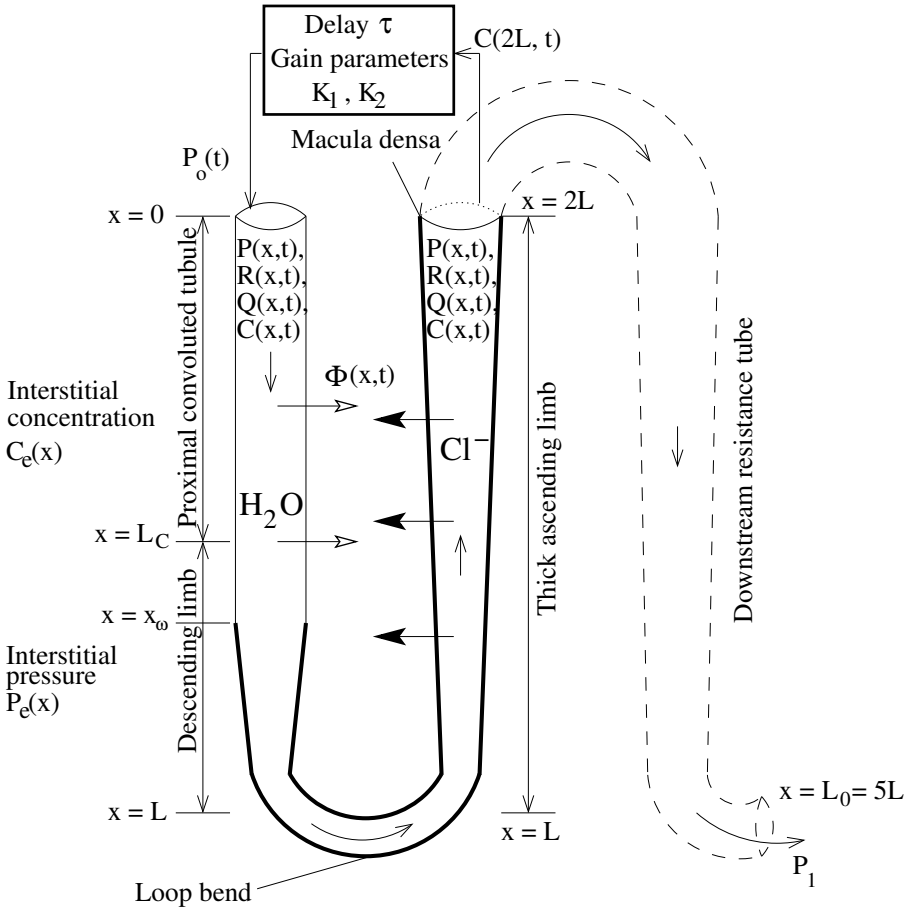

FIGURE 2.3: A schematic representation of short-looped TGF system. Hydrodynamic pressure $P_o(t) = P(0,t)$ drives flow into loop entrance ($x = 0$) at time t. Oscillations in inflow pressure result in oscillations in loop pressure $P(x,t)$, flow rate $Q(x,t)$, water flux $\Phi(x,t)$, radius $R(x,t)$, and tubular fluid chloride concentration $C(x,t)$. Reprinted from Ryu and Layton (2013c).

ing limb spans the first ∼60% of the inner strip and a terminal water-impermeable descending limb spans the remainder of the inner strip. The entire TAL is water impermeable.

The total length of model nephron is set to be $L_0 = 25$ mm. The length of the descending segments, including the proximal tubule and descending limb, is assumed to be $L = 5$ mm and is equal to the length of the TAL. The length of the proximal convoluted tubules is set to $L_C = 3$ mm and is equal to the length of the cortical TAL. The length of the descending limb and the proximal straight tubule is assumed

to be $L_D = 2$ mm, which is equal to the length of the medullary TAL. Note that $L = L_C + L_D$ and $L_0 = 5L$. Fluid dynamics equations (Eq. (2.1), (2.13), (2.4)) are solved for $0 \leqslant x \leqslant L_0 (= 5L)$, corresponding to the entire model nephron, whereas the chloride conservation equation (Eq. (2.3)) is solved for $0 \leqslant x \leqslant 2L$, corresponding to the tubule only up to the MD.

To yield steady-state tubular radius and pressure profiles that are consistent with experiment measurements, we specified unpressurized tubular radius $\beta(x)$ (in μm) using the following piecewise function:

$$\beta(x) = \begin{cases} \beta_0, & 0 \leqslant x \leqslant x_w, \\ \beta_{0,1}(x), & x_w \leqslant x \leqslant L, \\ \beta_{1,2}(x), & L \leqslant x \leqslant 1.5L, \\ \beta_2, & 1.5L \leqslant x \leqslant a_d, \\ \beta_{2,3}(x), & a_d \leqslant x \leqslant L_0, \end{cases} \tag{2.15}$$

where $\beta_{i,j}(x)$ denotes a cubic polynomial defined in $x_0 \leqslant x \leqslant x_1$ such that $\beta_{i,j}(x_0) = \beta_i$ and $\beta_{i,j}(x_1) = \beta_j$, and $\beta'(x_0) = \beta'(x_1) = 0$. The parameters β_0, β_1, β_2, and β_3 (8.8, 5.4, 9.9, and 6.6 μm, respectively) were chosen such that in the time-independent steady state (when Q is a constant in time and space), the tubular radius was $\sim$5.5 at the loop bend and $\sim$10 μm at the MD (Knepper et al. (1977)), and so that the tubular fluid pressure was $\sim$8 mmHg at the MD (i.e., $x = 2L$) and $\sim$2 mmHg at the end of the model tubule (i.e., $x = L_0$). x_w denotes the position at which the water-impermeable segment of the descending limb begins; x_w is taken to be $L_C + 0.6L_D$. a_d denotes the position past the MD at which the tubular radius begins to decrease and is set to $2.5 \times L$.

In normal rats, SNGFR is $\sim$30 nl/min. Micropuncture experiments by Young and Marsh (1981) have indicated that approximately two-third of the water and NaCl are reabsorbed along the proximal convoluted tubule; thus, the fluid flow rate

Table 2.4: Parameter values for loop model

Symbol	*Description*	*Dimensional value*
α_{DL}	Proximal tubule and DL compliance	0.45×10^{-5} cm·mmHg^{-1}
α_{TAL}	TAL compliance	0.266×10^{-5} cm·mmHg^{-1}
β_0	Initial boundary value for $\beta_{0,1}(x)$	8.843 μm
β_1	End boundary value for $\beta_{0,1}(x)$	5.43 μm
β_2	End boundary value for $\beta_{1,2}(x)$	9.98 μm
β_3	End boundary value for $\beta_{2,3}(x)$	6.55 μm
$C_{e,o}$	Interstitial Cl^- concentration at the upper cortex	150 mM
C_o	Cl^- concentration at proximal tubule entrance	160 mM
L_0	Total length of model nephron	2.5 cm
L_C	Length of the proximal convoluted tubule or the cortical TAL	0.3 cm
L_D	Length of the short descending limb or the medullary TAL	0.2 cm
x_ω	Position where water-impermeable segment of the descending limb starts	0.42 cm
a_d	Position where unpressurized radius begins to decrease after the MD	1.25 cm
$\bar{P}_o$	Steady-state inflow pressure at the proximal tubule	13.0 mmHg
κ_{PCT}	Proximal convoluted tubule Cl^- permeability for $0 \leqslant x \leqslant L_C$	20.0×10^{-5} cm·s^{-1}
κ_{PST}	Proximal straight tubule Cl^- permeability for $L_C \leqslant x \leqslant x_\omega$	10.0×10^{-5} cm·s^{-1}
κ_{DL}	DL Cl^- permeability for $x_\omega \leqslant x \leqslant L$	1.5×10^{-5} cm·s^{-1}
κ_{TAL}	TAL Cl^- permeability for $L \leqslant x \leqslant 2L$	1.5×10^{-5} cm·s^{-1}
$V_{\mathrm{max,\ PCT}}$	Proximal convoluted tubule maximum active Cl^- transport rate	28.0 nmole·cm^{-2}s^{-1}
$V_{\mathrm{max,\ PST}}$	Proximal straight tubule maximum active Cl^- transport rate	2.5 nmole·cm^{-2}s^{-1}
$V_{\mathrm{max,\ DL}}$	Descending limb maximum active Cl^- rate	0.0 nmole·cm^{-2}s^{-1}
$V_{\mathrm{max,\ TAL}}$	TAL maximum active Cl^- transport rate	19.18 nmole·cm^{-2}s^{-1}
τ	Base-case TGF delay	3.5 s
K_1	Half of the range of pressure variation around $\bar{P}_o$	6 mmHg
K_2	TGF sensitivity, $-\gamma/(K_1 C'_{\mathrm{ss}}(2L))$	–

into the proximal straight tubule is ∼10 nl/min. We assume the same fractional reabsorption in dynamic state. Flow rate at the loop bend is believed to be ∼6–8 nl/min. Given these observations, we describe the transmural water flux $\Phi(x,t)$ as a piecewise constant function in terms of $Q(0,t)$:

$$\Phi(x,t) = \begin{cases} \frac{2}{3}\frac{Q(0,t)}{L_C}, & 0 \leqslant x \leqslant L_C, \\ \frac{1}{10}\frac{Q(0,t)}{0.6L_D}, & L_C \leqslant x \leqslant x_w, \\ 0, & x_w \leqslant x \leqslant L_0, \end{cases} \tag{2.16}$$

where L_C and x_ω are the positions where the proximal straight tubule (or, descending limb) and the water-impermeable segment of the descending limb begin, respectively (see Fig. 2.3). Together with appropriate inflow pressure and luminal radius, the model predicts a steady-state fluid flow rate of ∼7.0 nl/min at the loop bend (i.e., $x = L$).

To compute passive chloride transport, we define interstitial concentration for the descending segments and then assume symmetry to obtain the profile for the TAL:

$$C_e(x) = \begin{cases} C_{e,o}(A_1 \exp(A_3(x/L)) + A_2), & 0 \leqslant x \leqslant L, \\ C_{e,o}(-x + 2L), & L < x \leqslant 2L, \end{cases} \tag{2.17}$$

where $A_1 = (1 - C_{e,1}/C_{e,o})/(1 - \exp(A_3))$, $A_2 = 1 - A_1$, and $A_3 = 2$. The initial condition for the interstitial chloride concentration, $C_{e,o}$, is set to 150 mM. $C_{e,1}$ denotes an interstitial loop-bend concentration of 275 mM. The exponential form of $C_e(x)$ assumes that the steepest increase in interstitial concentration is found in the outer medulla, as is generally expected (Layton and Edwards (2010); Layton and Layton (2005)).

The proximal convoluted tubule is assumed to have a moderate Cl^- permeability of 20×10^{-5} cm·s^{-1} (Weinstein (1986)). The proximal straight tubule is assumed to be moderately NaCl permeable; the descending limb and TAL are assumed to have a low Cl^- permeability of 1.5×10^{-5} cm·s^{-1} (Mason et al. (1979)).

The base-case tubular wall compliance is set to $\alpha_{\mathrm{DL}} = 0.45 \times 10^{-5}$ cm·mmHg^{-1} for the proximal tubule and the descending limb, and to $\alpha_{\mathrm{TAL}} = 0.266 \times 10^{-5}$ cm·mmHg^{-1} for the TAL. These values are 1/5 of measured compliance in isolated tubule studies (Young and Marsh (1981)). This choice of the tubular compliance is based on the consideration that the effective compliance of the tubular walls may be lowered *in vivo* by the stiffness of the interstitial matrix, and by the resistance exerted by neighboring nephrons whose tubular fluid may be oscillating in synchronization (Leyssac and Baumbach (1983)).

2.2.3 Numerical method

In the numerical simulations, we solve the differential equations describing tubular pressure, flow, radius, and chloride concentration. As for numerical simulation of the TAL model described in Section 2.1.4, we similarly derive the following advection-diffusion equation for the pressure P:

$$\frac{\partial}{\partial t}P - \frac{R^2}{4\mu\frac{dR}{dP}}\frac{\partial}{\partial x}R\frac{\partial}{\partial x}P = \frac{R^3}{16\mu\frac{dR}{dP}}\frac{\partial^2}{\partial x^2}P - \frac{\Phi}{2\pi R\frac{dR}{dP}}, \tag{2.18}$$

subject to the boundary conditions $P(0,t) = P_0(t)$ and $P(L_0,t) = P_1$.

Same numerical methods, which are applied to the TAL model in Section 2.1.4, are used to advance Eq. (2.18) with a spatial step $\Delta x = L_0/400 = 0.5/400 = 0.00125$ cm and a time step of $\Delta t = 1/3200 = 0.0003125$ s.

2.3 Coupled-Nephron Model

2.3.1 Model formulation

The mathematical model of coupled short-looped nephrons analogously follows that of short-looped model in Section 2.2. Model equations for tubular fluid pressure, volumetric flow rate, radius, and fluid chloride concentration in each nephron, as functions of time and space, can be formulated as in Eqs. (2.1), (2.13), (2.3), and

(2.4), respectively. A schematic diagram for the model of coupled-TGF system is given in Fig. 2.4.

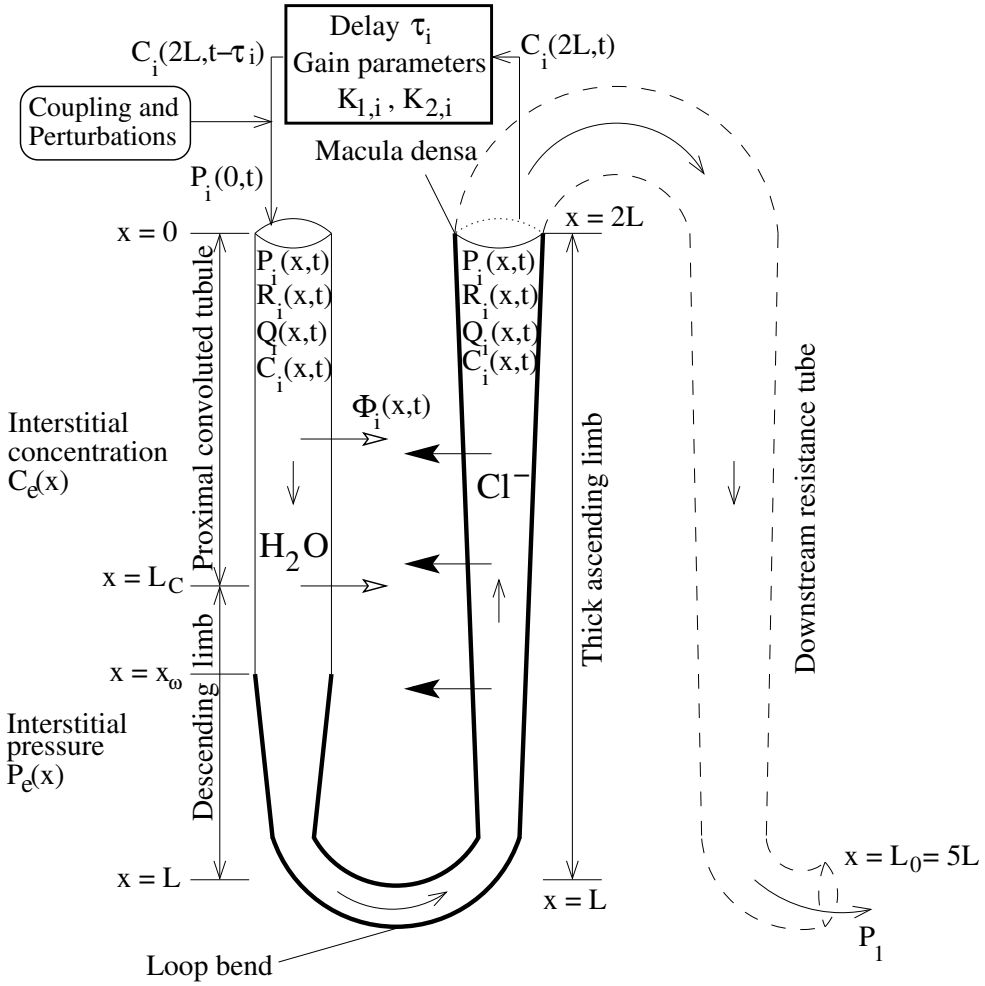

FIGURE 2.4: A schematic representation of coupled-TGF system in the ith nephron. Hydrodynamic pressure $P_i(0,t)$ drives flow into loop entrance ($x = 0$) at time t. Oscillations in pressure result in oscillations in loop pressure $P_i(x,t)$, flow rate $Q_i(x,t)$, radius $R_i(x,t)$, and tubular fluid chloride concentration $C_i(x,t)$. Reprinted from Ryu and Layton (2013b).

In a (uncoupled) short-looped model in Section 2.2, we assumed that inflow pressure to the proximal tubule is determined by the TGF response, given as a nonlinear function of the chloride concentration in the terminal segment of TAL. To represent internephron coupling, inflow pressure at the entrance of the proximal tubule in ith

nephron, $P_i(0,t)$, is defined as a sum of two terms. The first term represents the feedback-mediated inflow pressure in response to the nephron itself. The second term represents the sum of all coupled TGF responses that are caused by nearby nephrons. Thus we write

$$\begin{aligned} P_i(0,t) =& \bar{P}_{0,i} + K_{1,i}\tanh(K_{2,i}(C_{\text{op}} - C_i(2L, t-\tau_i))) \\ &+ \sum_{j\neq i} \phi_{i,j} K_{1,j}\tanh(K_{2,j}(C_{\text{op}} - C_j(2L, t-\tau_j))), \end{aligned} \tag{2.19}$$

where the coupling constant $\phi_{i,j}$ characterizes the strength of the coupling between nephrons i and j; $K_{1,i}$ denotes half of the range of pressure variation around its reference value $\bar{P}_{0,i}$ for the nephron i; $K_{2,i}$ quantifies TGF sensitivity; the operating concentration C_{op} is the steady-state luminal fluid chloride concentration adjacent to the MD when $P_i(0,t) = \bar{P}_{0,i}$ (i.e., when $C_{\text{op}} = C_i(2L, t-\tau_i)$); and $C(2L, t-\tau_i)$ is the chloride concentration alongside the MD (of nephron i) at time $t-\tau_i$, where τ_i represents the TGF delay for signal transmission from the MD to the AA.

2.3.2 Model parameters

Model parameter values for each nephron are applied same as those for the short-looped model, given in Table 2.4. Also, the physical anatomy of the model tubule and the length of each functionally different segment along the tubule are adapted from those of short-looped model. We similarly specify unpressurized tubular radius $\beta_i(x)$, transmural water flux $\Phi_i(x,t)$, tubular compliance of the loop α, maximum active Cl^- transport rate $V_{\max}$, and Cl^- permeability κ for each nephron i, as in the short-looped model. Moreover, we use the same profile for the interstitial chloride concentration $C_e(x)$ defined in (2.17).

2.3.3 Numerical method

To predict time-varying tubular pressure, flow, radius, and chloride concentration for each nephron i, we similarly use the advection-diffusion equation for the pressure

P_i as derived in Eq. (2.18).

$$\frac{\partial}{\partial t}P_i - \frac{R_i^2}{4\mu\frac{dR_i}{dP_i}}\frac{\partial}{\partial x}R_i\frac{\partial}{\partial x}P_i = \frac{R_i^3}{16\mu\frac{dR_i}{dP_i}}\frac{\partial^2}{\partial x^2}P_i - \frac{\Phi_i}{2\pi R_i\frac{dR_i}{dP_i}}, \tag{2.20}$$

subject to the boundary conditions $P_i(0,t) = P_{0,i}(t)$ and $P_i(L_0,t) = P_{1,i}$.

Same numerical methods, which were applied to the TAL model in Section 2.1.4, are used to advance Eq. (2.20) with a spatial step $\Delta x = L_0/400 = 0.5/400 = 0.00125$ cm and a time step of $\Delta t = 1/3200 = 0.0003125$ s.

3

Model Results and Analysis

In this chapter, we present analytic and numerical results for each model we consider. Because each model's emphasis and analysis substantially differ from each other, we start with the overview of model results in the beginning of each section. Results and all figures in each section are adapted from the published results in Ryu and Layton (2013a) (TAL model), Ryu and Layton (2013c) (short-looped nephron model), and Ryu and Layton (2013b) (coupled-nephron model) after minor changes with permission of reprints.

3.1 Thick Ascending Limb Model

The TAL model was developed to account for the potential effects of spatial TAL radius and NaCl transport rate on the stability of the TGF system. To do this, one may obtain an asymptotic behavior of the *in vivo* tubular fluid dynamics subsequent to a perturbation by a direct computation of the numerical solution to the TAL-model equations (Eqs. (2.3), (2.4), and (2.9)). However, to attain a thorough understanding how model behaviors systematically depend on model parameters, those computations can be time-consuming and impractical. Thus, as an alterna-

tive, we derived and analyzed a characteristic equation from a linearization of the full model equations.

To further facilitate a direct comparison between all considered model cases (H, IR, IT, IRT, and CIRT) in Section 2.1.2, the respective characteristic equation for each case was derived and its corresponding root curves were identified by means of bifurcation analysis. Guided by the information obtained from the characteristic equation, numerical simulations were also conducted to validate and supplement that information.

3.1.1 Characteristic equation

Before we derive the characteristic equation, we first nondimensionalize Eqs. (2.9) and (2.3). We use the following reference base-case units: unit length along the TAL, $L = 0.5$ cm; unit fluid pressure at the loop bend, $P_o = 10$ mmHg; unit luminal radius of TAL, $R_o = 10$ μm; unit chloride concentration, $C_o = C(0,t) = 275$ mM; unit flow rate in the TAL, $Q_o = 6$ nl min^{-1}; unit time, $t_o = \pi R_o^2 L/Q_o = 5\pi$ s (the TAL fluid transit time at flow rate Q_o). We define $\tilde{x} = x/L$, $\tilde{t} = t/t_o$, $\tilde{\tau} = \tau/t_o$, $\tilde{C} = C/C_o$, $\tilde{C}_e = C_e/C_o$, $\tilde{Q} = Q/Q_o$, $\tilde{V}_{max} = V_{max}/(C_o Q_o/(c_{A_o} L))$, $\tilde{K}_M = K_M/C_o$, $\tilde{\kappa} = \kappa/(Q_o/(c_{A_o} L))$, $\tilde{P} = P/P_o$, $\tilde{R} = R/R_o$, $\tilde{R}_{ss} = R_{ss}/R_o$, $\tilde{\beta} = \beta/R_o$, $\tilde{\mu} = \mu/(\pi P_o R_o^4/Q_o L)$, $\tilde{\alpha} = \alpha P_o/R_o$, where $c_{A_o} = 2\pi R_o$. Then, expressing Eqs. (2.9) and (2.3) in terms of nondimensional variables, simplifying, and dropping the tildes, we obtain

$$\frac{\partial}{\partial t}P - \frac{R^2}{4\mu\alpha}\frac{\partial}{\partial x}R\frac{\partial}{\partial x}P = \frac{R^3}{16\mu\alpha}\frac{\partial^2}{\partial x^2}P, \tag{3.1}$$

$$R^2\frac{\partial}{\partial t}C = -2RC\frac{\partial}{\partial t}R - Q\frac{\partial}{\partial x}C - R_{ss}\left(\frac{V_{\max}C}{K_M + C} + \kappa(C - C_e)\right). \tag{3.2}$$

We now linearize Eq. (3.1) about its steady-state by assuming infinitesimal per-

turbations in C, P, and R:

$$C(x,t) = C_{ss}(x) + \epsilon C_\epsilon(x,t), \tag{3.3}$$

$$P(x,t) = P_{ss}(x) + \epsilon P_\epsilon(x,t), \tag{3.4}$$

$$R(x,t) = R_{ss}(x) + \epsilon R_\epsilon(x,t), \tag{3.5}$$

where $\epsilon \ll 1$, and $C_{ss}(x)$, $P_{ss}(x)$ and $R_{ss}(x)$ denote the steady-state Cl^- concentration, pressure, and radius, respectively. From nondimensionalized forms of Eqs. (2.1) and (2.4), one can show that

$$R_{ss}^4 \frac{\partial}{\partial x} P_{ss} = -8\mu, \tag{3.6}$$

$$R_{ss} = \alpha(P_{ss} - P_e) + \beta, \tag{3.7}$$

$$R_\epsilon = \alpha P_\epsilon. \tag{3.8}$$

Note that steady-state tubular flow rate is normalized to 1. Then, by taking the spatial derivative of Eq. (3.6), we get

$$R_{ss}^3 \frac{\partial^2}{\partial x^2} P_{ss} = -4R_{ss}^2 \frac{\partial}{\partial x} R_{ss} \frac{\partial}{\partial x} P_{ss} = \frac{32\mu}{R_{ss}^2} \frac{\partial}{\partial x} R_{ss}. \tag{3.9}$$

Also, substituting (3.7) into (3.6), we obtain an equation for P_{ss}

$$(\alpha(P_{ss} - P_e) + \beta)^4 \frac{\partial}{\partial x} P_{ss} = -8\mu. \tag{3.10}$$

Next, we substitute (3.4) and (3.5) into (3.1) and keep only the $O(\epsilon)$ terms

$$R_{ss} \frac{\partial}{\partial t} P_\epsilon - \frac{1}{4\mu\alpha} \left(R_{ss}^3 \frac{\partial}{\partial x} R_\epsilon \frac{\partial}{\partial x} P_{ss} + R_{ss}^3 \frac{\partial}{\partial x} R_{ss} \frac{\partial}{\partial x} P_\epsilon + 3R_{ss}^2 R_\epsilon \frac{\partial}{\partial x} R_{ss} \frac{\partial}{\partial x} P_{ss} \right)$$
$$= \frac{1}{16\mu\alpha} \left(R_{ss}^4 \frac{\partial^2}{\partial x^2} P_\epsilon + 4R_{ss}^3 R_\epsilon \frac{\partial^2}{\partial x^2} P_{ss} \right). \tag{3.11}$$

Simplifying (3.11) from Eqs. (3.6) and (3.9), we obtain the following advection-diffusion equation for P_ϵ,

$$\frac{\partial}{\partial t} P_\epsilon + \frac{\partial}{\partial x} P_\epsilon \left(\frac{2}{R_{ss}^2} - \frac{1}{4\mu\alpha} R_{ss}^2 \frac{\partial}{\partial x} R_{ss} \right) - 2P_\epsilon \left(\frac{1}{R_{ss}^3} \frac{\partial}{\partial x} R_{ss} \right) = \frac{R_{ss}^3}{16\mu\alpha} \frac{\partial^2}{\partial x^2} P_\epsilon, \tag{3.12}$$

subject to the boundary conditions:

$$P_\epsilon(0,t) = P'(C_{\text{op}})C_\epsilon(1,t-\tau), \tag{3.13}$$

$$P_\epsilon(L_0,t) = 0. \tag{3.14}$$

As in the previous studies (Layton et al. (1991); Pitman et al. (1993); Layton et al. (1997b, 2009); Layton (2010)), we assume that $C_\epsilon(x,t)$ can be written as $C_\epsilon = f(x)e^{\lambda t}$, for some function $f(x)$ and a constant λ. Thus,

$$P_\epsilon(0,t) = P'(C_{\text{op}})f(1)e^{\lambda(t-\tau)}. \tag{3.15}$$

Assuming that the solution for Eqs. (3.12)–(3.14) has the form

$$P_\epsilon(x,t) = P'(C_{\text{op}})f(1)g(x)e^{\lambda(t-\tau)}, \tag{3.16}$$

and substituting into Eq. (3.12), we obtain the second-order differential equation for $g(x)$

$$\frac{R_{ss}^3}{16\mu\alpha}g''(x) - \left(\frac{2}{R_{ss}^2} - \frac{1}{4\mu\alpha}R_{ss}^2\frac{\partial}{\partial x}R_{ss}\right)g'(x) + \left(\frac{2}{R_{ss}^3}\frac{\partial}{\partial x}R_{ss} - \lambda\right)g(x) = 0, \tag{3.17}$$

with boundary conditions $g(0) = 1$ and $g(L_0) = 0$.

Next, we linearize the solute conservation equation (3.2),

$$\begin{aligned}(R_{ss}+\epsilon R_\epsilon)^2\frac{\partial}{\partial t}(C_{ss}+\epsilon C_\epsilon) = &-2(R_{ss}+\epsilon R_\epsilon)(C_{ss}+\epsilon C_\epsilon)\frac{\partial}{\partial t}(R_{ss}+\epsilon R_\epsilon)\\ &+\frac{(R_{ss}+\epsilon R_\epsilon)^4}{8\mu}\frac{\partial}{\partial x}(P_{ss}+\epsilon P_\epsilon)\frac{\partial}{\partial x}(C_{ss}+\epsilon C_\epsilon)\\ &-R_{ss}\left(\frac{V_{\max}(C_{ss}+\epsilon C_\epsilon)}{K_M+C_{ss}+\epsilon C_\epsilon}+\kappa(x)(C_{ss}+\epsilon C_\epsilon - C_e)\right).\end{aligned} \tag{3.18}$$

Note that at steady state $\epsilon = 0$, the steady-state solutions satisfies

$$\frac{R_{ss}^4}{8\mu}\frac{\partial}{\partial x}P_{ss}\frac{\partial}{\partial x}C_{ss} = (K(C_{ss}) + \kappa(C_{ss}-C_e))R_{ss}, \tag{3.19}$$

where the active transport term is denoted by $K(C) = \frac{V_{\max}C}{K_M+C}$.

Keeping only the $O(\epsilon)$ terms in Eq. (3.18), we arrive at the evolution equation for C_ϵ

$$R_{ss}^2\frac{\partial}{\partial t}C_\epsilon = -2\alpha R_{ss}C_{ss}\frac{\partial}{\partial t}P_\epsilon - (K'(C_{ss})+\kappa)R_{ss}C_\epsilon + \frac{R_{ss}^3}{8\mu}\left(4R_\epsilon\frac{\partial}{\partial x}P_{ss}\frac{\partial}{\partial x}C_{ss} + R_{ss}\frac{\partial}{\partial x}P_{ss}\frac{\partial}{\partial x}C_\epsilon + R_{ss}\frac{\partial}{\partial x}P_\epsilon\frac{\partial}{\partial x}C_{ss}\right). \quad (3.20)$$

Substituting $C_\epsilon = f(x)e^{\lambda t}$, $P_\epsilon(x,t) = P'(C_{\text{op}})f(1)g(x)e^{\lambda(t-\tau)}$, and $R_\epsilon(x,t) = \alpha P_\epsilon(x,t)$ into the above equation and canceling out $e^{\lambda t}$, we obtain

$$\lambda R_{ss}^2 f(x) = -2\alpha\lambda R_{ss}C_{ss}P'(C_{\text{op}})f(1)g(x)e^{-\lambda\tau} - (K'(C_{ss})+\kappa)R_{ss}f(x)$$
$$\frac{R_{ss}^3}{8\mu}(R_{ss}P'_{ss}f' + R_{ss}C'_{ss}P'(C_{op})f(1)g'(x)e^{-\lambda\tau} + 4\alpha C'_{ss}P'_{ss}P'(C_{\text{op}})f(1)g(x)e^{-\lambda\tau}). \quad (3.21)$$

Applying Eq. (3.6) and rearranging,

$$f'(x) + ((K'(C_{ss})+\kappa)R_{ss} + \lambda R_{ss}^2)f(x) = e^{-\lambda\tau}P'(C_{\text{op}})f(1)\left(\frac{R_{ss}^4}{8\mu}C'_{ss}g'(x) - 2\alpha g(x)(\lambda R_{ss}C_{ss} + 2\frac{C'_{ss}}{R_{ss}})\right). \quad (3.22)$$

Recall we have fixed Cl^- concentration at the loop bend (i.e $x = 0$). Thus,

$$C_\epsilon(0,t) = f(0)e^{\lambda t} = 0 \Rightarrow f(0) = 0. \quad (3.23)$$

Given the initial condition (3.23), the solution for (3.22) can be found to be

$$f(s) = exp\left(-\int_0^s P(x)\,\mathrm{d}x\right)\left(\int_0^s Q(x)\exp\left(\int_0^x P(y)\,\mathrm{d}y\right)\,\mathrm{d}x\right), \quad (3.24)$$

where

$$P(x) = (K'(C_{ss})+\kappa)R_{ss} + \lambda R_{ss}^2, \quad (3.25)$$

$$Q(x) = e^{-\lambda\tau}P'(C_{\text{op}})f(1)\left(\frac{R_{ss}^4}{8\mu}C'_{ss}g'(x) - 2\alpha g(x)(\lambda R_{ss}C_{ss} + 2\frac{C'_{ss}}{R_{ss}})\right). \quad (3.26)$$

Setting $s = 1$ and canceling the factor $f(1)$, we arrive at the characteristic equation

$$1 = e^{-\lambda\tau} P'(C_{\text{op}}) \int_0^2 \left(\frac{R_{ss}^4}{8\mu} C'_{ss} g' - 2\alpha g(\lambda R_{ss} C_{ss} + 2\frac{C'_{ss}}{R_{ss}}) \right) \times \exp\left(- \int_x^2 (K'(C_{ss}) + \kappa) R_{ss} + \lambda R_{ss}^2 \, \mathrm{d}y \right) \mathrm{d}x. \tag{3.27}$$

To facilitate a comparison of (3.27) with the characteristic equations derived for homogeneous rigid and compliant TAL models (Layton et al. (1991); Layton (2010)), we apply (3.6) to (3.19) to obtain

$$\frac{d}{dx} C_{ss} = -(K(C_{ss}) + \kappa(C_{ss} - C_e)) R_{ss}. \tag{3.28}$$

Taking the spatial derivative of (3.28) yields

$$\begin{aligned} C''_{ss} &= -(K'(C_{ss}) C'_{ss} + \frac{V'_{\max} C_{ss}}{K_M + C_{ss}} + \kappa(C'_{ss} - C'_e)) R_{ss} - (K(C_{ss}) + \kappa(C_{ss} - C_e)) R'_{ss} \\ &= -(K'(C_{ss}) C'_{ss} + \frac{V'_{\max} C_{ss}}{K_M + C_{ss}} + \kappa(C'_{ss} - C'_e)) R_{ss} + \frac{R'_{ss} C'_{ss}}{R_{ss}}. \end{aligned} \tag{3.29}$$

Dividing by C'_{ss} from both sides and rearranging,

$$(K'(C_{ss}) + \kappa) R_{ss} = -\frac{C''_{ss}}{C'_{ss}} + \frac{R'_{ss}}{R_{ss}} + \kappa \frac{C'_e}{C'_{ss}} R_{ss} - \frac{V'_{\max} C_{ss}}{(K_M + C_{ss}) C'_{ss}} R_{ss}. \tag{3.30}$$

Substituting (3.30) into (3.27) and simplifying, we finally get

$$1 = \frac{\gamma e^{-\lambda\tau}}{R_{ss}(1)} \int_0^1 \left(\frac{R_{ss}^5}{8\mu} g' - 2\alpha g(\lambda R_{ss}^2 \frac{C_{ss}}{C'_{ss}} + 2) \right) \times \exp\left(- \int_x^1 \left(\frac{\kappa C'_e}{C'_{ss}} + \lambda R_{ss} - \frac{V'_{\max} C_{ss}}{(K_M + C_{ss}) C'_{ss}} \right) R_{ss} \, \mathrm{d}y \right) \mathrm{d}x, \tag{3.31}$$

where $\gamma \equiv P'(C_{\text{op}}) C'_{ss}(1)$ is the TGF gain and $g(x)$ satisfies Eq. (3.17). Equation (3.31) assumes compliant TAL walls and allows spatially varying radius and maximum active transport, i.e., it applies to the CIRT case. It can also be simplified and applied to other cases.

In the rigid-tube limit where $\alpha \to 0$, (3.31) reduces to

$$1 = \frac{\gamma e^{-\lambda\tau}}{8\mu R(1)} \int_0^1 R^5 g' \exp\left(- \int_x^1 \left(\frac{\kappa C_e'}{C_{ss}'} + \lambda R - \frac{V_{\max}' C_{ss}}{(K_M + C_{ss}) C_{ss}'} \right) R \, \mathrm{d}y \right) \mathrm{d}x. \quad (3.32)$$

Note that R_{ss} is replaced by R for a rigid TAL.

Multiplying (3.17) by $16\mu\alpha$ and setting $\alpha = 0$, it becomes

$$g''(x) + 4\frac{R'}{R} g'(x) = 0, \quad (3.33)$$

with boundary conditions $g(0) = 1$ and $g(L_0) = 0$. Solving for $g(x)$, we get

$$g(x) = -\frac{1}{C_1} \int_0^x \frac{1}{R^4} \, \mathrm{d}y + 1, \quad (3.34)$$

$$g'(x) = -\frac{1}{C_1 R^4(x)}, \quad (3.35)$$

where $C_1 = \int_0^{L_0} R^{-4} \, \mathrm{d}x$. Plugging (3.35) into (3.32),

$$1 = -\frac{\gamma}{8\mu C_1} \frac{e^{-\lambda\tau}}{R(1)} \int_0^1 R \cdot \exp\left(- \int_x^1 \left(\frac{\kappa C_e'}{C_{ss}'} + \lambda R - \frac{V_{\max}' C_{ss}}{(K_M + C_{ss}) C_{ss}'} \right) R \, \mathrm{d}y \right) \mathrm{d}x. \quad (3.36)$$

With appropriate functions for R and $V_{\max}$, Eq. (3.36) can be applied to the IR, IT and IRT cases.

To derive the characteristic equation for a TGF model of a rigid TAL with inhomogeneous radius and maximum active transport, we begin with the solute conservation equation, in nondimensional form, given by Layton et al. (1991)

$$R^2 \frac{\partial}{\partial t} C + Q(C(1, t - \tau)) \frac{\partial}{\partial x} C = -R \left(K(C) + \kappa (C - C_e) \right), \quad (3.37)$$

where $K(C) = \frac{V_{\max} C}{K_M + C}$. Q represents the fluid flow through the tube, which depends on the MD chloride concentration at an earlier time $t - \tau$, i.e., $Q = Q(C(L, t - \tau))$.

We linearize Eq. (3.37) by applying Eq. (3.3) and gathering $O(1)$ and $O(\epsilon)$ terms, respectively,

$$\frac{d}{dx}C_{ss} = -\frac{R}{Q_{\text{op}}}(K(C_{ss}) + \kappa(C_{ss} - C_e)), \tag{3.38}$$

$$R^2\frac{\partial}{\partial t}C_\epsilon + Q_{\text{op}}\frac{\partial}{\partial x}C_\epsilon + Q'(C_{\text{op}})C_\epsilon(1, t-\tau)\frac{\partial}{\partial x}C_{ss} = -(K'(C_{ss}) + \kappa)RC_\epsilon, \tag{3.39}$$

where $Q(C_{ss}(1))$ and $C_{ss}(1)$ have been replaced with Q_{op} and C_{op}, respectively. Now by setting $Q_{\text{op}} = 1$ plugging $C_\epsilon = f(x)e^{\lambda t}$ into Eq. (3.39), we obtain

$$f'(x) + f(x)(\lambda R + \kappa + K'(C_{ss}))R = -Q'(C_{\text{op}})C'_{ss}f(1)e^{-\lambda\tau}. \tag{3.40}$$

This first-order linear differential equation has the solution

$$f(s) = -\exp\left(-\int_0^s (K'(C_{ss}) + \kappa)R + \lambda R^2\,\mathrm{d}x\right)$$
$$\left(\int_0^s Q'(C_{\text{op}})C'_{ss}f(1)e^{-\lambda\tau}\exp\left(\int_0^x (K'(C_{ss}) + \kappa)R + \lambda R^2\,\mathrm{d}y\right)\mathrm{d}x\right), \tag{3.41}$$

where we have used the boundary condition $f(0) = 0$. Setting $s = 1$ and canceling the factor $f(1)$ yields

$$1 = -Q'(C_{\text{op}})e^{-\lambda\tau}\int_0^1 C'_{ss}\exp\left(-\int_x^1 (K'(C_{ss}) + \kappa)R + \lambda R^2\,\mathrm{d}y\right)\mathrm{d}x. \tag{3.42}$$

Finally, using (3.38), one can obtain

$$1 = -\gamma_{\text{rigid}}\frac{e^{-\lambda\tau}}{R(1)}\int_0^1 R\cdot\exp\left(-\int_x^1\left(\frac{\kappa C'_e}{C'_{ss}} + \lambda R - \frac{V'_{\max}C_{ss}}{(K_M + C_{ss})C'_{ss}}\right)R\,\mathrm{d}y\right)\mathrm{d}x, \tag{3.43}$$

where $\gamma_{\text{rigid}} \equiv Q'(C_{\text{op}})C'_{ss}(1)$. Comparing (3.36) and (3.43), we see that in the limit $\alpha \to 0$, the gain factors for the rigid and compliant TAL models is related by

$$\gamma = 8\mu C_1\gamma_{\text{rigid}}. \tag{3.44}$$

Furthermore, if we assume for the rigid TAL model that $V_{\max}$ and R are spatially homogeneous, then (3.36) by setting $R = 1$ and $V'_{\max} = 0$, becomes

$$1 = -\frac{\gamma}{8\mu L_0}e^{-\lambda\tau}\int_0^1 e^{-\lambda(1-x)}\exp\left(-\int_x^1\frac{\kappa C'_e}{C'_{ss}}\,\mathrm{d}y\right)\mathrm{d}x \tag{3.45}$$

which was also derived in Ref. Layton (2010). Equation (3.45) will be used for the H case.

3.1.2 Model results

We first compare the steady-state behaviors of the five cases. We computed steady-state TAL tubular fluid chloride concentration profiles $C_{ss}(x)$, using TAL transport parameters corresponding to each of the five cases in Table 2.2, by integrating Eq. (3.28). Those $C_{ss}(x)$ profiles with $x = 0$ corresponding to loop bend and $x = 0.5$ cm corresponding to macula densa, and the external chloride concentration profile $C_e(x)$ (plotted in dotted), are shown in Figure 3.1. At steady state, the chloride concentration profiles for the IRT and CIRT cases are identical. Among the five cases, the IT case, which has the highest transport rate, given by the product $V_{\max}R$, near the loop bend, yields a $C_{ss}(x)$ that has the steepest slope near $x = 0$. As a result, along the cases with rigid TAL walls, the IT case has the highest degree of instability in the near-zero delay parameter regime, as we will see below.

To better understand the effects of inhomogeneities of TAL on the dynamics of the TGF system, we used the model's characteristic equations (Eqs. (3.31), (3.36), and (3.45)) to predict parameter boundaries that separate qualitatively differing dynamic behaviors. Then, we used numerical solutions of the full (nonlinear) model (Eqs. (2.3), (2.4) and (2.9)) to validate and to supplement the information provided by the characteristic equations.

A solution to the characteristic equation (3.31) is a number in an infinite series $\lambda_1, \lambda_2, \ldots$, where $\lambda_n \in \mathbb{C}$. The real and imaginary parts of λ_n correspond to the strength and frequency, respectively, of a solution of the model equations. We determined parameter regions that have differing combinations of signs of $\mathrm{Re}(\lambda_n)$ by computing values of γ–τ pairs that correspond to $\mathrm{Re}(\lambda_n) = 0$, i.e., roots that may indicate a solution bifurcation or transition between stable solution behaviors. These

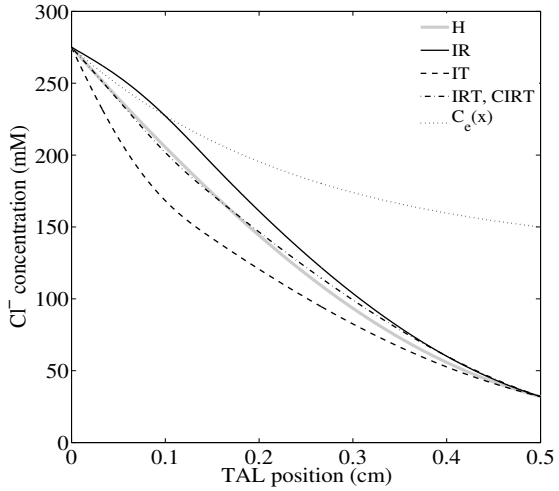

FIGURE 3.1: Steady-state tubular fluid chloride concentration profiles in TAL, computed from Eq. (3.28), for the five cases, corresponding to the parameter sets in Table 2.2. $x = 0$, loop bend; $x = 0.5$ cm, macula densa. At steady state, the chloride concentration profiles for the IRT and CIRT cases are identical. The profile for C_e (dotted) is included for comparison. Reprinted from Ryu and Layton (2013a).

γ–τ pairs, in γ–τ plane, were obtained for five model cases by using the corresponding characteristic equations. Bifurcation results for the H and IR cases are shown in Fig. 3.2, panels A and B, respectively. Results for each of the four models with inhomogeneous parameters (IR, IT, IRT, and CIRT) are given in Fig. 3.3. Note that Fig. 3.2B and Fig. 3.3A are the same, but with different γ-axis scales for the comparison with other model cases.

H case. Consider first the H case. For sufficiently small γ or τ such that (γ, τ) that fall below all curves $\mathrm{Re}(\lambda_n) = 0$ in Fig. 3.2A, the time-independent steady-state solution, indicated by "$\rho_n < 0$", is the only stable solution to which any initial solution, or any transient perturbation of a steady-state solution converges. For (τ, γ) values above the curve $\mathrm{Re}(\lambda_n) = 0$ for some n, a perturbation of the steady-state solution results in a LCO. An example is the region where $\mathrm{Re}(\lambda_2) > 0$ and $\mathrm{Re}(\lambda_1) < 0$, and where a LCO of a frequency corresponding to either $\mathrm{Im}(\lambda_1)$ or $\mathrm{Im}(\lambda_2)$ can be elicited. Model solutions can exhibit multiple stable dynamic modes,

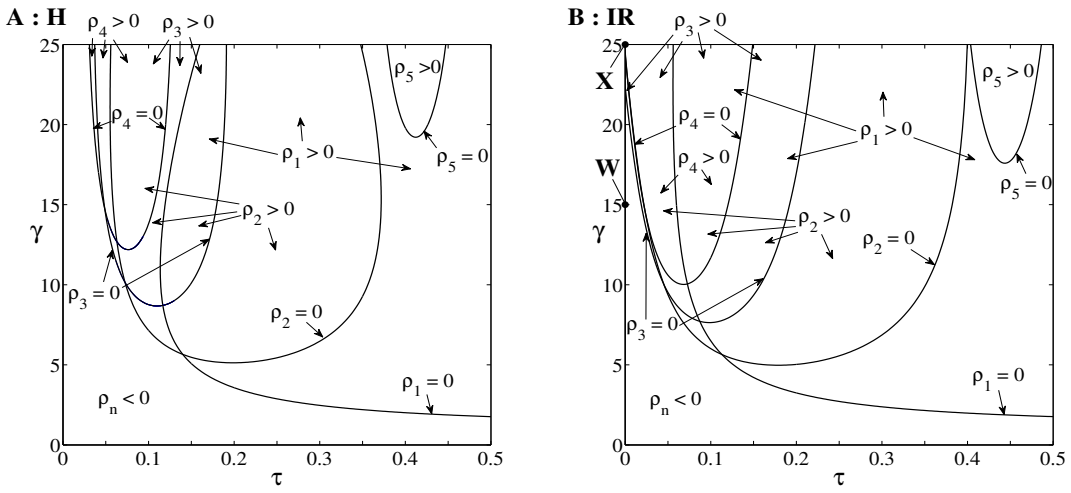

FIGURE 3.2: Root loci for H case (A) and IR case (B). MD chloride concentration oscillations corresponding to the points **W** and **X** are given in Figs. 3.4W and 3.4X. Reprinted from Ryu and Layton (2013a).

i.e., multistability (Layton et al. (2006)), as the crossings of the root curves introduce new parameter regimes (Layton et al. (2009)).

Figure 3.2B exhibits bifurcation curves for the IR case, where TAL radius is given as a piecewise-increasing function. A comparison between Figs. 3.2A and 3.2B reveals that the inhomogeneous TAL radius lowers the root curves. But more surprisingly, oscillatory states become attainable at $\tau = 0$ and sufficiently large γ ($\gamma > 22.35$ for the linearized IR model). In contrast, root curves do not cross the γ-axis in the H case, which implies that, with $\tau = 0$, a transient perturbation always result in a steady-state solution. These results imply that a nonzero delay is not a necessary condition for the emergence of LCO, and that the spatial distribution of TAL radius is an important bifurcation parameter.

To better understand the effects of spatial inhomogeneity in TAL radius and its role in the emergence of LCO at zero TGF delay, we analyze Eq. (3.2) for the IR case. Replacing the steady-state radius R_{ss} by a piecewise-increasing function $R(x)$

and dividing by R^2, Eq. (3.2) becomes

$$\frac{\partial}{\partial t}C = -\frac{Q(C(1,t-\tau))}{R^2}\frac{\partial}{\partial x}C - \frac{1}{R}\left(K(C) + \kappa(C - C_e)\right) \tag{3.46}$$

Because the TAL walls are assumed rigid, $\frac{\partial R}{\partial t} = 0$. Suppose that at time t the TAL [Cl^-] profile approximates the steady-state profile, but the MD [Cl^-], denoted by C_{MD}, falls slightly below C_{op}. TGF then acts to increase the inflow fluid flow rate at the entrance of the proximal tubule. If $\tau = 0$, then tubular flow Q increases instantaneously at the loop bend ($x = 0$) and throughout the TAL. Because $\frac{\partial C}{\partial x} < 0$, a larger Q implies that the right-hand side of Eq. (3.46) is positive; thus, C is increasing in time. However, when R is smaller near the loop bend, chloride concentration will change faster near the loop bend than at the macula densa. Consequently, for large γ values, the TGF response may induce a rapid rise in chloride concentration near the loop bend, which, after the TAL transit time, results in an increase in C_{MD} that may be sufficiently large so that it exceeds C_{op}. A LCO thus results. An analogous argument can be made for the case where C_{MD} exceeds C_{op} slightly.

Note that if TAL radius is larger near the loop bend, chloride concentration changes faster near the macula densa than near the loop bend; thus, no LCO will be generated at zero delay.

IT case. We then computed root curves for the IT case, where TAL maximum active NaCl transport rate V_{max} is specified as a piecewise-decreasing function. Compared to the IR case, root curves for IT case, shown in Fig. 3.3B, are even lower, with the curves crossing the γ-axis at as low a γ value as 5.47 (compare with Fig. 3.2B for the IR case). For the parameter values considered, these results suggest that spatially inhomogeneous V_{max} reduces the stability of the TGF system, to a greater extent than spatially inhomogeneous TAL radius.

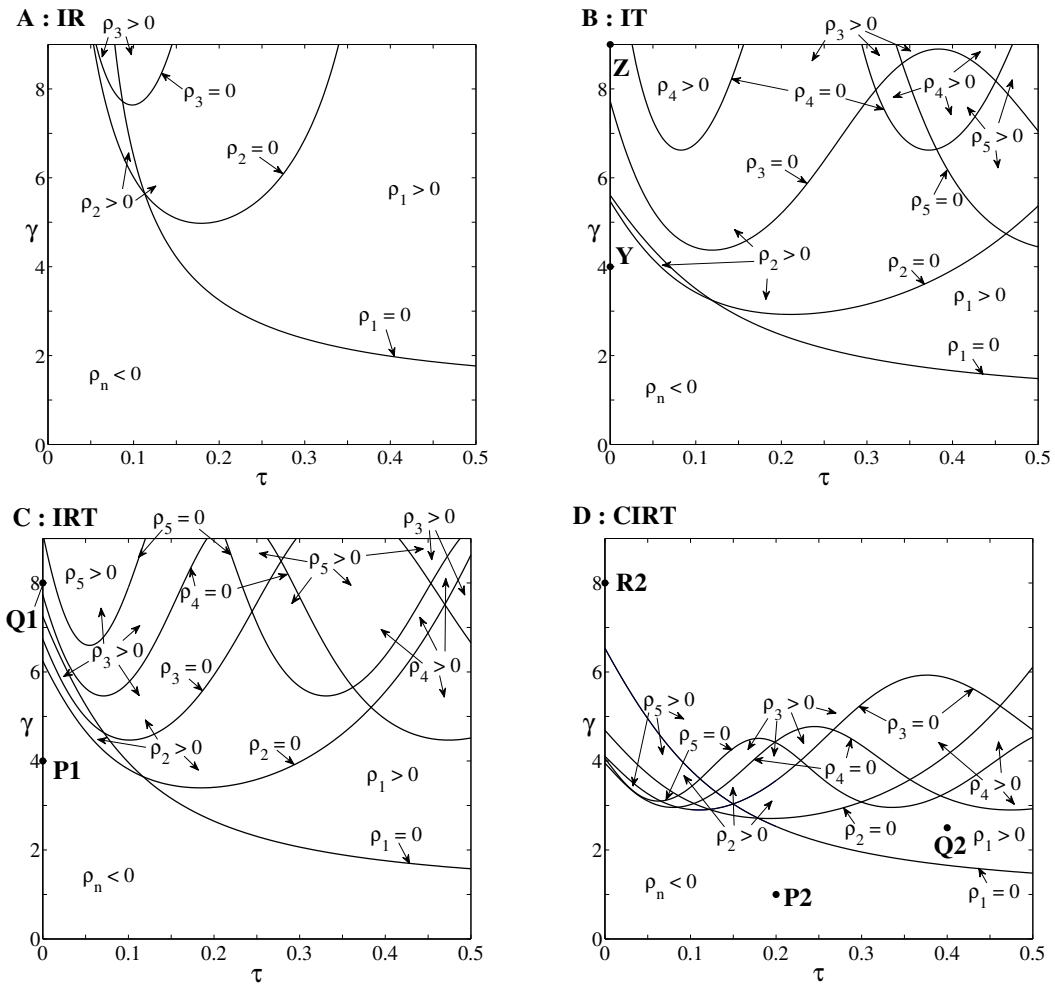

FIGURE 3.3: Root loci for IR case (A), IT case (B), IRT case (C), and CIRT case (D). MD chloride concentration oscillations corresponding to the points **Y** and **Z** in panel B are given in Figs. 3.4Y and 3.4Z; MD chloride concentration oscillations corresponding to the points **P1** and **Q1** in panel C, and to **P2**, **Q2**, and **R2** in panel D are given in Fig. 3.5. Reprinted from Ryu and Layton (2013a).

IRT case. The IRT case represents both inhomogeneous TAL radius and $V_{\max}$. A smaller TAL radius near the loop bend lowers the stability of the system at small delays. However, a smaller TAL circumference also reduces the effective TAL transport rate. As shown in Fig. 3.3C, these two factors result in crossings of the root curves with the γ-axis at γ values that are finite but larger than the IT case, with a smallest γ value of 6.25 (compare to 5.47 for the IT case).

The explanation of the emergence of LCO at zero τ value for the IT and IRT cases is similar to that for the IR case: A higher $V_{\max}$ near the loop bend implies a larger $\frac{\partial C}{\partial t}$ there, compared to at the MD. As a result, following a perturbation in Q, C_{MD} may overshoot, which leads to LCO.

CIRT case. In the CIRT case, TAL compliance is introduced with $\alpha = 0.226 \times 10^{-5}$ cm mmHg^{-1}, taken to be 1/5 of measured compliance in isolated tubule studies (Young and Marsh (1981)). This choice of the TAL compliance is based on the consideration that the effective compliance of the TAL tubular walls may be lowered *in vivo* by various factors including the possible tethering of the TAL to other tubules via the interstitial matrix, resistance of the renal capture, and resistance exerted by neighboring TALs that may be oscillating in synchronization (Layton (2010)). Root curves are shown in Fig. 3.3D for $n \leqslant 5$. Compared with the IRT case (Fig. 3.3C), root curves corresponding to the CIRT case suggest that TAL compliance increases the tendency of the system to oscillate, especially at high frequency. This is consistent with a previous study that used a simple TAL model with homogeneous TAL transport (Layton (2010)). Indeed, if we used the isolated-tubule TAL compliance ($\alpha = 1.33 \times 10^{-5}$ cm mmHg^{-1}), oscillatory states became attainable at even lower (possibly unphysiologically low) gain values (~ 1.5 at $\tau = 0.2$); result not shown.

Crossing of the root curves with the γ-axis has not been revealed in the TGF models that include a detailed representation of the TAL, but not the spatial inhomogeneity of its transport properties and dimension (Layton et al. (1991); Layton (2010)). To validate the emergence of LCO at zero delay, we computed numerical solutions to the full model equations (Eqs. (2.3), (2.4), and (2.9)) for selected values of gain γ and delay τ. We chose two points from each of the IR and IT cases, labeled **W** and **X** in Fig. 3.2B, and **Y** and **Z** in Fig. 3.3B. These points were all chosen along the γ-axis and correspond to the following pairs of delays and gains:

$(\tau_W, \gamma_W) = (0, 15), (\tau_X, \gamma_X) = (0, 25), (\tau_Y, \gamma_Y) = (0, 4)$, and $(\tau_Z, \gamma_Z) = (0, 9)$. The time-profiles for the MD $[Cl^-]$ following a transient perturbation are shown in Figure 3.4. Points **W** and **Y**, which lie within the "$\rho_n < 0$" regime and at $\tau = 0$, correspond to time-independent steady states. Points **X** and **Z**, which lie above "$\rho_4 = 0$" and "$\rho_3 = 0$", respectively, correspond to oscillatory solutions; see Figs. 3.4X and 3.4Z. These results indicate an agreement between the full model and the linearized model: that LCOs may be obtained at zero TGF delay for some spatially varying TAL transport rates and dimensions.

We performed similar simulations for the IRT case, for two points along the γ-axis, with $(\tau_{P1}, \gamma_{P1}) = (0, 4)$, $(\tau_{Q1}, \gamma_{Q1}) = (0, 8)$; and for the CIRT case, for the following τ–γ pairs: $(\tau_{P2}, \gamma_{P2}) = (0.2, 1)$, $(\tau_{Q2}, \gamma_{Q2}) = (0.4, 2.5)$, and $(\tau_{R2}, \gamma_{R2}) = (0, 8)$. Locations of these points are indicated in Figs. 3.3C and 3.3D. The MD $[Cl^-]$ time-profiles corresponding to these points are displayed in Figure 3.5. Both points **P1** and **P2**, which lie below all root curves, i.e., within the "$\rho_n < 0$" regime, yields a time-independent steady state. Points **Q1**, **Q2** and **R2** correspond to oscillatory solutions with frequencies that depend on the γ values.

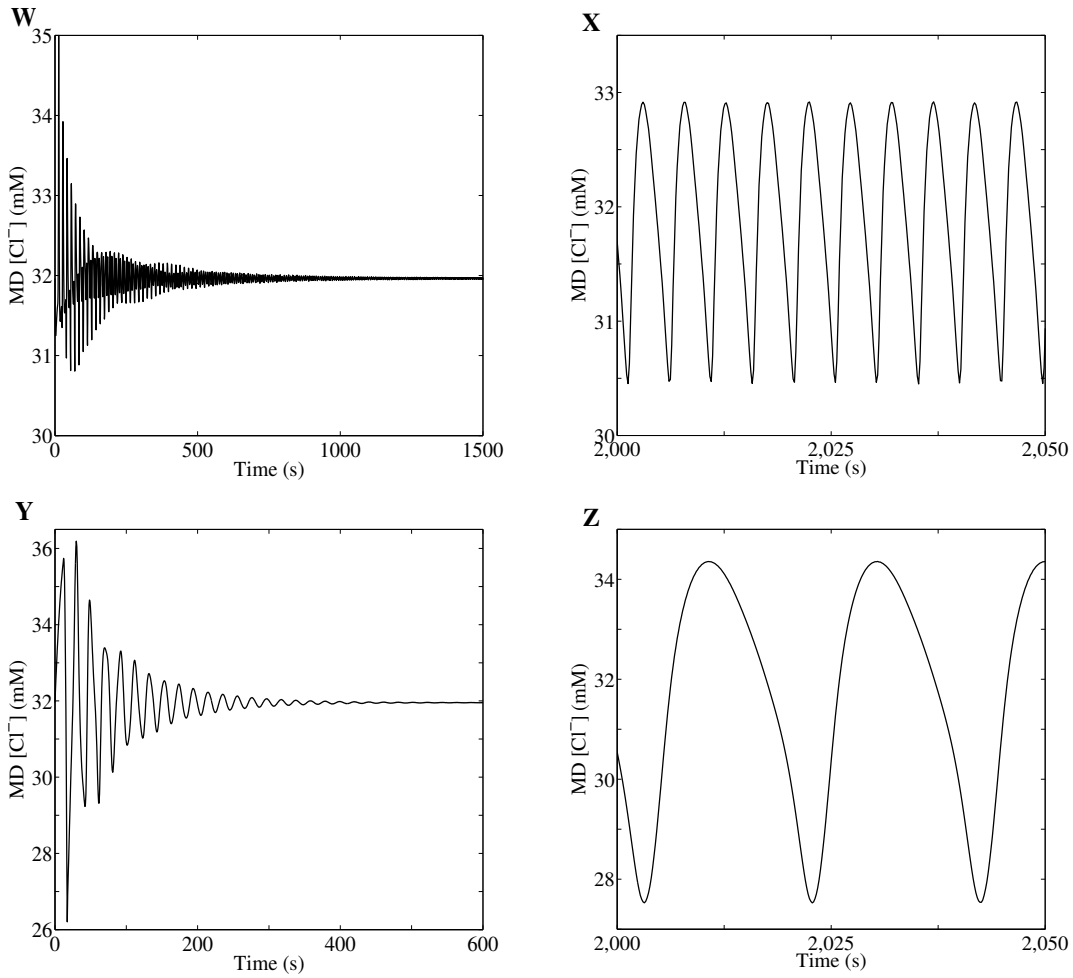

FIGURE 3.4: Sample solutions for points (**W**: $\tau = 0$, $\gamma = 15$), (**X**: $\tau = 0$, $\gamma = 25$) from Fig. 3.2B (IR case), and (**Y**: $\tau = 0$, $\gamma = 4$) and (**Z**: $\tau = 0$, $\gamma = 9$) from Fig. 3.3B (IT case), obtained via numerical simulations using full model equations (Eqs. (2.3)–(2.4) and (2.9)) Reprinted from Ryu and Layton (2013a).

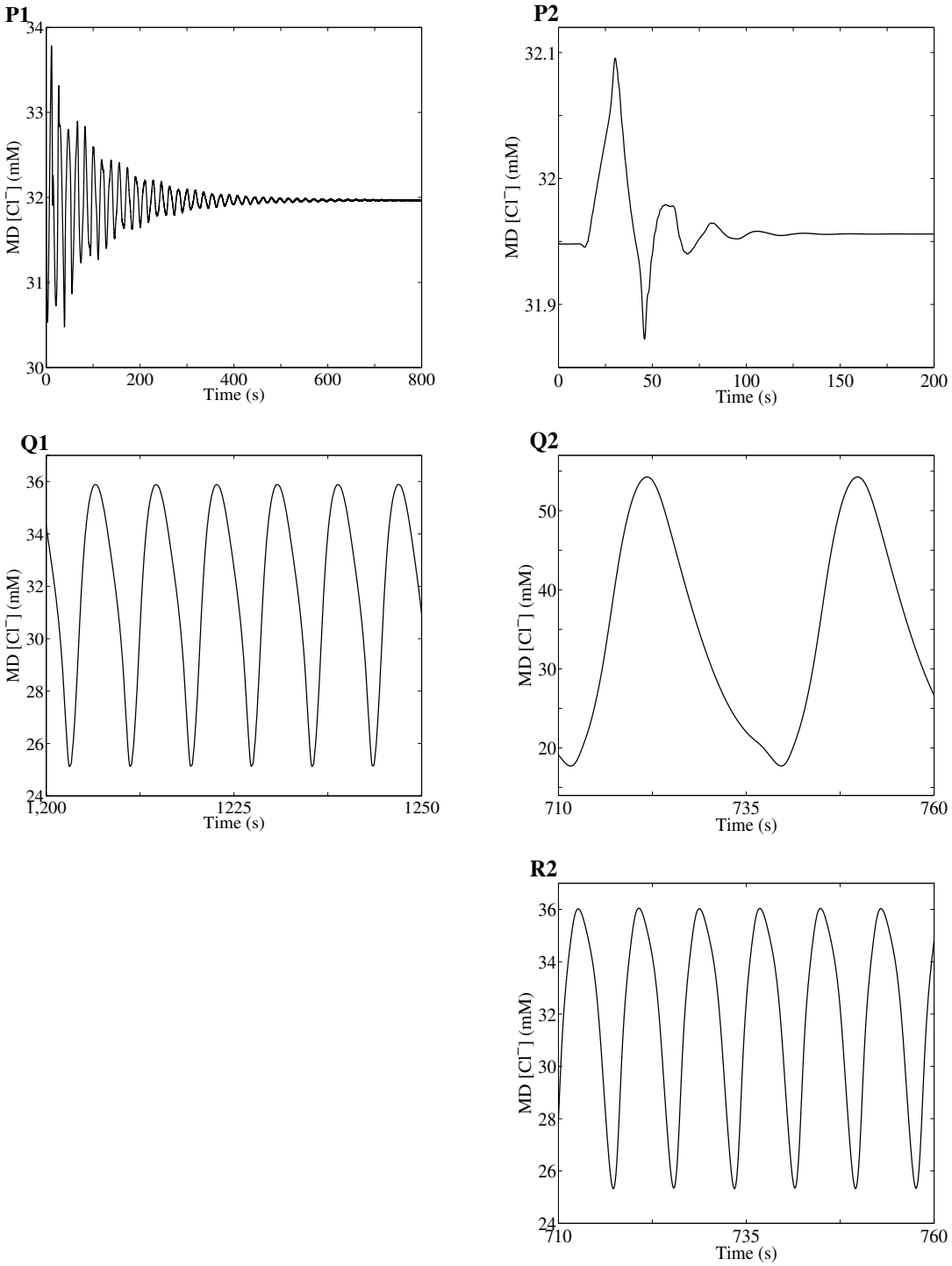

FIGURE 3.5: Sample solutions for points (**P1**: $\tau = 0$, $\gamma = 4$), (**Q1**: $\tau = 0$, $\gamma = 8$), from Fig. 3.3C (IRT case, $\alpha = 0$), and for points (**P2**: $\tau = 0.2$, $\gamma = 1$), (**Q2**: $\tau = 0.4$, $\gamma = 2.5$), and (**R2**: $\tau = 0$, $\gamma = 8$) from Fig. 3.3D (CIRT case, $\alpha = 0.226 \times 10^{-5}$ cm mmHg^{-1}), obtained via numerical simulations using full model equations (Eqs. (2.3)–(2.4) and (2.9)). Reprinted from Ryu and Layton (2013a).

3.1.3 Analysis of the characteristic equation

In this section, we provide a rigorous justification for the existence of roots along the γ-axis in TAL models with inhomogeneous radius and maximum transport rate. To that end, we analyze the characteristic equations corresponding to the H, IR, and IT cases and compare the results. First, we examine the characteristic equation Eq. (3.45) for the H case and show that no root exists for $\tau = 0$ and some $\gamma > 0$. By setting $\tau = 0$ and $\rho = 0$ (where $\lambda = \rho + i\omega$), we simplify Eq. (3.45) to

$$1 = -\frac{\gamma}{8\mu L_0} \int_0^1 e^{-i\omega(1-x)} \exp\left(- \int_x^1 \frac{\kappa C_e'}{C_{ss}'} \, \mathrm{d}y \right) \, \mathrm{d}x. \tag{3.47}$$

Substituting $e^{-i\omega(1-x)} = \cos(\omega(1-x)) - i\sin(\omega(1-x))$ into (3.47), we note that if a root exists for some $\gamma > 0$ and some ω, then the imaginary part of the resulting equation must satisfy

$$0 = \int_0^1 \sin(\omega(1-x)) \exp\left(- \int_x^1 \frac{\kappa C_e'}{C_{ss}'} \, \mathrm{d}y \right) \, \mathrm{d}x, \tag{3.48}$$

where the sine term in the integrand is oscillatory and the exponential term corresponds to the amplitude of integrand, which we denote by $F(x)$.

Consider the amplitude part of $F(x)$, i.e., $\exp(-f(x))$, where $f(x) = \int_x^1 \frac{\kappa C_e'}{C_{ss}'} \, \mathrm{d}y$. Note that $f(x)$ is a decreasing function of x because C_{ss}' and C_e' are positive, and $f(1) = 0$; thus, $\exp(-f(x))$ is an increasing function of x. Next, note that $\sin(\omega(1-x))$ is oscillatory with equidistant x-intercepts, i.e., the n-th root of $\sin(\omega(1-x)) = 0$ is given by

$$x_n = 1 - \frac{2\pi n}{\omega} \text{ such that } x_n - x_{n-1} = x_{n-1} - x_{n-2}.$$

It follows that $F(x)$ is an oscillatory function with increasing amplitude, such that the area bounded by a pair of consecutive x-intercepts increases and switches sign. Thus, the total positive and negative areas do not cancel, which implies that the

right side of Eq. (3.48) is never zero and a root does not exist for a positive γ. Consequently, in the H case, the root curves do not cross the γ-axis.

Now consider the characteristic equation for the IR case:

$$1 = \frac{\gamma}{8\mu C_1}\frac{e^{-\lambda\tau}}{R(1)}\int_0^1 R\cdot\exp\left(-\int_x^1 \frac{\kappa C_e'}{C_{ss}'}R + \lambda R^2\,\mathrm{d}y\right)\,\mathrm{d}x. \tag{3.49}$$

Setting $\tau = 0$ and $\rho = 0$, the above equation becomes

$$1 = \frac{\gamma}{8\mu C_1}\frac{1}{R(1)}\int_0^1 R\cdot\exp(-g_1(x))\exp(-i\omega h_1(x))\,\mathrm{d}x, \tag{3.50}$$

where $g_1(x) = \int_x^1 \frac{\kappa C_e'}{C_{ss}'}R\,\mathrm{d}y$ and $h_1(x) = \int_x^1 R^2\,\mathrm{d}y$.

For a root to exist for some $\gamma > 0$ and $\omega > 0$, the imaginary part of (3.50) must satisfy

$$0 = \int_0^1 R\cdot\exp(-g_1(x))\sin(\omega h_1(x))\,\mathrm{d}x. \tag{3.51}$$

Similar to $f(x)$ in (3.48), $g_1(x)$ is decreasing so that $R\cdot\exp(-g_1(x))$ is an increasing function. However, when we consider the distance between x-intercepts of $\sin(\omega h_1(x))$, we must take into account the concavity of $h_1(x)$. Because $h_1''(x) = -2RR' < 0$, $h_1(x)$ is concave down and the distance between consecutive x-intercepts is decreasing. Thus, even though the amplitude of the integrand is increasing from 0 to 1, some ω may exist such that the positive and negative areas exactly cancel. Indeed, for $\omega = 13$ and with nondimensional parameters, the right-hand side of Eq. (3.51) is evaluated to be 0.0169; for $\omega = 14$, the right-hand side of Eq. (3.51) is -0.0109. Thus, by the intermediate value theorem, the right-hand side vanishes for some $\omega \in (13, 14)$. This result explains the crossing of the γ-axis by the root curves in the IR case.

Consider the opposite radius variation, where where R *decreases* from the loop bend to the MD. Then the distance between two consecutive roots of $\sin(\omega h_1(x)) = 0$

increases as x increases due to $h_1''(x) > 0$. This implies that the positive and negative areas do not cancel and the right-hand side of Eq. (3.51) should be positive for any ω. Thus, for this radius function, we expect no γ-crossings; that was confirmed by numerical solution of the characteristic equation (results not shown).

Finally, consider the characteristic equation for IT case:

$$1 = -\frac{\gamma}{8\mu C_1} e^{-\lambda\tau} \int_0^1 e^{-\lambda(1-x)} \exp\left(-\int_x^1 \frac{\kappa C_e'}{C_{ss}'} - \frac{V_{\max}' C_{ss}}{(K_M + C_{ss}) C_{ss}'} \, \mathrm{d}y \right) \mathrm{d}x. \tag{3.52}$$

Setting $\tau = 0$ and $\rho = 0$, Eq. (3.52) becomes

$$1 = \frac{\gamma}{8\mu C_1} \int_0^1 \exp(-g_2(x)) \exp(-i\omega h_2(x)) \, \mathrm{d}x, \tag{3.53}$$

where $g_2(x) = \int_x^1 \frac{\kappa C_e'}{C_{ss}'} - \frac{V_{\max}' C_{ss}}{(K_M + C_{ss}) C_{ss}'} \, \mathrm{d}y$ and $h_2(x) = 1 - x$.

If a root exists for some $\gamma > 0$ and $\omega > 0$, then the imaginary part of (3.53) must satisfy

$$0 = \int_0^1 \exp(-g_2(x)) \sin(\omega h_2(x)) \, \mathrm{d}x. \tag{3.54}$$

Similar to the H case, $\sin(\omega h_2(x))$ is oscillatory with equidistant x-intercepts. However, the second term in the integrand of g_2, $\frac{V_{\max}' C_{ss}}{(K_M + C_{ss}) C_{ss}'}$, is nonnegative because $V_{\max}' \leqslant 0$; thus, $g_2(x)$ has both increasing and decreasing parts, and so does $\exp(-g_2(x))$. As a result, despite the equidistant distribution of the x-intercepts of $\sin(\omega h_2(x))$, the amplitude part of the integrand in Eq. (3.54) is not monotonic, so that some ω may exist such that the positive and the negative areas exactly cancel. This result indicates the existence of γ-intercepts by the root curves in the IT case.

3.2 Short-Looped Nephron Model

The short-looped nephron model was developed to serve as an essential component for the tubular system with TGF mechanism, by incorporating the detailed dynamics along the proximal tubule and descending limb into our TAL model. Specifically, in contrast to the TAL model which includes only a detailed representation of the TAL, our whole-loop model explicitly represents a short-looped nephron so that it can be used to conduct the sensitivity-study of the TGF regulation in a single nephron to tubular fluid pressure perturbations.

As in the TAL model, we analogously derived the characteristic equation of short-looped model. However, the information provided by the characteristic equation may introduce some discrepancies in model predictions between the linearized and nonlinear full models, which can be attributed to simplifying assumptions made in the linearization process. If one desires to attain a more realistic picture of actual model behaviors for thorough understanding of TGF autoregulation, parameter boundaries, which separate differing model behaviors, need to be directly identified by solving nonlinear full equations instead of finding roots of the characteristic equation.

By obtaining the bifurcation diagrams, we first considered the effect of tubular wall compliance on the stability of the TGF system. Similarly, we studied the effect of the explicit representation of the proximal tubule and descending limb in comparison to our TAL-only model. Based on the information provided by the bifurcation diagram of the short-looped model, we also investigated the effects of transient or sustained flow perturbations on the TGF system and on distal fluid and NaCl delivery. By these means, we assessed the regulatory ability of TGF system in response to those perturbations.

3.2.1 Characteristic equation

In this section, we provide the derivation of a characteristic equation for short-looped nephron model. Using the same normalizing factors applied to TAL model in Section 3.1.1, the equations for tubular pressure (2.18) and chloride concentration (2.3) in nondimensional form are given by

$$\frac{\partial}{\partial t}P - \frac{R^2}{4\mu\alpha}\frac{\partial}{\partial x}R\frac{\partial}{\partial x}P = \frac{R^3}{16\mu\alpha}\frac{\partial^2}{\partial x^2}P - \frac{\Phi}{2\alpha R}, \tag{3.55}$$

$$R^2\frac{\partial}{\partial t}C = -2RC\frac{\partial}{\partial t}R - Q\frac{\partial}{\partial x}C - C\frac{\partial}{\partial x}Q - R_{ss}\left(\frac{V_{\max}C}{K_M + C} + \kappa(C - C_e)\right). \tag{3.56}$$

We then linearize Eq. (3.55) by assuming infinitesimal perturbations in C, P, R, Q, and Φ:

$$P(x,t) = P_{ss}(x) + \epsilon P_\epsilon(x,t), \tag{3.57}$$

$$R(x,t) = R_{ss}(x) + \epsilon R_\epsilon(x,t), \tag{3.58}$$

$$C(x,t) = C_{ss}(x) + \epsilon C_\epsilon(x,t), \tag{3.59}$$

$$Q(x,t) = Q_{ss}(x) + \epsilon Q_\epsilon(x,t), \tag{3.60}$$

$$\Phi(x,t) = \Phi_{ss}(x) + \epsilon \Phi_\epsilon(x,t), \tag{3.61}$$

where $\epsilon \ll 1$, and $P_{ss}(x)$, $R_{ss}(x)$, $C_{ss}(x)$, $Q_{ss}(x)$, and $\Phi_{ss}(x)$ denote the steady-state pressure, radius, Cl^- concentration, flow rate, and water flux, respectively. Note that from nondimensionalized forms of Eqs. (2.1), (2.13), and (2.4) one can show that

$$-8\mu Q_{ss} = R_{ss}^4\frac{\partial}{\partial x}P_{ss}, \tag{3.62}$$

$$-8\mu Q_\epsilon = R_{ss}^4\frac{\partial}{\partial x}P_\epsilon + 4R_{ss}^3R_\epsilon\frac{\partial}{\partial x}P_{ss}, \tag{3.63}$$

$$\frac{\partial}{\partial x}Q_{ss} = -\Phi_{ss}, \tag{3.64}$$

$$\frac{\partial}{\partial x}Q_\epsilon = -2\alpha R_{ss}\frac{\partial}{\partial t}P_\epsilon - \Phi_\epsilon, \tag{3.65}$$

$$R_{ss} = \alpha(P_{ss} - P_e) + \beta, \tag{3.66}$$

Note that Q_{ss} and Φ_{ss} are piecewise-linear functions of x. Then, taking spatial derivative of Eq. (3.62) and substituting Eq. (3.64) yields

$$4R_{ss}^3\frac{\partial}{\partial x}R_{ss}\frac{\partial}{\partial x}P_{ss}+R_{ss}^4\frac{\partial^2}{\partial x^2}P_{ss}=-8\mu\frac{\partial}{\partial x}Q_{ss}=-8\mu(-\Phi_{ss})=8\mu\Phi_{ss}, \tag{3.67}$$

Next, we substitute (3.57) and (3.58) into (3.55) and keep only the $O(\epsilon)$ terms

$$R_{ss}\frac{\partial}{\partial t}P_\epsilon-\frac{1}{4\mu\alpha}\left(R_{ss}^3\frac{\partial}{\partial x}R_\epsilon\frac{\partial}{\partial x}P_{ss}+R_{ss}^3\frac{\partial}{\partial x}R_{ss}\frac{\partial}{\partial x}P_\epsilon+3R_{ss}^2R_\epsilon\frac{\partial}{\partial x}R_{ss}\frac{\partial}{\partial x}P_{ss}\right)$$
$$=\frac{1}{16\mu\alpha}\left(R_{ss}^4\frac{\partial^2}{\partial x^2}P_\epsilon+4R_{ss}^3R_\epsilon\frac{\partial^2}{\partial x^2}P_{ss}\right)-\frac{1}{2\alpha_i}\Phi_\epsilon. \tag{3.68}$$

Using the definition and the assumption for $\Phi(x,t)$ from Eq. (2.16),

$$\Phi(x,t)=\frac{Q(0,t)-Q(x,t)}{x}=h(x)Q(0,t), \tag{3.69}$$

where $h(x)$ is defined as a piece-wise constant function of x from Eq. (2.16). If we solve for $Q(0,t)$ in terms of $Q(x,t)$ from the second equality in (3.69) and substitute the resulting expression back into the first equality, we obtain equations for $\Phi(x,t)$ and for $\Phi_\epsilon(x,t)$:

$$\Phi(x,t)=\left(\frac{h(x)}{1-xh(x)}\right)Q(x,t)=H(x)Q(x,t), \tag{3.70}$$

$$\Phi_\epsilon(x,t)=H(x)Q_\epsilon(x,t), \tag{3.71}$$

Simplifying (3.68) from Eqs. (3.62), (3.63), (3.67), and (3.71), we obtain the following advection-diffusion equation for P_ϵ

$$\frac{\partial}{\partial t}P_\epsilon+\frac{\partial}{\partial x}P_\epsilon\left(2\frac{Q_{ss}}{R_{ss}^2}-\frac{1}{4\mu\alpha}R_{ss}^2\frac{\partial}{\partial x}R_{ss}-\frac{H}{16\mu\alpha}R_{ss}^3\right)$$
$$=\frac{2P_\epsilon}{R_{ss}^2}\left(\Phi_{ss}+\frac{Q_{ss}}{R_{ss}}\frac{\partial}{\partial x}R_{ss}-HQ_{ss}\right)+\frac{R_{ss}^3}{16\mu\alpha}\frac{\partial^2}{\partial x^2}P_\epsilon, \tag{3.72}$$

subject to the boundary conditions:

$$P_\epsilon(0,t)=P'(C_{\rm op})C_\epsilon(2,t-\tau), \tag{3.73}$$

$$P_\epsilon(L_0,t)=0, \tag{3.74}$$

where $P'(C_{\text{op}}) \equiv \frac{dP}{dC}\big|_{C=C_{\text{op}}}$. The boundary condition at $x = 0$ (i.e., Eq. (3.73)) specifies the change in P_o in response to a deviation in MD Cl^- concentration; that response has a delay of τ. The other boundary condition (Eq. (3.74)) imposes a fixed pressure value at $x = L_0$.

As in the previous studies (Layton et al. (1991); Pitman et al. (1993); Layton et al. (1997b, 2009); Layton (2010)), we assume $C_\epsilon(x,t) = f(x)e^{\lambda t}$, for some function $f(x)$ and $\lambda \in \mathbb{C}$. Thus, the boundary condition (Eq. (3.73)) becomes

$$P_\epsilon(0,t) = P'(C_{\text{op}})f(2)e^{\lambda(t-\tau)}, \tag{3.75}$$

Assuming that the solution for Eqs. (3.72)–(3.74) has the form

$$P_\epsilon(x,t) = g(x)P'(C_{\text{op}})f(2)e^{\lambda(t-\tau)}, \tag{3.76}$$

and substituting into Eq. (3.72) for P_ϵ, we obtain the second-order differential equation for $g(x)$

$$\begin{aligned}\frac{R_{ss}^3}{16\mu\alpha}g''(x) - \left(2\frac{Q_{ss}}{R_{ss}^2} - \frac{1}{4\mu\alpha}R_{ss}^2\frac{\partial}{\partial x}R_{ss} - \frac{H}{16\mu\alpha}R_{ss}^3\right)g'(x)\\ + \left(\frac{2\Phi_{ss}}{R_{ss}^2} + 2\frac{Q_{ss}}{R_{ss}^3}\frac{\partial}{\partial x}R_{ss} - 2H\frac{Q_{ss}}{R_{ss}^2} - \lambda\right)g(x) = 0,\end{aligned} \tag{3.77}$$

with boundary conditions $g(0) = 1$ and $g(L_0) = 0$.

Next, we linearize the solute conservation equation for each nephron by substituting Eqs. (3.57)–(3.60) and the nondimensional form of Eqs. (2.1) and (2.13) into (3.56),

$$\begin{aligned}(R_{ss}+\epsilon R_\epsilon)^2\frac{\partial}{\partial t}(C_{ss}+\epsilon C_\epsilon) =& -2(R_{ss}+\epsilon R_\epsilon)(C_{ss}+\epsilon C_\epsilon)\frac{\partial}{\partial t}(R_{ss}+\epsilon R_\epsilon)\\ &+\frac{(R_{ss}+\epsilon R_\epsilon)^4}{8\mu}\frac{\partial}{\partial x}(P_{ss}+\epsilon P_\epsilon)\frac{\partial}{\partial x}(C_{ss}+\epsilon C_\epsilon)\\ &-(C_{ss}+\epsilon C_\epsilon)\frac{\partial}{\partial x}(Q_{ss}+\epsilon Q_\epsilon)\\ &-R_{ss}\left(\frac{V_{\max}(C_{ss}+\epsilon C_\epsilon)}{K_M+C_{ss}+\epsilon C_\epsilon}+\kappa(C_{ss}+\epsilon C_\epsilon - C_e)\right).\end{aligned} \tag{3.78}$$

Note that the steady-state solutions satisfy

$$\frac{R_{ss}^4}{8\mu}\frac{\partial}{\partial x}P_{ss}\frac{\partial}{\partial x}C_{ss} = (K(C_{ss}) + \kappa(C_{ss} - C_e))R_{ss} - \Phi_{ss}C_{ss}, \tag{3.79}$$

where the active transport term is given by $K(C) = \frac{V_{\max}C}{K_M+C}$ and Eq. (3.64) was used.

Keeping only the $O(\epsilon)$ terms in Eq. (3.78) and using Eqs. (3.64)–(3.66), we arrive at the evolution equation for C_ϵ,

$$R_{ss}^2\frac{\partial}{\partial t}C_\epsilon = -2\alpha R_{ss}C_{ss}\frac{\partial}{\partial t}P_{\epsilon,i} - ((K'(C_{ss}) + \kappa)R_{ss} - \Phi_{ss})C_\epsilon + C_{ss}(2\alpha R_{ss}\frac{\partial}{\partial t}P_\epsilon + \Phi_\epsilon) \tag{3.80}$$

$$+ \frac{R_{ss}^3}{8\mu}\left(4R_\epsilon\frac{\partial}{\partial x}P_{ss}\frac{\partial}{\partial x}C_{ss} + R_{ss}\frac{\partial}{\partial x}P_{ss}\frac{\partial}{\partial x}C_\epsilon + R_{ss}\frac{\partial}{\partial x}P_\epsilon\frac{\partial}{\partial x}C_{ss}\right)$$

Substituting $C_\epsilon = f(x)e^{\lambda t}$, $P_\epsilon(x,t) = g(x)P_\epsilon(0,t)$, and $R_\epsilon(x,t) = \alpha P_\epsilon(x,t)$ into the above equation, we obtain

$$\lambda R_{ss,i}^2 f(x)e^{\lambda t} = \frac{R_{ss,i}^3}{8\mu}(4\alpha_i P'_{ss,i}C'_{ss}g_i P_{\epsilon,i}(0,t) + R_{ss,i}P'_{ss,i}f'e^{\lambda t} + R_{ss,i}C'_{ss,i}g'_i P_{\epsilon,i}(0,t)) \tag{3.81}$$

$$- ((K'(C_{ss}) + \kappa)R_{ss,i} - \Phi_{ss,i})f(x)e^{\lambda t} - \frac{H}{8\mu}C_{ss}R_{ss,i}^3 P_{\epsilon,i}(0,t)(R_{ss,i}g'_i(x) + 4\alpha_i P'_{ss,i}g_i(x)).$$

Applying Eq. (3.62) repeatedly, substituting Eq. (3.75), canceling out $e^{\lambda t}$, and rearranging,

$$Q_{ss}f'(x) + ((K'(C_{ss}) + \kappa)R_{ss} - \Phi_{ss} + \lambda R_{ss}^2)f(x) \tag{3.82}$$

$$= P'(C_{\text{op}})f(2)e^{-\lambda\tau}(C'_{ss} - HC_{ss})\left(\frac{R_{ss}^4}{8\mu}g'(x) - 4\alpha g(x)\frac{Q_{ss}}{R_{ss}}\right).$$

Recall we have fixed Cl^- concentration at the entrance to the proximal tubule (i.e $x = 0$). Thus,

$$C_\epsilon(0) = f(0)e^{\lambda t} = 0 \Rightarrow f(0) = 0. \tag{3.83}$$

Given the initial condition (3.83), the solution for (3.82) can be found to be

$$f(s) = \exp\left(-\int_0^s \Omega(x)\,\mathrm{d}x\right)\left(\int_0^s \Xi(x)\exp\left(\int_0^x \Omega(y)\,\mathrm{d}y\right)\,\mathrm{d}x\right), \tag{3.84}$$

where

$$\Omega(x) = \frac{(K'(C_{ss})+\kappa)R_{ss} - \Phi_{ss} + \lambda R_{ss}^2}{Q_{ss}}, \tag{3.85}$$

$$\Xi(x) = P'(C_{\mathrm{op}})f(2)e^{-\lambda\tau}\frac{(C'_{ss} - HC_{ss})}{Q_{ss}}\left(\frac{R_{ss}^4}{8\mu}g'(x) - 4\alpha_i g(x)\frac{Q_{ss}}{R_{ss}}\right). \tag{3.86}$$

Setting $s = 2$ and canceling the factor $f(2)$, we get the characteristic equation

$$\begin{aligned} 1 =& P'(C_{\mathrm{op}})e^{-\lambda\tau}\int_0^2 \frac{(C'_{ss} - HC_{ss})}{Q_{ss,i}}\left(\frac{R_{ss}^4}{8\mu}g'(x) - 4\alpha_i g(x)\frac{Q_{ss,i}}{R_{ss,i}}\right) \\ &\times \exp\left(-\int_x^2 \frac{(K'(C_{ss})+\kappa)R_{ss} - \Phi_{ss} + \lambda R_{ss}^2}{Q_{ss}}\,\mathrm{d}y\right)\,\mathrm{d}x. \end{aligned} \tag{3.87}$$

To facilitate a comparison of (3.87) with the characteristic equation derived for a compliant TAL model, we apply Eq. (3.62) to Eq. (3.79) and consider the resulting equation:

$$-Q_{ss}\frac{d}{dx}C_{ss} = (K(C_{ss}) + \kappa(C_{ss} - C_e))R_{ss} - \Phi_{ss}C_{ss}. \tag{3.88}$$

Taking spatial derivative of (3.88) yields

$$\begin{aligned} -Q'_{ss}C'_{ss} - Q_{ss}C''_{ss} =& (K'(C_{ss})C'_{ss} + \frac{V'_{\max}C_{ss}}{K_M + C_{ss}} + \kappa(C'_{ss} - C'_e) + \kappa'(C_{ss} - C_e))R_{ss} \\ &+ (K(C_{ss}) + \kappa(C_{ss} - C_e))R'_{ss} - \Phi_{ss}C'_{ss} \\ =& (K'(C_{ss})C'_{ss} + \frac{V'_{\max}C_{ss}}{K_M + C_{ss}} + \kappa(C'_{ss} - C'_e) + \kappa'(C_{ss} - C_e))R_{ss} \\ &+ \frac{R'_{ss}}{R_{ss}}(-Q_{ss}C'_{ss} + \Phi_{ss}C_{ss}) - \Phi_{ss,i}C'_{ss}. \end{aligned} \tag{3.89}$$

Dividing by C'_{ss} from both sides and rearranging,

$$(K'(C_{ss})+\kappa)R_{ss}-\Phi_{ss}=-Q'_{ss}-Q_{ss}(\frac{C'''_{ss}}{C'_{ss}}-\frac{R'_{ss}}{R_{ss}})-\Phi_{ss}\frac{C_{ss}}{C'_{ss}}\frac{R'_{ss}}{R_{ss}} \tag{3.90}$$
$$+\left(\kappa\frac{C'_e}{C'_{ss}}-\frac{V'_{\max}C_{ss}}{(K_M+C_{ss})C'_{ss}}-\frac{\kappa'(C_{ss}-C_e)}{C'_{ss}}\right)R_{ss}.$$

Substituting (3.90) into (3.87) and simplifying, we finally get

$$1=\gamma e^{-\lambda\tau}\frac{Q_{ss}(2)}{R_{ss}(2)}\int_0^2\Psi(x)\exp\left(-\int_x^2\Gamma(y)\,\mathrm{d}y\right)\,\mathrm{d}x, \tag{3.91}$$

where $\gamma=P'(C_{\mathrm{op}})C'_{ss}(2)$ is the TGF gain,

$$\Psi(x)=\frac{1}{Q_{ss}^2}\left(1-H\frac{C_{ss}}{C'_{ss}}\right)\left(\frac{R_{ss}^5}{8\mu}g'(x)-4\alpha g(x)Q_{ss}\right)$$
$$\Gamma(x)=\left(\kappa\frac{C'_e}{C'_{ss}}-\frac{V'_{\max}C_{ss}}{(K_M+C_{ss})C'_{ss}}-\frac{\kappa'(C_{ss}-C_e)}{C'_{ss}}+\lambda R_{ss}\right)\frac{R_{ss}}{Q_{ss}}-\frac{\Phi_{ss}}{Q_{ss}}\frac{C_{ss}}{C'_{ss}}\frac{R'_{ss}}{R_{ss}},$$

and $g(x)$ satisfies Eq. (3.77). Equation (3.91) assumes compliant tubular walls and allows spatially varying radius, maximum active transport, chloride permeability. The gain γ_j can be related to the parameters $K_{1,j}$ and $K_{2,j}$ in the pressure response function (Eq. (2.14)). Differentiating Eq. (2.14) with respect to C_i and setting C_i to C_{op}, we obtain $P'(C_{\mathrm{op}})=-K_1K_2$; thus

$$\gamma=-K_1K_2C'_{ss}(2). \tag{3.92}$$

We have previously derived a characteristic equation for a uncoupled nephron, in which only the TAL is explicitly represented, as provided in Section 3.1.1. Equation (3.91) can be reduced to that simpler TAL model. Because the TAL is water-impermeable with constant volumetric fluid flow rate, we set $Q_{ss}=1$, $H=0$, and $\Phi_{ss}=0$ in Eq. (3.91), and, after some algebraic manipulations, we obtain

$$1=\frac{\gamma e^{-\lambda\tau}}{R_{ss}(2)}\int_1^2\left(\frac{R_{ss}^5}{8\mu}g'-2\alpha g(\lambda R_{ss}^2\frac{C_{ss}}{C'_{ss}}+2)\right) \tag{3.93}$$
$$\times\exp\left(-\int_x^2\left(\kappa\frac{C'_e}{C'_{ss}}-\frac{V'_{\max}C_{ss}}{(K_M+C_{ss})C'_{ss}}-\frac{\kappa'(C_{ss}-C_e)}{C'_{ss}}+\lambda R_{ss}\right)R_{ss}\,\mathrm{d}y\right)\,\mathrm{d}x,$$

where $g(x)$ satisfies the reduced form of (3.77):

$$\frac{R_{ss}^3}{16\mu\alpha}g''(x) - \left(\frac{2}{R_{ss}^2} - \frac{1}{4\mu\alpha}R_{ss}^2\frac{\partial}{\partial x}R_{ss}\right)g'(x) + \left(\frac{2}{R_{ss}^3}\frac{\partial}{\partial x}R_{ss} - \lambda\right)g(x) = 0, \quad (3.94)$$

with boundary conditions $g(0) = 1$ and $g(L_0) = 0$. Note that the outer integral in Eq. (3.93) ranges from 1 to 2, corresponding to the segments from the loop bend to the MD. This equation corresponds to Eq. (3.31) in the TAL model.

3.2.2 Model results

Steady-state model predictions

We first computed steady-state behaviors for a short-looped nephron using parameters given in Table 2.4. The model equations (Eqs. (2.1), (2.13), (2.3)–(2.4)) were solved numerically, as described in Section 2.1.4, to obtain steady-state spatial profiles of tubular fluid pressure, radius, flow rate, and chloride concentration along the loop. The results are shown in Fig. 3.6. Panel A shows the tubular fluid pressure drop along the loop. Steady-state inflow pressure at the proximal tubule is ∼13 mmHg and continuously decreases to ∼10 mmHg at the loop bend and to ∼8 mmHg at the end of the TAL. Based on transmural pressure difference (Eq. (2.4)), steady-state tubular radius is computed and shown in panel B. The steady-state water flux term $\Phi(x)$ along each segment determines the fluid flow rate (panel C). First, along the proximal convoluted tubule, two-third of the water is reabsorbed so that the water flow rate decreases from ∼30 (SNGFR) to ∼10 nl/min; then along the proximal straight tubule and the water-permeable descending limb segment, ∼3/10 of the water is reabsorbed so the flow rate reaches at 7 nl/min in the beginning of the water-impermeable descending limb. After the water-permeable segments ($x > x_\omega$), tubular fluid flow rate remains constant at 7 nl/min owing to the zero water permeability along the rest of the loop.

Panel D shows steady-state tubular fluid Cl^- concentration profile together with

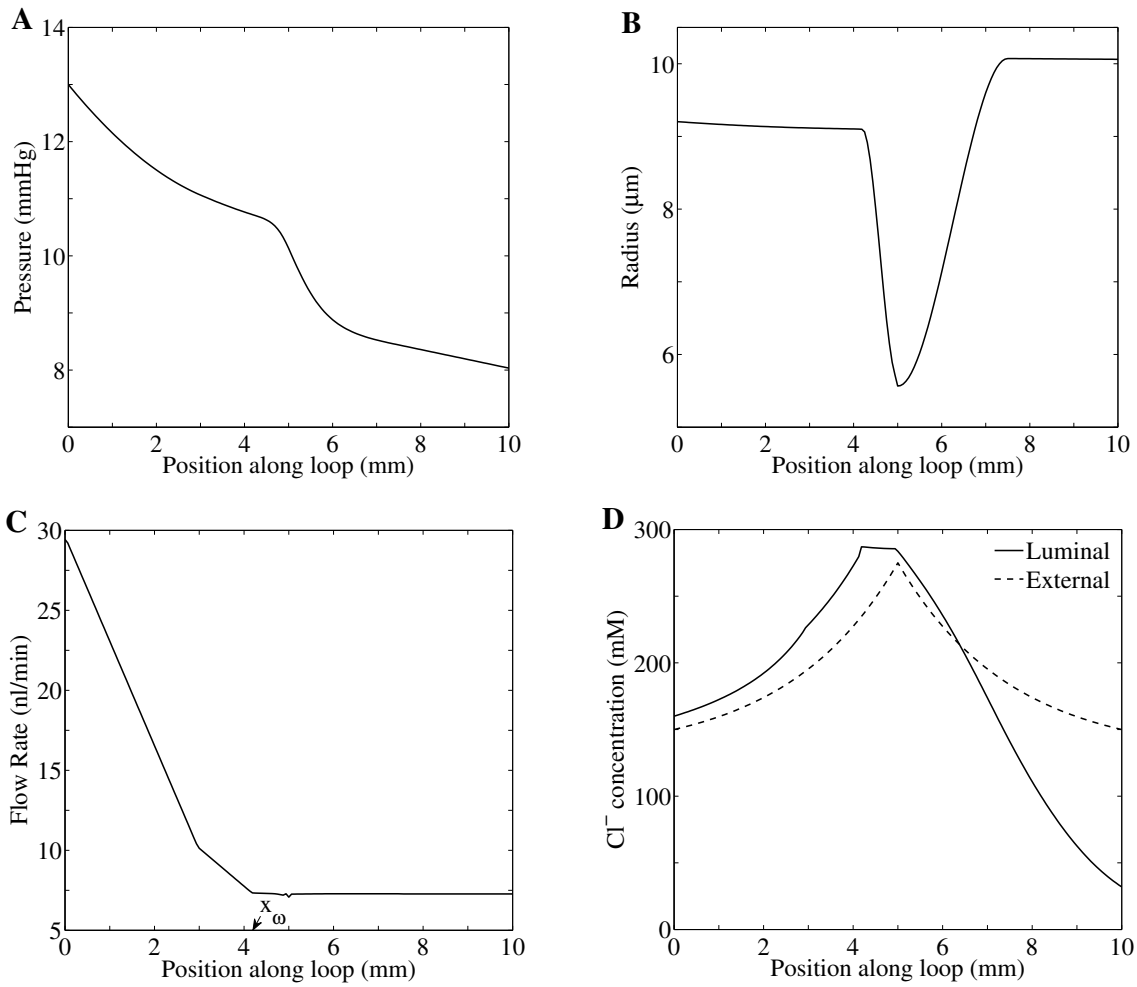

FIGURE 3.6: Steady state tubular fluid pressure (panel A), luminal radius (panel B), tubular flow rate (panel C), Cl^- concentration (panel D) as functions of position. x_ω in panel C denotes the position at which the water-impermeable segment of the descending limb starts. Reprinted from Ryu and Layton (2013c).

the external chloride concentration profile $C_e(x)$ (dashed line). Along the water-permeable segments ($x < x_\omega$), tubular fluid Cl^- concentration increases because of the substantial water reabsorption. Along the water-impermeable segment of the descending limb ($x_w \leqslant x < 5$ mm), Cl^- concentration remains almost constant. At the loop bend ($x = 5$ mm), chloride permeability, κ, and maximum active Cl^- transport rate, $V_{\max}$, change. Along the TAL, NaCl is vigorously pumped out without accompanying water loss. Thus, chloride concentration progressively decreases,

finally reaching the target concentration, $C_{\rm op}$, at the MD.

Tubular wall compliance lowers the stability of the TGF system

By solving the nonlinear model equations (Eqs. (2.1), (2.13), (2.3)–(2.4)) numerically, we computed parameter boundaries, as functions of gain γ and delay τ, that separate differing model behaviors. The TGF gain γ is a measure of the closed feedback loop sensitivity at steady state. This value depends on two derivatives (slopes), $P_o'(C_{\rm op})$ and $C_{\rm ss}'(2L)$, given by

$$\gamma = \left.\frac{dP_o}{dC_{\rm MD}}\right|_{C_{\rm MD}=C_{\rm op}} \left.\frac{dC_{\rm ss}}{dx}\right|_{x=2L} = -K_1K_2C_{\rm ss}'(2L), \tag{3.95}$$

where $C_{\rm MD} = C(2L, t-\tau)$, $C_{\rm op}$ is the target chloride concentration at the MD, and $C_{\rm ss}$ is the steady-state chloride concentration profile shown in Fig. 3.6D (solid curve). The dependence of P_o on $C_{\rm MD}$ is given in Eq. (2.5). The first derivative $\left.\frac{dP_o}{dC_{\rm MD}}\right|_{C_{\rm MD}=C_{\rm op}}$ comes from the TGF response to a deviation of $C_{\rm MD}$ from $C_{\rm op}$. In other words, this quantifies the sensitivity of the TGF system to deviations from the target MD concentration (Holstein-Rathlou and Marsh (1989)). This derivative can be obtained by differentiating the right-hand side of Eq. (2.5) with respect to $C_{\rm MD}$ and setting $C_{\rm MD}$ to $C_{\rm op}$, i.e., $P_o'(C_{\rm op}) = -K_1K_2$. The other derivative $\left.\frac{dC_{\rm ss}}{dx}\right|_{x=2L}$ is the slope of the chloride concentration at the MD when the system is at steady state. Note that γ is positive since $C_{\rm ss}'(2L)$ is negative as shown in Fig. 3.6D.

In the regions marked "Steady state" in Fig. 3.7, the only stable solution is the time-independent steady state. The change in behavior of solutions across the curves between "Steady state" and the above regions arises from a Hopf bifurcation. Across the boundaries, a stable time-independent steady-state solution bifurcates into a regular oscillatory solution. In particular, "f_n" (n = 1, 2, 3) labels a region that supports stable LCO-solutions with the $n^{\rm th}$ frequency, with f_1 being the natural fre-

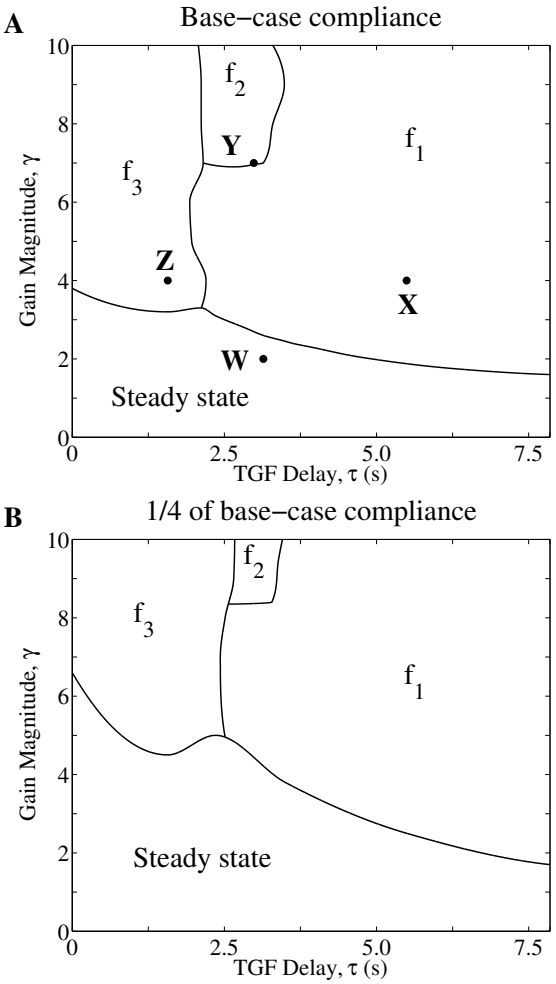

FIGURE 3.7: Behaviors of model solutions, based on numerical simulations using base-case compliance (A) and 1/4 of base-case compliance (B). MD chloride concentration oscillations corresponding to the points **W**, **X**, **Y**, and **Z** are given in Fig. 3.8. Reprinted from Ryu and Layton (2013c).

quency. The model predicts that for sufficiently small values of γ, i.e. for points (γ, τ) within the region "Steady state", any initial solution, or any transient perturbation of a steady-state solution, results in the convergence to the time-independent steady-state solution; this is the only stable solution. But for points (γ, τ) in the regions marked "f_n" above the "Steady state" region, a perturbation of the steady-state solution results in a LCO with its corresponding frequency f_n. Thus, within different regions in the bifurcation diagram, a transient perturbation results in qual-

itatively different solutions, either the steady-state or LCO, and if LCO, solutions with different frequencies. The emergence of LCO at zero TGF delay ($\tau = 0$) with sufficiently high gain values (> 3.8) can be attributed to the spatial inhomogeneity of the TAL radius shown in Fig. 3.6B, a result that was previously discussed in the TAL model.

Simulated oscillations in tubular fluid Cl^- concentration at the MD were computed for four points, labeled **W**, **X**, **Y**, and **Z** in Fig. 3.7A. These points correspond to the following pairs of delays (in second) and gains: $(\tau_W, \gamma_W) = (3.14, 2), (\tau_X, \gamma_X) = (3.93, 4), (\tau_Y, \gamma_Y) = (2.98, 7)$, and $(\tau_Z, \gamma_Z) = (1.57, 4)$. The time-profiles of the MD $[Cl^-]$ following a transient perturbation are shown in Figure 3.8. Point **W**, which lies within the "Steady state" regime, corresponds to a time-independent steady state. Points **X**, **Y**, and **Z**, which lie in the f_1, f_2, and f_3 regions, respectively, correspond to oscillatory solutions, with LCO frequencies $f_1 = 37.68$, $f_2 = 88.66$, and $f_3 = 152.2$ mHz, respectively.

Next, to assess the impact of tubular wall compliance on TGF-mediated dynamics, we computed model solutions using tubular wall compliance values that are 1/4 of base-case compliance, i.e., we set $\alpha_{\mathrm{DL}} = 0.11 \times 10^{-5}$ cm·mmHg^{-1} and $\alpha_{\mathrm{TAL}} = 0.066 \times 10^{-5}$ cm·mmHg^{-1}. The resulting bifurcation diagram is shown in Fig. 3.7B. By comparing Figs. 3.7A and 3.7B, one notes that the lower tubular wall compliance increases the stability of the TGF system. For instance, for TGF delay $\tau = 3.5$ s, LCO can be obtained using the base-case compliance for a gain value of as low as $\gamma = 2.45$, whereas with the reduced compliance, LCOs are predicted above $\gamma = 3.8$. In contrast, if wall compliance is increased to 5/2 of base-case value (or 1/2 of the measured values, i.e., $\alpha_{\mathrm{DL}} = 1.125 \times 10^{-5}$ cm·mmHg^{-1} and $\alpha_{\mathrm{TAL}} = 0.665 \times 10^{-5}$ cm·mmHg^{-1}), the steady-state regime becomes smaller, indicating that the increased compliance further reduces the stability of the TGF system (results not shown).

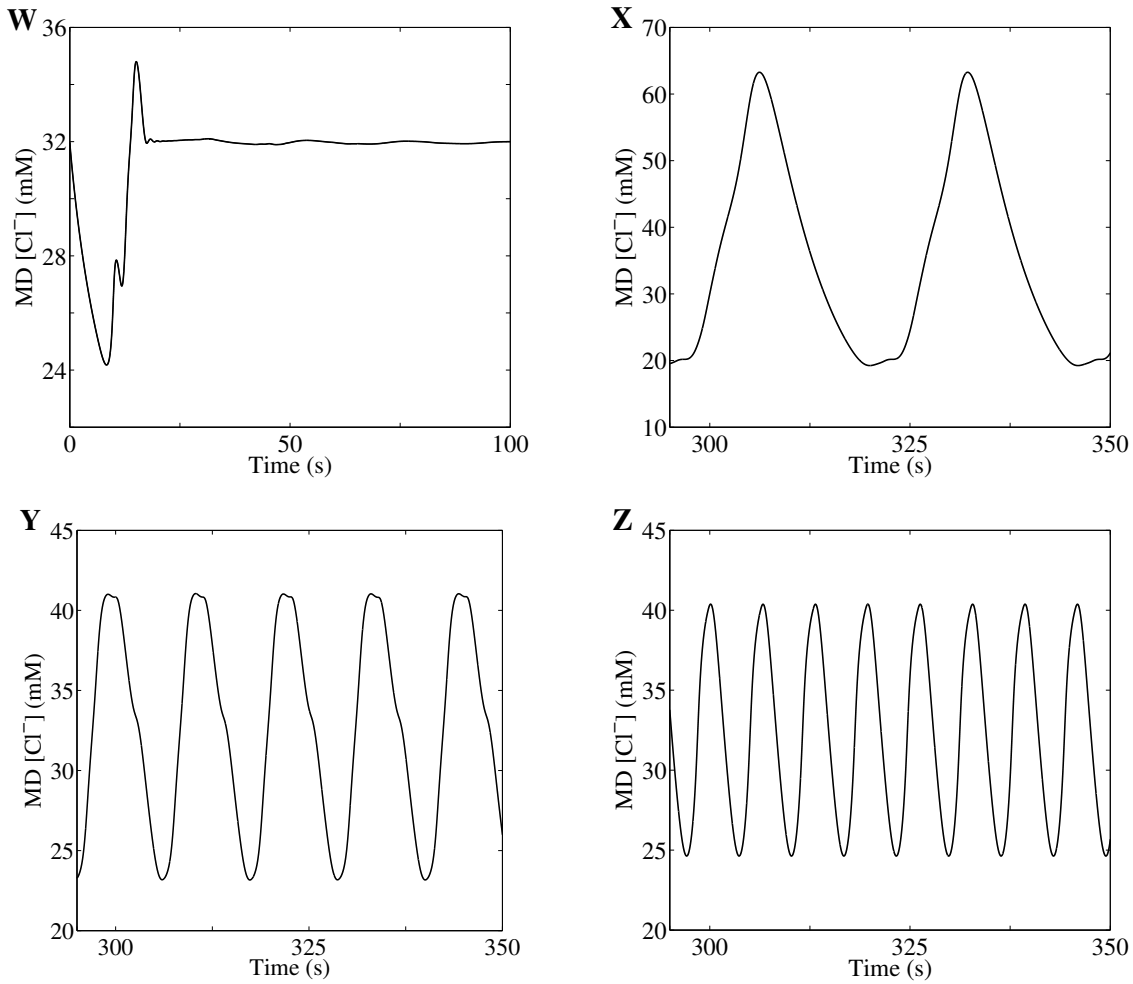

FIGURE 3.8: Sample solutions for points (**W**: $\tau = 3.14$ s, $\gamma = 2$), (**X**: $\tau = 3.93$ s, $\gamma = 4$), (**Y**: $\tau = 2.98$ s, $\gamma = 7$), and (**Z**: $\tau = 1.57$ s, $\gamma = 4$) from Fig. 3.7A. Oscillation frequencies for **X**, **Y**, and **Z** are estimated to be 37.68, 88.66, and 152.2 mHz, respectively. Reprinted from Ryu and Layton (2013c).

Explicit representation of proximal tubule and descending limb lowers the stability of the TGF system

To better understand the impact of the explicit representation of the proximal tubule and descending limb on model dynamics, we compared base-case dynamics with a model that explicitly represents the TAL only, i.e., TAL model. Loop-bend inflow pressure was set to ∼10 mmHg and the base-case TAL compliance was applied in the TAL model. Bifurcation curves were computed and are shown in Fig. 3.9A.

A comparison with base-case curves (Fig. 3.9B) shows that bifurcation curves are noticeably lower in the base case. For a TGF delay of 3.5 s, the base case predicts oscillations above a critical gain value of $\gamma = 2.45$, whereas the TAL model predicts a substantially higher critical gain value of $\gamma = 3.27$. These results suggest that explicit representation of the proximal tubule and descending limb of the loop of Henle lowers the stability of the system.

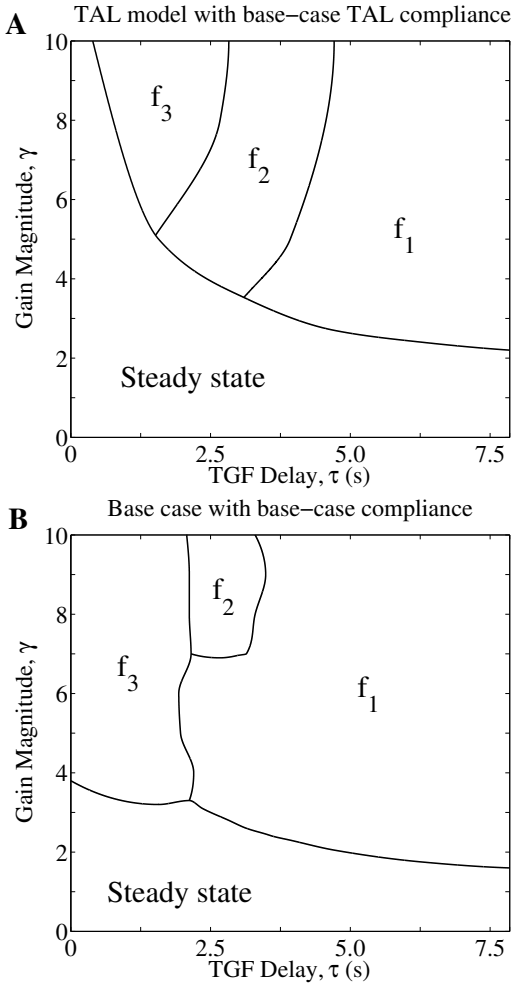

FIGURE 3.9: Behaviors of model solutions for the TAL model (A) using base-case TAL compliance and for the base-case whole-loop model (B) from Fig. 3.7A. Reprinted from Ryu and Layton (2013c).

LCO increases distal NaCl delivery but fluid delivery remains relatively stable

We studied the effects, in the context of distal fluid and NaCl delivery, of LCO that arises from transient pressure perturbations. To that end, we computed and compared fluid and chloride delivery rates at the MD in the steady state with corresponding time-averaged rates during LCO. Results for gain values from 0 to 10 with TGF delay $\tau = 3.5$ s, are summarized in Fig. 3.10A, where the time-averaged variables are normalized by their corresponding steady-state base-case values. Gray bar indicates 100% of steady-state base-case values for comparison. Dimensional results for selected γ values are given in Table 3.1. As shown in Fig. 3.7A, for a TGF delay of 3.5 s, LCO emerges at the critical gain value $\gamma_c \approx 2.45$. As γ exceeds γ_c, fluid delivery is lowered by LCO, to a maximum of -1.41% at $\gamma \approx 5$. In contrast, time-averaged MD chloride concentration progressively rises with increasing γ. The result of these two competing factors is that, for sufficiently large γ values, distal chloride delivery increases with γ, to $+9.3\%$ at $\gamma = 10$.

Figure 3.10B shows a phase plot, where the values of chloride delivery are plotted as a function of TAL fluid flow rate determined at the MD, for $\gamma = 3$, 5, 7, and 10. Arrows indicate direction of time evolution. As γ increases, the peak chloride delivery rate increases substantially, to a maximum of $\sim$90% for $\gamma = 10$. In contrast, the decrease in the minimum is restricted to $\sim$40%. Maxima of fluid flow and chloride delivery rates increase significantly as γ increases while minima are restricted. The dots in center of the plot show time-averaged values for fluid flow and chloride delivery rates for different gain values.

To understand why distal chloride delivery is increased by LCO, whereas distal fluid delivery remains relatively stable, we study the time-profiles in the fluid flow,

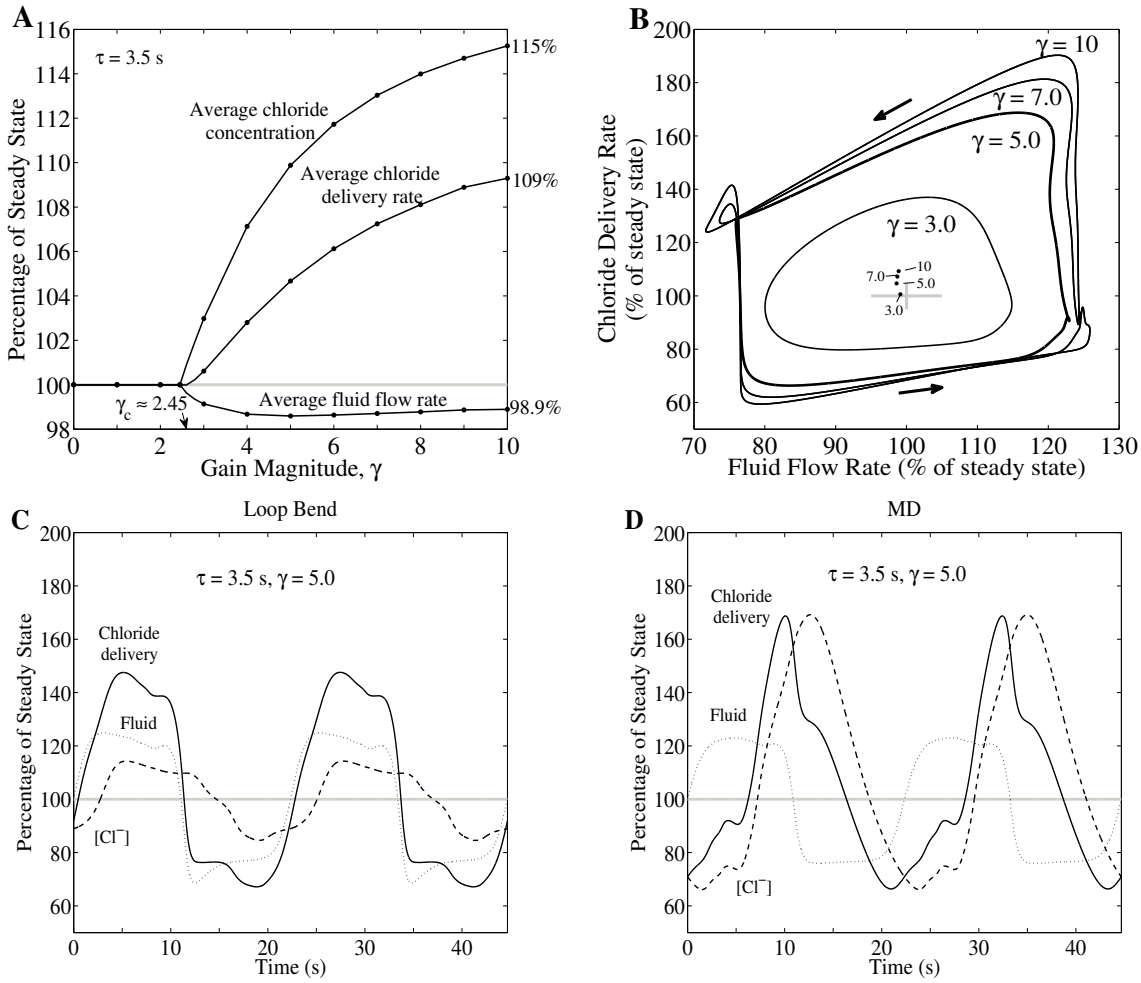

FIGURE 3.10: Effect of TGF gain γ on chloride delivery, with TGF delay $\tau = 3.5$ s. A: Time-average MD fluid flow rate, chloride concentration, and chloride fluid delivery rate as functions of gain magnitude γ. These variables are expressed as percentages of their corresponding steady-state base-case values. Gray bar indicates 100% of steady-state base-case values for comparison. B: phase plots, showing MD chloride delivery as a function of TAL fluid flow rate, for selected gain values γ. Arrows indicate direction of time evolution. Maxima of fluid flow and chloride delivery rates increase significantly as γ increases while minima are restricted. Inset: time-averaged fluid flow rate and chloride delivery. C and D: oscillations profiles in fluid flow rate (dotted curve), chloride concentration (dashed curve), and chloride delivery rate (solid curve) at the loop bend (panel C) and at the MD (panel D), for $\gamma = 5$. Variables are expressed as percentages of corresponding steady-state base-case values. Chloride delivery rate is the product of fluid flow rate and chloride concentration. Reprinted from Ryu and Layton (2013c).

Table 3.1: Base-case time-averaged MD variables for selected gain values with TGF delay $\tau = 3.5$ s

Gain Magnitude, γ	Fluid Flow Rate, nl/min	$[Cl^-]$, mM	Cl^- Delivery Rate, pmol/min
Steady State			
$\gamma \leqslant \gamma_c$	7.273	31.96	232.5
LCO			
3	7.210	32.91	233.9
5	7.170	35.12	243.3
7	7.179	36.13	249.3
10	7.192	36.84	254.1

chloride concentration, and chloride delivery at the loop bend and at the MD, obtained for $\gamma = 5$ and $\tau = 3.5$ s. Figures 3.10C and D show these variables at the loop bend and at the MD, respectively, normalized by the corresponding steady-state base-case values.Chloride delivery rate is the product of fluid flow rate and chloride concentration. As shown in Fig. 3.10C, the oscillations of loop-bend variables are symmetric around respective steady-state values. However, while MD oscillations in fluid flow are approximately symmetric around its steady-state value, chloride concentration oscillations exhibit sharp crests, relative to their troughs (Fig. 3.10D), and are shifted upwards relative to those of fluid delivery. The upward shift and sharp crests relative to their troughs can be explained by the Michaelis-Menten-like kinetics that characterize the active NaCl transport of the TAL, which limits the extent to which MD $[Cl^-]$ can be lowered as the NaCl reabsorption approaches static head, where the luminal $[Cl^-]$ is sufficiently low that active NaCl reabsorption is balanced by passive backleak. Furthermore, because of the dependence of MD chloride concentration and other related variables on TAL transit time, the chloride concentration waveform is phase-shifted relative to the fluid flow waveform, a prediction that is consistent with experimental recordings (Holstein-Rathlou and Marsh

(1989)). As a result, the chloride delivery rate, given by the instantaneous product of fluid flow rate and chloride concentration, exhibits phase and upwards shifts as well. The competing effects of the sharp crests and upward-shifted waveform result in the increase in the time-averaged distal chloride delivery rate shown in Fig. 3.10A for $\gamma > \gamma_c$. A comparison of Fig. 3.10C and Fig. 3.10D indicates that the waveform distortion, specifically in the chloride concentration, that increases distal chloride delivery happens mostly along the TAL: time-averaged fluid flow rates are approximately equal, 98.5 and 98.6% of respective steady-state values, at the loop bend and MD, respectively. But while at the loop bend chloride concentration and flow rate remain almost at steady-state values (101 and 100% of steady state), MD values exhibit significant increases over steady-state values (110 and 105% for chloride concentration and delivery rate, respectively).

High-frequency oscillations reduces the effect of LCO on distal NaCl delivery

As results in Fig. 3.8 suggest, oscillations of different frequencies can be excited at different TGF gain and delay values. To study how the oscillation frequency impacts distal NaCl delivery to the MD, we computed time-averaged MD fluid flow rate, chloride concentration, and chloride fluid delivery for gain values from 0 to 10, and for TGF delay $\tau = 3$ s. Key variables are normalized by their corresponding steady-state values and summarized in Fig. 3.11A. Model solution behaviors are similar to the previous simulation results in Fig. 3.10A for $\gamma < 6.97$. When γ exceeds 6.97, model parameters cross a bifurcation curve and enter a f_2-LCO regime (see Fig. 3.16A). Owing to its shorter period and smaller amplitude, relative to f_1-LCO, f_2-LCO exhibits a drop in time-averaged chloride concentration and delivery rate. Indeed, for $\gamma = 7$, the time-averaged chloride delivery rate is predicted to be only 0.8% higher than steady-state value.

Model results, shown in Fig. 3.11B as a phase plot of chloride delivery versus

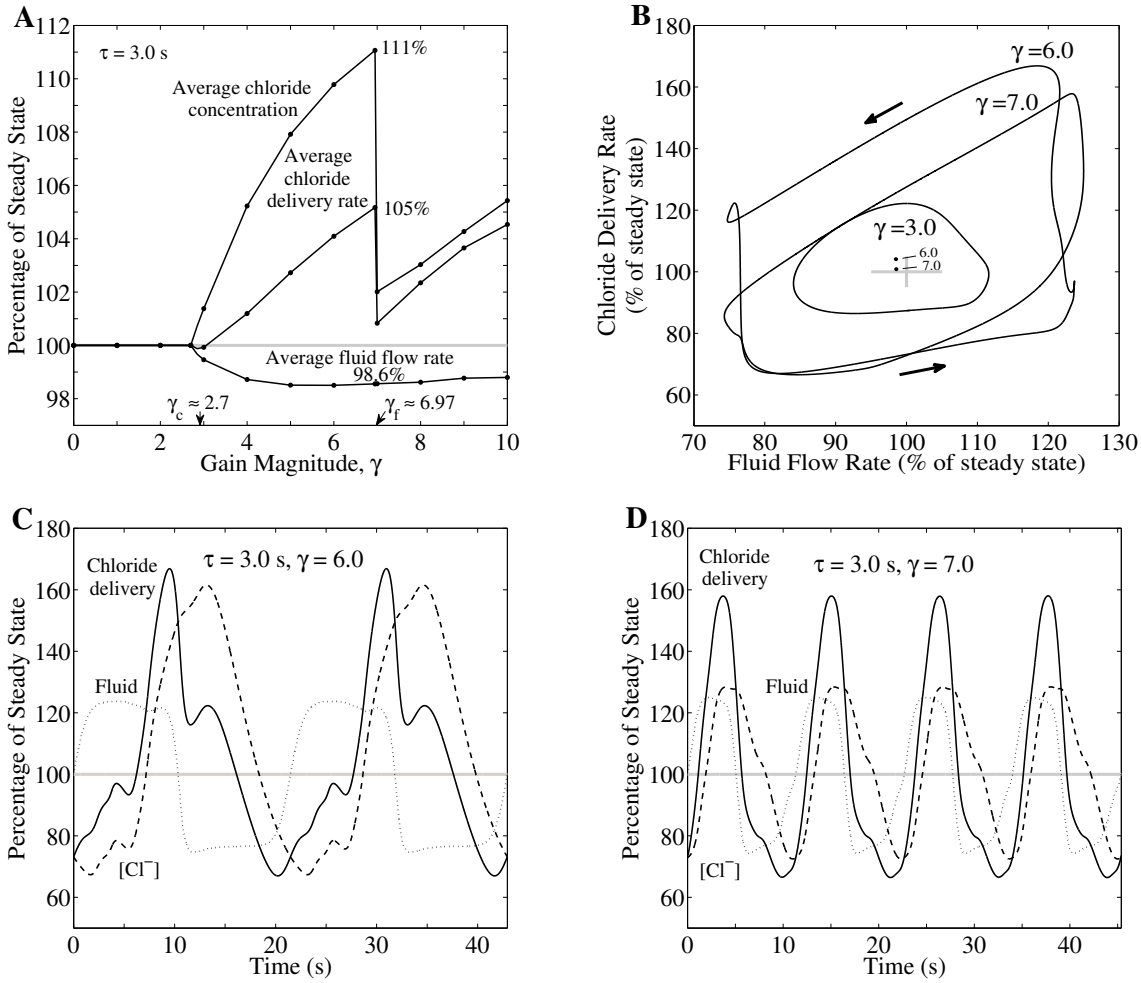

FIGURE 3.11: Effect of TGF gain γ on chloride delivery, with TGF delay $\tau = 3$ s. A: Time-average MD fluid flow rate, chloride concentration, and chloride fluid delivery rate as functions of gain magnitude γ. B: phase plots, showing MD chloride delivery rate as a function of TAL fluid flow rate determined at the MD, for selected gain values γ. C and D: oscillations in TAL fluid flow rate (dotted curve), chloride concentration at the MD (dashed curve), and chloride delivery rate to the MD (solid curve), for $\gamma = 6$ and $\gamma = 7$, respectively. Reprinted from Ryu and Layton (2013c).

fluid flow rate, further illustrate the frequency-dependency of LCO-mediated distal chloride delivery. Arrows indicate direction of time evolution. The area enclosed by the phase curve corresponding to $\gamma = 7$ is noticeably smaller compared to $\gamma = 6$, which indicates a reduction in the oscillation amplitude. The oscillation profiles in Figs. 3.11C and 3.11D show that the $\gamma = 7$ profiles are also more nearly sinusoidal

compared to the $\gamma = 6$ profiles and to Fig. 3.10D. Variables are expressed as percentages of steady-state base-case values. The more sinusoidal waveforms result in smaller deviations from steady-state delivery rates. Thus, the time-averaged chloride delivery rate is decreased for higher-frequency oscillations as indicated in Fig. 3.11B, inset.

Mean TAL flow affects TGF waveform distortion and distal NaCl delivery

We then conducted simulations designed to characterize the influence of mean TAL flow on the strength of the nonlinearities in the transduction process that produces a nonlinear waveform in $[Cl^-]$ at the MD, and on distal chloride delivery. In separate simulations, we scaled water reabsorption rate along the proximal tubule and water-permeable descending limb segment to attain steady-state TAL fluid flow of $Q_L \approx 6.3$ and $Q_H \approx 8.2$ nl/min (base-case $Q_B \approx 7.3$ nl/min) while keeping tubular fluid pressure ∼2 mmHg at the end of the model tubule (i.e., $x = L_0$). TAL maximum active transport rate $V_{\max}$ was simultaneously adjusted so that steady-state MD $[Cl^-]$ is ∼32 mM in all cases.

With γ and τ set to 5 and 3.5 s, respectively, all three cases predicted LCO. The model predicted that the TGF-mediated oscillations have larger amplitudes and are less sinusoidal at lower baseline flow rates (compare Fig. 3.12, panels B and C, and compare the areas of the three regions in Fig. 3.12A). These results can be attributed to the larger fractional change in flow during oscillations at a lower mean flow. Also, owing to the inverse relationship between flow and transit time (transit time becomes infinite as flow approaches zero), the case where the mean flow is lower should exhibit larger, more asymmetric, swings in transit time, leading to a stronger slope asymmetry. Taken together, the differences in waveform and oscillation amplitude yield a larger increase in distal chloride delivery at a lower mean TAL flow rate (+11.4% at Q_L compared to +1.82% at Q_H); see inset of Fig. 3.12A.

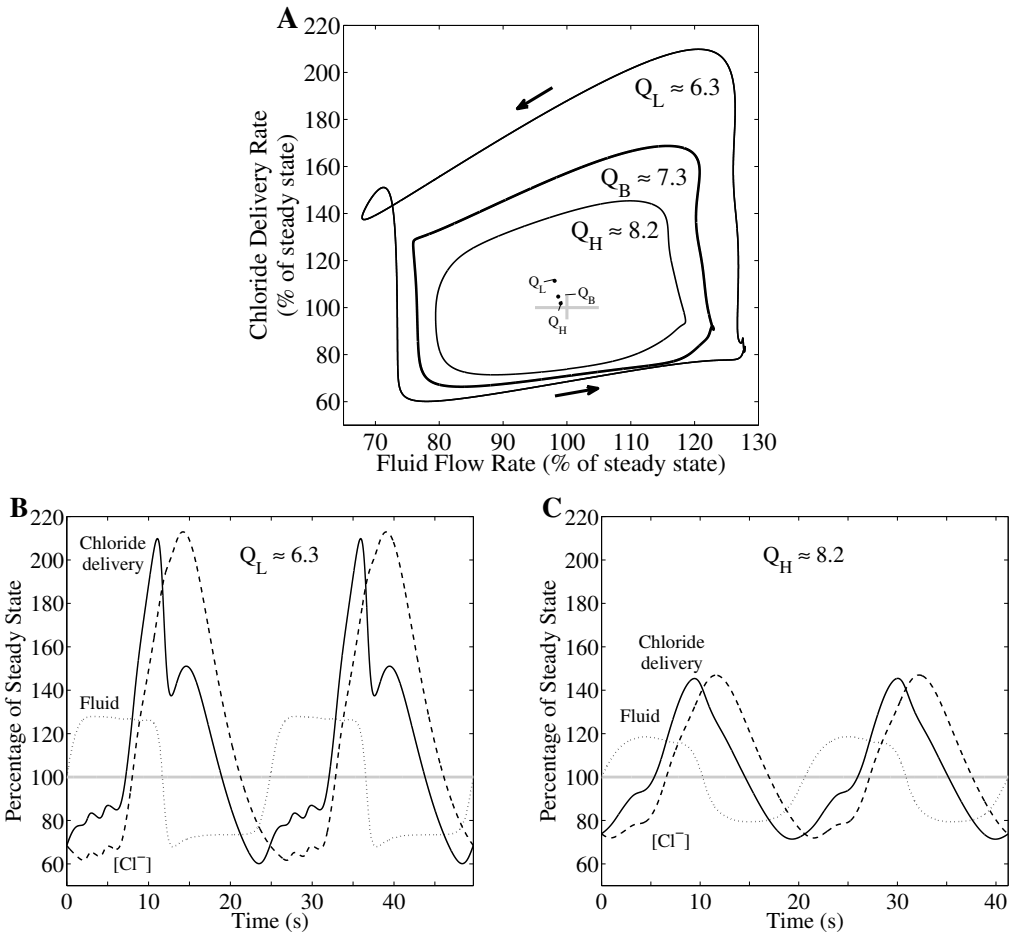

FIGURE 3.12: Effect of TAL fluid flow rate on chloride delivery with TGF delay $\tau = 3.5$ s and gain $\gamma = 5$. A: phase plots, showing chloride delivery rate to MD as a function of TAL fluid flow rate, for selected TAL fluid flow rates (in nl/min), $Q_L = 6.3$, $Q_B = 7.3$ (base-case), and $Q_H = 8.2$ nl/min. Inset: time-averaged fluid flow and chloride delivery rates. As fluid flow rate in the TAL is increased, time-averaged chloride delivery rate is decreased while time-averaged flow rate is increased. B and C: oscillations in TAL fluid flow rate (dotted curve), chloride concentration at the MD (dashed curve), and chloride delivery rate to the MD (solid curve). Variables are expressed as percentages of corresponding steady-state base-case values. Reprinted from Ryu and Layton (2013c).

Results were obtained for two cases: no TGF control (open-loop, open circle), TGF control with LCO (closed-loop, closed circle). For perturbations of ± 20%, 25%, and 30%, the LCO were suppressed by the perturbations. A: time-averaged flow rate at MD, given as a percentage of respective base-case values, in response to the

sustained perturbations in inflow pressure. Dotted line is obtained via extrapolation. B: time-averaged chloride concentration at MD, as percentage of respective base-case values. C: time-averaged chloride delivery rate to MD, as a percentage of respective base-case values.

In the presence of sustained perturbations, LCO significantly increases distal NaCl delivery

Next we simulated an experimental technique in which sustained perturbations are imposed on proximal tubule fluid flow in a nephron where the TGF feedback loop is closed and functional (Holstein-Rathlou (1991); Holstein-Rathlou and Leyssac (1987); Holstein-Rathlou and Marsh (1989)). We computed the responses of MD variables for proximal tubule pressure perturbations of up to $\pm 30\%$ and for $\gamma = 5$. Model responses to the perturbations, illustrated in Fig. 3.13, are given as percentage deviations from base-case LCO values at zero perturbation. Analogous responses for the control case in which TGF was disabled were also computed. The deviations of MD variables from base-case steady-state values in response to sustained perturbations are summarized in Table 3.2.

When TGF was assumed absent, the open-loop case yielded large deviations from steady-state values. Deviations in MD fluid flow rates were similar to the proximal tubule pressure perturbations, whereas deviations in chloride concentrations and chloride flow rates were much larger.

Compared to the open-loop case, the closed-loop case predicted substantially smaller deviations from steady-state MD variables. When perturbations of $\pm 15\%$ were applied, fluid delivery varied by $\sim 6\%$. Substantially larger variations were obtained for MD chloride concentration (up to 36%) and for chloride delivery (up to 41%). These results suggest that while TGF regulates chloride delivery, LCO results in larger deviation in distal NaCl delivery than in distal fluid delivery, which

may lead to enhanced NaCl excretion. The reduced regulatory ability of TGF by LCO was previously observed with transient perturbations. A comparison of the two types of perturbations indicates that transient perturbations yield relatively small deviations in time-averaged MD fluid delivery, chloride concentration, chloride delivery from steady-state values (1, 10, and 5%, respectively), whereas the sustained perturbations of ±15% result in much larger deviations (up to 6, 36, and 41%, respectively). The drop in MD chloride concentration (and thus chloride delivery rate) at ±20% perturbation is due to the suppression of LCO. When yet larger perturbations are applied, MD $[Cl^-]$ and Cl^- flow continue to rise, despite the absence of LCO.

Table 3.2: Deviations of MD variables from steady-state base-case, for gain $\gamma = 5$

Perturbation,	Fluid Flow, %		$[Cl^-]$, %		Cl^- Delivery, %	
%	OL	LCO	OL	LCO	OL	LCO
-30	-37.7	-15.0 (∗)	-70.4	-62.6 (∗)	-81.5	-68.2 (∗)
-25	-31.6	-10.3 (∗)	-66.6	-33.7 (∗)	-77.1	-40.4 (∗)
-20	-25.4	-6.63 (∗)	-61.4	-23.1 (∗)	-71.2	-28.2 (∗)
-15	-19.2	-6.13	-52.9	-17.8	-62.0	-23.3
-10	-12.9	-5.35	-40.2	-9.58	-47.9	-16.0
-5	-6.46	-3.54	-22.6	-0.230	-27.6	-6.30
0	0	-1.40	0	9.87	0	4.69
5	6.53	1.11	19.7	19.6	35.6	17.3
10	13.1	3.53	27.3	28.2	79.4	28.9
15	19.8	6.01	34.5	36.0	131.2	40.7
20	26.6	6.01 (∗)	129.7	25.0 (∗)	190.6	32.5 (∗)
25	33.4	9.54 (∗)	167.8	41.2 (∗)	257.1	54.6 (∗)
30	40.3	15.4 (∗)	206.7	69.7 (∗)	330.1	95.8 (∗)

OL, open-loop without feedback; ∗LCO are suppressed by the perturbations.

For each perturbation, the waveforms of TAL fluid flow rate at the MD (panel A), chloride concentration at the MD (panel B), and chloride delivery rate to the

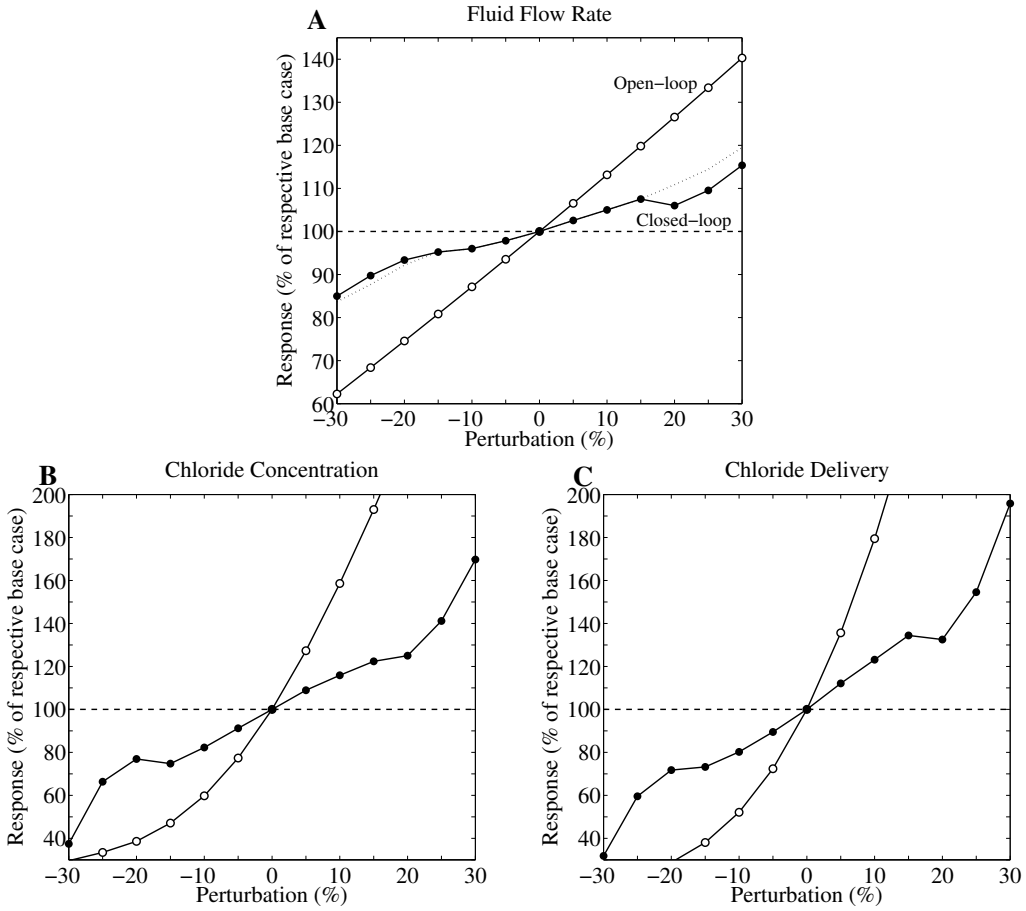

FIGURE 3.13: Effect of sustained perturbations of inflow pressure on MD fluid flow rates, chloride concentrations, and chloride delivery rates, for TGF gain $\gamma = 5$ and delay $\tau = 3.5$ s. Results were obtained for two cases: no TGF control (open-loop, open circle), TGF control with LCO (closed-loop, closed circle). For perturbations of $\pm$ 20%, 25%, and 30%, the LCO were suppressed by the perturbations. A: time-averaged flow rate at MD, given as a percentage of respective base-case values, in response to the sustained perturbations in inflow pressure. Dotted line is obtained via extrapolation. B: time-averaged chloride concentration at MD, as percentage of respective base-case values. C: time-averaged chloride delivery rate to MD, as a percentage of respective base-case values. Reprinted from Ryu and Layton (2013c).

MD (panel C) are in the appropriate relative phase relationship. Horizontal gray line in each panel corresponds to steady-state base-case value. Solid Curves labeled 0% in each panel represents the LCO for $\gamma = 5$ and $\tau = 3.5$ s, for no perturbation; Dashed and dotted curves correspond to sustained perturbations of +15% and -15%,

respectively.

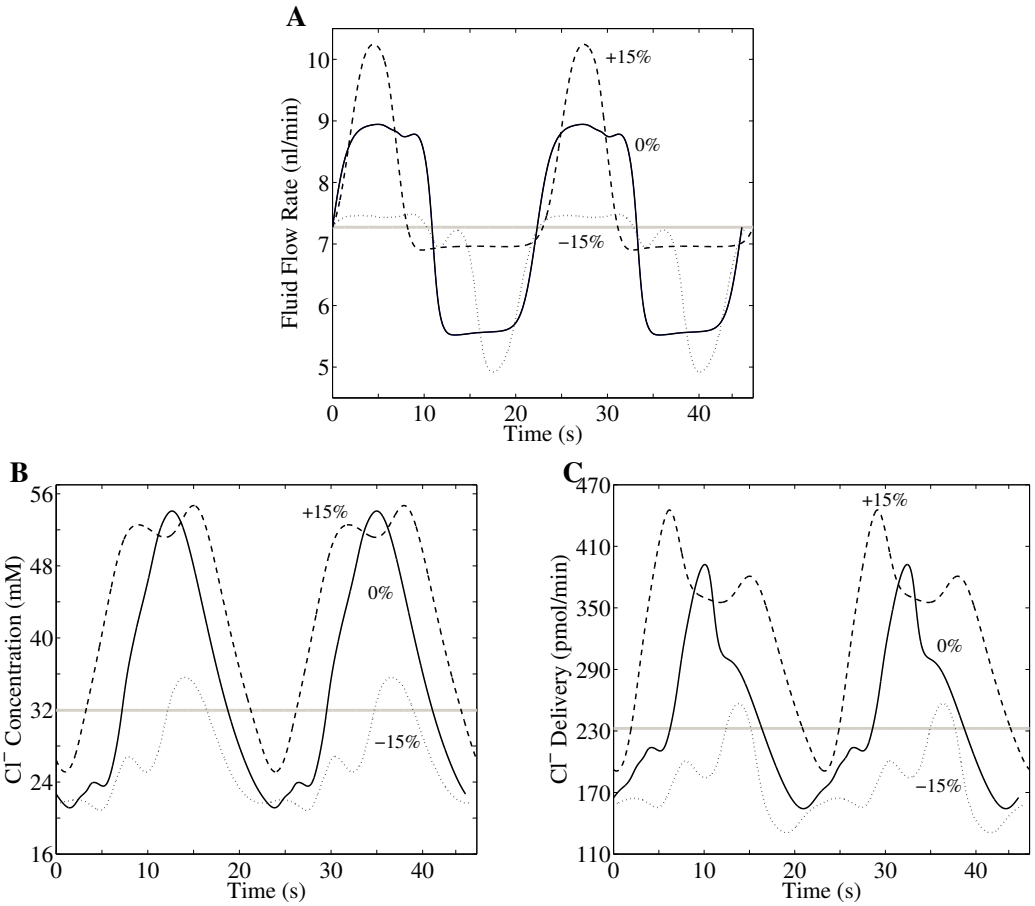

FIGURE 3.14: Waveforms in response to the sustained perturbations in inflow pressure of -15%, 0%, and +15% for TGF gain $\gamma = 5$ and delay $\tau = 3.5$ s. For each perturbation, the waveforms of TAL fluid flow rate at the MD (panel A), chloride concentration at the MD (panel B), and chloride delivery rate to the MD (panel C) are in the appropriate relative phase relationship. Horizontal gray line in each panel corresponds to steady-state base-case value. Solid Curves labeled 0% in each panel represents the LCO for $\gamma = 5$ and $\tau = 3.5$ s, for no perturbation; Dashed and dotted curves correspond to sustained perturbations of +15% and -15%, respectively. Reprinted from Ryu and Layton (2013c).

LCO waveforms for fluid flow, chloride concentration, and chloride flow at the MD are shown in Fig. 3.14 for three cases: sustained proximal tubule pressure perturbations of -15%, 0%, and +15%. Compared to the profiles obtained for transient perturbations (Figs. 3.10D and 3.11C), the marked nonlinearity of the TGF system is

more evident in the distortion of the waveforms obtained in the cases with sustained perturbations. It is particularly noteworthy that the vertical shifts of the profiles were exaggerated, augmenting the deviations of delivery responses from steady state.

Effect of distal tubule and collecting duct representation on the model behaviors is nearly negligible

Recall that to avoid specifying the poorly-characterized pressure at the end of the TAL, the model represents a downstream resistance tube that is loosely associated with the distal tubule and the contiguous collecting duct system. The downstream resistance tube is assumed water impermeable and its unpressurized luminal radius $\beta(x)$ was chosen so that the hydrostatic pressure at $x = L_0$ is $\sim$2 mmHg. *In vivo*, however, water is reabsorbed along the distal tubules and, in anti-diuresis, along the collecting duct. Also, the collecting ducts undergo a series of coalescences in the inner medulla.

To assess the sensitivity of model results to the differences in physical and transport properties between the simple downstream resistance tube and the distal tubules and collecting duct system, we conducted sensitivity studies in which we varied the parameter a_d, which is the location at which the unpressurized luminal radius $\beta(x)$ begins to decrease after the MD (see Eq. (6)). We obtained model results for $a_d = 2.25 \times L, 2.5 \times L$ (base case), and $2.75 \times L$. For all three cases, β_0, β_1, β_2, were set to base-case values, so that the steady-state (pressurized) tubular radius remained unchanged up to the MD (as shown in Fig. 3.6B). β_3 and $V_{\max,\mathrm{TAL}}$ were chosen for the three cases to produce MD chloride concentration of $\sim$32 mM as well as $P(L_0) = 2$ mmHg. These values are shown in Table 3.3.

The three $\beta(x)$ profiles are illustrated in Fig. 3.15. In all three cases, the TGF-mediated dynamic behaviors appear nearly insensitive to changes in downstream

Table 3.3: Individual parameter values for three cases in the sensitivity study

a_d	2.25 ×L	2.5 ×L	2.75 ×L
β_3 (μm)	6.70	6.55	6.38
$V_{\max,\mathrm{TAL}}$ (nmol·cm^{-2}s^{-1})	18.08	19.18	18.05

resistance tube representation. For instance, with the base-case compliance, the boundaries between different regions in the bifurcation diagram are qualitatively similar in all cases, with relative differences of $< 0.1\%$. The impact on other model predictions, and on results obtained for the tubular compliance having 1/4 of the base-case, is similarly small, and all cases yielded the prediction that compliance in tubular walls increases the tendency for the TGF system to oscillate.

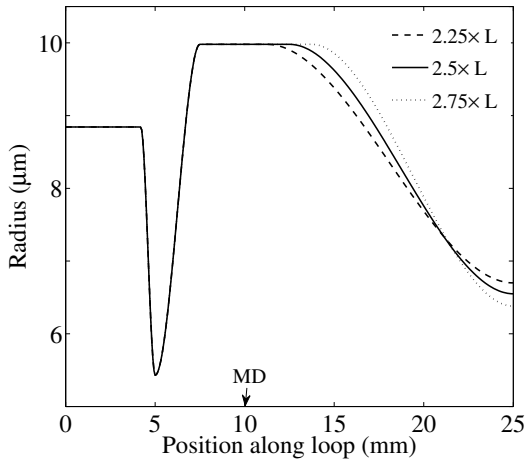

FIGURE 3.15: Profiles of the unpressurized luminal radius $\beta(x)$ for three different cases: $a_d = 2.25 \times L$ (dashed line), $2.5 \times L$ (base-case, solid line), $2.75 \times L$ (dotted line). $x = 5$ and $x = 10$ mm correspond to the loop bend and the MD, respectively. Reprinted from Ryu and Layton (2013c).

3.3 Coupled-Nephron Model

We developed the coupled-nephron model with the whole-loop representation to study the effect of internephron coupling on the TGF-mediated dynamics. Model equations for each individual nephron were formulated, based the (uncoupled) loop

model, and the coupling effect was incorporated to represent the interaction between neighboring nephrons through their TGF systems.

Our main goal of this coupled-TGF study is to help elucidate how coupling may impact the TGF-mediated dynamics and to what extent coupling introduces the complexities to TGF-mediated model behaviors. To obtain a better understanding of the roles of internephron coupling, we similarly applied linear stability and bifurcation analyses, as in TAL and short-looped models, to derive the characteristic equation for coupled-TGF system. By identifying parameter regions that correspond to qualitatively different solution behaviors, we compared model predictions of coupled-TGF system with (uncoupled) short-looped model. We also determined the range of parameter values for which irregular TGF-mediated oscillations emerge as a result of internephron coupling.

3.3.1 Characteristic equation

As in the short-looped model, we analogously derive a characteristic equation for coupled-nephron model. Using the same normalizing factors applied to TAL model in Section 3.1.1, the equations for tubular pressure and chloride concentration of each ith nephron in nondimensional form are Eq. (3.55)–(3.56)

$$\frac{\partial}{\partial t}P_i - \frac{R_i^2}{4\mu\alpha_i}\frac{\partial}{\partial x}R_i\frac{\partial}{\partial x}P_i = \frac{R_i^3}{16\mu\alpha_i}\frac{\partial^2}{\partial x^2}P_i - \frac{\Phi_i}{2\alpha_i R_i}, \tag{3.96}$$

$$R_i^2\frac{\partial}{\partial t}C_i = -2R_iC_i\frac{\partial}{\partial t}R_i - Q_i\frac{\partial}{\partial x}C_i - C_i\frac{\partial}{\partial x}Q_i - R_{ss,i}\left(\frac{V_{\max,i}C_i}{K_{M,i}+C_i} + \kappa_i(C_i - C_e)\right). \tag{3.97}$$

Throughout the derivation of the characteristic equation for coupled-nephron model, we assume that the nephrons share the same transport parameters (i.e., $V_{\max,i}, K_{M,i}$, and, κ_i are the same for all i); thus their steady-state Cl^- concentration profiles are the same. Given these assumptions, we then linearize Eq. (3.96) by using (3.57)–(3.61). Also, analogously using the expressions given in (3.62)–(3.71) for ith

nephron, we obtain the following advection-diffusion equation for $P_{\epsilon,i}$

$$\frac{\partial}{\partial t}P_{\epsilon,i} + \frac{\partial}{\partial x}P_{\epsilon,i}\left(2\frac{Q_{ss,i}}{R_{ss,i}^2} - \frac{1}{4\mu\alpha_i}R_{ss,i}^2\frac{\partial}{\partial x}R_{ss,i} - \frac{H}{16\mu\alpha_i}R_{ss,i}^3\right)$$

$$= \frac{2P_{\epsilon,i}}{R_{ss,i}^2}\left(\Phi_{ss,i} + \frac{Q_{ss,i}}{R_{ss,i}}\frac{\partial}{\partial x}R_{ss,i} - HQ_{ss,i}\right) + \frac{R_{ss,i}^3}{16\mu\alpha_i}\frac{\partial^2}{\partial x^2}P_{\epsilon,i}, \tag{3.98}$$

subject to the boundary conditions:

$$P_{\epsilon,i}(0,t) = P_i'(C_{\text{op}})C_{\epsilon,i}(2,t-\tau_i) + \sum_{j\neq i}\phi_{i,j}P_j'(C_{\text{op}})C_{\epsilon,j}(2,t-\tau_j), \tag{3.99}$$

$$P_{\epsilon,i}(L_0,t) = 0, \tag{3.100}$$

where $P_i'(C_{\text{op}}) \equiv \left.\frac{dP_i}{dC_i}\right|_{C_i=C_{\text{op}}}$. The boundary condition at $x = 0$ (i.e., Eq. (3.99)) specifies the change in $P_{i,0}$ in response to a deviation in MD Cl^- concentration; that response has a delay of τ_i. The other boundary condition (Eq. (3.100)) imposes a fixed pressure value at $x = L_0$.

As in the short-looped model, we assume that $C_{\epsilon,i}(x,t)$ can be written as $C_{\epsilon,i} = f_i(x)e^{\lambda_i t}$, for some function $f_i(x)$ and $\lambda_i \in \mathbb{C}$. We further assume that

$$C_{\epsilon,i} = C_{\epsilon,j} \equiv C_\epsilon, \quad f_i(x) = f_j(x) \equiv f(x), \quad \lambda_i = \lambda_j \equiv \lambda \tag{3.101}$$

With this notation, the boundary condition (Eq. (3.99)) becomes

$$P_{\epsilon,i}(0,t) = P_i'(C_{\text{op}})f(2)e^{\lambda(t-\tau_i)} + \sum_{j\neq i}\phi_{i,j}P_j'(C_{\text{op}})f(2)e^{\lambda(t-\tau_j)}, \tag{3.102}$$

or, if we define $\phi_{j,j} \equiv 1$,

$$P_{\epsilon,i}(0,t) = \sum_{j=1}^{N}\phi_{i,j}P_j'(C_{\text{op}})f(2)e^{\lambda(t-\tau_j)}. \tag{3.103}$$

where N denotes the number of model nephrons. Assuming that the solution for Eqs. (3.98)–(3.100) has the form

$$P_{\epsilon,i}(x,t) = g_i(x)\left(\sum_{j=1}^{N}\phi_{i,j}P_j'(C_{\text{op}})f(2)e^{\lambda(t-\tau_j)})\right), \tag{3.104}$$

and substituting into Eq. (3.98) for $P_{\epsilon,i}$, we obtain the second-order differential equation for $g_i(x)$

$$\frac{R_{ss}^3}{16\mu\alpha_i}g_i''(x) - \left(2\frac{Q_{ss}}{R_{ss}^2} - \frac{1}{4\mu\alpha_i}R_{ss}^2\frac{\partial}{\partial x}R_{ss} - \frac{H}{16\mu\alpha}R_{ss}^3\right)g_i'(x) + \left(\frac{2\Phi_{ss}}{R_{ss}^2} + 2\frac{Q_{ss}}{R_{ss}^3}\frac{\partial}{\partial x}R_{ss} - 2H\frac{Q_{ss}}{R_{ss}^2} - \lambda\right)g_i(x) = 0, \tag{3.105}$$

with boundary conditions $g_i(0) = 1$ and $g_i(L_0) = 0$.

Next, we linearize the solute conservation equation for each nephron by substituting Eqs. (3.57)–(3.60) and the nondimensional form of Eqs. (2.1) and (2.13) into (3.97),

$$\begin{aligned}(R_{ss,i} + \epsilon R_{\epsilon,i})^2\frac{\partial}{\partial t}(C_{ss} + \epsilon C_\epsilon) = &- 2(R_{ss,i} + \epsilon R_{\epsilon,i})(C_{ss} + \epsilon C_\epsilon)\frac{\partial}{\partial t}(R_{ss,i} + \epsilon R_{\epsilon,i}) \\ &+ \frac{(R_{ss,i} + \epsilon R_{\epsilon,i})^4}{8\mu}\frac{\partial}{\partial x}(P_{ss,i} + \epsilon P_{\epsilon,i})\frac{\partial}{\partial x}(C_{ss} + \epsilon C_\epsilon) \\ &- (C_{ss} + \epsilon C_\epsilon)\frac{\partial}{\partial x}(Q_{ss,i} + \epsilon Q_{\epsilon,i}) \\ &- R_{ss,i}\left(\frac{V_{\max}(C_{ss} + \epsilon C_{\epsilon,i})}{K_M + C_{ss} + \epsilon C_\epsilon} + \kappa(C_{ss} + \epsilon C_\epsilon - C_e)\right).\end{aligned} \tag{3.106}$$

Note that the steady-state solutions satisfy

$$\frac{R_{ss,i}^4}{8\mu}\frac{\partial}{\partial x}P_{ss,i}\frac{\partial}{\partial x}C_{ss} = (K(C_{ss}) + \kappa(C_{ss} - C_e))R_{ss,i} - \Phi_{ss,i}C_{ss}, \tag{3.107}$$

where the active transport term is given by $K(C) = \frac{V_{\max}C}{K_M + C}$ and Eq. (3.64) was used.

Keeping only the $O(\epsilon)$ terms in Eq. (3.106) and using Eqs. (3.64)–(3.66), we arrive

at the evolution equation for C_ϵ,

$$\begin{aligned} R_{ss,i}^2 \frac{\partial}{\partial t} C_\epsilon = &- 2\alpha R_{ss,i} C_{ss} \frac{\partial}{\partial t} P_{\epsilon,i} - ((K'(C_{ss}) + \kappa) R_{ss,i} - \Phi_{ss,i}) C_\epsilon \\ &+ C_{ss}(2\alpha R_{ss,i} \frac{\partial}{\partial t} P_{\epsilon,i} + \Phi_{\epsilon,i}) \\ &+ \frac{R_{ss,i}^3}{8\mu} \left(4R_{\epsilon,i} \frac{\partial}{\partial x} P_{ss,i} \frac{\partial}{\partial x} C_{ss} + R_{ss,i} \frac{\partial}{\partial x} P_{ss,i} \frac{\partial}{\partial x} C_\epsilon + R_{ss,i} \frac{\partial}{\partial x} P_{\epsilon,i} \frac{\partial}{\partial x} C_{ss} \right) \end{aligned} \tag{3.108}$$

Substituting $C_\epsilon = f(x)e^{\lambda t}$, $P_{\epsilon,i}(x,t) = g_i(x) P_{\epsilon,i}(0,t)$, and $R_{\epsilon,i}(x,t) = \alpha_i P_{\epsilon,i}(x,t)$ into the above equation, we obtain

$$\begin{aligned} \lambda R_{ss,i}^2 f e^{\lambda t} = &\frac{R_{ss,i}^3}{8\mu} (4\alpha_i P'_{ss,i} C'_{ss} g_i P_{\epsilon,i}(0,t) + R_{ss,i} P'_{ss,i} f' e^{\lambda t} + R_{ss,i} C'_{ss,i} g'_i P_{\epsilon,i}(0,t)) \\ &- ((K'(C_{ss}) + \kappa) R_{ss,i} - \Phi_{ss,i}) f e^{\lambda t} - \frac{H}{8\mu} C_{ss} R_{ss,i}^3 P_{\epsilon,i}(0,t)(R_{ss,i} g'_i(x) + 4\alpha_i P'_{ss,i} g_i(x)). \end{aligned} \tag{3.109}$$

Applying Eq. (3.62) repeatedly, substituting Eq. (3.103), canceling out $e^{\lambda t}$, and re-arranging,

$$\begin{aligned} &Q_{ss,i} f'(x) + ((K'(C_{ss}) + \kappa) R_{ss,i} - \Phi_{ss,i} + \lambda R_{ss,i}^2) f(x) \\ &= \left(\sum_{j=1}^{N} \phi_{i,j} P'_j(C_{\text{op}}) f(2) e^{-\lambda \tau_j} \right) (C'_{ss} - H C_{ss}) \left(\frac{R_{ss,i}^4}{8\mu} g'_i(x) - 4\alpha_i g_i(x) \frac{Q_{ss,i}}{R_{ss,i}} \right). \end{aligned} \tag{3.110}$$

Recall we have fixed Cl^- concentration at the entrance to the proximal tubule (i.e $x = 0$). Thus,

$$C_\epsilon(0) = f(0) e^{\lambda t} = 0 \Rightarrow f(0) = 0. \tag{3.111}$$

Given the initial condition (3.111), the solution for (3.110) can be found to be

$$f(s) = \exp\left(-\int_0^s \Omega(x)\, \mathrm{d}x \right) \left(\int_0^s \Xi(x) \exp\left(\int_0^x \Omega(y)\, \mathrm{d}y \right) \mathrm{d}x \right), \tag{3.112}$$

where

$$\Omega(x) = \frac{(K'(C_{ss}) + \kappa)R_{ss,i} - \Phi_{ss,i} + \lambda R_{ss,i}^2}{Q_{ss,i}}, \tag{3.113}$$

$$\Xi(x) = \left(\sum_{j=1}^{N} \phi_{i,j} P_j'(C_{\mathrm{op}}) f(2) e^{-\lambda\tau_j}\right) \frac{(C_{ss}' - HC_{ss})}{Q_{ss,i}} \left(\frac{R_{ss,i}^4}{8\mu} g_i'(x) - 4\alpha_i g_i(x) \frac{Q_{ss,i}}{R_{ss,i}}\right). \tag{3.114}$$

Setting $s = 2$ and canceling the factor $f(2)$, we get the characteristic equation

$$\begin{aligned} 1 = &\sum_{j=1}^{N} \phi_{i,j} P_j'(C_{\mathrm{op}}) e^{-\lambda\tau_j} \int_0^2 \frac{(C_{ss}' - HC_{ss})}{Q_{ss,i}} \left(\frac{R_{ss,i}^4}{8\mu} g'(x) - 4\alpha_i g_i(x) \frac{Q_{ss,i}}{R_{ss,i}}\right) \\ &\times \exp\left(-\int_x^2 \frac{(K'(C_{ss}) + \kappa)R_{ss,i} - \Phi_{ss,i} + \lambda R_{ss,i}^2}{Q_{ss,i}} \,\mathrm{d}y\right) \mathrm{d}x. \end{aligned} \tag{3.115}$$

If we apply Eq. (3.62) to Eq. (3.107), the resulting equation becomes

$$-Q_{ss,i} \frac{d}{dx} C_{ss} = (K(C_{ss}) + \kappa(C_{ss} - C_e))R_{ss,i} - \Phi_{ss,i} C_{ss}. \tag{3.116}$$

Taking spatial derivative of (3.116) yields

$$\begin{aligned} -Q_{ss,i}' C_{ss}' - Q_{ss,i} C_{ss}'' =& (K'(C_{ss}) C_{ss}' + \frac{V_{\max}' C_{ss}}{K_M + C_{ss}} + \kappa(C_{ss}' - C_e') + \kappa'(C_{ss} - C_e))R_{ss,i} \\ &+ (K(C_{ss}) + \kappa(C_{ss} - C_e))R_{ss,i}' - \Phi_{ss,i} C_{ss}' \\ =& (K'(C_{ss}) C_{ss}' + \frac{V_{\max}' C_{ss}}{K_M + C_{ss}} + \kappa(C_{ss}' - C_e') + \kappa'(C_{ss} - C_e))R_{ss,i} \\ &+ \frac{R_{ss,i}'}{R_{ss,i}}(-Q_{ss,i} C_{ss}' + \Phi_{ss,i} C_{ss}) - \Phi_{ss,i} C_{ss}'. \end{aligned} \tag{3.117}$$

Dividing by C_{ss}' from both sides and rearranging,

$$\begin{aligned} (K'(C_{ss}) + \kappa)R_{ss,i} - \Phi_{ss,i} = &-Q_{ss,i}' - Q_{ss,i}(\frac{C_{ss}''}{C_{ss}'} - \frac{R_{ss,i}'}{R_{ss,i}}) - \Phi_{ss,i} \frac{C_{ss}}{C_{ss}'} \frac{R_{ss,i}'}{R_{ss,i}} \\ &+ \left(\kappa \frac{C_e'}{C_{ss}'} - \frac{V_{\max}' C_{ss}}{(K_M + C_{ss})C_{ss}'} - \frac{\kappa'(C_{ss} - C_e)}{C_{ss}'}\right) R_{ss,i}. \end{aligned} \tag{3.118}$$

Substituting (3.118) into (3.115) and simplifying, we finally get

$$1 = \sum_{j=1}^{N} \phi_{i,j}\gamma_j e^{-\lambda\tau_j} \frac{Q_{ss}(2)}{R_{ss}(2)} \int_0^2 \Psi(x) \exp\left(-\int_x^2 \Gamma(y)\,\mathrm{d}y\right)\,\mathrm{d}x, \tag{3.119}$$

where $\gamma_j = P_j'(C_{\mathrm{op}})C_{ss}'(2)$ is the TGF gain,

$$\Psi(x) = \frac{1}{Q_{ss,i}^2}\left(1 - H\frac{C_{ss}}{C_{ss}'}\right)\left(\frac{R_{ss,i}^5}{8\mu}g_i'(x) - 4\alpha g_i(x)Q_{ss,i}\right),$$

$$\Gamma(x) = \left(\kappa\frac{C_e'}{C_{ss}'} - \frac{V_{\max}'C_{ss}}{(K_M + C_{ss})C_{ss}'} - \frac{\kappa'(C_{ss} - C_e)}{C_{ss}'} + \lambda R_{ss,i}\right)\frac{R_{ss,i}}{Q_{ss,i}} - \frac{\Phi_{ss,i}}{Q_{ss,i}}\frac{C_{ss}}{C_{ss}'}\frac{R_{ss,i}'}{R_{ss,i}},$$

and $g_i(x)$ satisfies Eq. (3.105). Equation (3.119) assumes compliant tubular walls and allows spatially varying radius, maximum active transport, chloride permeability. The gain γ_j can be related to the parameters $K_{1,j}$ and $K_{2,j}$ in the pressure response function (Eq. (2.19)). Differentiating Eq. (2.19) with respect to C_i and setting C_i to C_{op}, we obtain $P_j'(C_{\mathrm{op}}) = -K_{1,j}K_{2,j}$; thus

$$\gamma_j = -K_{1,j}K_{2,j}C_{ss}'(2). \tag{3.120}$$

In the case of two coupled nephrons ($N = 2$) one may obtain for $i = 1$:

$$\frac{1}{\omega(\lambda)} = \gamma_1 e^{-\lambda\tau_1} + \phi_{1,2}\gamma_2 e^{-\lambda\tau_2}, \tag{3.121}$$

where

$$\omega(\lambda) \equiv \frac{Q_{ss}(2)}{R_{ss}(2)} \int_0^2 \Psi(x) \exp\left(-\int_x^2 \Gamma(y)\,\mathrm{d}y\right)\,\mathrm{d}x. \tag{3.122}$$

Eq. (3.121) can be written as

$$1 - \frac{1}{\gamma_1 e^{-\lambda\tau_1}\omega(\lambda)} = -\phi_{1,2}\frac{\gamma_2}{\gamma_1}e^{-\lambda(\tau_2 - \tau_1)}. \tag{3.123}$$

An identical equation holds for $i = 2$, but with the indices reversed. If we assume that the coupling is symmetric, i.e., if $\phi_{1,2} = \phi_{2,1} = \phi$, then one obtains

$$\left(1 - \frac{1}{\gamma_1 e^{-\lambda\tau_1}\omega(\lambda)}\right)\left(1 - \frac{1}{\gamma_2 e^{-\lambda\tau_2}\omega(\lambda)}\right) = \phi^2 \tag{3.124}$$

3.3.2 Model results

We used the model's characteristic equation (3.124) to study the dynamics of our coupled-nephron model. We first performed a bifurcation analysis and solved Eq. (3.124) to obtain parameter regions that indicate qualitatively differing model behaviors. Then, we numerically solved the full equations (Eqs. (2.1), (2.13), (2.3), and (2.4)) to validate and supplement the information provided by the characteristic equation. In this study, we restricted our analysis to the simple case of two coupled nephrons, indexed by 'A' and 'B'. When comparison is made with the uncoupled case, nephron index was omitted. Throughout this study, we assumed symmetric coupling, which implies the effect of the first nephron on the second is the same as the second nephron on the first, i.e., $\phi \equiv \phi_{AB} = \phi_{BA}$. The coupling coefficient ϕ was taken to be 0.2 (Källskog and Marsh (1990); Chen et al. (1995)).

Recall that steady-state behaviors for an uncoupled nephron using parameters given in Table 2.4 were computed in our short-looped model and summarized in Fig. 3.6.

Two coupled nephrons having identical bifurcation parameter: TGF gain and delay

To investigate the impact of internephron coupling on TGF-mediated dynamics, we used the model's characteristic equation (3.124) to compare model behaviors of an uncoupled TGF system with those of a coupled system. We first considered the case of two coupled identical nephrons, where $\gamma \equiv \gamma_A = \gamma_B$ and $\tau \equiv \tau_A = \tau_B$.

For a given set of model parameters, the solutions to the characteristic equation (3.124) are an infinite series of complex-valued eigenvalues, $\{\lambda_{n,m}\}_{n=1,2,\ldots,m=A,B}$, where $\lambda_{n,m} \equiv \rho_{n,m} + i\omega_{n,m}$. The real and imaginary parts of $\lambda_{n,m}$ correspond to the strength and frequency, respectively, of the oscillations in model nephron 'm'. We identified parameter regions that correspond to different combinations of the signs of $\mathrm{Re}(\lambda_{n,m})$, i.e., $\rho_{n,m}$ (positive, negative, or zero). To compute parameter boundaries,

we solved the characteristic equation (3.124) for $\rho_{n,m} = 0$, which may correspond to a solution bifurcation or a transition in dynamics states of solutions, as a function of bifurcation parameters γ and τ. These γ–τ pairs were obtained for two cases: (1) an uncoupled system with $\phi = 0$; (2) a coupled system with $\phi = 0.2$. The results are shown in Fig. 3.16, panels A and B, respectively. The physiologic range for TGF gain and delay values was set to be $(\gamma, \tau) \in [0, 10] \times [0, 0.5]$.

For the uncoupled TGF system, the time-independent steady-state solution appears only for sufficiently small γ such that the points (γ, τ) lie below all curves $\rho_n = 0$. In this solution regime, which is labeled '$\rho_n < 0$' in Fig. 3.16A, any initial solution or any transiently perturbed steady-state solution converges to the time-independent steady-state solution. But for γ such that the points (γ, τ) lie above the curve corresponding to $\rho_n = 0$ for some n, a perturbation of the steady-state solution gives rise to a LCO, indicated by '$\rho_n > 0$' for $n = 1, 2, 3, 4$. It is noteworthy that, with spatially inhomogeneous TAL radius as shown in Fig. 3.6B, the curves for $\rho_n = 0$, $n = 1, 2, 3, 4$ cross the γ-axis, a results that was not observed when a TAL radius was assumed to be homogeneous (Layton (2010)). Such γ-axis crossings implies that a nonzero (or, sufficiently long) TGF delay is not necessary for the emergence of oscillatory solutions. A detailed analysis of the TGF system with spatially inhomogeneous TAL radius and transport properties were given in TAL model (see Section 3.1 herein).

When internephron coupling is introduced, i.e., $\phi = 0.2$, model behaviors become noticeably more complex, as shown in Fig. 3.16B. One notable effect of coupling is that the number of root curves within the physiologic range doubles from four ($\rho_n = 0, n = 1, 2, 3, 4$) to eight ($\rho_{n,m} = 0, n = 1, 2, 3, 4; m = A, B$). This doubling in the number of root curves can be explained by a spectral splitting in which each eigenvalue associated with differing n's is splitted into the number N of nearby eigenvalues where N is the number of coupled nephrons. For two identical nephrons

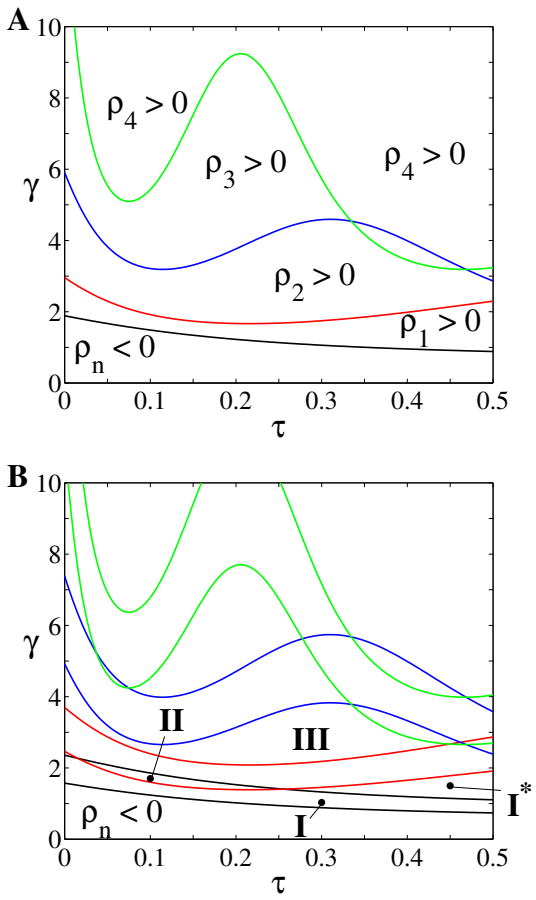

FIGURE 3.16: Panel A: root loci, for an uncoupled nephron, as a function of TGF gain γ and delay τ. B: root loci for two identical coupled nephrons. Black, red, blue, green curves correspond to $\rho_1 = 0$, $\rho_2 = 0$, $\rho_3 = 0$, and $\rho_4 = 0$, respectively. The TGF delay τ is expressed in non-dimensional form in this figure and in subsequent figures. Reprinted from Ryu and Layton (2013b).

($N = 2$), the root loci arising from spectral splitting gives rise to parameter regions not found in the uncoupled case: e.g., where $\rho_{1,A} > 0$ and $\rho_{1,B} < 0$, and where also $\rho_{n,A} < 0$ and $\rho_{n,B} < 0$ for $n > 1$ (marked 'I' in Fig. 3.16B); where $\rho_{1,A} > 0$ and $\rho_{1,B} > 0$, and where also $\rho_{n,A} < 0$ and $\rho_{n,B} < 0$ for $n > 1$ (marked 'I*' in Fig. 3.16B); where $\rho_{1,A} > 0$ and $\rho_{1,B} < 0$, and $\rho_{2,A} > 0$ and $\rho_{2,B} < 0$, and $\rho_{n,A} < 0$ and $\rho_{n,A} < 0$ for $n > 2$ (marked 'II' in Fig. 3.16B); and where $\rho_{n,A} > 0$ and $\rho_{n,B} > 0$ for $n = 1, 2$, and $\rho_{n,A} < 0$ and $\rho_{n,A} < 0$ for $n > 2$ (marked 'III' in Fig. 3.16B). The signs of $\rho_{n,m}$ for the different parameter regions described in Fig. 3.16B is given in

Table 3.4. Other regions where some $\rho_{n,m}$'s are positive and others are negative can be identified likewise.

Table 3.4: Signs of $\rho_{n,m}$ for four parameter regions described in Fig. 3.16B

$\rho_{n,m}$	I	I*	II	III
$\rho_{1,A}$	$+$	$+$	$+$	$+$
$\rho_{1,B}$	$-$	$+$	$-$	$+$
$\rho_{2,A}$	$-$	$-$	$+$	$+$
$\rho_{2,B}$	$-$	$-$	$-$	$+$
$\rho_{n,A}, \rho_{n,B}$ $(n > 2)$	$-$	$-$	$-$	$-$

Besides doubling the number of root curves, the model predicts that coupling decreases the size of the parameter region that support a time-independent steady-state solution, because stable oscillatory solutions can be attained at lower gain values relative to the uncoupled TGF system (compare the area of the $\rho_n < 0$ region in Fig. 3.16, panels A and B). This result implies the stability of the TGF system is reduced by internephron coupling, consistent with the results in the previous modeling studies (Pitman et al. (2004); Layton et al. (2011)).

To validate the predictions of the characteristic equations, we investigate dynamic behaviors of the full nonlinear model. We computed numerical solution to model equations Eqs. ((2.1), (2.13), (2.3), and (2.4)) for two identical nephrons, for selected values of gain γ and delay τ. Four points, labeled **W**, **X**, **Y**, and **Z** in Fig. 3.17A, were selected which correspond to the following delays and gains pairs: $(\gamma_W, \tau_W) = (1, 0.15)$, $(\gamma_X, \tau_X) = (2, 0.4)$, $(\gamma_Y, \tau_Y) = (4.5, 0.2)$, and $(\gamma_Z, \tau_Z) = (3, 0.1)$. The time profiles for the TGF-mediated inflow pressure following a transient perturbation and their corresponding power spectra are summarized in Fig. 3.17. Panels X1, Y1, and Z1 show three oscillations in the inflow pressure with different frequencies; panels X2, Y2, Z2 show corresponding power spectra. Peaks in these spectra, and in the spectra

of subsequent figures, have frequency labels that are in mHz. Point **W**, which lies within the "$\rho_n < 0$" region, corresponds to a time-independent steady state. **X**, **Y**, and **Z** correspond to oscillatory solutions, which LCO frequencies $f_1 = 36$, $f_2 = 85$, and $f_3 = 152$ mHz, receptively.

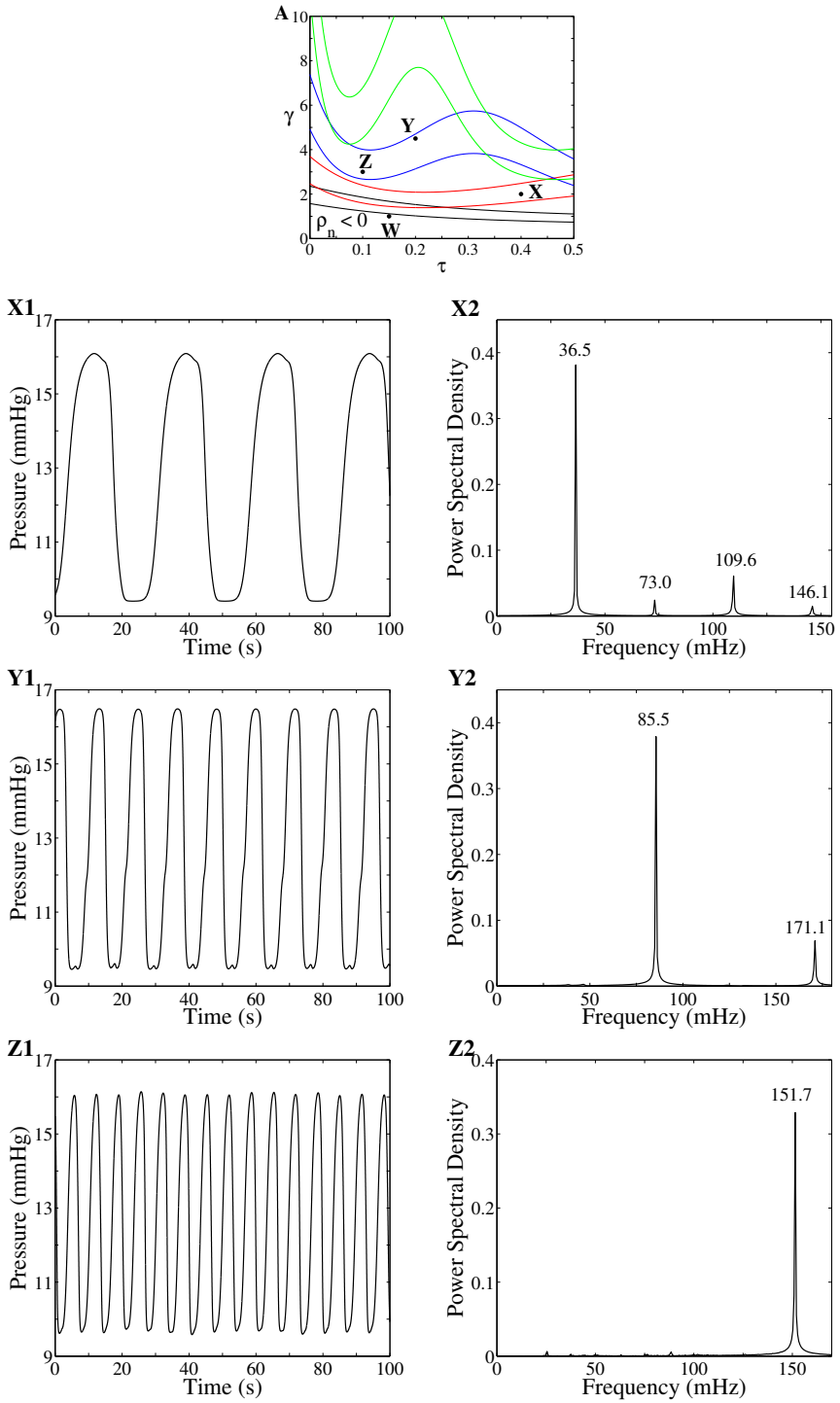

FIGURE 3.17: Sample solutions at the points **X**, **Y**, and **Z**, marked in panel A. Panels X1, Y1, and Z1 show three oscillations in the inflow pressure with different frequencies; panels X2, Y2, Z2 show corresponding power spectra. Peaks in these spectra, and in the spectra of subsequent figures, have frequency labels that are in mHz. (Point **W**: $\gamma = 1, \tau = 0.15$; **X**: $\gamma = 2, \tau = 0.4$; **Y**: $\gamma = 4.5, \tau = 0.2$; **Z**: $\gamma = 3, \tau = 0.1$). Reprinted from Ryu and Layton (2013b).

Two coupled nephrons with only one nephron having varying TGF gain and delay

TGF gain and delay *in vivo* likely differ among nephrons. In this section, we studied cases where one model nephron (A) havs fixed TGF gain and delay while the other model nephron (B) has variable parameters.

We computed root loci, corresponding to nephron B, that are encompassed within physiologic ranges for gain γ_B and delay τ_B given by $(\gamma_B, \tau_B) \in [0, 10] \times [0, 0.5]$. Also, note that each nephron naturally corresponds to a specific set of eigenvalues, i.e., nephrons A and B are associated with eigenvalues $\lambda_{n,A}$ and $\lambda_{n,B}$, respectively, for $n = 1, 2, 3, 4, \ldots$. The root curves were obtained for three sets of fixed parameters for nephron A: $(\gamma_A, \tau_A) = (4, 0.3)$, $(6.8, 0.18)$, and $(8, 0.1)$. The results are shown in Fig. 3.18. We refer $\rho_{n,B} = 0$ to $\rho_n = 0$ in each panel, denoted by black, red, blue, green curves, corresponding to $n = 1, 2, 3, 4$, respectively.

In all three cases, $\rho_{n,A}$ for $n = 1, 2, 3, 4$ is always positive for the parameter space displayed. Below the black curve corresponding to $\rho_{1,B} = 0$ in each panel, $\rho_{1,B}$ is negative, whereas above that curve $\rho_{1,B}$ is positive. In fact, below all the curves, all eigenvalues associated with nephron B have negative real parts, i.e. $\rho_{n,B} < 0$ for all n. However the stable model solution for nephron B is not a time-independent steady-state because the stable solution for nephron A is oscillatory and nephron B is driven by nephron A to oscillate. Similarly, above the red, blue, and green curves corresponding to $\rho_{2,B} = 0, \rho_{3,B} = 0$, and $\rho_{4,B} = 0$, respectively, $\rho_{2,B}$, $\rho_{3,B}$, and $\rho_{4,B}$ are positive, and below the curves, those ρ's, respectively, are negative. By a comparison of the boundary curves among three cases, one can conclude although one nephron (nephron A) has a different choice of fixed gain and delay values, the qualitatively distinct parameter boundaries that separate model behaviors remain nearly the same.

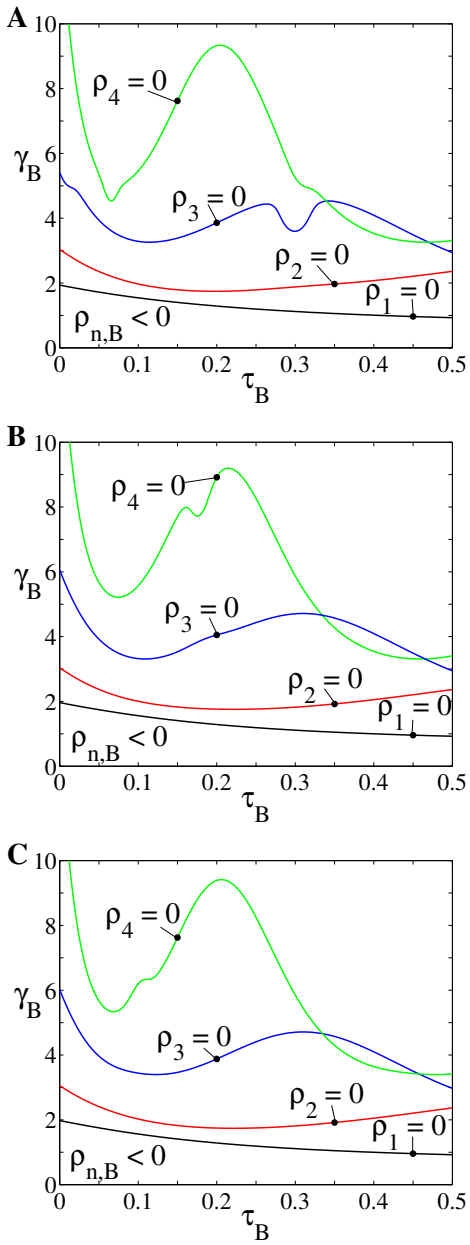

FIGURE 3.18: Root loci corresponding to coupled nephron B with nephron A having fixed gain and delay (we refer $\rho_{n,B} = 0$ to $\rho_n = 0$ in each panel, denoted by black, red, blue, green curves, corresponding to $n = 1, 2, 3, 4$, respectively). (A) $(\gamma_A, \tau_A) = (4, 0.3)$; (B) $(\gamma_A, \tau_A) = (6.8, 0.18)$; (C) $(\gamma_A, \tau_A) = (8, 0.1)$. Reprinted from Ryu and Layton (2013b).

Two coupled nephrons with identical gains, varying delays

We next considered another special case of parameters in two coupled nephrons: the gains in two nephrons were assumed to be identical, i.e., $\gamma \equiv \gamma_A = \gamma_B$, but

with differing time delays. We determined the roots corresponding to $\rho_n = 0$ for $n = 1, 2, 3, 4$ by solving the characteristic equation (Eq. (3.124)) as a function of τ_A and τ_B for two choices of gains: $\gamma = 1.5$ and $\gamma = 5$. The results are shown in Fig. 3.19. In Fig. 3.19 and in the explanation below, any root curve such that $\rho_{n,A} = 0$ or $\rho_{n,B} = 0$ is denoted by $\rho_n = 0$. Black, red, blue, green curves correspond to $\rho_1 = 0$, $\rho_2 = 0$, $\rho_3 = 0$, and $\rho_4 = 0$, respectively.

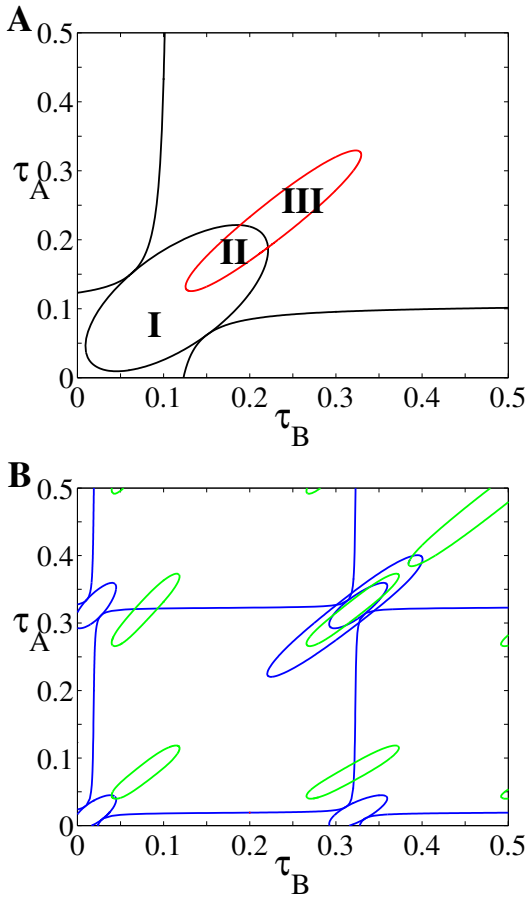

FIGURE 3.19: Root loci corresponding to two coupled nephron with identical gains $\gamma = 1.5$ (A) and $\gamma = 5$ (B) as functions of delays τ_A and τ_B. Black, red, blue, green curves correspond to $\rho_1 = 0$, $\rho_2 = 0$, $\rho_3 = 0$, and $\rho_4 = 0$, respectively. Reprinted from Ryu and Layton (2013b).

For a relatively low gain value of $\gamma = 1.5$, bifurcation diagram Fig. 3.19A exhibits five qualitatively distinct parameter regions: (1) the left-lower region below the big

oval, where the real parts of all eigenvalues are negative; (2) the left-upper and right-lower regions, and the region marked 'I', where one and only one of $\rho_{1,A}$ and $\rho_{1,B}$ is positive, and $\rho_n < 0$ for $n > 1$; (3) the region marked 'II', where one and only one of $\rho_{1,A}$ and $\rho_{1,B}$ is positive and one and only one of $\rho_{2,A}$ and $\rho_{2,B}$ is positive, and $\rho_n < 0$ for $n > 2$; (4) the small oval but outside the big oval marked 'III', where both $\rho_{1,A}$ and $\rho_{1,B}$ are positive, and one and only one, of $\rho_{2,A}$ and $\rho_{2,B}$ is positive, and $\rho_n < 0$ for $n > 2$; and (5) the right-upper regions, where both $\rho_{1,A}$ and $\rho_{1,B}$ are positive, and $\rho_n < 0$ for $n > 1$. The results indicate that the full model equations (Eqs. (2.1), (2.13), (2.3), and (2.4)) may have three stable solutions: a time-independent steady-state solution, a f_1-LCO, and a f_2-LCO. These results can also be related to results obtained for the γ–τ plane for identical nephrons. Consider first the diagonal line corresponding to $\tau_A = \tau_B$ in Fig. 3.19A. That line intercepts the root curves four times: two times with $\rho_1 = 0$ at $\tau_A = \tau_B = 0.0187, 0.212$ and another two times with $\rho_2 = 0$ at $\tau_A = \tau_B = 0.127, 0.328$. Then consider the same line in the γ–τ plane, which corresponds to the $\gamma = 1.5$ line in Fig. 3.16B: that line also has the same interceptions with the root curves: $\tau = 0.0187, 0.127, 0.212, 0.328$ for $\gamma = 1.5$. In both of Figs. 3.16B and 3.19A, the two interceptions $(\gamma, \tau) = (1, 5, 0.0187)$ and $(\gamma, \tau) = (1, 5, 0.127)$ may correspond to changes in model solution behaviors, from a stable steady state to a f_1-LCO and from a f_1-LCO to a f_2-LCO, respectively.

As gain γ is increased, model behavior becomes more complex. At $\gamma = 5$, all root curves observed for $\gamma = 1.5$ disappear and new root curves arise across which one of ρ_3 or ρ_4 changes sign: see Fig. 3.19B. As a consequence, stable solutions with a frequency corresponding to λ_n for $n = 3$ or 4, may arise. The diagonal line $\tau_A = \tau_B$ intercepts the root curves ten times.Most of those interceptions can also be observed by considering the line corresponding to $\gamma = 5$ in the γ–τ plane in Fig. 3.16B. Additional interceptions, which are not apparent in Fig. 3.16B, were observed at the small oval for $\rho_3 = 0$ and the oval for $\rho_4 = 0$ in the right-upper region of Fig. 3.19B.

Coupled nonidentical nephrons

A number of experimental recordings have shown that proximal tubule pressure oscillations obtained in SHR appear irregular and resemble deterministic chaos (Holstein-Rathlou and Leyssac (1986)). It is also known that internephron coupling is stronger in SHR. Hence, we examined the extent to which TGF coupling may affect (or intensify) the spectral complexity of TGF-mediated oscillations.

We solved the full model equations (Eqs. (2.1), (2.13), (2.3), and (2.4)) for two nephrons, A and B with parameters: $(\gamma_A, \tau_A) = (3, 0.1)$ and $(\gamma_B, \tau_B) = (5, 0.2)$. The time profiles of TGF-mediated tubular fluid pressure, flow rate, Cl^- concentration at the MD for nephron A are summarized in Fig. 3.20. The power spectra corresponding to tubular fluid pressure are shown in Fig. 3.21. In nephron A, three peaks were observed in the frequencies of MD fluid pressure: $\sim$46.9, $\sim$105, and $\sim$151.8 mHz. Among the three, the first and third frequencies are the strongest. These two frequencies correspond to the fundamental frequency of nephron B, which is in the single-frequency region, and the third-frequency of nephron A, which is in the bistable region, respectively, as can be seen in Fig. 3.16B. Power spectra corresponding to flow rate and Cl^- concentration exhibit similar complexity with multiple peaks (results not shown). These model results suggest that irregular oscillations in tubular pressure, which resemble the characteristics of fluid pressure in SHR, can be introduced by internephron coupling. Moreover, our extended coupled TGF system has the increased tendency to exhibit irregular TGF-mediated oscillations in fluid pressure inasmuch as the parameter regions which support solution multistability are increased by coupling.

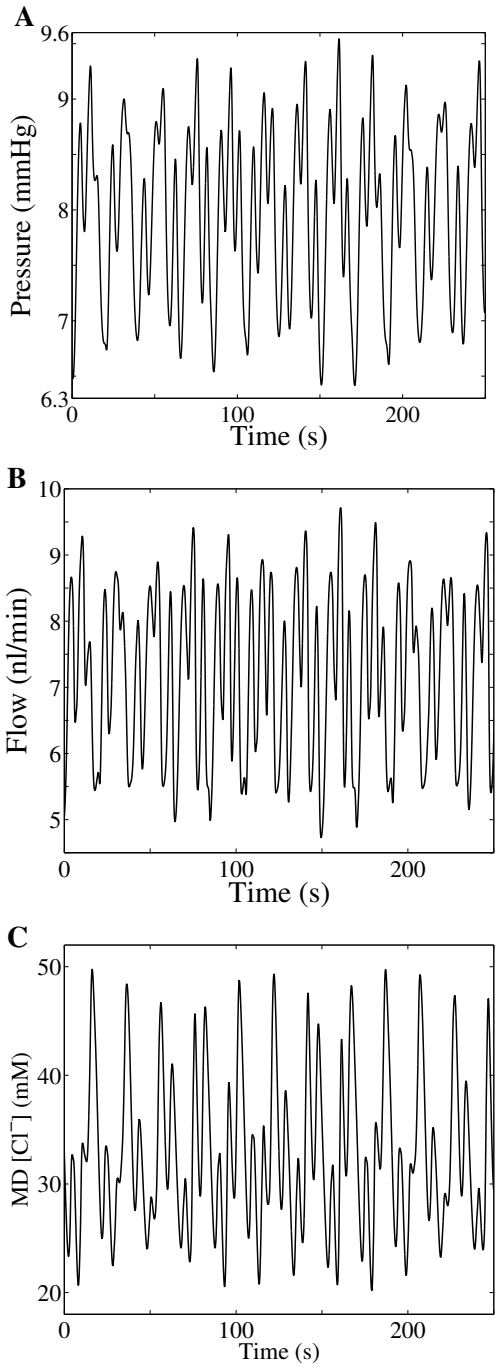

FIGURE 3.20: Oscillations in tubular fluid pressure (A), flow rate (B), and $[Cl^-]$ (C) at the macula densa in nephron A of two coupled nephrons. The parameters of the two nephrons, A and B, were set to $(\gamma_A, \tau_A) = (3, 0.1)$ and $(\gamma_B, \tau_B) = (5, 0.2)$. Reprinted from Ryu and Layton (2013b).

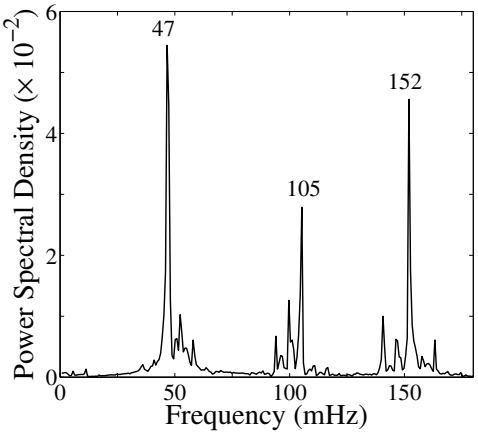

FIGURE 3.21: Power spectra corresponding to oscillations in tubular fluid pressure for two coupled nephrons (Fig. 3.20A) in linear ordinate. Reprinted from Ryu and Layton (2013b).

4

Stochastic Model

Feedback delays play an essential role in determining qualitatively and quantitatively different TGF-mediated dynamic behaviors, as observed in our model results presented in the preceding Chapters. In particular, when noise that may arise from various sources of perturbations, such as heart beat, movement, and hormone levels, is introduced, the resulting dynamics may become significantly rich and complex, revealing a variety of model behaviors due to the interaction of noise with delays. In this chapter, we aim to study the effect of that interaction on the stability of the feedback-mediated dynamic behaviors.

For analytic simplicity we consider a time-delayed transport equation that represents the motion of chloride ions in the rigid-TAL fluid. We first show the existence and uniqueness of the steady-state solution for the deterministic Dirichlet boundary problem, using bifurcation analysis and the contraction mapping theorem. We then extend our analysis to the stochastic system with random boundary conditions to provide an analogous proof for the existence and uniqueness of the statistically stationary solution.

Finally we apply multiscale analysis to a linear time-delayed transport equation

and derive approximate stochastic (reduced) equations for the amplitudes of solutions near the critical delay of the deterministic system. Specifically, we will consider the case when the system is in the subcritical region, but close enough to the critical delay to better understand how the noise can interact with the delay of the system, affecting overall solution behaviors.

4.1 Deterministic System

We first consider the deterministic system subject to Dirichlet boundary condition to provide the basic analytic results for further study of the stochastic system. In the rigid-TAL model developed by Layton et al. (1991), the mass conservation equation to represent the chloride concentration, in nondimensional form, is given by

$$\frac{\partial}{\partial t}C + F(C(1,t-\tau))\frac{\partial}{\partial x}C = -K(C) + \kappa(C - C_e),$$

where x represents axial position along the TAL ($0 \leqslant x \leqslant 1$) with rigid walls, t is time, $K(C) = \frac{V_{\max}C}{K_M+C}$, and C_e is time-independent extratubular (interstitial) chloride concentration which is assumed to be fixed. F represents the fluid flow through the TAL, which depends on the MD chloride concentration at an earlier time $t-\tau$, i.e., $F = F(C(1,t-\tau))$. Note that the equation can be obtained by nondimensionalizing Eq. (2.3) and assuming constant R because of the rigidity of the TAL. Under further assumption with no passive diffusion by setting $\kappa = 0$, we arrive at the following time-delayed transport equation for C

$$\frac{\partial}{\partial t}C + F(C(1,t-\tau))\frac{\partial}{\partial x}C = -K(C), \quad x \in (0,1),\ t > 0, \tag{4.1}$$

with Dirichlet boundary condition $C(0,t) = m > 0$ on the left side and initial condition $C(x,0) = C_0(x) \in \mathcal{C}([0,1])$. For a delay term $F(C(1,t-\tau))$, we must specify $C(1,t) = \eta(t+\tau)$ for $t \in [-\tau, 0]$ with $\eta \in \mathcal{C}([0,\tau])$. Also, F is a smooth function and K is Lipschitz continuous with $K(0) = 0$. Based on Eq. (4.1), the (reduced) integral TGF model was derived in Ref. Pitman et al. (2002).

Before we conduct a stability analysis, we show well-posedness of the main equation (4.1) using the method of characteristics in PDE theory (Evans (1998)).

Proposition 1. *Given $C(x,0) = C_0(x)$ and $C(1,t) = \eta(t+\tau)$ for $t \in [-\tau, 0]$, the initial value problem (4.1) is well-posed, i.e,. the solution exists.*

Proof. Since $C(1,t) = \eta(t+\tau)$ for $t \in [-\tau, 0]$ is given, the drift term $F(C(1, t-\tau))$ is determined for $t \in [0, \tau]$ and is independent of x. Then, by the method of characteristics, the (classical) solution exists and is unique up to $t = \tau$, given initial condition in $\mathcal{C}([0,1])$ and boundary condition $C(0,t) = m$ for $t \geqslant 0$. For the next time interval $t \in [\tau, 2\tau]$, we determine the term $F(C(1, t-\tau))$ for $t \in [\tau, 2\tau]$ given $C(1,t)$ on $t \in [0, \tau]$, and use the same argument to find the solution for next time interval. Using this argument repeatedly, the unique solution can be obtained for all $t \geqslant 0$ by the induction method. Thus, given the Dirichlet boundary condition, the initial value problem (4.1) is well-posed. The solution exists. □

4.1.1 Steady-state solution

Now, we consider the time-independent steady-state solution of Eq. (4.1). If we write $C(x,t) = z(x)$, $z(x)$ solves the following ODE

$$F(z(1))z_x + K(z) = 0, \quad x \in (0,1), \tag{4.2}$$

subject to initial condition $z(0) = m > 0$. $F(z(1))$ corresponds to the steady-state TAL flow rate in the TGF model, denoted by b, which is a positive constant. Note that upon choosing different normalizing factors in nondimensionalization to obtain Eq. (4.1), as in Section 3.1.1, the value of b can vary.

Proposition 2. *Given that K is a strictly positive for all $z > 0$ with $K(0) = 0$ and Lipschitz continuous, there is a unique function $z(x)$, satisfying (4.2), which is strictly positive and decreasing for all x in $[0,1]$.*

Proof. The solution of (4.2) is dependent only on the function K. Because K is positive and Lipschitz continuous, and Eq. (4.2) is separable on z, the existence of a solution with $z(0) = m > 0$ follows from Lipschitz continuity of K. Moreover, the strict positivity of K for positive z and F for any z implies $z_x < 0$ from Eq. (4.2), i.e., $z(x)$ is decreasing.

To prove $z(x) > 0$ for all $x \in [0, 1]$, we use a contradiction argument. Suppose that $z(x)$ is nonzero solution and there exist $x_1 \in [0, 1]$ such that $z(x_1) = 0$. We know $\bar{z} \equiv 0$ is a solution because of $K(0) = 0$. The uniqueness then implies that $z = \bar{z}$ as the ODE is autonomous, which results in a contradiction. Thus, $z(x)$ cannot have zero solution in $[0, 1]$. □

The simplest case we can consider is that K is linear: $K(C) = kC$ for some $k > 0$. Let us assume $F(z(1)) = b = 1$ again. For this case, the solution can be found easily using the property of exponential functions, $z(x) = me^{-kx}$. However, for the general form of K, we might not be able to solve for $z(x)$ explicitly, but rather implicitly. By separation of variables,

$$\int \frac{dz}{K(z)} = -x + c.$$

Note that $K(z)$ cannot be zero because of $z(x) > 0$ for all x in Proposition 2 (which represents the steady-state chloride concentration). Using the initial condition, $z(0) = m$ for some $m > 0$, c can be specified.

For a nonlinear function of $K(z) = \frac{V_{\max} z}{K_M + z}$ in the TGF model, the implicit form of $z(x)$ is derived by:

$$\frac{dz}{K(z)} = \frac{K_M + z}{V_{\max} z} dz = \frac{1}{V_{\max}} \left[\frac{K_M}{z} + 1 \right] dz = -dx,$$

$$\frac{1}{V_{\max}} \left[K_M \ln|z| + z \right] = -x + c.$$

Applying the initial condition $z(0) = m$, we finally find the solution

$$[K_M \ln|z| + z] = -V_{\max} x + [K_M \ln(m) + m]\,.$$

4.1.2 Stability

Our main goal of this section is to study the stability of the solution for the linearized system, depending on delay τ by linear stability and bifurcation analysis. We linearize our main equation (4.1) about its steady state $z(x)$ in (4.2) to obtain the linearized system. To analyze the stability of the solutions to that linear system, we particularly employ the method of separation of variables.

If we use $C(x,t) = z(x) + w(x,t)$ and substitute it into Eq. (4.1), we obtain the equation for w given by

$$w_t + F(z(1) + w(1, t-\tau))(z_x + w_x) + K(z+w) = 0, \quad w(0,t) = 0.$$

Using Taylor's expansion for F and K, it is written as

$$w_t + [F(z(1)) + F'(z(1))w(1,t-\tau) + O(w^2)](z_x + w_x) \\ + [K(z) + K'(z)w \quad + O(w^2)] = 0.$$

From Eq. (4.2) (i.e., $F(z(1))z_x + K(z) = 0$), it follows that

$$w_t + F(z(1))w_x + F'(z(1))z_x(x)w(1,t-\tau) + K'(z)w \\ = O(w^2) + O(w(1,t-\tau)w_x(x,t)).$$

Dropping the higher order terms, we arrive at the linear equation for $w(x,t)$:

$$w_t + bw_x + g(x)w(1,t-\tau) + k(x)w(x,t) = 0, \quad x \in (0,1),\ t > 0 \tag{4.3a}$$

$$w(0,t) = 0, \quad t \geqslant 0, \tag{4.3b}$$

$$w(x,0) = \psi(x), \quad x \in [0,1], \tag{4.3c}$$

$$w(1,t) = \phi(t+\tau), \quad t \in [-\tau, 0], \tag{4.3d}$$

where $\psi \in \mathcal{C}([0,1])$ and $\phi \in \mathcal{C}([0,\tau])$ are given functions. Note that in the TGF model, the constant $b = F(z(1))$, and functions $g(x) = F'(z(1))z_x(x)$ and $k(x) =$

$K'(z(x))$ are all positive for $x \in [0,1]$. Because of the positive drift term $b > 0$, we do not need to impose a boundary condition at $x = 1$.

Our primary interest for the linear system (4.3) is to see whether a small perturbation $w(x,t)$ grows or decays over time for different values of τ. Specifically, we seek exponentially growing solutions of the form $w(x,t) = e^{\lambda t} f(x)$ for some $\lambda \in \mathbb{C}$ and some function f due to the linearity of the problem (4.3). Using this specific form of the solutions, we conduct bifurcation analysis to find the existence of the critical delay of the system. Much of the following bifurcation analysis can be also found in Layton et al. (1991).

If we assume that the solution of (4.3) has the form $w(x,t) = e^{\lambda t} f(x)$ for some function f, plugging this expression for $w(x,t)$ in Eq. (4.3a) and canceling $e^{\lambda t}$ terms lead to the equation for $f(x)$

$$bf'(x) + (k(x) + \lambda) f(x) + g(x) e^{-\lambda \tau} f(1) = 0, \quad f(0) = 0. \tag{4.4}$$

We can easily solve this ODE by multiplying both sides by an integrating factor $\mu(x) = \exp(\int_0^x \frac{k(y)+\lambda}{b} dy)$ and using the initial condition $f(0) = 0$,

$$f(s) = -\exp\left(-\int_0^s \frac{k(y)+\lambda}{b}\, dy\right) \int_0^s \frac{g(x) e^{-\lambda\tau} f(1)}{b} \exp\left(\int_0^x \frac{k(y)+\lambda}{b} dy\right) dx. \tag{4.5}$$

Setting $s = 1$ and canceling $f(1)$ out from both sides, we finally arrive at the following characteristic equation that $b, g(x), k(x)$ satisfy with different $\lambda \in \mathbb{C}$ depending on $\tau \geqslant 0$:

$$1 = -\frac{e^{-\lambda\tau}}{b} \int_0^1 g(x) \exp\left(-\int_x^1 \frac{k(y)+\lambda}{b} dy\right) dx. \tag{4.6}$$

Plugging $g(x) = F'(z(1)) z_x(x)$ and $k(x) = K'(z(x))$ back to (4.6), the equation becomes

$$1 = -\frac{e^{-\lambda\tau} F'(z(1))}{b} \int_0^1 z_x(x) \exp\left(-\int_x^1 \frac{K'(z(y)) + \lambda}{b}\, dy\right) dx. \tag{4.7}$$

Substituting the relation for $K'(z)$, which is obtained by differentiating Eq. (4.2) with respect to x,

$$K'(z(x)) = -b\frac{z_{xx}}{z_x} = -b\frac{d}{dx}(\log z_x) \tag{4.8}$$

into (4.7), calculating the resulting integral, and rearranging terms, we obtain the characteristic equation

$$1 = e^{-\lambda\tau}F'(z(1))z'(1)\left(\frac{e^{-\frac{\lambda}{b}}-1}{\lambda}\right), \tag{4.9}$$

which was also derived in Eq. (20) of Ref. Layton et al. (1991).

Recall that in the TGF model, $F'(z(1))z'(1)$ quantifies the gain value, denoted by γ, of feedback loop. The first derivative $F'(z(1))$ represents the sensitivity of the TGF system to deviations from the target MD chloride concentration (Holstein-Rathlou and Marsh (1989)) and the second derivative $z'(1)$ is the slope of the chloride concentration at the MD when the system is at steady state. The gain γ can be another bifurcation parameter independent of τ, which is assumed to be fixed ($\gamma = \gamma_0$) for the rest of our analysis as it is not of our main interest. A detailed analysis in which the effects of τ and γ are individually analyzed with $b = 1$ can be found in Ref. Layton et al. (1991).

Bifurcation analysis for the critical delay τ_0

In this section, we provide bifurcation analysis to determine the critical delay of the linear system (4.3), as previously conducted by Layton et al. (1991). If we can solve (4.9) for λ in terms of τ and γ ($=F'(z(1))z'(1)$), the explicit form of $w(x,t)$ can be obtained by using $w(x,t) = e^{\lambda t}f(x)$. However, Eq. (4.9) is implicit for λ and the solution space of λ is infinite-dimensional, which make solving Eq. (4.9) difficult. Instead, we write $\lambda(\tau,\gamma) = \rho(\tau,\gamma) + ia(\tau,\gamma)$, where ρ and a are functions of τ and γ. If $\rho < 0$, $w(x,t)$ decays to zero as time evolves. Conversely, if $\rho > 0$, $w(x,t)$

may exhibit sustained deviations from zero solution. Given the fixed value of γ, to find the critical delay, at which the stability of the solution behavior of the form $w(x,t) = e^{\lambda t} f(x)$ may change, it suffices to show that if $\rho = 0$, there exists τ such that

$$1 - e^{-\lambda\tau}\gamma\left(\frac{e^{-\frac{\lambda}{b}} - 1}{\lambda}\right) = 0. \tag{4.10}$$

By setting $\rho = 0$ (i.e., $\lambda = ia$ for some $a \neq 0$) and using trigonometric identities, the above equation can be simplified

$$\frac{a}{2} = -\gamma \sin\left(\frac{a}{2b}\right)\left[\cos\left(a(\tau + \frac{1}{2b})\right) - i\sin\left(a(\tau + \frac{1}{2b})\right)\right]. \tag{4.11}$$

The real and imaginary parts of this equation satisfy

$$\frac{a}{2} = -\gamma \sin\left(\frac{a}{2b}\right)\cos\left(a(\tau + \frac{1}{2b})\right), \tag{4.12}$$

$$0 = \gamma \sin\left(\frac{a}{2b}\right)\sin\left(a(\tau + \frac{1}{2b})\right), \tag{4.13}$$

respectively. Eq. (4.13) implies either $\frac{a}{2b} = n\pi$ or $a(\tau + \frac{1}{2b}) = n\pi$ for $n = 0, \pm 1, \pm 2, \ldots$. To obtain the relation between γ and τ, we drop the first solution $\frac{a}{2b} = n\pi$ because it only gives the trivial solution, i.e., $a = 0$. Substituting $a(\tau + \frac{1}{2b}) = n\pi$ into (4.12) and solving for γ yield the following expression:

$$\gamma(\tau) = (-1)^{n+1}\frac{\left(\frac{bn\pi}{2b\tau+1}\right)}{\sin\left(\frac{n\pi}{2b\tau+1}\right)}, \tag{4.14}$$

for $n = 1, 2, 3, \ldots$. Given the fixed $\gamma_0 > 0$, if there exists $\tau_0 > 0$ such that $\gamma_0 = \gamma(\tau_0)$ for some n and $\frac{\partial\rho}{\partial\tau}\big|_{\tau=\tau_0} > 0$, which is computed from (4.10), it can be implied that the sign of ρ changes from negative and positive values as τ passes through τ_0 from below. Thus, the stability of $w(x,t)$ is determined accordingly. To consider the physiologically relevant range of τ, we restrict our analysis to the case when $0 < \tau \leqslant 1$. Now we provide our main Theorem.

Theorem 3. *For the solution of the form $w(x,t) = e^{\lambda t} f(x)$ to (4.3), there exists a critical delay $\tau_0 > 0$ such that if $\tau < \tau_0$, the trivial solution to (4.3) is asymptotically stable; if $\tau > \tau_0$, the trivial solution is unstable.*

Proof. We begin with $n = 1$. Then, (4.14) becomes

$$\gamma(\tau) = \frac{\left(\frac{b\pi}{2b\tau+1}\right)}{\sin\left(\frac{\pi}{2b\tau+1}\right)}. \tag{4.15}$$

Differentiating the above equation with respect to τ, one can show that $\frac{d\gamma}{d\tau}$ is always positive for $0 < \tau \leqslant 1$ after some tedious algebra. Also, we can find the range of γ to be $[0, 10]$. Then, it follows that the function γ is invertible in a neighborhood of $\gamma_0 \in (0, 10)$ so that, for any given $\gamma_0 \in (0, 1)$, there exists some $\tau_0 > 0$ such that $\gamma^{-1}(\gamma_0) = \tau_0$ by the inverse function theorem. Also, one can check $\frac{\partial \rho}{\partial \tau}\big|_{\tau=\tau_0} > 0$ when $\gamma = \gamma_0$ from (4.10), implying that the sign of ρ changes from negative to positive as τ passes through τ_0. These two conditions, thus, prove the existence of the critical delay τ_0, at which the stability of the solution $w(x,t) = e^{\lambda t} f(x)$ changes. Specifically, $w(x,t)$ decays so that the trivial solution is stable for $\tau < \tau_0$, whereas $w(x,t)$ exponentially grows in time, implying that the zero solution is unstable for $\tau > \tau_0$. □

We only prove the existence of τ_0 for $n = 1$. To check if there exists another τ_0 that satisfies (4.14) and $\frac{\partial \rho}{\partial \tau}\big|_{\tau=\tau_0} > 0$ for given γ_0, and find the smallest value among all of such τ_0, we should repeatedly apply the same argument for different n values. However, it involves a number of computations of $\frac{\partial \rho}{\partial \tau}\big|_{\tau=\tau_0}$ with additional algebra and it would not complete our analysis to apply any solution of (4.3) (see below). Thus, we omit the details here. In fact, Layton et al. (1991) numerically showed that other τ_0 for different n values does not exist for $n > 1$ or is bigger than τ_0 for $n = 1$, suggesting that τ_0 in Theorem 3 corresponds to the primary bifurcation point.

It is also noteworthy that the critical delay τ_0 in Theorem 3 is only true for the solutions of the form $e^{\lambda t}f(x)$. Nonetheless, Theorem 3 ensures the existence of the critical delay for the linearized problem, inferred by the existence of τ_0 for a special case. Based on this τ_0 value, we may study how the stability of the TGF system alters. To generalize our results to any solution of (4.3), we turn to the next section.

Contraction mapping for sufficiently small τ: I. linear system

We have shown the existence of the critical delay τ_0 for the linearized problem (4.3), by looking for a special solution with the form of $e^{\lambda t}f(x)$. To generalize this result for any solution, we aim to obtain an alternative, perhaps more complete way to view our problem (4.3) by defining a suitable map and studying the solution in terms of this map. We desire to show that the map is a contraction for sufficiently small τ, which implies that the steady-state solution is a unique fixed point for (4.3) by the contraction mapping theorem.

Let us first consider the linearized problem for $w(x,t)$ in (4.3). Given $(\psi,\phi) \in \mathcal{C}([0,1]) \times \mathcal{C}([0,\tau])$, the solution $w(x,t)$ is well-defined for all $t > 0$ using the method of characteristics. Let $w(x,t;\psi,\phi)$ denote this solution. Observe that for $t \in [0,\tau], w(x,t;\psi,\phi)$ solves

$$w_t + bw_x + k(x)w = -g(x)\phi(t), \quad x \in (0,1),\ t > 0 \tag{4.16a}$$

$$w(0,t) = 0, \quad t \geqslant 0, \tag{4.16b}$$

$$w(x,0) = \psi(x), \quad x \in [0,1]. \tag{4.16c}$$

In order to advance the solution in time with the initial and boundary conditions, we define the following map.

Definition 4. Let $\mathcal{X} = \mathcal{C}([0,1]) \times \mathcal{C}([0,\tau])$. A map $M : \mathcal{X} \to \mathcal{X}$ is defined by

$$M(\psi,\phi) = (\Psi,\Phi)$$

where

$$\Psi(x) = w(x, \tau; \psi, \phi), \quad \text{for } x \in [0, 1],$$

$$\Phi(t) = w(1, t; \psi, \phi), \quad \text{for } t \in [0, \tau].$$

Now, let w solve (4.3a)–(4.3d) with $(\psi, \phi) = (\psi_0, \phi_0) \in \mathcal{X}$ given. Let us define the pair $(\psi_n, \phi_n) \in \mathcal{X}$ by

$$(\psi_n, \phi_n) = M^n(\psi_0, \phi_0).$$

This is the nth iterate of the map M applied to (ψ_0, ϕ_0). It is easy to see that

$$w(x, \tau n; \psi_0, \phi_0) = \psi_n(x), \quad x \in [0, 1],$$

and

$$w(1, \tau(n-1) + t; \psi_0, \phi_0) = \phi_n(t), \quad t \in [0, \tau].$$

Definition 5. Given the function space $\mathcal{X}$ in Definition 4, define the norm in $\mathcal{X}$ as $||(\psi, \phi)||_{\mathcal{X}} = ||\psi||_{\mathcal{C}([0,1])} + ||\phi||_{\mathcal{C}([0,\tau])}$ where $||\cdot||_{\mathcal{C}(\Omega)}$ is the sup-norm on $\mathcal{C}(\Omega)$.

For the rest of our analysis, we will simply use $||\cdot||_\infty$ for $||\cdot||_{\mathcal{C}(\Omega)}$.

Lemma 6. *The space $\mathcal{X}$ with the norm in Definition 5 is a Banach space.*

Lemma 7. *M is linear on the Banach space $\mathcal{X}$: for any $\alpha, \beta \in \mathbb{R}$,*

$$M(\alpha(\psi_1, \phi_1) + \beta(\psi_2, \phi_2)) = \alpha M(\psi_1, \phi_1) + \beta M(\psi_2, \phi_2).$$

Proof. Let $f_1 = (\psi_1, \phi_1), f_2 = (\psi_2, \phi_2) \in \mathcal{X}$, and $M(f_1) = (\Psi_1, \Phi_1), M(f_2) = (\Psi_2, \Phi_2)$. Let $w(x, t; f_1) = w_1(x, t)$ be the solution of Eqs. (4.16a)–(4.16c) with $(\psi, \phi) = (\psi_1, \phi_1)$ for $t \in [0, \tau]$. Similarly, let $w(x, t; f_2) = w_2(x, t)$ be the solution with (ψ_2, ϕ_2). Using the linearity of (4.16a) and the initial condition (4.16c), it immediately follows that $\alpha w_1(x, t) = w(x, t; \alpha f_1), \beta w_2(x, t) = w(x, t; \beta f_2)$. Then,

$\alpha w_1 + \beta w_2 = w(x,t;\alpha f_1 + \beta f_2)$ for $t \in [0,\tau]$.

$$\begin{aligned} M(\alpha f_1 + \beta f_2) &= (\alpha w_1(x,\tau) + \beta w_2(x,\tau), \alpha w_1(1,t) + \beta w_2(1,t)) \\ &= \alpha(w_1(x,\tau), w_1(1,t)) + \beta(w_2(x,\tau), w_2(1,t)) \\ &= \alpha(\Psi_1, \Phi_1) + \beta(\Psi_2, \Phi_2) \\ &= \alpha M(f_1) + \beta M(f_2). \end{aligned}$$

Thus, M is linear on $\mathcal{X}$. □

Now we provide our main theorem for M.

Theorem 8. *M^2 is a contraction on $\mathcal{X}$ for a sufficiently small τ so that the trivial solution of (4.3) is linearly stable.*

Proof. To prove that M_τ is a contraction for sufficiently small τ, it suffices to show that if $f_1 = (\psi_1, \phi_1), f_2 = (\psi_2, \phi_2) \in \mathcal{X}$, there exists $0 \leqslant \lambda_\tau < 1$ such that

$$||M_\tau(f_1) - M_\tau(f_2)||_{\mathcal{X}} \leqslant \lambda_\tau ||f_1 - f_2||_{\mathcal{X}}. \tag{4.17}$$

Let $w(x,t;f_1) = w_1(x,t)$ and $w(x,t;f_2) = w_2(x,t)$ denote the solutions of Eqs. (4.16a)–(4.16c) with f_1 and f_2, respectively, for $\tau \in [0,\tau]$. Also, let $M_\tau(f_1) = (\Psi_1, \Phi_1)$ and $M_\tau(f_2) = (\Psi_2, \Phi_2)$ by the definition of M_τ.

$$\begin{aligned} ||M_\tau(f_1) - M_\tau(f_2)||_{\mathcal{X}} &= ||(\Psi_1, \Phi_1) - (\Psi_2, \Phi_2)||_{\mathcal{X}} \\ &= ||(w_1(x,\tau) - w_2(x,\tau), w_1(1,t) - w_2(1,t))||_{\mathcal{X}} \\ &= ||(w_1(x,\tau) - w_2(x,\tau)||_{\mathcal{C}([0,1])} + ||w_1(1,t) - w_2(1,t))||_{\mathcal{C}([0,\tau])}, \end{aligned} \tag{4.18}$$

where the last equality follows from the norm defined in $\mathcal{X}$. To show (4.17), it suffices to show how each norm in the right-hand side of (4.18) depends on the norm of f_1 and f_2.

To obtain the inequality (4.17), we first decompose the map using the linearity,

$$M_\tau(\psi, \phi) = M_\tau(\psi, 0) + M_\tau(0, \phi), \tag{4.19}$$

where the first and second terms correspond to the homogeneous and inhomogeneous solutions, respectively. For the rest of our analysis, we assume τ is sufficiently small, specifically, $b\tau \leqslant 1$. To see how $||M_\tau(\psi,\phi)||_{\mathcal{X}}$ depends on $||\psi||_\infty$ and $||\phi||_\infty$, we solve (4.16a)–(4.16c) for $t \in [0,\tau]$ by the method of characteristics. That is,

$$\begin{aligned}
&X'(t) = b, \quad X(0) = x_0,\\
&T'(t) = 1, \quad T(0) = 0,\\
&Z'(t) = -g(X(t))\phi(t) - k(X(t))Z(t), \quad Z(0) = \psi(x_0),
\end{aligned}$$

where $Z(t) = w(X(t),t)$. Solving the first two ODEs yields $T(t) = t$ and $X(t) = x_0 + bt$. By multiplying an integrating factor $\mu(t) = \exp\left(\int_0^t k(X(y))dy\right)$ to the last equation for $Z(t)$, we obtain

$$\frac{d}{dt}(\mu(t)Z(t)) = -g(X(t))\phi(t)\mu(t).$$

Using the initial condition for Z, solving this ODE, and dividing by $\mu(t)$ again result in

$$Z(t) = \psi(x_0)\exp\left(-\int_0^t k(X(s))ds\right) - \int_0^t g(X(s))\phi(s)\exp\left(-\int_s^t k(X(y))\,dy\right)\,ds,$$

$$\begin{aligned}
w(x,t) = {}& \psi(x_0(x,t))\exp\left(-\int_0^t k(X(s;x,t))\,ds\right)\\
&- \int_0^t g(X(s;x,t))\phi(s)\exp\left(-\int_s^t k(X(y;x,t))dy\right)\,ds. \qquad (4.20)
\end{aligned}$$

Given (x,t), we want to find x_0 such that $X(t) = x$, and $X(s;x,t)$ such that $X(0;x,t) = x_0(x,t)$.

$$x = X(t) = x_0 + bt \quad \Rightarrow \quad x_0(x,t) = x - bt,$$

$$X(s;x,t) = x_0(x,t) + bs = x - bt + bs = x + b(s-t).$$

After substituting $x_0(x,t)$ and $X(s;x,t)$ into Eq. (4.20), we finally arrive at the

solution $w(x,t)$ for $t \in [0,\tau]$

$$w(x,t) = \psi(x-bt)\exp\left(-\int_0^t k(x+b(s-t))\,ds\right) - \int_0^t g(x+b(s-t))\phi(s)\exp\left(-\int_s^t k(x+b(y-t))dy\right)\,ds. \tag{4.21}$$

Note that at $x=1$, $\psi(x-bt)$, $g(x+b(s-t))$, and $k(x+b(s-t))$ are well-defined on $t \in [0,\tau]$ because of our assumption $b\tau \leqslant 1$. Plugging $x=1$ into (4.21) yields

$$\Phi(t) = w(1,t) = \psi(1-bt)\exp\left(-\int_0^t k(1+b(s-t))\,ds\right) - \int_0^t g(1+b(s-t))\phi(s)\exp\left(-\int_s^t k(1+b(y-t))\,dy\right)\,ds. \tag{4.22}$$

Let $\Phi_h(t)$ and $\Phi_I(t)$ denote the first and second terms, respectively, on the right-hand side of (4.22). At $t=\tau$, we need to consider two different solutions for $0 \leqslant x \leqslant b\tau$ and $b\tau < x \leqslant 1$. For $b\tau < x \leqslant 1$, the initial condition $\psi(x-b\tau)$ is well-defined. Thus,

$$\Psi(x) = w(x,\tau) = \psi(x-b\tau)\exp\left(-\int_0^\tau k(x+b(s-\tau))\,ds\right) - \int_0^\tau g(x+b(s-\tau))\phi(s)\exp\left(-\int_s^\tau k(x+b(y-\tau))\,dy\right)\,ds. \tag{4.23}$$

Analogously, let $\Psi_h(x)$ and $\Psi_I(x)$ denote the first and second terms in (4.23). On the other hand, if $0 \leqslant x \leqslant b\tau$, the characteristic lines meet the left-hand boundary where the value is zero. Also, $X(s;x,t) = bs$ because $x_0 = 0$. It follows that

$$\Psi(x) = w(x,\tau) = -\int_0^\tau g(bs)\phi(s)\exp\left(-\int_s^\tau k(by)\,dy\right)\,ds. \tag{4.24}$$

Using the expressions in Eqs. (4.22)–(4.24) and the decomposition in (4.19), we

compute $||M_\tau(\psi,\phi)||_{\mathcal{X}}$ to find a condition on τ such that M_τ is a contraction map.

$$\begin{aligned}||M_\tau(\psi,\phi)||_{\mathcal{X}} &\leqslant ||M_\tau(\psi,0)||_{\mathcal{X}} + ||M_\tau(0,\phi)||_{\mathcal{X}} \\ &= ||(\Psi_h,\Phi_h)||_{\mathcal{X}} + ||(\Psi_I,\Phi_I)||_{\mathcal{X}} \\ &= ||\Psi_h||_\infty + ||\Phi_h||_\infty + ||\Psi_I||_\infty + ||\Phi_I||_\infty. \end{aligned} \tag{4.25}$$

Using the positivity of function k, one can easily show that

$$||\Psi_h||_\infty \leqslant \lambda_1||\psi||_\infty, \quad ||\Phi_h||_\infty \leqslant ||\psi||_\infty, \tag{4.26}$$

for some $\lambda_1 < 1$. If we further assume that $K(u) = cu$ for some $c > 0$ and $g(x) = g > 0$ so that $k(x) = K'(z(x)) = c > 0$ for analysis simplicity, we can find the upper bounds on inhomogeneous part $\Phi_I(t)$ as well.

$$\begin{aligned}|\Phi_I(t)| &\leqslant \sup_{0\leqslant s\leqslant t}|\phi(s)|\left|\int_0^t g(1+b(s-t))\exp\left(c(s-t)\right)ds\right| \\ &= \sup_{0\leqslant s\leqslant t}|\phi(s)|\frac{g}{c}(1-\mathrm{e}^{-ct}), \\ ||\Phi_I||_\infty &\leqslant \sup_{0\leqslant t\leqslant \tau}|\Phi_I(t)| = \frac{g}{c}(1-\mathrm{e}^{-c\tau})||\phi||_\infty = \lambda_2||\phi||_\infty. \end{aligned} \tag{4.27}$$

If τ is sufficiently small so that $(1-\mathrm{e}^{-c\tau}) \ll 1$, we can find $\lambda_2 < 1$. Similarly, there exists $\lambda_3 < 1$ such that $||\Psi_I||_\infty \leqslant \lambda_3||\phi||_\infty$ for sufficiently small τ. Putting all upper bounds on terms in (4.25) together using (4.26)–(4.27), we obtain

$$||M_\tau(\psi,\phi)||_{\mathcal{X}} \leqslant (1+\lambda_1)||\psi||_\infty + (\lambda_2+\lambda_3)||\phi||_\infty.$$

Although $(\lambda_2 + \lambda_3)$ can be less than 1, M_τ cannot be a contraction because of $(1+\lambda_1) > 1$. However, if we apply M_τ again to $M_\tau(\psi,\phi)$, there exists λ such that

$$\begin{aligned}||M_\tau^2(\psi,\phi)||_{\mathcal{X}} = ||M_\tau(\Psi,\Phi)||_{\mathcal{X}} &\leqslant (1+\lambda_1)||\Psi||_\infty + (\lambda_2+\lambda_3)||\Phi||_\infty \\ &\leqslant (1+\lambda_1)(\lambda_1||\psi||_\infty + \lambda_3||\phi||_\infty) + (\lambda_2+\lambda_3)(||\psi||_\infty + \lambda_2||\phi||_\infty) \\ &= \tilde{\lambda}||\psi||_\infty + \hat{\lambda}||\phi||_\infty \\ &\leqslant \lambda||(\psi,\phi)||_{\mathcal{X}}, \end{aligned}$$

where $\tilde{\lambda} = (1+\lambda_1)\lambda_1 + (\lambda_2+\lambda_3),\ \hat{\lambda} = (1+\lambda_1)\lambda_3 + (\lambda_2+\lambda_3)\lambda_2$, and $\lambda = \max(\tilde{\lambda}, \hat{\lambda})$. If we choose τ small enough such that $\tilde{\lambda}, \hat{\lambda} < 1$, it follows $\lambda < 1$. To show (4.17) holds for some $\lambda_\tau < 1$, we substitute (ψ, ϕ) by $(\psi_1 - \psi_2, \phi_1 - \phi_2) = f_1 - f_2$ and use the linearity of M_τ. Thus, we conclude that M_τ^2 is a contraction on $\mathcal{X}$ for sufficiently small τ, which implies that the trivial (zero) solution is a unique fixed point for the linear system (4.3).

The argument described above can be extended for more general case of $g(x)$ and $k(x)$ if we carefully treat the inequality in (4.27). Because g and k are uniformly bounded functions, we can find constants $g,\ k > 0$ such that

$$||g||_\infty \leqslant g, \quad ||k||_\infty \leqslant k.$$

Using these inequalities, we obtain similar results to (4.27) with suitable $\lambda_2 < 1$ for sufficiently small τ. The rest of procedures analogously follow. □

Contraction mapping for sufficiently small τ: II. nonlinear system

Next, we generalize our results in previous section for the linear system to the nonlinear one. Specifically, we analogously construct a solution map to show the convergence of the solution of the nonlinear system (4.1) to its steady-state solution for a sufficiently small delay.

Let us restate the nonlinear problem for $C(x,t)$

$$C_t + F(C(1,t-\tau))C_x = -K(C), \quad x \in (0,1),\ t > 0 \tag{4.28a}$$

$$C(0,t) = m, \quad t \geqslant 0, \tag{4.28b}$$

$$C(x,0) = \psi(x), \quad x \in [0,1], \tag{4.28c}$$

$$C(1,t) = \phi(t+\tau), \quad t \in [-\tau, 0]. \tag{4.28d}$$

where F and K are Lipschitz continuous and $K(u) > 0$ for all positive u with $K(0) = 0$. Given $(\psi, \phi) \in \mathcal{C}([0,1]) \times \mathcal{C}([0,\tau]) = \mathcal{X}$, let $C(x,t;\psi,\phi)$ denote the

well-defined solution for $t > 0$. For $t \in [0, \tau]$, it follows that $C(x, t; \psi, \phi)$ solves

$$C_t + F(\phi(t))C_x = -K(C), \quad x \in (0, 1), \ t > 0 \tag{4.29a}$$

$$C(0, t) = m, \quad t \geqslant 0, \tag{4.29b}$$

$$C(x, 0) = \psi(x), \quad x \in [0, 1]. \tag{4.29c}$$

As we defined a map M in the linearized system, we can similarly construct a new map N for the solution of (4.28).

Definition 9. A map $N : \mathcal{X} \to \mathcal{X}$ is defined by

$$N(\psi, \phi) = (\Psi, \Phi)$$

where

$$\Psi(x) = C(x, \tau; \psi, \phi), \quad \text{for } x \in [0, 1],$$

$$\Phi(t) = C(1, t; \psi, \phi), \quad \text{for } t \in [0, \tau].$$

Theorem 10. *Let $u_{ss}(x)$ be the steady-state solution of (4.28) and τ be sufficiently small. If an initial condition $\psi(x)$ satisfies $||\psi - u_{ss}||_\infty \leqslant k < \infty$, the solution advanced by a map N in Definition 9 exponentially converges to $u_{ss}(x)$ at the rate of $\lambda > 0$, i.e.,*

$$||u(\cdot, t) - u_{ss}(\cdot)||_\infty \leqslant ||\psi - u_{ss}||_\infty e^{-\lambda t}, \tag{4.30}$$

where λ depends on k.

Proof. Let u be the solution of the nonlinear problem (4.28) with $f_1 = (\psi_1, \phi_1)$ and v denote u_{ss} with $f_2 = (\psi_2, \phi_2) = (u_{ss}, C_{\text{op}})$. Then for $t \in [0, \tau]$, u and v solve

$$u_t + F(\phi_1)u_x = -K(u),$$

$$F(\phi_2)v_x = -K(v),$$

respectively. Subtracting the second equation from the first one, we obtain

$$h_t + F_1 h_x + (F_1 - F_2)v_x = -(K(u) - K(v)), \tag{4.31}$$

where $h = u - v, F_1 = F(\phi_1)$, and $F_2 = F(\phi_2)$. From the Fundamental Theorem of Calculus, we can rewrite the right-hand side of Eq. (4.31) as

$$\begin{aligned} -(K(u) - K(v)) &= -\int_0^1 \frac{d}{dr} K(ru + (1-r)v)\, dr \\ &= -\left(\int_0^1 \left. \frac{dK}{du} \right|_{u=\pi(r)} dr \right) (u - v) \\ &= -I(x,t)(u - v), \end{aligned} \tag{4.32}$$

where $\pi(r) = ru + (1-r)v$ for $r \in [0,1]$ and $I(x,t)$ corresponds to an integral with a derivative of K with respect to u as an integrand.

Substituting the expression (4.32) into (4.31) and using the method of characteristics to the resulting equation yield the following system of ODEs for $Z(t) = h(X(t),t),\ t \in [0,\tau]$

$$\begin{aligned} &X'(t) = F_1(t), \quad X(0) = x_0, \\ &T'(t) = 1, \qquad T(0) = 0, \\ &Z'(t) = (F_2 - F_1)v_x - I(X(t),t)Z(t), \quad Z(0) = \psi(x_0), \end{aligned} \tag{4.33}$$

where $\psi = \psi_1 - \psi_2$. Solving the first two ODEs gives $T(t) = t$ and $X(t) = x_0 + \int_0^t F_1(s)\, ds$. Also, because of the Lipschitz continuity of function F, there exists $C_1 > 0$ such that

$$|(F_2 - F_1)v_x| = |(F(\phi_1) - F(\phi_2))v_x| \leqslant C_1 ||\phi||_\infty ||v_x||_\infty, \tag{4.34}$$

where $\phi = \phi_1 - \phi_2$. Here we have used the fact that a continuous function (i.e., v_x) on a compact support is bounded. Substituting the inequality (4.34) into (4.33) yields the following differential inequality for $Z(t)$

$$-C||\phi||_\infty - I(X(t),t)Z(t) \leqslant Z'(t) \leqslant C||\phi||_\infty - I(X(t),t)Z(t), \quad Z(0) = \psi(x_0), \tag{4.35}$$

where $C = C_1 ||v_x||_\infty$. By multiplying an integrating factor

$$\mu(t) = \exp\left(-\int_0^t I(X(y),y)\, dy \right)$$

and applying Gronwall's inequality, we obtain

$$\psi(x_0)\exp\left(-\int_0^t I(X(s),s)\,ds\right) - C||\phi||_\infty \int_0^t \exp\left(-\int_s^t I(X(y),y)\,dy\right)\,ds$$

$$\leqslant Z(t) \leqslant \psi(x_0)\exp\left(-\int_0^t I(X(s),s)\,ds\right) + C||\phi||_\infty \int_0^t \exp\left(-\int_s^t I(X(y),y)\,dy\right)\,ds, \tag{4.36}$$

Given (x,t), we want to find x_0 such that $X(t) = x$, and $X(s;x,t)$ such that $X(0;x,t) = x_0(x,t)$.

$$x = X(t) = x_0 + \int_0^t F_1(y)\,dy \quad \Rightarrow \quad x_0(x,t) = x - \int_0^t F_1(y)\,dy,$$

$$X(s;x,t) = x_0(x,t) + \int_0^s F_1(y)\,dy = x + \int_t^s F_1(y)\,dy.$$

Finally, we find the following inequality for $h(x,t)$

$$h_h(x,t) - h_I(x,t) \leqslant h(x,t) \leqslant h_h(x,t) + h_I(x,t), \tag{4.37}$$

where

$$h_h(x,t) = \psi\left(x - \int_0^t F_1(y)\,dy\right)\exp\left(-\int_0^t I(x + \int_t^s F_1(y)\,dy, s)\,ds\right),$$

$$h_I(x,t) = C||\phi||_\infty \int_0^t \exp\left(-\int_s^t I(x + \int_t^s F_1(z)\,dz, y)\,dy\right)\,ds.$$

Plugging $x = 1$ and $t = \tau$, separately, into (4.37) yield

$$h_h(1,t) - h_I(1,t) \leqslant \Phi(t) = h(1,t) \leqslant h_h(1,t) + h_I(1,t), \tag{4.38}$$

$$h_h(x,\tau) - h_I(x,\tau) \leqslant \Psi(x) = h(x,\tau) \leqslant h_h(x,\tau) + h_I(x,\tau), \tag{4.39}$$

respectively, where $\Phi(t) = \Phi_1(t) - \Phi_2(t)$ and $\Psi(x) = \Psi_1(x) - \Psi_2(x)$ defined in Definition 9.

Using the expressions in (4.38)–(4.39), let us show (4.30) for sufficiently small τ. Recall that the function I is defined as

$$I(x,t) = \int_0^1 \left.\frac{dK}{du}\right|_{u=ru+(1-r)v} dr. \tag{4.40}$$

It is easy to check that the function $K(u)(= \frac{V_{\max} u}{K_M + u})$ is differentiable with respect to u. Moreover, for $0 \leqslant r \leqslant 1$,

$$\begin{aligned} ru + (1-r)v = r(u-v) + v &\leqslant r||u-v||_\infty + ||v||_\infty \\ &\leqslant r||\psi - v||_\infty + ||v||_\infty \leqslant k + k_1, \end{aligned}$$

where $||v||_\infty = ||u_{ss}||_\infty = k_1$. Applying this inequality to (4.40) implies that there exists some $\tilde{k} > 0$ such that

$$I \geqslant \min_{0 \leqslant w \leqslant k + k_1} \left. \frac{dK}{du} \right|_{u=w} = \frac{a}{(b + k + k_1)^2} \equiv \tilde{k}, \tag{4.41}$$

with $a = V_{\max} K_M$ and $b = K_M$. Substituting the lower bound on I into (4.38)–(4.39) gives

$$\begin{aligned} ||\Phi||_\infty = \sup_{0 \leqslant t \leqslant \tau} |\Phi(t)| &\leqslant ||h_h(1,t)||_\infty + ||h_I(1,t)||_\infty \\ &\leqslant ||\psi||_\infty + C||\phi||_\infty \sup_{0 \leqslant t \leqslant \tau} \left| \int_0^t \exp\left(\tilde{k}(s-t)\right) ds \right| \\ &= ||\psi||_\infty + \frac{C}{\tilde{k}} ||\phi||_\infty \sup_{0 \leqslant t \leqslant \tau} (1 - \mathrm{e}^{-\tilde{k}t}) \\ &\leqslant ||\psi||_\infty + \lambda_1 ||\phi||_\infty. \end{aligned} \tag{4.42}$$

If τ is sufficiently small so that $(1 - \mathrm{e}^{-\tilde{k}\tau}) \ll 1$, it follows that $\lambda_1 < 1$. Similarly, there exist $\lambda_2,\ \lambda_3 < 1$ such that

$$||\Psi||_\infty = \sup_{0 \leqslant x \leqslant 1} |\Psi(x)| \leqslant \lambda_2 ||\psi||_\infty + \lambda_3 ||\phi||_\infty. \tag{4.43}$$

Applying the inequalities in (4.42)–(4.43), we obtain

$$\begin{aligned} ||N_\tau(f_1) - N_\tau(f_2)||_{\mathcal{X}} = ||(\Psi_1, \Phi_1) - (\Psi_2, \Phi_2)||_{\mathcal{X}} &= ||\Psi||_\infty + ||\Phi||_\infty \\ &\leqslant (1 + \lambda_2)||\psi||_\infty + (\lambda_1 + \lambda_3)||\phi||_\infty. \end{aligned}$$

Because of $1 + \lambda_2 > 1$, we cannot find a suitable constant $\lambda < 1$ to satisfy (4.30).

However, if we apply N_τ again to both $N_\tau(f_1)$ and $N_\tau(f_2)$, respectively, it follows

$$\begin{aligned}
||N_\tau^2(f_1) - N_\tau^2(f_2)||_{\mathcal{X}} &= ||N_\tau(\Psi_1, \Phi_1) - N_\tau(\Psi_1, \Phi_1)||_{\mathcal{X}} \\
&\leqslant (1+\lambda_2)||\Psi_1 - \Psi_2||_\infty + (\lambda_1+\lambda_3)||\Phi_1 - \Phi_2||_\infty \\
&\leqslant (1+\lambda_2)(\lambda_2||\psi||_\infty + \lambda_3||\phi||_\infty) + (\lambda_1+\lambda_3)(||\psi||_\infty + \lambda_1||\phi||_\infty) \\
&= \tilde{\lambda}||\psi||_\infty + \hat{\lambda}||\phi||_\infty \\
&\leqslant \lambda||(\psi,\phi)||_{\mathcal{X}} = \lambda||f_1 - f_2||_{\mathcal{X}},
\end{aligned}$$

where $\lambda = \max(\tilde{\lambda}, \hat{\lambda})$ with

$$\tilde{\lambda} = (1+\lambda_2)\lambda_2 + (\lambda_1+\lambda_3), \quad \hat{\lambda} = (1+\lambda_2)\lambda_3 + (\lambda_1+\lambda_3)\lambda_1, \tag{4.44}$$

$$\lambda_1 = \lambda_3 = \frac{C}{\tilde{k}}(1 - e^{-\tilde{k}\tau}), \quad \lambda_2 = e^{-\tilde{k}\tau},$$

for $\tilde{k}$ in (4.41) and some $C > 0$. This inequality implies that if we choose τ small enough such that $\tilde{\lambda}, \hat{\lambda} < 1$, the distance between u and v exponentially converges to zero at the rate of λ that depends on k, i.e., (4.30) holds. Therefore, the steady-state solution for the nonlinear problem (4.28) is asymptotically stable. □

4.2 Stochastic System

4.2.1 Stationary solution for sufficiently small τ

In this section, we show the existence and uniqueness of an analogous version of the steady-state solution for random dynamical system with sufficiently small τ, as shown in Section 4.1 for the deterministic system. In particular, we are interested in the system perturbed via stochastic boundary conditions and its stability dependent on τ.

Let us consider the following nonlinear stochastic system for $C(x,t)$ with a

stochastic process $Y(t)$,

$$C_t + F(C(1,t-\tau))C_x = -K(C), \quad x \in (0,1),\ t > 0 \tag{4.45a}$$

$$C(0,t) = Y(t), \quad t \geqslant 0, \tag{4.45b}$$

$$C(x,0) = \psi(x), \quad x \in [0,1], \tag{4.45c}$$

$$C(1,t) = \phi(t+\tau), \quad t \in [-\tau, 0]. \tag{4.45d}$$

Here we assume that $Y(t)$ is a stationary stochastic process with constant mean $m > 0$ in (4.28b) and it is continuous in t. Also, for any $T < \infty$,

$$\mathbb{E}(\sup_{0 \leqslant t \leqslant T} |Y(t)|) < \infty, \quad \mathbb{E}(Y(0)) = m. \tag{4.46}$$

This stochastic boundary condition represents the noise entering the bounded domain through its left-hand side.

For a given $(\psi, \phi) \in \mathcal{X}$, the solution $C(\cdot, t; \psi, \phi)$, well-defined for all $t > 0$, is a stochastic process on the probability space $(\Omega, \mathcal{F}, \mathbb{P})$. For $t \in [0, \tau]$, it follows that $C(x, t; \psi, \phi)$ solves

$$C_t + F(\phi(t))C_x = -K(C), \quad x \in (0,1),\ t > 0 \tag{4.47a}$$

$$C(0,t) = Y(t), \quad t \geqslant 0, \tag{4.47b}$$

$$C(x,0) = \psi(x), \quad x \in [0,1]. \tag{4.47c}$$

Before we begin to analyze the system, we give the definitions of stochastic process and statistically stationary process.

Definition 11. Let $(\Omega, \mathcal{F}, \mathbb{P})$ be a probability space, $\mathcal{B}$ be a separable Banach space, and $I \subset \mathbb{R}$ be an interval (possibly infinite). A $\mathcal{B}$-valued stochastic process $\{U(t)\}_{t \in I}$ is a set of $\mathcal{B}$-valued random variables $U(t)$ on $(\Omega, \mathcal{F}, \mathbb{P})$ where $t \in I$.

Definition 12. A stochastic process $U(t)$ is a called *(statistically) stationary* if $\{U(t)\}$ has the same distribution as $\{U(t+h)\}$ for any $h > 0$ and the joint distributions of $\{U(t_1 + h), U(t_2 + h), \ldots, U(t_n + h)\}$ with $t_1 < t_2 < \ldots < t_n$ are same for all $h > 0$.

A special case which will be of our interest is the case where the probability space is taken to be $\Omega = \mathcal{C}([0,T],\mathcal{B})$ for $\mathcal{B} = \mathcal{C}([0,1])$ and $T > 0$ with a probability measure $\mathbb{P}$ and where the process U is given by

$$U(t)(\omega) = \omega(t), \quad \omega \in \Omega.$$

In this case, U is called the *canonical process* on Ω (Hairer (2009); van Zanten (2013)). Now we prove the existence and uniqueness of the stationary solution for (4.45) when τ is sufficiently small.

Theorem 13. *For sufficiently small τ, the nonlinear stochastic problem (4.45) admits a statistically stationary solution.*

Proof. **STEP I.**

The system is non-autonomous owing to the noise $Y(t)$ at the boundary. To prove the existence of an "attractor" for random dynamical system, we use pullback attractor method. Let us define a sequence of time $t_n = -n$ and its corresponding solution $C^n(\cdot,t)$ that satisfies (4.45a) for $t \geqslant t_n$ with initial and boundary conditions

$$C^n(0,t) = Y(t), \quad t \geqslant t_n, \tag{4.48}$$

$$C^n(x,t_n) = \psi^n(x), \quad x \in [0,1] \tag{4.49}$$

$$C^n(1,t) = \phi^n(t - t_n + \tau), \quad t \in [t_n - \tau, t_n] \tag{4.50}$$

Note that we define the solution not from $t = 0$, but from the past time at $t = t_n$. Given the sequence $\{C^n(\cdot,t)\}_{n\in\mathbb{N}}$ of continuous functions on an interval $[0,1]$ for $t \geqslant t_n$, we will show, for each $\omega \in \Omega$, this is a Cauchy sequence in a Banach space $\mathcal{H} = \mathcal{C}([0,1]\times[0,T])$ for $0 < T < \infty$, which ensures the existence of a convergent limit $\bar{U}(\omega)$ in $\mathcal{H}$.

To show that $\{C^n(\cdot,t)\}_{n\in\mathbb{N}}$ is a Cauchy sequence, let us consider the difference between two solutions, $V(\cdot,t) = C^n(\cdot,t;\psi^n,\phi^n) - C^m(\cdot,t;\psi^m,\phi^m)$ for $t \geqslant \min(t_n,t_m)$. Because the system is nonlinear, given $(\psi,\phi)=(\psi^n-\psi^m,\phi^n-\phi^m)$ V solves

$$V_t + F_n V_x + (F_n - F_m)C^m_x = -(K(C^n) - K(C^m)),$$

where $F_n = F(C^n)$ and $F_m = F(C^m)$ with almost zero-boundary condition at $x = 0$, specifically,

$$V(0,t) = \begin{cases} 0, & \text{for } t \geqslant \max(t_n, t_m) \\ Y(t), & \text{for } \min(t_n, t_m) \leqslant t < \max(t_n, t_m) \end{cases}$$

This indicates the system for V becomes autonomous after a short time period.

STEP II.

Recall that we defined a linear map N^2 in Definition 9 and showed the convergence of the solution for the nonlinear system to its steady state for sufficiently small τ, using the contraction mapping argument. Specifically,

$$||C_1(\cdot,t) - C_2(\cdot,t)||_{\mathcal{C}([0,1])} = \sup_{x\in[0,1]} |C_1(x,t) - C_2(x,t)| \to 0 \quad \text{as } t \to \infty,$$

where C_1 and C_2 are two different solutions for Eq. (4.28) with the convergence rate $\lambda < 1$. In other words, for any given $\epsilon > 0$, there exist $T_\epsilon < \infty$ such that

$$||C_1(\cdot,t) - C_2(\cdot,t)||_{\mathcal{C}([0,1])} < \epsilon, \quad \text{for } t \geqslant T_\epsilon,$$

indicating the difference of two solutions becomes negligibly small after sufficiently long time $T > 0$.

To apply this property to the solution V, we similarly consider a map for the nonlinear stochastic system to advance V in time, given the pair of functions $(\psi^n - \psi^m, \phi^n - \phi^m) \in \mathcal{X}$. However, the system is non-autonomous for $\min(t_n, t_m) \leqslant t < \max(t_n, t_m)$ due to the random boundary condition over that period. Thus, we need to consider two separate ranges of time: $\min(t_n, t_m) \leqslant t < \max(t_n, t_m)$ and $t \geqslant \max(t_n, t_m)$. Without loss of generality, let $n = m + 1$ so that $t_n \leqslant t_m$. Then, $V(\cdot,t) = C^n(\cdot,t;\psi^n,\phi^n)$ solves (4.45a) for $t_n \leqslant t \leqslant t_m$ subject to the boundary condition $Y(t)$. That is,

$$V_t + F_n V_x = -K(V) = -I(x,t)V,$$

where

$$I(x,t) = \int_0^1 \left.\frac{dK}{du}\right|_{u=rV} dr.$$

Using the method of characteristics to the above PDE for V yields the following system of ODEs for $Z(t) = V(X(t),t))$,

$$\begin{aligned} X'(t) &= F_n(t), \quad X(0) = x_0, \\ T'(t) &= 1, \qquad T(0) = t_n, \\ Z'(t) &= -I(X(t),t)Z(t), \quad Z(0) = \psi^n(x_0). \end{aligned} \tag{4.51}$$

Solving the first two ODEs gives $T(t) = t_n + t$ and $X(t) = x_0 + \int_{t_n}^t F_n(s)\,ds$. Solving for Z with the initial condition in (4.51), we obtain

$$Z(t) = \psi^n(x_0) \exp\left(-\int_{t_n}^t I(X(s),s)\,ds\right).$$

Given (x,t), we want to find x_0 such that $X(t) = x$, and $X(s;x,t)$ such that $X(0;x,t) = x_0(x,t)$.

$$x = X(t) = x_0 + \int_{t_n}^t F_n(y)\,dy \quad \Rightarrow \quad x_0(x,t) = x - \int_{t_n}^t F_n(y)\,dy,$$

$$X(s;x,t) = x_0(x,t) + \int_{t_n}^s F_n(y)\,dy = x - \int_s^t F_n(y)\,dy.$$

Finally, we find $V(x,t)$

$$V(x,t) = \psi^n\left(x - \int_{t_n}^t F_n(y)\,dy\right) \exp\left(-\int_{t_n}^t I\left(x - \int_s^t F_n(y)\,dy, s\right)\,ds\right). \tag{4.52}$$

At $t = t_m$, $\psi^n\left(x - \int_{t_n}^{t_m} F_n(y)\,dy\right)$ is well-defined for $\int_{t_n}^{t_m} F_n(y)\,dy < x \leqslant 1$. The solution becomes

$$V(x,t_m) = \psi^n\left(x - \int_{t_n}^{t_m} F_n(y)\,dy\right) \exp\left(-\int_{t_n}^{t_m} I\left(x - \int_s^{t_m} F_n(y)\,dy, s\right)\,ds\right). \tag{4.53}$$

On the other hand, if $0 \leqslant x \leqslant \int_{t_n}^{t_m} F_n(y)\,dy$, the characteristic lines meet the left-hand boundary where the value is $Y(t)$. Then, it follows that

$$V(x,t_m) = Y\left(t_m - t^*\right) \exp\left(-\int_{t_n}^{t_m} I\left(x - \int_s^{t_m} F_n(y)\,dy, s\right)\,ds\right), \tag{4.54}$$

where t^* satisfies $x = \int_{t_n}^{t^*} F_n(y)\,dy$. If $||\psi^n||_\infty = k$, then we can find some $\tilde{k} > 0$ that depends on k such that

$$\tilde{k} \leqslant I.$$

It implies that there exists $\lambda(k) < 1$, as similarly found in (4.44) for the deterministic system, such that

$$||V(\cdot,t_m)||_{\mathcal{C}([0,1])} \leqslant \lambda(k) \max(||Y||_{\mathcal{C}([t_n,t_m])}, k). \tag{4.55}$$

Given $V(\cdot,t_m)$ as an initial condition, we can advance V in time by constructing a suitable map as in the deterministic system (see Definition 9) with zero boundaries, but the stochastic boundary condition $Y(t)$ could be arbitrarily large for $t_n \leqslant t < t_m$. Thus, depending on how large $||Y||_{\mathcal{C}([t_n,t_m])}$ is, the number of steps, which is necessary to apply the map to make the solution small, is random.

STEP III.

Let us define a random variable $||Y||_{\mathcal{C}([t_n,t_m])} = Y_n$ while keeping the condition $n = m+1$. Also, let us define a map $\bar{N}$ similarly as in Definition 9 and the solution $(\bar{\psi}_i, \bar{\phi}_i)$ generated by the ith iteration of $\bar{N}$ be

$$(\bar{\psi}_i, \bar{\phi}_i) = \bar{N}^i(\bar{\psi}_0, \bar{\phi}_0), \tag{4.56}$$

where

$$\bar{\psi}_0(x) = V(x,t_m), \quad \text{for } x \in [0,1],$$
$$\bar{\phi}_0(t) = V(1,t), \qquad \text{for } t \in [t_n,t_m].$$

Applying similar argument given in Theorem 10, we can show that, for sufficiently small τ,

$$||\bar{\psi}_i||_\infty \leqslant ||\bar{\psi}_0||_\infty e^{-\frac{ci}{(1+||\bar{\psi}_0||_\infty)^2}}. \tag{4.57}$$

with a suitable constant $c > 0$. Let $\epsilon > 0$ be arbitrarily given. Then, we have

$$\mathbb{P}(A_i(\epsilon)) = \mathbb{P}(||\bar{\psi}_i||_\infty > \epsilon) \leqslant \mathbb{P}\left(||\bar{\psi}_0||_\infty e^{-\frac{ci}{(1+||\bar{\psi}_0||_\infty)^2}} > \epsilon\right). \tag{4.58}$$

By Markov's inequality, (4.58) implies

$$\begin{aligned}
\mathbb{P}(A_i(\epsilon)) &\leqslant \epsilon^{-1}\mathbb{E}\left(||\bar{\psi}_0||e^{-\frac{ci}{(1+||\bar{\psi}_0||)^2}}\right) \\
&= \epsilon^{-1}\mathbb{E}\left(||\bar{\psi}_0||e^{-\frac{ci}{(1+||\bar{\psi}_0||)^2}}\left(\mathbb{1}_{(||\bar{\psi}_0||<1)} + \mathbb{1}_{(||\bar{\psi}_0||>1)}\right)\right) \\
&\leqslant \epsilon^{-1}\left(\mathbb{E}(||\bar{\psi}_0||)e^{-\bar{c}i} + \mathbb{E}\left(||\bar{\psi}_0||e^{-\frac{\bar{c}i}{||\bar{\psi}_0||^2}}\right)\right),
\end{aligned}$$

where $\bar{c} = c/4$. Also, using Cauchy-Schwarz inequality,

$$\begin{aligned}
\mathbb{E}\left(||\bar{\psi}_0||e^{-\frac{\bar{c}i}{||\bar{\psi}_0||^2}}\right) &= \mathbb{E}\left(||\bar{\psi}_0||e^{-\frac{\bar{c}i}{||\bar{\psi}_0||)^2}}\left(\mathbb{1}_{(||\bar{\psi}_0||^2<\sqrt{i})} + \mathbb{1}_{(||\bar{\psi}_0||^2>\sqrt{i})}\right)\right) \\
&\leqslant \left(\mathbb{E}(||\bar{\psi}_0||)e^{-\bar{c}\sqrt{i}} + \mathbb{E}\left(||\bar{\psi}_0||e^{-\frac{\bar{c}i}{||\bar{\psi}_0||^2}}\mathbb{1}_{(||\bar{\psi}_0||^2>\sqrt{i})}\right)\right) \\
&\leqslant \left(\mathbb{E}(||\bar{\psi}_0||)e^{-\bar{c}\sqrt{i}} + \sqrt{\mathbb{E}(||\bar{\psi}_0||^2))}\sqrt{\mathbb{P}(||\bar{\psi}_0||^2 > \sqrt{i})}\right) \\
&\leqslant \left(\mathbb{E}(||\bar{\psi}_0||)e^{-\bar{c}\sqrt{i}} + \sqrt{\mathbb{E}(||\bar{\psi}_0||^2)}e^{-\frac{\tilde{c}\sqrt{i}}{2}}\right),
\end{aligned}$$

where some $\tilde{c} > 0$ assuming that Y_n has the normal distribution. Moreover, since Y_n has a bounded mean in (4.46), we finally obtain

$$\mathbb{P}(A_i(\epsilon)) \leqslant \epsilon^{-1}\left(\mu\left(e^{-\bar{c}i} + e^{-\bar{c}\sqrt{i}}\right) + \mu_1 e^{-\frac{\tilde{c}i}{2}}\right), \tag{4.59}$$

with some $\mu_1 > 0$. Applying the Borel-Cantelli Lemma to (4.59), we can show that

$$\sum_{i=1}^{\infty}\mathbb{P}(A_i) < \infty \quad \Rightarrow \quad ||\bar{\psi}_i||_\infty \to 0 \text{ a.s.}$$

This implies that for sufficiently small τ, if we take the limit as $n, m \to \infty$, the difference of $C^n - C^m$ after sufficiently long time, i.e., for $t \geqslant 0$, becomes small

$$\lim_{n,m\to\infty}\sup_{x\in[0,1]}|C^n(x,t) - C^m(x,t)| = 0 \text{ for all } t \geqslant 0,$$

almost surely. For each $\omega \in \Omega$, $\{C^n(\omega)\}_{n\in\mathbb{N}}$ is Cauchy in $\mathcal{H}$ and, thus, there exists a convergent limit $\bar{C}(\omega)$ in Banach space $\mathcal{H}$.

To show that $\bar{C}$ is a $\mathbb{P}$-measurable function, we note that $C^n(\cdot, t; \psi^n, \phi^n)$ is measurable on $[0, 1]$ for all t defined. Since the pointwise limit of a sequence of measurable functions is measurable, $\bar{C}$ is measurable function with respect to $\mathbb{P}$, i.e., the limit $\bar{C}$ is a random process on the probability space $(\Omega, \mathcal{F}, \mathbb{P})$. Finally, using the pullback attractor argument, we have the following equality

$$\bar{C}(t+h,\omega) = \lim_{n\to\infty} C^n(t+h,\omega) = \lim_{n\to\infty} C^{n+h}(t, \pi_{-h}\omega) = \bar{C}(t, \pi_{-h}\omega), \quad \text{for any } h > 0,$$

where π_{-h} is a suitably defined map on Ω and the second equality is from the stationary property of C^n. This equality implies that $\bar{C}$ is a stationary process from Definition 12. Thus, the problem (4.45a)–(4.45d) admits a stationary solution for sufficiently small τ. □

4.2.2 Numerical simulation

To supplement and support our analytic results, we numerically solve (4.45) for different values of τ. To impose the left-hand boundary condition $Y(t)$, we use a stationary Ornstein-Uhlenbeck process that satisfies the following stochastic differential equation (SDE)

$$dY(t) = \alpha(\mu - Y(t))dt + \sigma dW(t), \tag{4.60}$$

where α, μ, and σ are constants and $W(t)$ denotes a standard one-dimensional Brownian motion.

To show the convergence of the nonlinear system toward its stationary solution for sufficiently small τ and the emergence of oscillatory solutions for relatively large τ, we numerically computed (4.45a) given $(\psi, \phi) = (z(x) + 0.01, C_{\text{op}} - 0.01)$ in (4.45c)–(4.45d), where $z(x)$ is the steady-state solution in the deterministic system, which is

prescribed. Here, the two functions F and K in (4.45a) have the following form:

$$F(C) = 1 + K_1 \tanh(K_2(C_{\text{op}} - C)),$$

$$K(C) = \frac{V_{\max} C}{K_M + C},$$

where the nondimensional values of K_1, K_2, C_{op}, $V_{\max}$, and K_M were adapted from our TAL model. See Tables 2.1 and 2.2. Recall that the form of F was chosen from experimental data for TGF system (Layton et al. (1991)). Because of the positive drift term b, Eq. (4.45a) was advanced in time using upwind scheme. For the boundary condition $Y(t)$, SDE in (4.60) was solved using Gillespie algorithm developed by Gillespie (1996). Without the noise, i.e., $Y(t) = 0$, the value of τ_0 is ≈ 2.05. Based on this value, we first consider the case of delay $\tau = 0.15$ such that the system lies in the subcritical region for two different sets of coefficients in $Y(t)$: $(\mu, \alpha, \sigma) = (1, 5, 0.05)$ and $(\mu, \alpha, \sigma) = (1, 20, 0.5)$. Both a trajectory of $Y(t)$ and its corresponding solution $C(x, t)$ at $x = 1$, as functions of t, are given in Figs. 4.1 and 4.2, respectively.

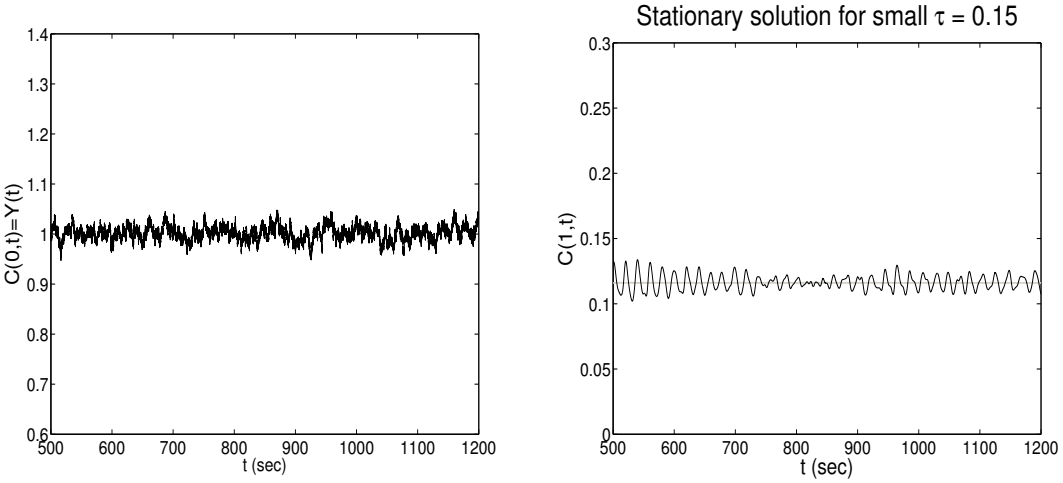

FIGURE 4.1: $C(0, t) = Y(t)$ with $\mu = 1, \alpha = 5, \sigma = 0.05$ (left) and corresponding solution $C(1, t)$ for $\tau = 0.15$ (right). The gray line corresponds to the steady-state solution in the deterministic system for comparison.

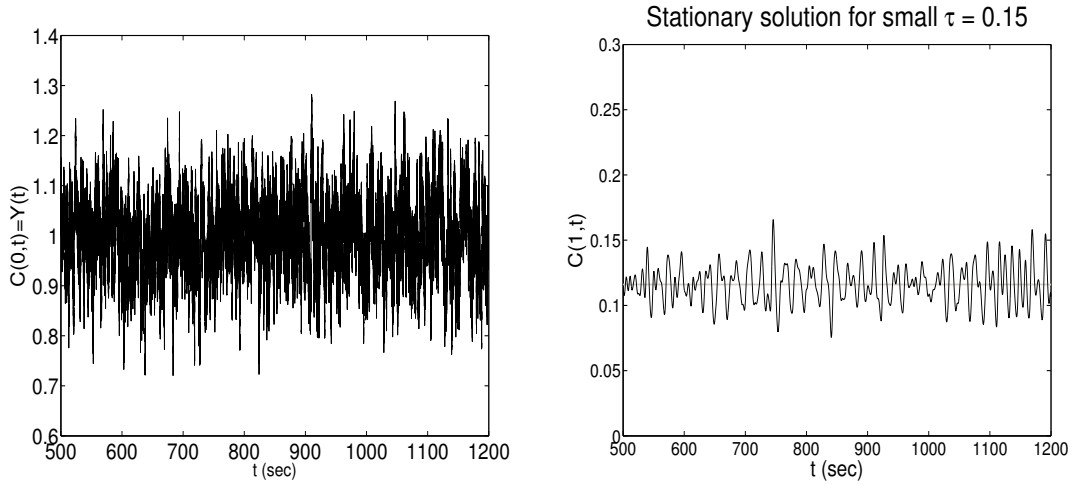

FIGURE 4.2: $C(0,t) = Y(t)$ with $\mu = 1, \alpha = 20, \sigma = 0.5$ (left) and corresponding solution $C(1,t)$ for $\tau = 0.15$ (right). The gray line corresponds to the steady-state solution in the deterministic system for comparison.

In the absence of noise, our analysis shows that there is a critical delay τ_0 such that the solution asymptotically converges to its steady state for $\tau < \tau_0$. The random solution, in the present of noise, also converges toward its stationary solution for sufficiently small τ. Fig. 4.1 supports our analytic results that (4.45) admits a stationary solution near $\sim$0.116 which corresponds to the steady-state value in the deterministic system. Even if we increase the value of σ to be 0.5 so that the amplitude of perturbations in $Y(t)$ becomes larger compared to that of the left panel in Fig. 4.1, the corresponding solution exhibits to have more variations from the steady state solution of the deterministic system, as illustrated in the right panel of Fig. 4.2.

We similarly computed time profiles for $Y(t)$ and $C(1,t)$ for large value of $\tau = 0.21$. Applying $Y(t)$ with $\sigma = 0.01$, the corresponding solution $C(1,t)$, as a function of t, is shown in Fig. 4.3. Compared to the solution corresponding to $\tau = 0.15$, plotted in gray line, the solution corresponding to $\tau = 0.21$ exhibits oscillatory behaviors with markedly increased amplitudes. Note that the range of $C(1,t)$ in all three Figures are set to be same to show a clear distinction between amplitudes of solutions for different τ and σ. Although the oscillations emerge as the delay is

increased, the solution exhibits regular behaviors, unlike the case of small delays, in that the amplitude as well as the period of oscillations are almost same in time. These regular behaviors can be explained by the delay in the system. Once τ passes through its critical value τ_0, the system enters the supercritical region so that the effect of delay may dominate the overall dynamics, as a result of the competition of the noise. If the increased effect of noise is further introduced to the system, the resulting dynamics may exhibit much more complex behaviors, which can help explain the irregular oscillations observed in experimental observation of the TGF system.

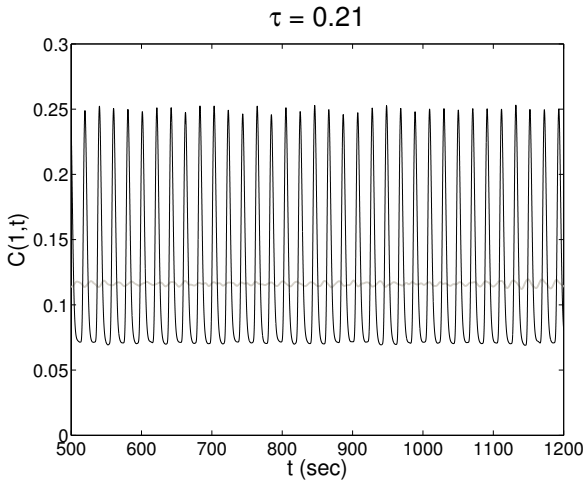

FIGURE 4.3: $C(1,t)$ with random left-hand boundary $Y(t)$ ($\mu = 1, \alpha = 5, \sigma = 0.01$) for relatively large value of $\tau = 0.21$. The gray line corresponds to the stationary solution for $\tau = 0.15$ with same left-hand boundary $Y(t)$ for comparison.

4.3 Multiscale Analysis

4.3.1 Introduction

In this section, we provide multiscale analysis to study the effect of noise in the stability of (linear) stochastic delayed PDE. We specifically consider the case where the delay is sufficiently close to the critical delay of the deterministic system and

the noise is small relative to the proximity of the delay to the critical delay, so that the overall dynamics are sensitive to the noise via an interaction with delays. For example, in the absence of noise so that the system becomes deterministic, the solution of (4.3) decays over time if the delay lies in the subcritical region. In contrast, when the noise is introduced to the system, oscillations can emerge and be sustained even in the subcritical region. To better understand how those oscillatory behaviors are generated as a result of the interaction between the noise and the delay, we apply well-known multiscale analysis to study the sensitivity of our time-delayed TGF system to the noise that represents various external perturbations.

A recent study by Kuske (2005); Klosek and Kuske (2005) introduced multiscale analysis for stochastic (ordinary) delay differential equations. The amplitude equations of oscillatory solutions near the critical delay of the deterministic system were derived, using asymptotic expansions and standard multiscale techniques, to capture the solution behaviors over long times. Although they considered the relatively simple equation to provide analytical results that can help better describe the stochastic dynamical system with delays, the applied mathematical tools could be productively used to study other types of stochastic delayed system. In this study, we aim to similarly apply multiscale analysis to a more complicated equation, a stochastic delayed PDE, which arises from our TGF model.

For analytic simplicity, we consider the linearized transport equation in Eq. (4.3) with additive noise

$$dU = -(bU_x + gU(1, t-\tau) + kU)dt + \delta dW_t, \tag{4.61}$$

where $U(x,t)$ denotes a random solution and W_t is a standard 1-dimensional Brownian motion. The Itô interpretation of Eq. (4.61) corresponds to the stochastic integral equation

$$U(x,t) = U(x,0) - \int_0^t bU_x(x,s) + gU(1,s-\tau) + kU(x,s)\,ds + \int_0^t \delta dW_s. \tag{4.62}$$

If the magnitude of δ is large enough, the effect of noise would dominate the overall dynamics, which makes it difficult to understand how the interaction of delays to noise affects the solution behaviors. For this reason, we consider the case when $\delta \ll 1$ in order to examine the sensitivity of the dynamics to small noise. Specifically, when $\delta = 0$, the problem (4.61) reduces to the deterministic linearized equation in Eq. (4.3a). If we look for a solution of the form

$$U(x,t) = e^{\lambda t} f(x), \tag{4.63}$$

we find the critical delay τ_0 such that for $\tau < \tau_0$, $\Re(\lambda) < 0$ and for $\tau > \tau_0$, $\Re(\lambda) > 0$. The resulting ODE for $f(x)$ was derived in Eq. (4.4). Let a be a natural frequency such that $\lambda = ia$ when $\tau = \tau_0$. Substituting $\lambda = ia$ and $\tau = \tau_0$ into Eq. (4.4) and collecting real and imaginary parts separately, we obtain

$$bf'(x) + k(x)f(x) + g(x)\cos(a\tau_0)f(1) = 0, \quad af(x) = g(x)\sin(a\tau_0)f(1). \tag{4.64}$$

To express the delay term τ in terms of the critical value τ_0, we use a small parameter ϵ such that $0 < \epsilon \ll 1$, which will be used as a measurement of proximity to the critical delay:

$$\tau = \tau_0 + \epsilon^2 \tau_1. \tag{4.65}$$

To facilitate asymptotic analysis, the coefficient τ_1 is assumed to be $O(1)$ constant, which we will set to be -1 in order for the system to be in subcritical region.

To illustrate the sensitivity of the delayed system to small noise, we numerically solved Eq. (4.61) with $\delta = .01$ for three different values of ϵ^2, the proximity of the critical delay, in (4.65): $\epsilon^2 = .01, .002, .0002$. Time profiles of the solution at $x = 1$, $U(1,t)$, are shown in Figure 4.4. In the absence of noise, our previous bifurcation analysis in Theorem 3 shows that there is a critical delay τ_0 such that oscillations decay for $\tau < \tau_0$ and grow for $\tau > \tau_0$. Here $\tau_0 \approx 0.205$. When the noise is introduced to the system, however, numerical simulations demonstrate that if $0 < \tau_0 - \tau \ll 1$,

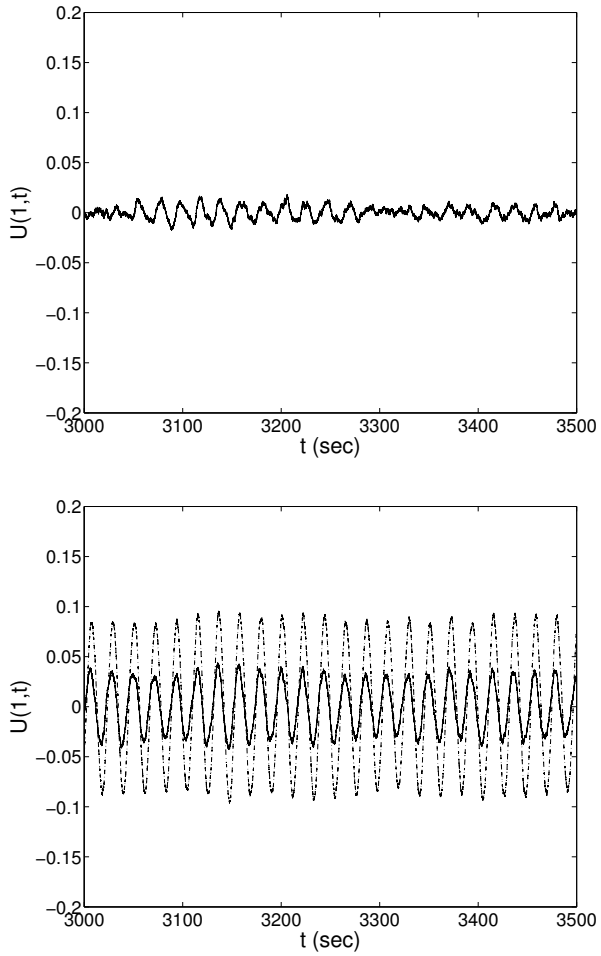

FIGURE 4.4: The numerical simulation of (4.61) for $\tau = \tau_0 - \epsilon^2$ and $\delta = .01$. In the top image, $\epsilon^2 = .01$. In the bottom image, the solid line is for $\epsilon^2 = .002$ and the dash-dotted line corresponds to $\epsilon^2 = .0002$. As ϵ decreases, the solution exhibits a more marked oscillatory behavior even though $\tau < \tau_0$.

the periodic behavior of solutions becomes amplified through the interaction of noise and delay. This effect is noticeably intensified as $\tau_0 - \tau = \epsilon^2$ decreases while keeping $\delta \ll 1$, as can be seen by comparing top image and bottom images in Fig. 4.4.

4.3.2 Main results

We employ the multiscale analysis to study the influence of the noise over a long time. Here we specifically provide a generalization of the previous work by Klosek

and Kuske (2005), in which SDE with additive noise was analyzed, to a case of SPDE with additive noise (Eq. (4.61)). We first assume that the oscillatory solutions can be written as a combination of two qualitatively different parts: fast-time deterministic dynamics and slow-time stochastic dynamics. Specifically, we look for a periodic solution with a stochastically varying amplitude on a slow-time scale T, which is treated as independent of a fast-time scale t. To prescribe the periodic modes, we use the natural frequency a for deterministic oscillatory solutions when $\tau = \tau_0$ (bifurcation point), as generally introduced in the multiscale approximation (Klosek and Kuske (2005)). Given all these assumptions and adapting the same variables used in the previous work (Klosek and Kuske (2005)), we now write the leading order approximation for the solution to (4.61)

$$U(x,t) \sim \hat{U}(x,t) = A(x,T)\cos at + B(x,T)\sin at, \quad T = \epsilon^2 t, \quad 0 < \epsilon \ll 1. \tag{4.66}$$

This form assumes that, below the critical delay but with noise, the leading order behavior of the solution can be described by two separate dynamics with different time scales: fast-time dynamics that correspond to the deterministic oscillations and slow-time dynamics that correspond to the effect of noise. The choice of slow time scale T is implied by solving Eq. (4.61) with (4.65); it results in an eigenvalue λ with $O(\epsilon^2)$ real part.

Our goal of this study is to derive the amplitude equations for $A(x,T)$ and $B(x,T)$ to efficiently describe the solution behaviors in a long time period instead of a direct computation of Eq. (4.61). Specifically, we assume that those equations have the following forms:

$$dA = \psi_A dT + \sigma_A d\xi_1(T), \tag{4.67}$$

$$dB = \psi_B dT + \sigma_B d\xi_2(T), \tag{4.68}$$

where $\xi_1(T)$ and $\xi_2(T)$ are independent Brownian motions, and the coefficients ψ_A, σ_A, ψ_B, and σ_B are unknown. To determine these coefficients in terms of $a, \tau_0, \tau_1, \epsilon$,

and σ to obtain the complete equations (4.67)–(4.68), we derive two expressions of dU in (4.61) by substituting $\hat{U}$ for U: the first expression is by applying Itô formula to (4.66) and the second is by direct substitution of (4.66) into (4.61).

For fixed x, Itô formula for U in (4.66) implies

$$dU = \left(\frac{\partial U}{\partial t}dt + \frac{\partial U}{\partial A}dA + \frac{\partial U}{\partial B}dB + \frac{\partial^2 U}{\partial A^2}(dA)^2 + \frac{\partial^2 U}{\partial B^2}(dB)^2 \right). \tag{4.69}$$

Because U is linear in both A and B, the second derivatives of U with respect to them, respectively, are zero. Substituting the expressions in (4.67)–(4.68) to this formula, we obtain

$$\begin{aligned} dU =& a(-A(x,T)\sin at + B(x,T)\cos at)dt + (\psi_A \cos at + \psi_B \sin at)dT \\ &+ \sigma_A \cos at d\xi_1(T) + \sigma_B \sin at d\xi_2(T). \end{aligned} \tag{4.70}$$

Second expression for dU is obtained by substitution of (4.66) into (4.61)

$$\begin{aligned} dU =& -\left[b\left(\frac{\partial A}{\partial x}\cos at + \frac{\partial B}{\partial x}\sin at \right) + g(x)(A(1, T-\epsilon^2\tau)\cos a(t-\tau) \right. \\ &\left. + B(1, T-\epsilon^2\tau)\sin a(t-\tau)) + k(x)(A(x,T)\cos at + B(x,T)\sin at) \right] dt + \delta dW(t). \end{aligned} \tag{4.71}$$

Given the above two expressions in (4.70)–(4.71) for dU, we equate them, collect the coefficients of same orders of ϵ, and find the solvability conditions for ψ_A, ψ_B, σ_A, and σ_B. To consider the case where the delayed system is sensitive to the noise, we restrict $\delta \ll 1$ (as well as $\epsilon \ll 1$) to apply an asymptotic expansion to the terms containing ϵ. First, using trigonometric identities we expand out the two terms, $\cos a(t-\tau)$ and $\sin a(t-\tau)$, in the right-hand side of (4.71),

$$\cos a(t-\tau) = \cos at \cos a\tau + \sin at \sin a\tau, \tag{4.72}$$

$$\sin a(t-\tau) = \sin at \cos a\tau - \cos at \sin a\tau. \tag{4.73}$$

Then, we use asymptotic expansions for $\cos a\tau$ and $\sin a\tau$ around τ_0 after substituting

(4.65) to obtain

$$\cos a\tau = \cos a(\tau_0 + \epsilon^2\tau_1) = \cos a\tau_0 - \epsilon^2 a\tau_1 \sin a\tau_0 + O(\epsilon^4), \tag{4.74}$$

$$\sin a\tau = \sin a(\tau_0 + \epsilon^2\tau_1) = \sin a\tau_0 + \epsilon^2 a\tau_1 \cos a\tau_0 + O(\epsilon^4). \tag{4.75}$$

Also, we have

$$A(1, T - \epsilon^2\tau) = A(1, T) + \epsilon^2 \frac{A(1, T - \epsilon^2\tau) - A(1, T)}{\epsilon^2} = A(1, T) + \epsilon^2 \Delta A(1, T), \tag{4.76}$$

$$B(1, T - \epsilon^2\tau) = B(1, T) + \epsilon^2 \frac{B(1, T - \epsilon^2\tau) - B(1, T)}{\epsilon^2} = B(1, T) + \epsilon^2 \Delta B(1, T), \tag{4.77}$$

where $\Delta A(1, T)$ and $\Delta B(1, T)$ will be treated as $O(1)$. To see this, let us write

$$A(x, T) = A(x, T - \epsilon^2\tau) + \int_{T-\epsilon^2\tau}^{T} \psi_A \, ds + \int_{T-\epsilon^2\tau}^{T} \sigma_A \, d\xi_1(s),$$

using the integral form of (4.67). The first integral on the right-hand side is $O(\epsilon^2)$. To bound the variance of the second integral, we use the property of Itô integral

$$\text{var}\left(\int_{T-\epsilon^2\tau}^{T} \sigma_A \, d\xi_1(s)\right) \leqslant \int_{T-\epsilon^2\tau}^{T} \sigma_A^2 \, ds = O(\epsilon^2) \cdot O(\sigma_A^2).$$

Given these upper bounds, it follows that $\Delta A(1, T)$ is asymptotically $O(1)$. The same argument can be used to show $\Delta B(1, T) \sim O(1)$.

Plugging all expansions (4.72)–(4.75) and expressions (4.76)–(4.77) into the right-hand side of (4.71), equating the resulting expression with the right-hand side of (4.70), and collecting the coefficients of $O(1)$ terms with respect to ϵ, we obtain

$$\begin{aligned} O(1): \quad & -aA(x, T)\sin at + aB(x, T)\cos at \\ & = -b\left(\frac{\partial A(x, T)}{\partial x}\cos at + \frac{\partial B(x, T)}{\partial x}\sin at\right) \\ & - g(x)(A(1, T)(\cos at \cos a\tau_0 + \sin at \sin a\tau_0) \\ & + B(1, T)(\sin at \cos a\tau_0 - \cos at \sin a\tau_0)) \\ & - k(x)(A(x, T)\cos at + B(x, T)\sin at). \end{aligned} \tag{4.78}$$

Collecting the coefficients of $\cos at$ and $\sin at$, respectively, we have the following two equations:

$$aB(x,T) = -b\frac{\partial A(x,T)}{\partial x} - g(x)(A(1,T)\cos a\tau_0 - B(1,T)\sin a\tau_0) - k(x)A(x,T)$$

$$= -\left(b\frac{\partial A(x,T)}{\partial x} + g(x)\cos a\tau_0 A(1,T) + k(x)A(x,T)\right) + g(x)B(1,T)\sin a\tau_0,$$

$$aA(x,T) = b\frac{\partial B(x,T)}{\partial x} + g(x)(A(1,T)\sin a\tau_0 + B(1,T)\cos a\tau_0) + k(x)B(x,T)f(x)$$

$$= b\frac{\partial B(x,T)}{\partial x} + g(x)\cos a\tau_0 B(1,T) + k(x)B(x,T) + g(x)A(1,T)\sin a\tau_0.$$

Using Eq. (4.64), we conclude that both equalities for $\cos at$ and $\sin at$ hold so that $O(1)$ terms in (4.78) cancel.

Next, we collect next higher $O(\epsilon^2)$ terms

$$(\psi_A\cos at + \psi_B\sin at)dT + \sigma_A\cos at d\xi_1(T) + \sigma_B\sin at d\xi_2(T)$$

$$= g(x)\{\Delta A(1,T)(\cos at\cos a\tau_0 + \sin at\sin a\tau_0)$$

$$+ \Delta B(1,T)(\sin at\cos a\tau_0 - \cos at\sin a\tau_0)$$

$$+ a\tau_1 A(1,T)(-\cos at\sin a\tau_0 + \sin at\cos a\tau_0)$$

$$+ a\tau_1 B(1,T)(-\sin at\sin a\tau_0 + \cos at\cos a\tau_0)\}dT + O(\epsilon^4) + \delta dW(t). \tag{4.79}$$

Here $\epsilon^2 dt = dT$ has been substituted. If we ignore the higher order terms to have only $O(\epsilon^2)$, we obtain the equations for drift and diffusion coefficients ψ_A, ψ_B, σ_A, and σ_B, in the equations for $A(x,T)$ and $B(x,T)$. First, if we only collect the drift terms in (4.79) and use Eq. (4.64) again, we then obtain

$$\psi_A\cos at + \psi_B\sin at \tag{4.80}$$

$$= [-a^2\tau_1(A(x,T) + B(x,T)\cot a\tau_0) + a\Delta A(x,T)\cot a\tau_0 - a\Delta B(x,T)]\cos at$$

$$+ [a^2\tau_1(A(x,T)\cot a\tau_0 - B(x,T)) + a\Delta A(x,T) + a\Delta B(x,T)\cot a\tau_0]\sin at.$$

To determine ψ_A and ψ_B, we use the projection onto resonant modes of deterministic oscillations, i.e., $\cos at$ and $\sin at$, as similarly used in the previous analysis (Klosek

and Kuske (2005)). While treating the functions of T as independent of t, we multiply both sides in (4.80) by $\cos at$ and take the integrals over one period of that periodic mode with respect to a fast-time scale t, i.e., $2\pi/a$,

$$\int_0^{2\pi/a} \cos at[\psi_A \cos at + \psi_B \sin at]dt = \int_0^{2\pi/a} \cos at \cdot (*)dt, \tag{4.81}$$

where $(*)$ corresponds to the right-hand side of (4.80). Due to the orthogonality of $\cos at$ and $\sin at$ in $L^2([0, 2\pi/a])$, computing the above integral yields the condition for ψ_A in (4.67). Similarly, we obtain the condition for ψ_B in (4.68) by applying $\sin at$ instead. The expression of drift terms, ψ_A and ψ_B, are given by

$$\psi_A(x,T) = -a^2\tau_1(A(x,T) + B(x,T)\cot a\tau_0) + a\Delta A(x,T)\cot a\tau_0 - a\Delta B(x,T), \tag{4.82}$$

$$\psi_B(x,T) = a^2\tau_1(A(x,T)\cot a\tau_0 - B(x,T)) + a\Delta A(x,T) + a\Delta B(x,T)\cot a\tau_0. \tag{4.83}$$

We similarly project the equation of diffusion terms onto $\cos at$ and $\sin at$, while T is treated as independent of t as in (Klosek and Kuske (2005)). Moreover, we rewrite the noise term $dW(t)$ as a linear combination of two independent Brownian motions $W_j(t),\ j = 1, 2$, multiplied by each resonant mode of oscillations. Then, we rescale each $W_j(t)$ in terms of slow time variable T, using the property of Brownian motion, to be compatible with the diffusion terms on the left-side hand of (4.79):

$$dW(t) = \cos atdW_1(t) + \sin atdW_2(t), \tag{4.84}$$

$$\delta dW_j(t) = \frac{\delta}{\epsilon} dW_j(\epsilon^2 t) = \frac{\delta}{\epsilon} dW_j(T). \tag{4.85}$$

Using the expressions (4.84)–(4.85) and the orthogonality of $\cos at$ and $\sin at$ in $L^2([0, 2\pi/a])$, and computing the following integrals

$$\begin{aligned} &\int_0^{2\pi/a} \begin{pmatrix} \cos at \\ \sin at \end{pmatrix} [\sigma_A \cos atd\xi_1(T) + \sigma_B \sin atd\xi_2(T)]dt \\ &= \int_0^{2\pi/a} \begin{pmatrix} \cos at \\ \sin at \end{pmatrix} \frac{\delta}{\epsilon} [\cos atdW_1(T) + \sin atdW_2(T)]dt, \end{aligned} \tag{4.86}$$

imply the conditions on the diffusion terms in (4.67)–(4.68):

$$\sigma_A = \sigma_B = \frac{\delta}{\epsilon}. \tag{4.87}$$

In the integral (4.86), the slow-time variable T was treated as independent of t. Also we equate the independent Brownian motions: $\xi_1(T) = W_1(T),\ \xi_2(T) = W_2(T)$ in the method of multiscale analysis.

Substituting all derived coefficients (4.82)–(4.83) and (4.87) into (4.67)–(4.68), we finally obtain a system of SDDEs that provides the amplitude equations for A and B

$$\begin{bmatrix} dA(x,T) \\ dB(x,T) \end{bmatrix} = \left\{ \mathbf{P} \begin{bmatrix} A(x,T) \\ B(x,T) \end{bmatrix} + \mathbf{Q} \begin{bmatrix} A(x,T-\epsilon^2\tau) \\ B(x,T-\epsilon^2\tau) \end{bmatrix} \right\} dT + \mathbf{R} \begin{bmatrix} d\xi_1(T) \\ d\xi_2(T) \end{bmatrix}, \tag{4.88}$$

where

$$\begin{aligned} \mathbf{P} &= \begin{bmatrix} -a^2\tau_1 - a\cot a\tau_0/\epsilon^2 & -a^2\tau_1\cot a\tau_0 + a/\epsilon^2 \\ a^2\tau_1\cot a\tau_0 - a/\epsilon^2 & -a^2\tau_1 - a\cot a\tau_0/\epsilon^2 \end{bmatrix}, \\ \mathbf{Q} &= \begin{bmatrix} -a\cot a\tau_0/\epsilon^2 & -a/\epsilon^2 \\ a/\epsilon^2 & a\cot a\tau_0/\epsilon^2 \end{bmatrix}, \quad \mathbf{R} = \begin{bmatrix} \delta/\epsilon & 0 \\ 0 & \delta/\epsilon \end{bmatrix}. \end{aligned} \tag{4.89}$$

4.3.3 Analysis and numerical simulation

Suppose that $\delta = 0$ (and $\mathbf{R} = \mathbf{0}$) so that the system (4.88) becomes deterministic. The resulting problem can be viewed a system of delay differential equations. If we seek the solution of the form $\mathbf{V}(\mathbf{x})e^{\Lambda T}$ to (4.88), $U(x,t)$ in (4.66) can be approximated by

$$U(x,t) \sim V_1(x)e^{\Lambda T}\cos at + V_2(x)e^{\Lambda T}\sin at,$$

where $\mathbf{V}(\mathbf{x}) = \begin{bmatrix} V_1(x) \\ V_2(x) \end{bmatrix}$. The characteristic equation for Λ is given by

$$C(\Lambda) = \mathbf{P} + \mathbf{Q}e^{-\epsilon^2\tau\Lambda} - \Lambda\mathbf{I}.$$

For example, if $\tau_1 < 0$ so that $\tau < \tau_0$ in (4.65), the solution to (4.61) of the form (4.63) asymptotically approaches to zero, implying that the corresponding amplitudes A

and B converge to zero, respectively, on slow time scale. Thus, the real part of every eigenvalue that satisfies $C(\Lambda)$ is negative for $\tau < \tau_0$, indicating that the system (4.88) is stable, i.e., for any arbitrary initial conditions of A and B, the process approaches toward its steady state, zero, on slow time scale T. However, if $\tau_1 > 0$ such that the original system (4.61) enters the supercritical region, the given multiscale approximation (4.88) for amplitude equations is not stable, thus, would be valid only upto short time periods. After these periods, the exponential growth would dominate the overall solution behaviors.

To apply asymptotic expansions to obtain (4.88), we restrict our analysis to the case where $0 < \epsilon \ll 1$, so that the delay is set to be sufficiently close to the critical delay of the deterministic system. If we take the limit as $\epsilon \to 0$, we can obtain the multiscale approximation of the long time dynamics for the deterministic system (when $\delta = 0$). Specifically, SDEs for A and B given in (4.67)–(4.68) become the deterministic ODEs and, thus, A and B are differentiable with respect to T. Then it follows

$$\begin{aligned}
\Delta A(x,T) &= (-\tau) \cdot \frac{A(x,T-\epsilon^2\tau) - A(x,T)}{-\epsilon^2\tau} \\
&= (-\tau_0 - \epsilon^2\tau_1) \cdot \frac{A(x,T-\epsilon^2\tau) - A(x,T)}{-\epsilon^2\tau} \\
&\to \quad -\tau_0 \frac{\partial A(x,T)}{\partial T} \quad \text{as } \epsilon \to 0.
\end{aligned}$$

Similarly, we can show $\Delta B(x,T) \to -\tau_0 \frac{\partial B(x,T)}{\partial T}$ as $\epsilon \to 0$. Substituting these resulting limits into (4.82)–(4.83), and rearranging the terms by using $\psi_A(x,T) = \frac{\partial A(x,T)}{\partial T}$ and $\psi_B(x,T) = \frac{\partial A(x,T)}{\partial T}$ from (4.67)–(4.68) yield the following system of ODEs for A and B

$$\begin{aligned}
\psi_A(x,T) &= c(c_1 A(x,T) + c_2 B(x,T)), \\
\psi_B(x,T) &= c(c_2 A(x,T) - c_1 B(x,T)),
\end{aligned}$$

where

$$c = \frac{a^2\tau_1}{(1 + a\tau_0 \cot a\tau_0)^2 + (a\tau_0)^2},$$

$$c_1 = 1 + 2a\tau_0 \cot a\tau_0,$$

$$c_2 = -\cot a\tau_0(1 + a\tau_0 \cot a\tau_0) - a\tau_0.$$

These drifts terms, thus, correspond to the long time dynamics, which can be obtained similarly by the method of multiscale analysis, for the deterministic system as in Ref. Gopalsamy (1992).

To validate the multiscale approximation in (4.88), we compare the invariant density $p(x)$ for the value of $U(1,t)$ by numerically solving two equations, the original SPDE in (4.61) and the reduced envelop equation in (4.88). For two different values of $\epsilon^2 = .01$ and $= .0002$ while keeping $\delta = .01$, the approximations of the invariant density $p(x)$ are illustrated in Fig. 4.5. Each simulation to approximate a point for $p(x)$ was run for large time, $t > 5000$, and that simulation was repeatedly conducted over 5000 times to obtain a reasonably good approximation of $p(x)$. Comparing the solid lines (or dash-dotted lines) of two cases reveals that the variance of the process increases as ϵ decreases, as previously observed in Fig. 4.4. Although the amplitude slowly varies over time, as can be seen in the envelop of oscillations in Fig. 4.4 (dash-dotted line in bottom image), the various amplitudes of oscillations can be observed, thus, resulting in the variance of $p(x)$. This variance also indicates that oscillations with larger amplitudes more frequently appear as ϵ decreases, which confirms the emergence of the noticeably amplified oscillations in Fig. 4.4.

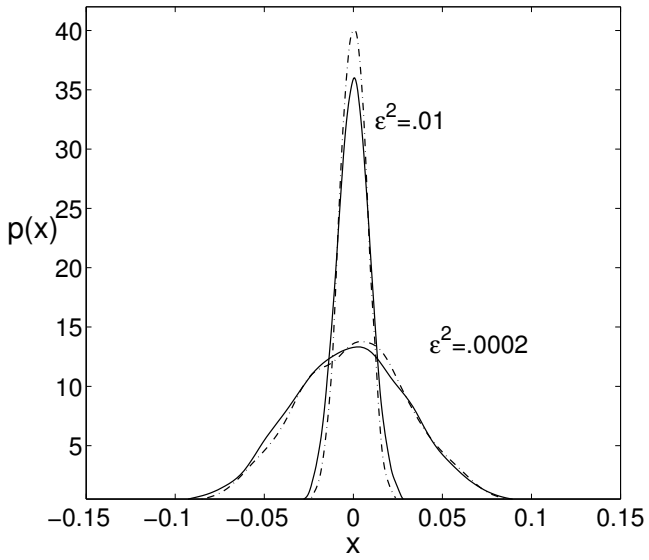

FIGURE 4.5: The invariant density $p(x)$ for $U(1,t)$ obtained from (4.61), plotted in solid lines, and (4.66), plotted in dash-dotted lines, for $\epsilon^2 = .01$ and $\epsilon^2 = .0002$. In both cases, $\delta = .01$ so that $\delta/\epsilon \ll 1$.

5

Discussion and Future Work

In this chapter, we summarize major contributions of each modeling study, compare the results with other models, and discuss possible direction for future research work.

5.1 Summary of Modeling Results

TAL model

We have developed three mathematical models of the TGF system in the rat kidney to investigate a variety of qualitative and quantitative features of the TGF-mediated dynamics. We first studied the TAL model to assess the impacts of the TAL spatial inhomogeneity and TAL wall compliance on the stability of TGF system.

One important observation in the TAL-model study is that oscillatory solutions become attainable at zero TGF delay and sufficiently high TGF gain values when the spatial inhomogeneity of TAL radius and NaCl transport rate is introduced to the system. In most of previous modeling studies (e.g., Layton et al. (1991); Pitman et al. (2002); Layton (2010)), it has been generally believed that LCO solutions emerge as a result of *sufficiently long delays and sufficiently high gains*. However, our model suggests that zero TGF delay with sufficiently high gain values can give rise to LCO

solutions if the TAL radius is smaller or the maximum TAL NaCl transport rate is higher near the loop bend. This finding, implied by analyzing the characteristic equation corresponding to the linearized model, was also validated by numerical simulation of the full nonlinear model, as can be seen in Figs. 3.4 and 3.5.

Another key finding of TAL-model study is that the introduction of TAL wall compliance increases the tendency of the TGF system to oscillate, reducing the overall stability (Layton (2010)). The inclusion of the TAL wall compliance was based on the consideration that, *in vivo*, the TAL likely expands and contracts depending on the transmural fluid pressure. The choice of the reduction factor (1/5) that was applied to isolated tubule measurements accounts for the limitation of the active movements of the tubular walls by neighboring TALs and their connecting tissues, thus, reducing *in situ* compliance (Leyssac and Baumbach (1983)). Despite the reduced compliance effect, however, our model indicates that a representation of TAL compliant walls greatly reduces the stability of TGF system, as can be shown by comparing root loci in bifurcation diagrams given in Figs. 3.3C and D. Moreover, it is noteworthy that locus curves corresponding to higher frequencies are much lowered compared to locus curve corresponding to "$\rho_1 = 0$", which indicates that the TGF system more likely exhibits high-frequency LCO.

Short-looped nephron model

Although the TAL model explicitly represents the TAL in detail, as a key component, to study TGF-mediated dynamics, other important components of the TGF loop such as the actions of the proximal tubule and descending limb of a short-looped nephron are represented by means of simple and phenomenological representations (Layton et al. (1991); Layton (2002, 2010)). However, because the proximal tubule as well as the outer-strip segment of the descending limb are water- and NaCl-permeable, substantial amounts of water and NaCl are reabsorbed into the

interstitial area along those segments, directly affecting TAL flow rate and overall TAL dynamics. In addition, MD chloride concentration, which is believed to be primary signal for the TGF response, depends significantly on the TAL flow rate due to the water-impermeability of TAL walls. Thus, to obtain more comprehensive understanding of TGF regulatory mechanisms through the entire tubular system, we have developed the short-looped nephron model that explicitly incorporates the dynamics of an entire short-looped of Henle.

Unlike our TAL model and other TGF previous studies (Layton et al. (1991, 2000, 2006); Oldson et al. (2003); Layton (2010)), the short-looped model explicitly computes tubular fluid pressure, flow rate, and chloride concentration along the proximal tubule and descending limb. To describe the water reabsorption along those segments, the transmural water flux was prescribed such that the $\sim 1/3$ and $\sim 7/30$ of the SNGFR reach the descending limb and the loop bend, respectively, which are quantitatively consistent with experimental measurements (Young and Marsh (1981)). Similar to TAL model, tubular wall compliance was also included to describe more realistic representation of the short-looped nephron. Given this whole-loop model formulation, we identified parameter boundaries that separate the dynamic behaviors of TGF system. Based on the bifurcation diagrams, we also investigated the effects of LCO on the regulatory ability of the TGF system.

The present short-looped model predicts TGF-mediated oscillations at frequencies that are largely consistent with *in vivo* observations. Experimental recordings in rats have shown that nephron flow and related variables may exhibit regular TGF-mediated oscillations with a frequency of $\sim$30–40 mHz (Holstein-Rathlou and Leyssac (1986); Holstein-Rathlou (1987); Holstein-Rathlou and Marsh (1989)). Given physiologically relevant parameters, the model can predict oscillations with a fundamental frequency of 37.7 mHz (Fig. 3.8X). It is also noteworthy that with higher gain and shorter feedback delay values, the model predicts oscillations at much higher frequen-

cies (first and second harmonics), as high as ∼150 mHz (Fig. 3.8Z), which have not been observed experimentally. Even if the lower tubular compliance than one-fourth of the base-case compliance (see Fig. 3.7B) is applied to the model, oscillations at high frequencies are still predicted, but with TGF gains >∼6 (with delays <∼2.5 s), which are higher than the gain value of ∼3.5 measured experimentally in normotensive rats (results not shown). Thus, the emergence of the high-frequency LCO may be, in part, attributable to tubular compliance used in the present study (see below), which is likely higher than *in situ* compliance (Leyssac and Baumbach (1983)).

Numerical simulations of the short-looped model equations also indicate that the dynamic regime supporting the steady-state behavior becomes smaller when the (increased) tubular compliance is introduced to the system, as demonstrated in TAL-model results. Although *ad hoc* choice of the reduction factor (1/5) in the tubular compliance was made due to the poorly-characterized *in situ* compliance, the model predictions are consistent with previous results by Layton (2010) and TAL model herein that the increased compliance in tubular walls further reduces the stability of the TGF system (see Fig. 3.7).

A comparison of the dynamic behaviors, guided by their respective bifurcation curves, between the TAL and short-looped models, demonstrates that the explicit representation of the descending portions along the loop of Henle reduces the stability of the TGF system (see Fig. 3.9). Moreover, loop-model results support an observation previously shown in TAL model that the spatial dependence of TAL physical and transport parameters can be an important bifurcation parameter. For example, because the TAL has a smaller radius near the loop bend as shown in Fig. 3.6B, the model predicts oscillatory solutions at zero TGF delay and TGF gains > 3.8, a result that is consistent with TAL-model study (see Fig. 3.7A for loop model and Fig. 3.3 for TAL model).

Incorporating the detailed dynamics along the entire loop of Henle, we inves-

tigated the effects of LCO generated by transient flow perturbations on the TGF regulatory functions of distal fluid and sodium delivery. To assess physiologically realistic effects of LCO, we specified the base-case feedback delay and gain near physiologic parameter values based on experimental measurements. Casellas and Navar (1984) estimated the average TGF response to be ∼4 s in normotensive rats. Also, the experimental studies of TGF mechanism in normotensive rats with open-loop (Briggs et al. (1984)) and closed-loop approaches (Knepper et al. (1977); Moore and Mason (1983)) showed feedback gain value of 1.5–3.3. A number of microperfusion studies have further demonstrated that the feedback responses in hypertensive rats are enhanced compared to those in normal rats. In particular, the parameter estimation study by Ditlevsen et al. (2007) reported a gain value of ∼ 8.3 for hypertensive rats, which exceeds most of previous gain estimates in normal rats. Based on these observation, we used $\tau = 3.5$ s and $\gamma = 5$ which likely lie in physiologic parameter ranges for normal rats.

With these base-case parameter values, the model predicts that the onset of LCO, as a consequence of transient pressure perturbations, results in the increased time-averaged distal NaCl delivery while distal fluid delivery is not much affected (see Fig. 3.10A). In addition, high-frequency LCO (Fig. 3.11A) or high mean TAL flow rate (Fig. 3.12A) reduces the degree of increased distal NaCl delivery. The waveform distortions, specifically, in MD chloride concentration (see Figs. 3.10C and D) suggest that the increased time-averaged distal NaCl delivery, which results in enhanced sodium excretion, can be attributed to the nonlinear signal transduction process in the TGF loop, as previously demonstrated in Refs. Layton et al. (1997a, 2012a,b).

Another important contribution of loop-model study is the investigation of the effect of sustained pressure perturbations on the resulting TGF-mediated dynamics. Our model results show that the distal fluid as well as chloride delivery are markedly

increased, even compared to the transient perturbations, in the presence of sustained perturbations, which may further limit TGF autoregulatory functions (Layton et al. (2000); Oldson et al. (2003)). Also, in contrast to the case of transient perturbations, in which the time-averaged chloride delivery monotonically rises with increasing feedback gain values, the response of distal chloride delivery to an increased amplitude of the sustained perturbations exhibits noticeably non-monotonic. The major contribution to such non-monotonic increase is the suppression of LCO when the sufficiently large perturbations are applied. Even though distal chloride delivery continues to rise after the suppression of LCO, its deviations from the steady-state remain relatively small compared to those obtained in the presence of LCO (see Fig. 3.13A, dotted line which is computed via extrapolation). The reduced deviations after the suppression of LCO at (perhaps unphysiologically) large sustained perturbations indicate that the TGF autoregulation becomes enhanced in response to the excessive variations in GFR. This enhanced regulation suggests that the kidney can maintain the GFR near an appropriate range despite abrupt rises (or drops) over long time periods in arterial blood pressure and, thus, operate its proper regulatory functions.

Oldson et al. (2003) also investigated the effect of TGF adaptation or resetting to sustained flow perturbations on the stability of the TGF-mediated dynamics. They identified the critical sensitivity curve, the boundary between stable steady-state flow and stable oscillatory flow, as functions of flow perturbations and the feedback sensitivity that corresponds to the first derivative appeared in (3.95) (Oldson et al. (2003)). They then assessed how the sensitivity curve is affected by the presence of sustained flow perturbations (or changes in extracellular fluid volume). Model results indicate that even though LCO is suppressed due to sufficiently large sustained perturbations, it can be reestablished through resetting the sensitivity curve, further reducing the ability of TGF regulation of distal fluid and NaCl delivery. Thus, TGF resetting may enhance the time-averaged distal NaCl delivery, which appears

to be opposite to the results of the present study, as well illustrated by the non-monotonicity of the responses to sustained perturbations in Fig. 3.13.

Coupled-nephron model

A series of experimental data in SHR have shown that TGF-mediated pressure in the nephrons' proximal tubule exhibits irregular oscillations with a high degree of spectral density (Holstein-Rathlou and Leyssac (1986, 1987); Yip et al. (1991)). To study the relevant mechanisms that may result in those complex behaviors, it has been shown that spectral complexity may arise from a number of factors, such as the combined action of bifurcations (Layton et al. (2009)) or internephron coupling between neighboring nephrons (Layton et al. (2006, 2011)). Nevertheless, the previous coupled-TGF models were formulated primarily based on the previous (uncoupled) TAL model (Layton et al. (1991); Layton (2010)); among all tubule segments, only the TAL was explicitly represented.

To help elucidate the underlying mechanisms of irregular tubular pressure oscillations using the more inclusive TGF-coupled model, we have developed a mathematical model of the coupled-TGF system based on our short-looped model formulation. As in the TAL model, we derived the characteristic equation (Eq. (3.124)) for two coupled nephrons by means of linearization to identify the parameter regions that correspond to qualitatively different dynamic behaviors. Results of the bifurcation analysis were also validated by numerical solution of the full model equations.

In contrast to previous modeling studies for coupled-TGF system (Pitman et al. (2004); Kesseler (2004); Layton et al. (2009, 2011)), our coupled-nephron model includes an explicit representation of the entire short loop of Henle in each nephron. As a result, even for the uncoupled system, the steady-state region in the coupled-nephron model becomes smaller than in the uncoupled TAL-only model (compare Fig. 3.3D in TAL model with Fig. 3.16A in coupled-nephron model). This result

supports a finding in the short-looped model that the explicit representation of the proximal tubule and descending limb reduces the stability of the TGF system. Also, the previous observation of TAL model that the spatial dependence of TAL parameters is an important bifurcation parameter for the emergence of LCO solutions was similarly observed. This can be seen by the γ-axis crossings of the root loci in Fig. 3.16, which are a result of the spatial inhomogeneous tubular radius along the TAL as shown in Fig. 3.6B.

Our main goal of the coupled-nephron study is to investigate the impact of coupling on the dynamics of coupled-TGF systems. Results of bifurcation analysis of the characteristic equation show that coupling increases the size of the regions that support oscillatory solutions, a result that is consistent with previous coupled-TGF models by Pitman et al. (2004); Layton et al. (2006, 2009, 2011). This finding can be seen by comparing the model behaviors of the uncoupled (panel A) and coupled (panel B) systems in Fig. 3.16. The steady-state region indicated by '$\rho_n < 0$' is decreased in size by internephron coupling. In addition, coupling significantly increases the sizes of parameter regions where $\rho_3 > 0$ or $\rho_4 > 0$, and it increases the sizes of regions supporting the multistable LCO with more than one positive ρ_n. Moreover, the increased tendency for coupled TGF system to exhibit oscillatory solutions is more marked in the present model than other coupled-TGF models with the TAL-only representation (e.g,. compare Fig. 2B in Layton et al. (2011) with Fig. 3.16B in the coupled-nephron model).

Based on information provided by bifurcation analysis, we also identified a set of parameters for two coupled nephrons in which irregular oscillations in nephron flows and related variables emerge; see Figs. 3.20 and 3.21. Indeed, model results suggest that a large class of parameter combinations can produce irregular oscillations because of the significantly increased size of parameter regions that support multistable LCO (see Figs. 3.16 and 3.19). The increased tendency for the present model to ex-

hibit irregular oscillatory solutions thus supports a role of coupling for the emergence of irregular oscillations in SHR, as previously discussed in Refs. (Layton et al. (2009, 2011)).

5.2 Significance of Our Findings

In most of previous TGF models with TAL-only representation (Layton et al. (1991); Pitman et al. (1993); Layton et al. (1995, 1997a,b); Layton (2010)), TAL physical and transport properties were assumed to be spatially homogeneous. Our TAL model extended those models to explicitly include two types of spatial inhomogeneity in TAL radius and NaCl transport rate, and used the resulting model to study the impacts of those inhomogeneities on the TGF-mediated dynamics. We found that nonzero feedback delay is not necessary for the emergence of LCO, and the spatial dependence of TAL radius and NaCl transport rate can be an important bifurcation parameter in determining the stability of TGF system. This new finding, which has not been previously demonstrated in other modeling studies, is confirmed by the results of our short-looped nephron model (see below).

Compared to the previous TAL model (Layton (2010)), the present model, specifically, CIRT case appears to be less stable in that LCO is attainable at a short (or even zero) feedback delay with sufficiently high gain values (compare Fig. 2B1 in Layton (2010) with Fig. 3.3D in our TAL model) due to the inclusion of TAL spatial inhomogeneity. Except those parameter regions, however, the primary bifurcation locus that separates the dynamic state of solution behaviors from the steady state into oscillations remains nearly same as that of TAL model in Layton (2010). This comparison suggests that if the TGF system lies in the parameter regions where the feedback delay is short and feedback gain is relatively high, TGF-mediated dynamic behaviors are significantly affected by the TAL physical and transport properties. Moreover, model results show that the introduction of TAL wall compliance in-

creases the tendency of the TGF system to oscillate, which is consistent with the previous result by Layton (2010).

Budu-Grajdeanu et al. (2007) previously studied the impact of three types of TAL spatial inhomogeneities, NaCl permeability, NaCl active transport, and TAL radius, on the nonlinear transduction process along the TAL. Although their model incorporated the effect of tubular inhomogeneity similar to our TAL model, TAL was assumed to be rigid and the TGF response was not explicitly represented (i.e., open-loop) in contrast to the present model. Despite these assumptions, Budu-Grajdeanu et al. (2007) found that the introduction of spatial inhomogeneities increases the degree of waveform distortions in MD chloride concentration. Based on this observation, they hypothesized that the inclusion of the spatial dependence of TAL physical and transport properties in a model of TGF system would introduce more complex TGF dynamics, e.g. the emergence of parameter regimes supporting high-frequency or multistable LCO, which is supported by the results of the present TAL-model study.

Pitman and coworkers (Layton et al. (1991)) developed the TAL model with rigid tubule and zero diffusion permeability (i.e., $\kappa = 0$ in Eq. (2.3)) for analytic simplicity unlike our TAL model. As a result, the root curves of the characteristic equation do not cross each other, whereas those for all considered model cases in TAL model do, as can be shown by comparing Fig. 4 in Layton et al. (1991) and Fig. 3.2 in TAL model herein. Such crossings, which can give rise to new parameter regimes where model solutions can exhibit multiple stable dynamic modes, i.e., multistability (Layton et al. (2006)), suggest that TAL backleak permeability can be an important bifurcation parameter, as previously discussed in Refs. Layton et al. (2006, 2009).

In our next study, we extended the TAL model to include an entire short-looped nephron, in which the impact of the explicit representation of the proximal tubule and descending limb on the stability of the TGF system was directly assessed in

comparison to the TAL-only model. Based on model results, we concluded that the introduction of the descending portions of nephron tubule reduces the stability of the feedback loop, which has not been demonstrated in the previous modeling studies. Also, γ-axis crossings of the bifurcation curves in the bifurcation diagram support the previous results of the TAL model that LCO becomes attainable at zero TGF delay with sufficiently high gain values if the spatial inhomogeneity of TAL radius is introduced. Furthermore, the previous finding of the TAL model that tubular wall compliance is another factor that affects the stability of the TGF system was confirmed by the short-looped model.

Based on the information provided by the bifurcation diagram, we investigated the effect of LCO on the distal fluid and NaCl delivery. Specifically, we considered two different TGF delay values for a clear comparison of the impact of LCO frequency on the TGF regulatory ability. For the TGF delay of 3.5 s, LCO does not undergo the frequency change as the gain value increases, whereas, for the delay of 3 s, LCO does from the fundamental (f_1) to the first harmonic (f_2) frequencies (see Fig. 3.7A). The change in LCO frequency causes a reduction in the degree of the increased time-averaged NaCl delivery, compared to the case of no frequency change. This finding, which was not previously shown in the similar TGF-regulation study by Layton et al. (2000), indicates that high-frequency LCO reduces the effect of LCO on distal NaCl delivery, resulting in an enhanced TGF autoregulatory ability compared to low-frequency LCO.

Using the whole-loop formulation, we also conducted a comparison study for the effect of mean TAL flow on TGF waveform distortion and distal NaCl delivery. By adjusting the scale of water reabsorption rate along the proximal tubule and water-permeable descending limb, and additional parameter values to yield different mean TAL flow while keeping the steady-state MD chloride concentration nearly same, we characterized how mean TAL flow affects distal NaCl delivery. The model pre-

dicts that a low mean TAL flow rate yields larger amplitudes and less sinusoidal of TGF-mediated LCO, resulting in the increased time-averaged distal NaCl delivery compared to a high TAL flow rate. This prediction can be attributed to a limited ability to lower MD chloride concentration when flow decreases, as the NaCl reabsorption approaches the static-head limit where the active NaCl reabsorption and passive backleak balance each other (Layton et al. (2012a,b)). Moreover, our findings suggest that the transport dynamics along the proximal tubule and descending limb, which directly influence the mean TAL flow rate, can be an important factor that impacts the TGF regulation of distal NaCl delivery. Although Layton et al. (2000) did not conduct a sensitivity-study of mean TAL flow due to the lack of the explicit representation of the descending segments of model tubule, similar results could have been obtained by applying appropriate transport parameters to yield different mean TAL flow and consistent steady-state MD chloride concentration in their rigid-tube TAL model.

The previous coupled-TGF study by Layton et al. (2011) considered a system of two nephrons having compliant TAL walls. Our coupled-nephron model extended that model to include the explicit representation of the proximal tubule and descending limb in each nephron, and investigated the effect of internephron coupling on the stability of coupled-TGF system. Model results indicate that the tendency for coupled system to exhibit oscillatory behaviors is noticeably increased compared to the previous model (Layton et al. (2011)). This observation could have been inferred from the results by our short-looped model, demonstrating that the explicit representation of the entire short-looped nephron decreases the stability of TGF system in a (uncoupled) nephron.

The coupled-nephron models developed by Bayram and coworkers (Bayram (2006, 2012); Bayram et al. (2009)) were based on the much simpler integral equation (Pitman et al. (2002)) with zero diffusion permeability. Their results are similar to ours

in that both predict that the region supporting oscillatory solutions increases with internephron coupling (Bayram et al. (2009); Bayram (2012)). However, unlike the present model, which can predict irregular oscillations (see Fig. 3.20), the models by Bayram and coworkers predict only regular oscillations.

A series of previous coupled-nephron models by Holstein-Ratholu and coworkers (Holstein-Rathlou et al. (2001); Andersen et al. (2002); Sosnovtseva et al. (2003); Marsh et al. (2005b,a); Sosnovtseva et al. (2003); Marsh et al. (2007, 2013)), used the detailed representation of the microvasculature including the structural components of AA, glomerulus, and EA. In contrast, our model represents the coupling effect by using phenomenological relations while neglecting those components. Instead, our model uses an explicit representation of the time dependent dynamic behaviors along the tubular system based on our short-looped model. Regardless of the major difference in model's emphasis, our model results support their findings that coupling can give rise to complex dynamic behaviors, e.g., irregular oscillations in nephron tubular pressure similar to those found in SHR. However, due to the lack of explicit implementation of hemodynamic coupling, our model cannot predict out-of-phase synchronization among coupled nephrons, whereas the models by Holstein-Ratholu and coworkers (e.g., Andersen et al. (2002); Sosnovtseva et al. (2003)) exhibit a variety of qualitatively different coupled-nephron behaviors, including in-phase, anti-phase (out-of-phase), and even chaotic phase synchronization as well as irregular oscillations.

Furthermore, the models by Holstein-Rathlou and coworkers included not only a detailed representation of AA dynamics in response to TGF activation, but also the myogenic response of AA interacting with TGF mechanism (Marsh et al. (2005a,b, 2013)), which were not present in the present model formulation. Hence, there are substantial differences in the origin of the complex behaviors between their and our models; in their models those complexities are originated primarily from microvas-

culature dynamics, whereas in our model they are from the nonlinear dynamics of tubular transport processes. Therefore, both model results are needed to provide more comprehensive explanation of the complex dynamic phenomena observed in SHR.

5.3 Model Limitations and Future Extensions

In all three TGF models, we used the downstream resistance tube after the terminal part of TAL instead of a realistic representation of the distal tubule and collecting system. This assumption makes it possible to avoid prescribing the poorly-characterized tubular fluid pressure at the MD. In addition, no water was assumed to be reabsorbed along the distal nephron, specifically, the segments after the MD. *In vivo*, however, a significant amount of water is reabsorbed along those segments, affecting the chloride concentration in surrounding interstitial areas and, thus, the tubular system. Although qualitative dynamic model behaviors are nearly insensitive to variations in the downstream resistance tube, as shown in our sensitivity study (Fig. 3.15), some quantitative aspects of the system behaviors such as the time-averaged distal NaCl delivery may be changed, affecting the TGF regulatory functions. Thus, to better assess the role of *in vivo* dynamics of the distal nephron in TGF mediation, one can further extend our short-looped nephron model to include physiologically more realistic representation of the distal nephron, which can be guided by a mathematical model in Ref. Moss and Layton (2014).

Another limitation in our short-looped model is the simplified PCT representation. In the rat kidney, PCT is rather convoluted, not straight as shown in Fig. 2.3. In fact, the total length of PCT is measured to be $\sim$5 mm (Corman et al. (1981)), which is same as the length of the whole descending portions of short-looped nephron used in our study. In addition, due to its physical properties, the transport processes and fluid flow rate along the PCT described in the present formulation may sig-

nificantly differ from *in vivo* dynamics. Modeling studies by Layton et al. (2006, 2009) previously showed that the longer length of the tubule increases the tendency of the TGF system to oscillate. Also, the present loop-model results indicated that the explicit representation of the proximal tubule reduces the stability of the TGF system. Taken together, it can be inferred that the TGF loop with an inclusion of a realistic (longer) PCT segment may exhibit the reduced stability. However, to thoroughly understand the TGF mediation along the tubular system, the roles of the detailed PCT dynamics in the context of renal autoregulation are worthy of further investigation.

Another direction of future extension is to introduce the spatial inhomogeneity of transport parameters to short-looped model. Similar to TAL model, the steady-state tubular radius of our short-looped model exhibits spatially inhomogenous, specifically, along the TAL. As a result, LCO is attainable even at zero TGF delay and sufficiently high gain values, consistent with TAL-model results. However, NaCl maximum transport rate was assumed to be spatial homogeneous along the PST, PCT, DL, and TAL, respectively. The previous modeling results by Budu-Grajdeanu et al. (2007) indicated that the introduction of TAL spatial inhomogeneities results in the increased degree of waveform distortions in MD chloride concentration. Based on this observation, it is worthy to further study the impact of spatially inhomogeneous NaCl transport rate and NaCl permeability along the whole tubular system on TGF autoregulation, as similarly conducted in the present short-looped model.

The loop-model equations that describe the detailed transport dynamics in a single nephron are formulated based on the Stokes equation. To avoid complication for analytic study and make numerical simulation more tractable, the three-dimensional equation was simplified under model assumptions such as no axial or radial intratubular diffusion, as previously justified in Ref. Layton (2002). Also, Poiseuille flow to represent the tubular fluid pressure (Eq. (2.1)) was based on the assumption that

the luminal radius remains almost constant that is much smaller relative to its total length. However, when the tubular wall compliance is introduced, the luminal radius is no longer constant, but rather changes depending on transmural pressure difference. Even though the reduced factor (1/5) was applied to the isolated tubule measurements and the resulting compliance has small magnitude relative to other model parameters, specifying the compliance while keeping Poiseuille model formulation may introduce some discrepancy in model results. To alleviate that discrepancy, the TGF system with compliant tubular walls can be further extended to be modeled by the more realistic formulation. Specifically, because the model tubule has sufficiently low Reynolds number of 10^{-2} order of magnitude, i.e., $\sim 2.6 \times 10^{-2} \ll 1$, the Stokes equation can be alternatively employed.

Despite their limitations, our TAL- and loop-TGF models can serve as an essential component in models of integrated renal hemodynamic regulation. For instance, our models could be productively combined with a model of glomerular filtration (e.g., Ref. Deen et al. (1972)) and a model of the afferent arteriole (e.g., Ref. Sgouralis and Layton (2012)) to study the interactions between the myogenic and TGF responses in the context of renal autoregulation, similar to Refs. Marsh et al. (2005b); Sgouralis and Layton (2013). Also, our short-looped model can be combined to a whole-kidney model by Moss and Layton (2014), in which the key factors that derive pressure natriuresis were investigated, to study the urine concentration mechanism as well as renal autoregulation.

In our coupled-nephron study, we represented internephron coupling using phenomenological relations. Specifically, we assumed the coupling is mainly from the propagation of TGF-induced electrotonic signal along the pre-glomerular vasculature. This assumption was based on micropuncture experiments (Holstein-Rathlou (1987); Källskog and Marsh (1990); Yip et al. (1992)) which show that TGF-induced constriction in an AA can cause a simultaneous but smaller constriction in a second

AA that are nearby from a common CRA. The interactions between nearby nephrons through their TGF systems then directly influence the inflow pressures at the proximal tubule, which were incorporated in the formulation of the TGF response in Eq. (2.19).

Another limitation of the present model formulation is the lack of hemodynamic coupling effect. In the presence of hemodynamic coupling while neglecting the vascular coupling, the increased vascular resistance due to the constriction of AA will increase blood flow into nearby AA, resulting in the increased tubular fluid flow rate of nearby nephron. Note that this effect is opposite to that of vascular coupling. By incorporating hemodynamic as well as vascular coupling along the pre-glomerular vasculature, we can better understand possible factors that generate in-phase and out-of-phase synchronization of coupled nephrons, and their implications for physiologic functions, as similarly studied in (Holstein-Rathlou et al. (2001); Andersen et al. (2002); Sosnovtseva et al. (2003); Marsh et al. (2005a,b, 2007, 2013)).

In the present coupled-TGF model, we considered only two nephrons. However, TGF coupling may extend to many nephrons (*vide infra*) as in (Marsh et al. (2007, 2013)). The systematic investigation of a model with many coupled nephrons, relative to two, would be much more complicated because it would involve finding the root loci of the characteristic equation in the higher-dimensional parameter space and performing a large number of additional numerical simulations.

Despite its limitations, the present coupled-TGF model can be used as a key component in studying important autoregulatory mechanisms in the kidney. By considering hemodynamic coupling in addition to vascular coupling as in Refs. (Holstein-Rathlou et al. (2001); Andersen et al. (2002); Sosnovtseva et al. (2003)), one can investigate the impacts of their interactions on the dynamics of the coupled TGF system. Moreover, applying a similar approach in Ref. Marsh et al. (2013), which considered the interactions between TGF and the myogenic response among multi-

nephrons, one can ultimately study the renal regulatory functions in a large-scale system.

5.4 Stochastic Model

Summary and major contribution

We have studied the influence of noise interacting with delays on the stability of the feedback dynamics. We first considered the stochastic system perturbed via noise at the boundary. By means of bifurcation analysis and the contraction mapping theory, we showed the stochastic system admits the statistically stationary solution for sufficiently small τ, even within the presence of noise at the boundary conditions. Similar to the deterministic system, the stochastic system exhibits two qualitatively different solution behaviors, converging towards its stationary solution or evolving to sustained oscillations, depending on feedback delay term τ. These analytic results, based on the proof from the deterministic system and the "pullback attractor" argument, were validated by numerical simulations of the nonlinear stochastic model equations.

In our next study, we have conducted the sensitivity-analysis of the stochastic delayed PDE to relatively small additive noise, which represents unknown external perturbations to the system. To better understand the effect of the noise on solution behaviors over long time periods, we used multiscale analysis for a linearized transport equation, separating deterministic and stochastic effects in fast and slow time scales, respectively. The case where the system is in the subcritical region, but sufficiently close to the critical delay, was particularly considered to assess the sensitivity of the stochastic system to the interaction between delays and noise. We derived the stochastic equations for the envelope of deterministic oscillations on slow time scale, which provide much more efficient way to analyze the solution behaviors compared to solving the original stochastic PDE with delays.

One of the biggest challenges in studying the behavior of dynamical systems with delays is that the systems are infinite dimensional, which makes the analytic approach significantly difficult. To reduce this difficulty and obtain more comprehensive understanding of the emergence of sustained oscillations due to noise, the multiscale method was employed by projecting the stochastic system onto the basis of the deterministic system at a bifurcation point, i.e., resonant modes, as widely used in dynamical systems without noise (Gopalsamy (1992); Hale and Verduyn-Lunel (1993)). This projection has been also introduced in the analysis of stochastic systems without delays (Yu et al. (2006); Kuske et al. (2007)). Also, to determine the right scale of the diffusion coefficients in amplitude equations, the noise term was written as a sum of resonant modes on the fast time scale with slowly varying stochastic coefficients in the method of multiscale analysis. The form is given by using two independent Brownian motions (see Eq. (4.84)).

Multiscale approach implicitly assumes that the sustained oscillations arise from competition between the deterministic dynamics, represented by the drift terms, and the stochastic dynamics, by the diffusion terms (Kuske (2003)). Under this assumption, we specifically look for solutions that are written in terms of the deterministic oscillations on the fast scale and the stochastic amplitudes on the slow scale. For this reason, if the noise becomes large enough to dominate the overall dynamics of the system, the multiscale approximation given in (4.66) is only valid for a short time period. Conversely, if the fluctuations on the fast scale becomes dominate because of $\tau > \tau_c$ (e.g., Fig. 4.3), the separation of the leading order approximation into two different time scales is not reasonable. Moreover, if the diffusion coefficient in amplitude equations has large scale relative to the proximity parameter ϵ, which renders the noise to dominate the dynamics on the slow time scale, the multiscale approximation is no longer valid. Given these consideration, to apply the multiscale analysis the system is required to have the noise with relatively small scale, e.g., $\delta \ll 1$ and

$0 < \epsilon \ll 1$ while keeping $\delta/\epsilon \ll 1$. In fact, numerical simulations indicate that solution behaviors obtained by the multiscale approximation is in good agreement with those by the original equation up to $\delta \sim \epsilon$, as previously discussed in Ref. (Klosek and Kuske (2005)).

Significance of model results

In the previous studies by Kuske (2005); Klosek and Kuske (2005), the multiplicative noise for linear case and the additive noise for nonlinear case, in particular, logistic equation, were also considered, in which reduced amplitude equations for each case were analogously derived. Using the same ansatz and assumptions on δ and ϵ but with additional steps, they showed that those reduced equations provide a good approximation of the real solution behaviors over long times. Specifically, for the case of nonlinear equation with additive noise, the multiscale method can be used in both the sub- and super-critical cases and the results were validated by computing the respective invariant density functions.

Despite its usefulness for understanding of long-time dynamics, their model was formulated as the first-order ODE with delays, whereas ours is PDE which significantly complicates the analysis. Moreover, because their model equation was not specifically related to a biological system with delays, the model results were not interpreted in the context of the feedback mechanism. In contrast, our stochastic model was motivated by the TGF system in the kidney to better understand a variety of qualitatively different phenomena, e.g., sustained (regular or irregular) oscillations, previously found in experimental data. Indeed, our results suggest that sustained oscillations in nephron flow may arise from the introduction of external perturbations, even when the system lies in the steady-state regime. This finding supports the results of previous modeling study by Ditlevsen et al. (2005, 2007), in which the effect of TGF gain that was modeled by a stochastic process on the TGF-mediated

dynamics was investigated, in that regular or irregular oscillations can emerge as a result of stochastic perturbations to the TGF system.

Although the studies by Ditlevsen et al. (2005, 2007) similarly provided a stochastic analysis of the stability of the TGF system, the underlying assumptions on noise are significantly different from those of our model. We assumed that noise directly influences the TAL transport process, thus perturbing the MD chloride concentration. Also, the bifurcation parameter itself, specifically, the feedback delay of the system is not changed by the effect of noise. In contrast, the models by Ditlevsen et al. (2005, 2007) assumed that one of the key parameters, the feedback gain, is directly perturbed via noise, modifying the intrinsic properties of the TGF system such as the dynamic state of model behaviors and consequently resulting in qualitatively different behaviors from those before the perturbation occurs. Due to the difference in the subjects that noise acts on, each model-results provide different implications.

First, the models by Ditlevsen et al. (2005, 2007) reproduced irregular oscillatory behaviors as similarly observed in the experimental data of SHR. However, the magnitude of perturbations present in (stochastically varying) TGF gain appears to be perhaps unphysiologically large (see the bottom image of Fig. 2 in Ditlevsen et al. (2005)), although the estimated value can be considered as the combined effect of all possible factors that determine the feedback effectiveness or gain. Also, unlike our stochastic study, the critical value of the feedback gain in the absence of noise was not explicitly identified, which makes it difficult to directly assess the sensitivity of the feedback system, i.e., the generation of sustained oscillations, to external noise. Nonetheless, their results implied that nephron's flow can exhibit irregular oscillations with time-varying amplitudes and periods, which significantly contribute to the spectral complexity, if intrinsic noise is introduced to a single parameter, feedback gain, of the TGF system.

In contrast, our goal of the stochastic study was to show how noise can induce

oscillations, via stochastic resonance, that would not appear in the deterministic system. To capture the interaction of noise with the delayed system, we considered relatively small additive noise that represents external perturbations but does not alter the TGF bifurcation parameters such as feedback gain and delay. We found that if the delay of the system is sufficiently close to its critical value so that the proximity between those two values is small relative to noise, sustained oscillations with slowly varying amplitude can emerge as a result of interactions with noise. This new observation has important physiological implication in that the interaction of small noise with the steady-state TGF dynamics can generate noise-induced oscillations, which may limit the regulatory ability of TGF system as demonstrated by the results of the present short-looped model. Although LCO predicted by our model exhibits constant period unlike that by the models (Ditlevsen et al. (2005)), its amplitude varies in slow time scale, which is governed by a stochastic process (see the amplitude equations in Eq. (4.88)). This time-varying amplitude with constant period may not be sufficient to explain the emergence of irregular oscillations with a high degree of spectral complexity as found in nephron's flow of SHR, but it can, in part, contribute to the complexities of model behaviors through the interactions with fluctuations present in another parameter such as the TGF gain. Thus, our stochastic study and the studies by Ditlevsen et al. (2005) are complementary in that the irregular oscillations can arise from the combined effects of noise that directly influences both a key bifurcation parameter and tubular transport process.

Model limitations and future extensions

For analytic simplicity, we made an assumption on zero diffusion permeability (i.e., $\kappa = 0$) to derive the main equation (4.1). However, experimental evidence indicated that the TAL has nonzero NaCl permeability (Mason et al. (1979); Wittner et al. (1988)), which may contribute to the complexity in model behaviors as previously shown in

(Layton et al. (2006); Layton (2010)). Thus, the case of nonzero diffusion permeability needs to be considered to better understand the impact of that parameter on the resulting TGF dynamics. Although this inhomogeneous term on the right-side of Eq. (4.1) would make rigorous analysis, e.g., finding explicit formula of the solutions, more difficult, model results can be used to compare to many other TAL models with nonzero permeability.

In the present multiscale analysis, we only considered the additive (constant) noise for linear system. However, because the solution is spatially dependent, the noise that is a function of x, i.e., $\delta(x)$, may be a more reasonable representation of external perturbations. Also, the noise effect can be described by the multiplicative noise, assuming that the scale of perturbations, in part, depends on the current value of the solution. Even though, to our knowledge, no analytic studies for both noise cases in SPDE with delays have been yet accomplished owing to difficulties in rigorous analysis of model equations, we can consider a special case where $\delta(x)$ is a periodic function of x.

Our stochastic model assumed that the feedback delay is constant in time. However, in the real TGF system, the delay is likely to change in time or to be different in nephron-to-nephron. Moreover, the interaction of the delays with noise may induce physiologically undesirable oscillatory behaviors as shown in Fig. 4.4. For instance, as demonstrated in our short-looped model, noise-induced LCO may significantly limit the ability of TGF autoregulation of distal NaCl delivery. Specifically, if the system is subject to excessive perturbations over long time periods, the time-averaged distal fluid and NaCl delivery remain to be increased, which may cause the excretion of substantial amounts of water and NaCl and thus fail to keep a balance of whole-organism water volume. It is, thus, essential to thoroughly examine the role of (deterministically or stochastically) time-dependent delays interacting with external noise on the stability of the systems for the realistic assessment of the mechanisms responsi-

ble for TGF autoregulation. By incorporating the effect of time-varying delays into our stochastic model, as in Refs. Appleby and Kelly (2004); Appleby and Buckwar (2005), the interaction of stochasticity with the delays can be further investigated to better understand the renal regulatory functions.

Bibliography

Andersen, M., Carlsson, N., Mosekilde, E., and Holstein-Rathlou, N. (2002), "Dynamic model of nephron-nephron interaction," in *Membrane Transport and Renal Physiology, The IMA Volumes in Mathematics and Its Applications*, eds. L. HE and W. AM, vol. 129, pp. 365–391, Springer, New York.

Angell, S., Pruthi, R., and Shortliffe, L. (1998), "The urodynamic relationship of renal pelvic and bladder presures, and urinary flow rate in rats with congenital vesicoureteral reflux," *J Urology*, 160, 150–156.

Appleby, J. and Buckwar, E. (2005), "Noise Induced Oscillation in Solutions of Stochastic Delay Differential Equations," *Dynamic Systems Appl*, 14.

Appleby, J. and Kelly, C. (2004), "Asymptotic and Oscillatory Properties of Linear Stochastic Delay Differential Equations with Vanishing Delay," *Funct Differential Equation*, 11.

Barfred, M., Mosekilde, E., and Holstein-Rathlou, N. (1996), "Bifurcation analysis of nephron pressure and flow regulation," *Chaos*, 6, 280–287.

Bayram, S. (2006), "Analysis of TGF-mediated dynamics in a system of many coupled nephrons," Ph.D. thesis, State University of New York at Buffalo.

Bayram, S. (2012), "Modeling TGF-mediated flow dynamics in a system of three coupled nephrons," *Int J Numer Methods Biomed Eng*, 28, 384–399.

Bayram, S., Stepien, T., and Pitman, E. (2009), "TGF-Mediated Dynamics in a System of Many Coupled Nephrons," *Bull Math Bio*, 71, 1482–1506.

Bell, P., Lapointe, J.-Y., Cardinal, J., and Chang, Y.-S. (1991), "Transport pathways in macula densa cells," *Kidney Int*, 39, S5944.

Beuter, H., Belair, J., and Labrie, C. (1993), "Feedback and delays in neurological diseases: A modeling study using dynamical systems," *Bull Math Bio*, 55, 525–541.

Blömker, D., Hairer, M., and Pavliotis, G. (2007), "Multiscale analysis for stochastic partial differential equations with quadratic nonlinearities," *Nonlinearity*, 20, 1721–1744.

Briggs, J. (1982), "A simple steady-state model for feedback control of glomerular filtration rate." *Kidney Int.*, 22(Suppl. 12), S143–S150.

Briggs, J. and Schnermann, J. (1987), "The tubuloglomerular feedback mechanism: functional and biochemical aspects," *Annu Rev Physiol*, 49, 251–273.

Briggs, J. and Schnermann, J. (1990), "The tubuloglomerular feedback mechanism," in *Hypertension: Pathophysiology, Diagnosis, and Management*, eds. J. Laragh and B. Brenner, chap. 68, Raven, New York.

Briggs, J., Shubert, G., and Schnermann, J. (1984), "Quantitative characterization of the tubuloglomerular feedback response: effect of growth," *Am J Physiol* (*Renal Fluid Electrolyte Physiol* 16), 247, F808–F815.

Buckwar, E., Kuske, R., L'Esperance, B., and Soo, T. (2006), "Noise-sensitivity in machine tool vibrations," *Int J Bifurcat Chaos*, 16, 2407–2416.

Budu-Grajdeanu, P., Moore, L., and Layton, H. (2007), "Effect of tubular inhomogeneities on filter properties of thick ascending limb of Henle's loop," *Math Biosci*, 209, 564–592.

Casellas, D. and Moore, L. (1990), "Autoregulation and tubuloglomerular feedback in juxtamedullary glomerular arterioles," *Am J Physiol* (*Renal Fluid Electrolyte Physiol* 27), 258, F660–F669.

Casellas, D. and Navar, L. (1984), "In vitro perfusion of juxtamedullary nephrons in rat," *Am J Physiol* (*Renal Fluid Electrolyte Physiol* 36), 245, F349–F358.

Chen, Y., Yip, K., Marsh, D., and Rathlou, N. H. (1995), "Magnitude of TGF-initiated nephron-nephron interaction is increased in SHR," *Am J Physiol* (*Renal Fluid Electrolyte Physiol* 38), 269, F198–F204.

Choi, M. Y., Kim, H. J., Kim, D., and Hong, H. (2000), "Synchronization in a system of globally coupled oscillators with time delay," *Phys. Rev. E*, 61, 371.

Corman, B., Roinel, N., and Rouffignac, C. D. (1981), "Water reabsorption capacity of the proximal convoluted tubule: a microperfusion study on rat kidney," *J Physiol*, 316, 379–392.

Crook, S. M., Ermentrout, G. B., Vanier, M. C., and Bower, J. M. (1997), "The role of axonal delay in the synchronization of networks of coupled cortical oscillators," *J. Comput. Neurosci.*, 4, 161–172.

Das, S. and Chatterjee, A. (2002), "Multiple scales without center manifold reductions for delay differential equations near Hopf bifurcations," *Nonlinear Dynam*, 30, 323–335.

Deen, W., Robertson, C., and Brenner, B. (1972), "A model of glomerular ultrafiltration in the rat," *Am J Physiol*, 223, 1178–1183.

Ditlevsen, S., Yip, K., and Holstein-Rathlou, N. (2005), "Parameter extimation in a stochastic model of the tubuloglomerular feedback mechanism in a rat nephron," *Math Biosci*, 194, 49–69.

Ditlevsen, S., Yip, K., Marsh, D., and Holstein-Rathlou, N. (2007), "Parameter estimation of feedback gain in a stochastic model of renal hemodynamics: differences between spontaneously hypertensive and Sprague-Dawley rats," *Am J Physiol Renal Physiol*, 292, F607–F616.

Dunn, K., Sandoval, R., Kelly, K., Dagher, P., Tanner, G., Atkinson, S., Bacallao, R., and Molitoris, B. (2002), "Functional studies of the kidney of living animals using multicolor two-photon microscopy," *Am J Physiol Cell Physiol*, 283, C905–C916.

Earl, M. G. and Strogatz, S. H. (2003), "Synchronization in oscillator networks with delayed coupling: a stability criterion," *J. Comput. Neurosci.*, 67, 036204.

Eaton, D. and Pooler, J. (2004), *Vander's Renal Physiology*, McGraw-Hill Medical, New York, 6th edn.

Ermentrout, B. and Ko, T.-W. (2009), "Delays and weakly coupled neuronal oscillators," *Phil. Trans. R. Soc. A*, 367, 1097–1115.

Evans, L. (1998), *Partial Differential Equations*, Graduate studies in mathematics, American Mathematical Society.

Garg, L., Mackie, S., and Tischer, C. (1982), "Effects of low potassium diet on Na-K-ATPase in rat nephron segments," *Pflügers Arch*, 394, 113–117.

Giacomelli, G. and Politi, A. (1998), "Multiple scale analysis of delayed dynamical systems," *Phys D*, 117, 26–42.

Gillespie, D. (1996), "Exact numerical simulation of the Ornstein-Uhlenbeck process and its integral," *Phys Rev E*, 54, 2084–2091.

Gils, S., Janssens, S., Kuznetsov, Y., and Visser, S. (2013), "On local bifurcations in neural field models with transmission delays," *J Math Bio*, 66, 837–887.

Gopalsamy, K. (1992), *Stability and Oscillations in Delay Differential Equations for Population Dynamics*, Kluwer, Dordrecht, The Netherlands.

Gottschalk, C. (1952), "A comparable study of renal interstitial pressure," *Am J Physiol*, 169, 180–187.

Gottschalk, C. and Mylle, M. (1957), "Micropuncture study of pressures in proximal and distal tubules and peritubular capillaries of the rat kidney during osmotic diuresis," *Am J Physiol*, 189, 323–328.

Hairer, M. (2009), *Introduction to Stochastic PDEs*, Lecture notes.

Hale, J. and Verduyn-Lunel, S. (1993), *Introduction to Functional Differential Equations*, Springer-Verlag, New York.

Han, J., Thompson, K., Chou, C., and Knepper, M. (1992), "Experimental tests of three-dimensional model of urinary concentratning mechanism," *J Am Soc Nephrol*, 2, 1677–1688.

Hattaway, A. (2004), "Modelling tubuloglomerular feedback in coupled nephrons," Ph.D. thesis, University of Massachusetts Amherst.

Holstein-Rathlou, N. (1987), "Synchronization of proximal intratubular pressure oscillations: evidence for interaction between nephrons," *Pflügers Arch*, 408, 438–443.

Holstein-Rathlou, N. (1991), "A closed-loop analysis of the tubuloglomerular feedback mechanism," *Am J Physiol* (*Renal Fluid Electrolyte Physiol* 30), 261, F880–F889.

Holstein-Rathlou, N. and Leyssac, P. (1986), "TGF-mediated oscillations in the proximal intratubular pressure: Differences between spontaneously hypertensive rats and Wistar-Kyoto rats," *Acta Physiol Scand*, 126, 333–339.

Holstein-Rathlou, N. and Leyssac, P. (1987), "Oscillations in the proximal intratubular pressure: a mathematical model," *Am J Physiol* (*Renal Fluid Electrolyte Physiol* 21), 252, F560–F572.

Holstein-Rathlou, N. and Marsh, D. (1989), "Oscillations of tubular pressure, flow, and distal chloride concentration in rats," *Am J Physiol* (*Renal Fluid Electrolyte Physiol* 25), 256, F1007–F1014.

Holstein-Rathlou, N. and Marsh, D. (1990), "A dynamic model of the tubuloglomerular feedback mechanism," *Am J Physiol* (*Renal Fluid Electrolyte Physiol* 27), 258, F1448–F1459.

Holstein-Rathlou, N. and Marsh, D. (1994a), "A dynamic model of renal blood flow autoregulation," *Bull Math Bio*, 56, 411–429.

Holstein-Rathlou, N. and Marsh, D. (1994b), "Renal blood flow regulation and arterial pressure fluctuations: a case study in nonlinear dynamics," *Physiol Rev*, 74, 637–681.

Holstein-Rathlou, N., Yip, K.-P., Sosnotseva, O., and Mosekilde, E. (2001), "Synchronization phenomena in nephron-nephron interaction," *Chaos*, 11, 417–426.

Jensen, K., Mosekile, E., and Holstein-Rathlou, N. (1986), "Self-sustained oscillations and chaotic behaviour in kidney pressure regulation," *Mondes Dévelop*, 54-55, 91–109.

Jensen, P., Christensen, O., and Steven, K. (1981), "A mathematical model of fluid transport in the kidney," *Acta Physiol Scand*, 112, 373–385.

Just, A. (2007), "Mechanisms of renal blood flow autoregulation: dynamics and contributions," *Am J Physiol Regul Integr Comp Physiol*, 292, R1–17.

Källskog, Ö. and Marsh, D. (1990), "TGF-initiated vascular interactions between adjacent nephrons in the rat kidney," *Am J Physiol* (*Renal Fluid Electrolyte Physiol* 28), 259, F60–F64.

Kang, J., Toma, I., Sipos, A., McCulloch, F., and Peti-Peterdi, J. (2006), "Quantitative imaging of basic functions in renal (patho)physiology," *Am J Physiol Renal Physiol*, 291, F495–F502.

Kesseler, K. (2004), "Analysis of feedback-mediated oscillations in two coupled nephrons," Ph.D. thesis, Duke University.

Kevrekidis, P. and Whitaker, N. (2003), "Effect of backleak in nephron dynamics," *Phys Rev E*, 67, 0619111–0619114.

Kim, S., Park, S. H., and Ryu, C. S. (1997), "Multistability in coupled oscillator systems with time delay," *Phys. Rev. Lett.*, 79, 2911.

Klosek, M. and Kuske, R. (2005), "Multiscale analysis of stochastic delay differential equations," *Multiscale Model Simul*, 3, 706–729.

Knepper, M., Danielson, R., Saidel, G., and Post, R. (1977), "Quantitative analysis of renal medullary anatomy in rats and rabbits," *Kidney Int*, 12, 313–323.

Kuske, R. (2003), "Multi-scale analysis of noise-sensitivity near a bifurcation," in *IUTAM Symposium on Nonlinear Stochastic Dynamics*, eds. N. S. Namachchivaya and Y. Lin, pp. 147–156, Dordrecht, The Netherlands.

Kuske, R. (2005), "Multi-scale dynamics in stochastic delay differential equations with multiplicative noise," *Stoch Dyn*, 5, 233–246.

Kuske, R., Gordillob, L., and Greenwood, P. (2007), "Sustained oscillations via coherence resonance in SIR," *J Theo Bio*, 245, 459–469.

Layton, A. (2010), "Feedback-mediated dynamics in a model of a compliant thick ascending limb," *Math Biosci*, 228, 185–194.

Layton, A. and Edwards, A. (2010), "Tubuloglomerular feedback signal transduction in a short loop of Henle," *Bull Math Biol*, 72, 34–62.

Layton, A. and Layton, H. (2005), "A Region-based Mathematical Model of the Urine Concentrating Mechanism in the Rat Outer Medulla: I. Formulation and base-case results," *Am J Physiol Renal Physiol*, 289, F1346–F1366.

Layton, A., Moore, L., and Layton, H. (2006), "Multistability in tubuloglomerular feedback and spectral complexity in spontaneously hypertensive rats," *Am J Physiol Renal Physiol*, 291, F79–F97.

Layton, A., Moore, L., and Layton, H. (2009), "Multistable dynamics mediated by tubuloglomerular feedback in a model of coupled nephrons," *Bull Math Biol*, 71, 515–555.

Layton, A., Bowen, M., Wen, A., and Layton, H. (2011), "Feedback-mediated dynamics in a model of coupled nephrons with compliant thick ascending limbs," *Math Biosci*, 230, 115–127.

Layton, A., Moore, L., and Layton, H. (2012a), "Signal Transduction in a compliant thick ascending Limb," *Am J Physiol Renal Physiol*, 302, F1188–F1202.

Layton, A., Pham, P., and Ryu, H. (2012b), "Tubuloglomerular Feedback signal transduction in a compliant short loop of Henle," *Int J Numer Methods Biomed Eng*, 28, 369–380.

Layton, H. (2002), "Mathematical models of the mammalian urine concentrating mechanism," in *Membrane Transport and Renal Physiology, The IMA Volumes in Mathematics and Its Applications*, eds. L. HE and W. AM, vol. 129, pp. 233–272, Springer, New York.

Layton, H., Pitman, E., and Moore, L. (1991), "Bifurcation analysis of TGF-mediated oscillations in SNGFR," *Am J Physiol* (*Renal Fluid Electrolyte Physiol* 30), 261, F904–F919.

Layton, H., Pitman, E., and Moore, L. (1995), "Instantaneous and steady-state gains in the tubuloglomerular feedback system," *Am J Physiol Renal Physiol*, 268, F163–F174.

Layton, H., Pitman, E., and Moore, L. (1997a), "Nonlinear filter properties of the thick ascending limb," *Am J Physiol* (*Renal Fluid Electrolyte Physiol* 42), 273, F625–F634.

Layton, H., Pitman, E., and Moore, L. (1997b), "Spectral properties of the tubuloglomerular feedback system," *Am J Physiol* (*Renal Fluid Electrolyte Physiol* 42), 273, F635–F649.

Layton, H., Pitman, E., and Moore, L. (2000), "Limit-cycle oscillations and tubuloglomerular feedback regulation of distal sodium delivery," *Am J Physiol Renal Physiol*, 278, F287–F301.

Leyssac, P. and Baumbach, L. (1983), "An oscillating intratubular pressure response to alterations in Henle loop flow in the rat kidney," *Acta Physiol Scand*, 117, 415–419.

Leyssac, P. and Holstein-Rathlou, N. (1986), "Effects of various transport inhibitors and oscillating TGF pressure responses in the rat," *Pflügers Arch*, 407, 285–291.

Loutzenhiser, R., Bidani, A., and Chilton, L. (2002), "Renal myogenic response: kinetic attributes and physiologic role," *Circ Res*, 90, 1316–1324.

Mackey, M. and Rudnick, R. (1994), "Global stability in a delayed partial differential equation describing cellular replication," *J Math Bio*, 33, 89–109.

Marsh, D. (1982), "Frequency response of autoregulation," *Kidney Int*, 22, S165–S172.

Marsh, D., Sosnovtseva, O., Pavlov, A., Yip, K., and Rathlou, N. H. (2005a), "Frequency encoding in renal blood flow regulation," *Am J Physiol Regul Integr Comp Physiol*, 288, R1160–R1167.

Marsh, D., Sosnovtseva, O., Chon, K., and Holstein-Rathlou, N. (2005b), "Nonlinear interactions in renal blood flow regulation," *Am J Physiol Regul Integr Comp Physiol*, 288, R1143–R1159.

Marsh, D., Sosnovtseva, O., Mosekilde, E., and Rathlou, N. H. (2007), "Vascular coupling induces synchronization, quasiperiodicity, and chaos in a nephron tree," *Chaos*, 17, 015114–1—015114–10.

Marsh, D., Wexler, A., Brazhe, A., Postnov, D., Sosnovtseva, O., and Rathlou, N. H. (2013), "Multinephron dynamics on the renal vascular network," *Am J Physiol*, 304, F88–F102.

Mason, J., Gutsche, H., Moore, L., and Müller-Suur, R. (1979), "The early phase of experimental acute renal failure. IV. The diluting ability of the short loops of Henle," *Pflügers Arch*, 379, 11–18.

Moore, L. and Mason, J. (1983), "Perturbation analysis of tubuloglomerular feedback in hydropenic and hemorrhaged rats," *Am J Physiol* (*Renal Fluid Electrolyte Physiol* 14), 245, F554–F563.

Moss, R. and Layton, A. (2014), "Dominant factors that govern pressure natriuresis in diuresis and antidiuresis: a mathematical model," *Am J Physiol Renal Physiol,* in press.

Nyengaard, J. and Bendtsen, T. (1992), "Glomerular number and size in relation to age, kidney weight, and body surface in normal man," *Anat Rec*, 232, 194–201.

Oldson, D., Layton, H., and Moore, L. (2003), "Effect of sustained flow perturbations on stability and compensation of tubuloglomerular feedback," *Am J Physiol Renal Physiol*, 285, F972–F989.

Persson, A., abd P Westerlund, Z. S., Greger, R., Schlatter, E., and Gonzalez, E. (1991), "Macula densa cell function," *Kidney Int*, 39, S3944.

Peti-Peterdi, J., Morishima, S., Bell, P., and Okada, Y. (2002), "Two-photon excitation fluorescence imaging of the living juxtaglomerular apparatus," *Am J Physiol Renal Physiol*, 283, F197–F201.

Pieroux, D., Erneux, T., Gavrielides, A., and Kovanis, V. (2000), "Hopf bifurcation subject to a large delay in a laser system," *SIAM J Appl Math*, 61, 966–982.

Pitman, E. and Layton, H. (1989), "Tubuloglomerular Feedback in a Dynamic Nephron," *Commun Pure Appl Math*, 42, 759–787.

Pitman, E., Layton, H., and Moore, L. (1993), "Dynamic flow in the nephron: filtered delay in the TGF pathway," *Contemp Math*, 114, 317–336.

Pitman, E., Zaritski, R., Moore, L., and Layton, H. (2002), "A reduced model for nephron flow dyanmics mediated by tubuloglomerular feedback," in *Membrane Transport and Renal Physiology, The IMA Volumes in Mathematics and Its Applications*, eds. L. HE and W. AM, vol. 129, pp. 345–364, Springer, New York.

Pitman, E., Zaritski, R., Kesseler, K., Moore, L., and Layton, H. (2004), "Feedback-mediated dynamics in two coupled nephrons," *Bull Math Biol*, 66, 1463–1492.

Ren, Y., Garvin, J., Liu, R., and Carretero, O. (2007), "Crosstalk between the connecting tubule and the afferent arteriole regulates renal microcirculation," *Kidney Int*, 71, 1116–1121.

Ryu, H. and Layton, A. (2013a), "Effect of tubular inhomogeneities on feedback-mediated dynamics of a model of a thick ascending limb," *Math Med Biol*, 30, 191–212.

Ryu, H. and Layton, A. (2013b), "Feedback-mediated dynamics in a model of coupled nephrons with compliant short loop of Henle," *AMS Contemporary Mathematics, Biological Fluid Dynamics: Modeling, Computations, and Applications,* in press.

Ryu, H. and Layton, A. (2013c), "Tubular fluid flow and distal NaCl delivery mediated by tubuloglomerular feedback in the rat kidney," *J Math Biol,* in press.

Sakai, T., Craig, D., Wexler, A., and Marsh, D. (1986), "Fluid waves in renal tubules," *Biophys J*, 50, 805–813.

Schnermann, J. and Briggs, J. (2008), "Function of the juxtaglomerular apparatus: Control of glomerular hemodynamics and renin secretion," in *Seldin and Giebisch's The Kidney: Physiology and Pathophysiology*, eds. A. RJ and H. SC, pp. 589–626, Elsevier Academic Press, Amsterdam; Boston, 4th edn.

Sgouralis, I. and Layton, A. (2012), "Autoregulation and conduction of vasomotor responses in a mathematical model of the rat afferent arteriole," *Am J Physiol Renal Physiol*, 303, F229–F239.

Sgouralis, I. and Layton, A. (2013), "Theoretical Assessment of Renal Autoregulatory Mechanisms," *Am J Physiol Renal Physiol,* in press.

Siu, K., Sung, B., Cupples, W., Moore, L., and Chon, K. (2009), "Detection of low-frequency oscillations in renal blood flow," *Am J Physiol Renal Physiol*, 297, F155–F162.

Sosnovtseva, O., Postnov, D., Mosekilde, E., and Holstein-Rathlou, N. (2003), "Synchronization of tubular pressure oscillations in interacting nephrons," *Chaos, Solitons & Fractals*, 15, 343–369.

Stephenson, J. (1972), "Concentration of urine in a central core model of the renal counterflow system," *Kidney Int*, 2, 85–94.

van Zanten, H. (2013), *An Introduction to Stochastic Processes in Continuous Time*, Lecture notes.

Wade, J., Lee, A., Ecelbarger, C., Mitchell, C., Bradford, A., Terris, J., Kim, G.-H., and Knepper, M. (2000), "UT-A2: a 55-kDa urea transporter in thin descending limb whose abundance is regulated by vasopressin," *Am J Physiol Renal Physiol*, 278, F52–F62.

Wagner, A., Holstein-Rathou, N., and Marsh, D. (1997), "Internephron coupling by conducted vasomotor responses in normotensive and spontaneously hypertensive rats," *Am J Physiol* (*Renal Physiol* 41), 272, F372–F379.

Weinstein, A. (1986), "An equation for flow in the renal proximal tubule," *Bull Math Biol*, 48, 29–57.

Wittner, M., Stefano, A. D., Wangemann, P., Nitschke, R., Greger, R., Bailly, C., Amiel, C., Roinel, N., and de Roufignac, C. (1988), "Differential effects of ADH on sodium, chloride, potassium, calcium and magnesium transport in cortical and medullary thick ascending limbs of mouse nephron," *Pflügers Arch.*, 412, 516–523.

Yip, K., Holstein-Rathlou, N., and Marsh, D. (1991), "Chaos in blood flow control in genetic and renovascular hypertensive rats," *Am J Physiol* (*Renal Fluid Electrolyte Physiol* 30), 261, F400–F408.

Yip, K., Holstein-Rathlou, N., and Marsh, D. (1992), "Dynamics of TGF-initiated nephron-nephron interactions in normotensive rats and SHR," *Am J Physiol* (*Renal Fluid Electrolyte Physiol* 31), 262, F980–F988.

Young, D. and Marsh, D. (1981), "Pulse wave propagation in rat renal tubules: implications for GFR autoregulation," *Am J Physiol* (*Renal Fluid Electrolyte Physiol* 9), 240, F446–F458.

Yu, N., Kuske, R., and Li, Y. (2006), "Stochastic phase dynamics: multiscale behavior and coherence measures," *Phys Rev E Stat Nonlin Soft Matter Phys*, 73, 2407–2416.

Yu, W., Sandoval, R., and Molitoris, B. (2005), "Quantitative intravital microscopy using a Generalized Polarity concept for kidney studies," *Am J Physiol Cell Physiol*, 289, C1197–C1208.

Biography

NAME

Hwayeon Ryu

EDUCATION

Duke University, **Ph.D.,** *Mathematics* May 2014

Duke University, **M.S.,** *Mathematics* May 2011

Korea University in South Korea, **B.S.,** *Mathematics* Aug 2008

PUBLICATIONS

• Ryu and Layton (2013b), Feedback-mediated dynamics in a model of coupled nephrons with compliant short loop of Henle, *AMS Contemporary Mathematics, Biological Fluid Dynamics: Modeling, Computations, and Applications*, in press.

• Ryu and Layton (2013c), Tubular fluid flow and distal NaCl delivery mediated by tubuloglomerular feedback in the rat kidney, *J Math Biol*, in press.

• Ryu and Layton (2013a), Effect of tubular inhomogeneities on feedback-mediated dynamics of a model of a thick ascending limb, *Math Med Biol*, 30(3):191–212.

• Layton, Pham, and Ryu (2012b), Signal transduction in a compliant short loop of Henle, *Int J Numer Methods Biomed Eng*, 28:369–383.